UNDERSTANDING SOLID-ELECTROLYTE INTERPHASE FORMATION AT THE LITHIUM METAL ANODE OF LITHIUM-SULFUR BATTERIES

A Dissertation

by

LUIS EDUARDO CAMACHO FORERO

Submitted to the Office of Graduate and Professional Studies of
Texas A&M University
in partial fulfillment of the requirements for the degree of

DOCTOR OF PHILOSOPHY

Chair of Committee,	Perla B. Balbuena
Committee Members,	Jodie Lutkenhaus
	Jorge M. Seminario
	Dong Hee Son
Head of Department,	Arul Jayaraman

December 2019

Major Subject: Chemical Engineering

ABSTRACT

Lithium-sulfur (Li-S) batteries are one of the most promising chemistries for the next generation of energy storage devices. In a standard Li-S cell, the metallic lithium anode is an essential component of the battery due to its low density, extremely high theoretical specific capacity, and very low negative electrochemical potential. However, several challenges related to the use of Li metal have prevented this battery technology from becoming commercially available. For instance, Li-anodes are highly reactive, which results in the continuous decomposition of the electrolyte and the formation of the solid-electrolyte interphase (SEI) layer. This, combined with the non-uniform deposition of Li-ions during plating at the anode surface, can seriously affect the performance, cycling, and safety of the battery. In addition, it has been suggested that a controlled SEI formation at the metallic Li anode can yield enhanced battery performance. Hence, a comprehensive understanding of how the SEI layer is formed can help elucidate improvements in this battery technology.

In this work, the formation of the SEI layer in Li-S batteries is investigated using density functional theory (DFT) and *ab initio* molecular dynamics (AIMD) simulations. The stability of liquid organic-based electrolyte components, salt concentration, electron-rich environments, and the use of inorganic solid-state electrolyte (SSE) materials are explored in order to provide molecular-level fundamental insights into how the nature and composition of the electrolyte can alter the initial stages of the SEI formation.

The products of electrolyte decomposition and electro-/chemical reaction pathways of liquid electrolyte component such as solvent and salts are predicted from AIMD simulations of electrolyte-anode interfaces. Energetics of reactions from DFT ground-state optimizations are also presented to confirm the decomposition mechanisms. Some significant differences are then drawn regarding the use of low and high salt concentrations. Simulations under electron-rich environments show additional multi-electron electrochemical reactions of solvent and salt decomposition taking place due to the excess of electrons and the presence of radical anions in the solution. Finally, the initial stages of formation, stability, and main constituents of interfaces between Li-metal and S-based electrodes with sulfide-based SSEs are characterized in detail.

DEDICATION

To my family for their unconditional love and support

ACKNOWLEDGEMENTS

First of all, I would like to express my most sincere gratitude to Dr. Balbuena – my advisor – who, from the first moment, deposited her confidence in my abilities by granting me the opportunity to be part of her research group. I am grateful for her constant support, guidance, mentorship, encouragement, and, of course, patience. I will always cherish all those invaluable experiences she supported over the years: external courses, workshops, conferences, collaborations, external research, and teaching since they have been an instrumental part of learning how to be the researcher I have become. Above all, thank you for leading by example and showing me how to be a better human being. I would also like to thank my committee members, Drs. Lutkenhaus, Seminario, and Son, for their guidance and support through the course of this journey.

Thanks also go to my coworkers in Dr. Balbuena's group for their insightful discussions and support, and to my friends for making my time at Texas A&M University a joyful experience. In addition, I would like to thank Taylor W. Smith and Dr. Vijay Murugesan for their contributions to this research work, and Dr. Roberto C. Longo for his assistance with Quantum ESPRESSO.

Finally, I am forever thankful to my loving mother and father for their endless support and relentless encouragement for me to pursue education and knowledge; to my sweet siblings and niece for their smiles that made those harsh moments more endurable; and to my adorable fiancée for her patience, love, and sharing this amazing path with me. And to those kids with big dreams, education *is* the path to accomplish *anything* in life.

CONTRIBUTORS AND FUNDING SOURCES

Contributors

This work was supervised by a dissertation committee consisting of Professors Perla B. Balbuena [advisor], Jodie Lutkenhaus, and Jorge M. Seminario of the Department of Chemical Engineering and Professor Dong Hee Son of the Department of Chemistry.

Experimental results and analyses presented in Chapter 3 and Appendix A were provided by Dr. Vijayakumar Murugesan from Pacific Northwest National Laboratory (PNNL). Simulations of polysulfide decomposition reactions in Chapter 3 and some AIMD simulations described in Chapter 4 were conducted in part by Taylor W. Smith, a former Master of Science student of the Department of Materials Science and Engineering.

All other work conducted for this dissertation was completed by the student independently.

Funding Sources

This work was supported by the U.S. Department of Energy's Office of Energy Efficiency and Renewable Energy (EERE), Office of Vehicle Technologies under Contract No. DE-EE0006832 and DE-EE0007766 under the Advanced Battery Materials Research (BMR) Program, and also as part of the Battery 500 Consortium under Award No. DE-EE0008210. Supercomputing resources were provided by the Texas A&M University High Performance Computing Center (HPRC), the Texas Advanced Computing Center (TACC), and the National Energy Research Scientific Computing Center (NERSC), a U.S. DOE's Office of Science User Facility under Contract No. DE-

AC02-05CH11231. The experimental work was funded by the Joint Center for Energy Storage Research (JCESR) program under the U.S. Department of Energy's Office of Basic Energy Sciences. Finally, additional financial support was provided by the Texas A&M Energy Institute Fellowship, Phillips 66 Graduate Fellowship, and the Electrochemical Society under travel awards from the Battery Division and Symposium Sponsor (Mercedes-Benz R&D America).

NOMENCLATURE

AIMD	*Ab Initio* Molecular Dynamics
DFT	Density Functional Theory
DME	1,2-Dimethoxyethane
DOL	1,3-Dioxolane
EC	Ethylene Carbonate
GGA	Generalized Gradient Approximation
LIB	Li-ion Battery
LiFSI	Lithium bis(fluorosulfonyl)imide
Li-S	Lithium-Sulfur
LiTFSI	Lithium bis(trifluoromethanesulfonyl)imide
MD	Molecular Dynamics
PAW	Projector-Augmented Wave
PBE	Perdew-Burke-Ernzerhof
PS	Polysulfide
SEI	Solid-Electrolyte *Interphase*
SSE	Solid-State Electrolyte
VASP	Vienna *ab initio* Simulation Package
XPS	X-ray Photoelectron Spectroscopy

TABLE OF CONTENTS

Page

LIST OF FIGURES

Page

LIST OF TABLES

Page

1. INTRODUCTION

The increasing demand for smart portable electronic devices and electric/hybrid vehicles; rapid technological advancements; and the desire to move toward sustainable sources of energy (e.g., solar, wind) have led to a hasty expansion of the battery market.[1] Although conventional Li-ion batteries (LIBs) have dominated the secondary (i.e., rechargeable) battery market over the last decades, state-of-the-art LIBs are already reaching their limited theoretical energy density due to their Li-intercalation chemistry and high cost. As a result, alternative technologies are currently being studied and developed.[2-3] Among the potential chemistries to substitute the traditional LIBs, the lithium-sulfur (Li-S) battery is one of the most promising candidates due to its reduced cost, low toxicity, and high theoretical specific energy (2567 Wh kg^{-1}).[4-5]

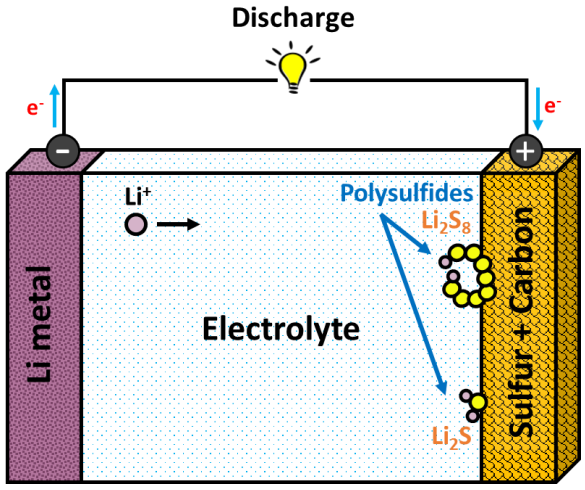

Figure 1.1 Illustration of a standard Li-S battery during discharge.Filled yellow and pink circles indicate Li and S atomic species, respectively.

Figure 1.1 shows the schematic of a standard rechargeable Li-S cell, where the anode is typically pure lithium metal and the cathode is a sulfur-based composite; containing elemental sulfur, a conductive additive, and a binder. The battery operates by sequential reduction of S_8 to Li_2S at the cathode during the discharge (lithiation), which yields the formation of intermediate products known as lithium polysulfides (PS): Li_2S_8, Li_2S_6, Li_2S_4, Li_2S_2, and Li_2S. During charge (delithiation), on the other hand, deposited species such as Li_2S and Li_2S_2 are expected to be oxidized, leading to the formation of the original S_8 rings.[6] However, despite decades of development, there are still several limitations that need to be addressed before Li-S batteries are feasible for mass commercialization.[5]

At the cathode, sulfur (S_8) has a theoretical specific capacity of 1675 mAh g^{-1}; however, it must be combined with a conductive additive – typically carbon – due to its insulating nature, reducing the overall energy density of the cell.[7-8] In addition, one of the most common problems in Li-S batteries is the "shuttle" of long-chain Li_2S_n (where $4 \leq n \leq 8$) from the cathode to the anode.[9-10] Long-chain PS species are normally soluble in organic-based liquid electrolytes and can diffuse to the anode, where are reduced to insoluble Li_2S_2 and Li_2S,[5, 7] resulting in the formation of an interfacial layer that can extensively grow and passivate the lithium anode.[11-12] In an effort to minimize this shuttle effect by retaining the PS at the cathode side, a variety of novel cathode material architectures (e.g., carbon nanotubes, graphene, and carbon fibers)[13] and separators[14] have been studied. Additionally, another successful approach to anchor the PSs at the cathode

is the use of functionalized polymer composite frameworks, which work as an interlocking binding mechanism due to multifunctional binders and sulfur hosts.[15]

In a typical Li-S battery, lithium-metal is considered as the ideal candidate for anode materials because of its low density, extremely high theoretical specific capacity (3860 mAh g^{-1}), and very low negative electrochemical potential (-3.040 V vs. SHE).[16] However, the use of Li anodes raises concerns due to its high reactivity and tendency to form dendrites upon cycling, which can lead to reduced energy density followed by failure of the cell.[17] Additionally, as a consequence of lithium's reactive nature, electrolyte stability is key to control parasitic reduction reactions of the electrolyte taking place at the surface of the anode leading to the formation of a multicomponent film known as the solid-electrolyte interphase (SEI) layer.[18] The nature and properties of the SEI layer are critical to the battery operation since it is one of the main causes for continued irreversible capacity loss.

The SEI formation takes place when the redox potential Φ of the electrodes falls out of the electrochemical window of the electrolyte, see Figure 1.2. In the case of the Li-S battery, if the Fermi level of the metallic lithium anode is above the LUMO (lowest unoccupied molecular orbital) of the electrolyte, the electrolyte is reduced. Similarly, the electrolyte is oxidized when the sulfur-cathode composite's Fermi is lower than the electrolyte's HOMO (highest occupied molecular orbital).[19-20] Likewise, this concept can also be extended to solid-state electrolytes[21], in such case, the LUMO and HOMO become the conduction band minimum (CBM) and valence band maximum (VBM), respectively; and E_g would be the electronic band gap of the solid material.

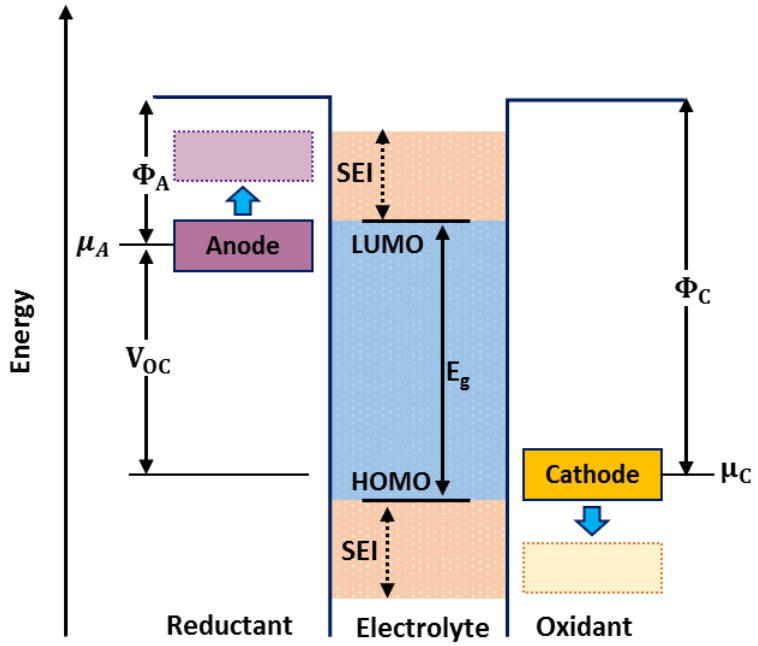

Figure 1.2 Representation of the open-circuit (OV) energy diagram of an electrolyte. Φ_A, Φ_C, μ_A, and μ_B are the work function and redox potential of the anode and cathode, respectively. E_g is the electrolyte stability window. Based on the diagram by Goodenough and Kim.[20]

It is extensively believed that the characteristics of the SEI can play a critical role in controlling dendrite growth and surface passivation at the Li metal surface. In order for a SEI film to act as a protective layer, it must have the following properties:[22] (i) proper thickness – thick enough to completely prevent electron transport to electrolyte, but not too thick to increase Li-ion diffusion resistance; (ii) high ionic conductivity; (iii) strong mechanical performance to adapt the shocking and non-uniform volume change during repeated Li plating and stripping; and (iv) extraordinary stability in morphology, structure, and chemistry during long-term cycling.

The SEI layer constituents and, consequently, their properties are critically dependent on the nature of the electrolyte. Therefore, a lot of efforts have been devoted to developing electrolyte modification.[23] In general, electrolytes can be divided into three

states: liquid, quasi-solid, and solid. Liquid electrolytes consist of solvents and Li salts, where the solvents are typically carbonate-based or ether-based organic compounds such as ethylene carbonate (EC), dimethyl carbonate (DMC), propylene carbonate (PC), 1,3-dioxolane (DOL), 1,2-dimethoxyethane (DME), and diethylene glycol dimethyl ether (DEGDME).[22] In this area, most research has focused on additives and Li salt concentration since it is difficult to find solvents that are stable against Li anodes. With regards to quasi-solid electrolytes, the most common type of materials being used are room-temperature ionic liquids and gel polymer electrolyte such as poly(ethylene oxide) (PEO).[23] Finally, solid-state electrolytes (SSE) materials are being explored as an alternative because, unlike liquid organic-based electrolytes, inorganic SSEs are usually non-flammable and have the potential to suppress PS shuttle and Li dendrites; however, these materials are typically characterized by having low Li-ion conductivity and poor contact resistance at the electrode interfaces.[24-26] Nevertheless, a few SSE families have been the focus of research due to their potential application for next-generation batteries.[23, 27] For instance, oxides such as perovskites (e.g., $Li_{3.3}La_{0.56}TiO_3$) and garnet-type crystals (e.g., $Li_7La_3Zr_2O_{12}$) have exhibited high ionic conductive and electrochemical stability against metallic lithium.[24] In addition, N-doped phosphates (LiPON) materials have shown to form a stable SEI layer at Li anodes. Sulfide SSEs, which are typically prepared from mechanical milling at low-temperatures, have particularly drawn a lot of attention as a promising electrolyte family because of their Li-ion superconductor behavior, mechanical flexibility, and, especially, compatible interface with sulfur cathodes.[28-29]

Although some relationships could be drawn from previous studies regarding the effect of electrolytes on the formation and products comprising the SEI layer, a more comprehensive understanding on how different variables can modify the formation of this film at the Li anode is still required. For this reason, the main goal of this dissertation is to *elucidate how the nature and composition of the electrolyte affect the initial stages of SEI formation as well as other electrochemical phenomena governing the electrode-electrolyte interfaces in Li-S batteries*. To achieve this goal, first-principles atomistic simulation methods such as density functional theory (DFT) and *ab initio* molecular dynamics AIMD are employed to provide an atomistic description of those interfaces. In Chapter 2, a general overview of the computational and theoretical methods used in this dissertation – including DFT, AIMD, and Bader charges – is presented. However, specific computational details and models are further described in each chapter. In addition, this study could be divided into two main parts depending on the state of matter of the electrolytes being studied, e.g., liquid and solid. For instance, Chapters 3 to 5 address interfaces between liquid electrolytes and the Li-metal anode, and solid-state electrolytes are considered in Chapters 6 and 7. First, in Chapter 3, the reactivity of the Li anode surface is evaluated by studying the stability and reduction pathways of different components of the liquid electrolyte such as solvent, Li salt, and PS species. Then, the effect of low and high salt concentration on the formation of the SEI products and electrolyte degradation is investigated in Chapter 4. In order to provide some insights on how an external potential may impact the electrolyte decomposition, the role of electron-rich environments on the reduction pathway and energetics of electrolyte components is

discussed in Chapter 5. Additionally, Chapter 6 addresses the interfacial stability of lithium metal and SSEs, and the characteristics of formed SEI films (stability and composition). Consequently, the use of SSEs brings an inherent challenge on the interfacial compatibly and resistance at both anode and cathode electrodes. Thus, as a result of such interconnected chemistry, interfacial phenomena between S-based cathodes and SSE materials are studied in Chapter 7. Finally, in Chapter 8, the conclusions of this dissertation and future directions are given.

2. THEORETICAL BACKGROUND

The recent advances in high-performance computing and physical and theoretical chemistry have led first-principles based computational methods to play a significant role in the development of new technologies. For instance, recent joint efforts from computational modeling and *in situ* experimental techniques have allowed a better understanding of complex problems in battery systems such as interfacial phenomena and SEI formation[19] and, in general, the design of new or enhanced materials for numerous applications. For that reason, and in order to provide the reader with some theoretical background of the computational methods used throughout this dissertation, a brief overview of quantum mechanical methods is provided in the following sections of this chapter, including some key aspects of DFT and AIMD simulations.

2.1. The Schrödinger Equation

In 1924, Louis de Broglie[30] postulated that matter, regardless of the size of the particle, exhibits a particle-wave duality behavior. However, the wave nature becomes more important for particles at the atomistic level, e.g., electrons and protons. Therefore, expressing the *wave-like* behavior of electrons in a mathematical form became the focus of the scientific community at the time.[31] Only a couple of year later, in 1926, Erwin Schrödinger derived an equation that can describe the quantum mechanical behavior of a system.[32] The time-independent Schrödinger can be simply written as:

$$\hat{H}\psi = E\psi \tag{2.1}$$

In this equation, $\hat{\mathrm{H}}$ is the Hamiltonian operator, the wave function ψ is a set of eigenstates of the Hamiltonian, and E_n is the energy states of the system or eigenvalues that satisfy the time-independent Schrödinger equation. The lowest energy state is known as the *ground state* energy, a useful quantity that helps determine physical observables related to the electronic structure of a system. However, in order to find the exact solution of the equation, a precise form of the Hamiltonian operator is required. $\hat{\mathrm{H}}$ can be written in terms of the operator of the kinetic and potential energies of the nuclei and the electrons:[33]

$$\hat{H} = \hat{T}_n + \hat{T}_e + \hat{V}_{ne} + \hat{V}_{ee} + \hat{V}_{nn} \tag{2.2}$$

where the two first terms correspond to the kinetic energy of the nuclei and electrons, and the other three potential energy operators describe the Coulomb interaction between the nuclei-electrons, electrons-electrons, and nuclei-nuclei. In addition, an important observation in quantum mechanics is that nuclei are a few orders of magnitude heavier than electrons, as a result, it can be assumed that electrons respond more instantly to changes in their surrounding than nuclei. Therefore, we can split the problem into two parts. This is known as the *Born-Oppenheimer approximation.*[34] First, the equations that describe the motion of the electrons are solved at fixed nuclei positions. Then, the ground-state energy of the electrons can be written as a function of the positions of the nuclei. In other words, the Schrödinger equation can be expressed in terms of the electrons only, and the solution to this equation provides the ground-state energy of the electrons.

In a collection of atoms, the electrons are interacting with multiple nuclei, resulting in a multi-body description of the Schrödinger equation, which can be written as[35]

$$\left[-\frac{\hbar}{2m}\sum_{i=1}^{N}\nabla_i^2+\sum_{i=1}^{N}V(\boldsymbol{r_i})+\sum_{i=1}^{N}\sum_{j<i}U(\boldsymbol{r_i},\boldsymbol{r_j})\right]\psi=E\psi \qquad (2.3)$$

where *m* is the electron mass, and the three terms of the Hamiltonian (from left to right) correspond to the kinetic energy of the electrons, the interaction between nuclei and electrons, and the interaction between different electrons. Therefore, ψ becomes the electronic wave function of *N* electrons; each with spatial coordinates, $\boldsymbol{r_i}$, and *E* is the ground-state energy of the electrons. Although it is possible to solve this equation for simple systems such as the H atom, it becomes too complex to be solved for groups of atoms, which, in fact, are used to treat problems such as the ones described in this work. As a result, several approximations were introduced to deal with the N-electron problem. For instance, the Hartree-Fock (HF) method (1930) assumes that the *N-electron* wave function can be expressed as a linear combination of the non-interacting one-electron ψ in the form of a Slater determinant.[36] However, the applicability to real systems and the accuracy of this method were still limited. In 1965, Kohn and Sham developed a method based on electron density and functional theorems. This new scheme was called the *density functional theory* (DFT)[37] and it is the fundamental theoretical basis of the present work.

2.2. Density Functional Theory

A key observation in this theory is that, unlike macroscopic objects that can be differentiated among them, electrons are exactly the same, that is, experimentally, we cannot assign tags or labels to the electrons. The quantity that can be measured is the probability of finding the *N* electrons at a certain set of spatial coordinates, $\boldsymbol{r_1},\ldots,\boldsymbol{r_N}$.

Therefore, the density of electrons ***n(r)***, which is a similar quantity to the probability, can be written in terms of the individual electron wave functions as follows:[35]

$$n(\boldsymbol{r}) = 2\sum_{i} \psi_i^*(\boldsymbol{r})\psi_i(\boldsymbol{r}) \tag{2.4}$$

In this equation, the asterisk denotes the complex conjugate, and the *2* comes from Pauli's exclusion principle, which states that each wave function can be occupied by two electrons with different spins. One key take away message from this equation is that the electron density is only a function of three coordinates, contrary to the initial postulate of the Schrödinger equation where the full wave function depends on *3N* coordinates.

In 1964, Kohn and Hohenberg presented two fundamental mathematical theorems that, soon, would be become the basis for developing the density functional theory. The theorems state that[35] (*i*) the ground state energy form the Schrödinger equation is a sole functional of the electron density, *E*[***n(r)***]; and (*ii*) if the *true* functional form is known, then, the full solution of the Schrödinger equation is the electron density that minimizes the energy of the overall functional.[38] Up to this point, there was still not a way to find the correct electron density. In 1965, Kohn and Sham (KS) showed that ***n(r)*** could be obtained by solving a series of equations that involve single-electron wave functions $\psi_i(\boldsymbol{r})$.[37] They defined the form of the equation for each electron as:

$$\left[-\frac{\hbar}{2m}\nabla^2 + V(\boldsymbol{r}) + V_H(\boldsymbol{r}) + V_{XC}(\boldsymbol{r})\right]\psi_i(\boldsymbol{r}) = \varepsilon_i\psi_i(\boldsymbol{r}) \tag{2.5}$$

Here, the terms of the left correspond to the kinetic energy, and three potentials: V, V_H, and V_{XC}. V(**r**) defines the electron-nuclei interactions. The second potential, known as the Hartree potential, describes the interaction (Coulomb repulsion) between the electron

considered in by the equation and the electron density of all the electrons including itself. This self-interaction is clearly unphysical and has to be compensated in the third potential in addition to all other electron-electron interactions not included in the other terms due to the use of single-electron wave equations. V_{XC} is the exchange-correlation potential and has the form of $\frac{\delta E_{XC}(\boldsymbol{r})}{\delta n(\boldsymbol{r})}$, where E_{XC} is the energy of the exchange-correlation (XC) functional. Assuming that the form of this functional is known, the solution of the KS equations relies on a self-consistent iterative algorithm to solve *n(r)*, see Figure 2.1.

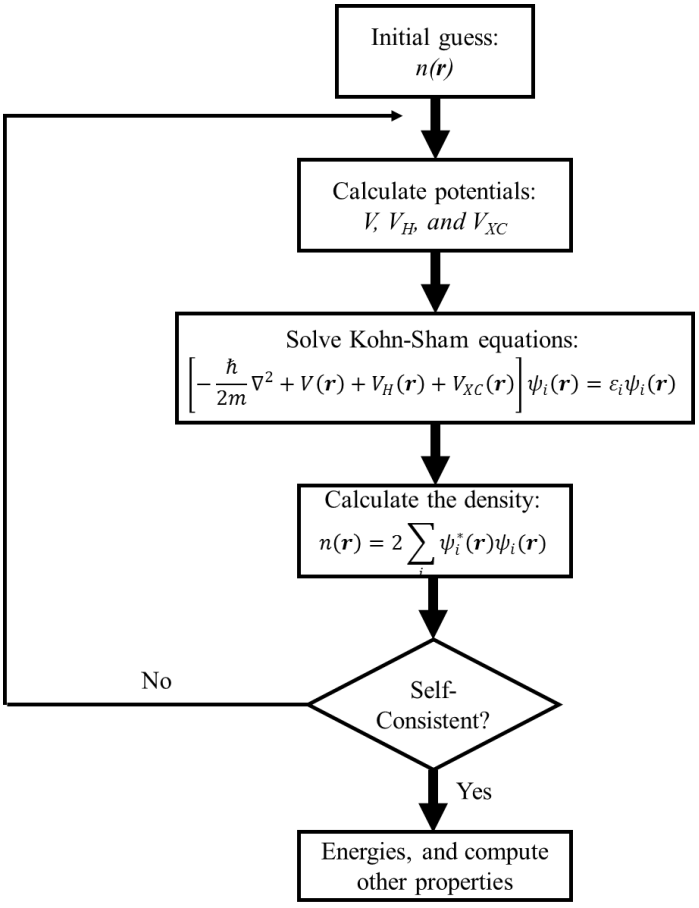

Figure 2.1 Schematic representation of the iterative self-consistent method to solve the KS equations.

Another property that is useful for describing atomistic systems, in general, is the force. The force acting on an atom with coordinates $\boldsymbol{r}$ can be written according to the Hellmann-Feynman theorem[39-40] as the gradient of the ground state energy E_0:

$$\boldsymbol{F_I} = -\nabla_I E_0(\boldsymbol{r}) = \langle \Psi_0(\boldsymbol{r}) | \nabla_I \hat{H}(\boldsymbol{r}) | \Psi_0(\boldsymbol{r}) \rangle \quad (2.6)$$

In the case of geometry optimization, i.e., the relaxation of a group of atoms to their state of lowest energy, the force acting over the atoms should be zero. Therefore, an external optimization loop can be added to the self-consistent algorithm shown in Figure 2.1. In every ionic relaxation step, new nuclei positions are obtained, and, as a result, a new electron density (and energy) needs to be computed. The positions of the ions are updated every loop until the difference in the ground state energies of two consecutive ionic steps is negligible.

2.2.1. Exchange-Correlation Functional

According to the Hohenberg-Kohn theorem, the existence of the exchange-correlation function is guaranteed; however, the exact or *universal* form of the functional $E_{XC}[\psi_i]$ is unknown. As a result, many approximations have been implemented for practical applications of DFT. For instance, if a uniform electron gas is assumed, the electron density is constant. Therefore, we can determine the XC potential at each position as a function only of the electron density at that particular location, i.e., the functional depends only on the local $n(\boldsymbol{r})$. This method is called the *local density approximation* (LDA).[41] Another widely known and used type of functional is the *generalized gradient approximation* (GGA), where the functional depends not only on the local electron density but also on the local gradient in the electron density. A few examples of GGA functionals

are the Perdew-Wang (PW91),[42] Becke-Lee-Yang-Parr (BLYP),[43-44] and the Perdew-Burke-Ernzerhof (PBE)[45]. GGA functionals work very well for most structural properties within 1 to 3% error. However, the band gaps are typically underestimated.[31] One way to overcome these issues is to use hybrid functionals. Here, an HF contribution is included within the exchange part of the functional, so that the exchange-correlation energy has the form:[35, 44]

$$E_{xc} = yE_x^{HF} + (1-y)E_x^{GGA} + E_c^{GGA} \quad (2.7)$$

where y is a fractional number between 0 and 1, E_x and E_c are the exchange and correlation energies, respectively. Some of the most popular hybrid functionals are B3LYP,[46] PBE0,[47] and HSE[48].

2.2.2. Pseudopotential

One of the most effective approaches to reduce the computational cost of DFT simulations is through the use of pseudopotentials. Pseudopotentials are a representation of the core electrons, which are not quite relevant in defining the bonding and other physical characteristics of materials. This is called the *frozen core approximation* since the properties of the core electron are then fixed in this effective way. The pseudopotentials are constructed for a single atom of one element. Two popular types of pseudopotentials are the ultrasoft pseudopotentials (USPPs)[49] and the projector augmented-wave (PAW)[50-51] method. The USPPs require significantly lower cutoff energies than other approaches; however, some empirical parameters are needed. On the other hand, the PAW approach gives more accurate results than USPPs when dealing with strong magnetic moments or with atoms that have very different electronegativity. A

particular advantage of using PAW pseudopotentials is that the method returns the all-electron charge density of the valence orbitals,[31] a property that becomes very useful when working with charge transfer analysis such as in electrochemical systems.

2.2.3. Basis Sets

The solution to Schrödinger's equation or, in another form, the KS equations, can have *any* shape, which could be very demanding computationally. One way to address this is by approximating the solution to a linear combination of known basic functions. For instance, to model atoms and molecules with highly localized orbitals, Gaussian or other local basis sets centered at the atoms can be used.[52] On the other hand, nonlocal functions such as plane-wave basis sets are also commonly used to treat materials, particularly, solids. In addition, a plane-wave basis set often requires 100s of plane waves per atom, whereas local basis sets typically need 10-20 functions to reach acceptable accuracy.[31]

2.2.4. Reciprocal Space and *k*-points

To reduce the calculation size when working with solids, the solid must be modeled as a supercell made of several repeated primitive or unit cells. The supercell is constructed in such a way that it can be extended to infinity by using periodic boundary conditions (PBCs). Solving Schrödinger's equation for a periodic system implies that the wave function has to satisfy the Bloch's theorem,[53] which means that the solution can be expressed as a linear combination of the solution at each $\boldsymbol{k}$ independently:

$$\phi_k(\boldsymbol{r}) = \exp(i\boldsymbol{k}\cdot\boldsymbol{r})\, u_k(\boldsymbol{r}) \tag{2.8}$$

where $u_k(\boldsymbol{r})$ is periodic in space with the supercell's periodicity, and $\exp(i\boldsymbol{k}\cdot\boldsymbol{r})$ is a plane wave. Due to mathematical complexity, the supercells are transformed from the real space

($\boldsymbol{r}$) into the reciprocal space ($\boldsymbol{k}$). One important observation is that the larger the lattice vectors in real space are, the reciprocal space lattice vectors become shorter. Similar to the case of the primitive cell in real space, which is the minimum volume required to account for all the relevant information, the reciprocal space can also be confined to what is known as the irreducible *Brillouin Zone* (IBZ) by using symmetry operations of rotation and inversion. To describe the properties within the IBZ, the reciprocal space has to be sampled by a number of finite points called *k*-points. Two key observations need to be considered when selecting the *k*-point mesh; they have to be (*i*) as few as possible to reduce computational time and (*ii*) enough to represent the actual system.[31, 35]

A widely used method to generate a mesh of evenly spaced *k*-points in the IBZ was developed by Monkhorst and Pack (1976)[54]. Here we only need to specify how many *k*-points are required along each reciprocal lattice vector. For instance, if a cubic cell (in real space) is considered and *M k*-points are sufficiently enough to converge the desirable properties of the material, then the calculation will be performed using *M* x *M* x *M k*-points, if the lattice vectors are not equal, the *k*-points will need to be adjusted accordingly.

2.3. *Ab Initio* Molecular Dynamics

In addition to DFT, another method that is commonly used to study materials at the atomistic level is classical molecular dynamics (MD).[31, 35] In this method, the movements of the atoms is determined by classical mechanics. Thus, the nature of the atoms is treated as sphere-like particles that follow Newton's equations of motion:

$$\boldsymbol{F} = m\boldsymbol{a} = m\frac{d\boldsymbol{v}}{dt} = m\frac{d^2\boldsymbol{r}}{dt^2} \tag{2.9}$$

where $\boldsymbol{F}$, $\boldsymbol{a}$, $\boldsymbol{v}$, and $\boldsymbol{r}$ are the force, acceleration, velocity, and position vectors; m and t are the mass of the particle in motion and time. In general, the energy state of a group of N atoms can be defined by the total kinetic (K) and potential (U) energies (E=K+U):

$$K = \frac{1}{2}\sum_{i=1}^{N} m_i \boldsymbol{v_i^2} \tag{2.10}$$

$$U = U(\boldsymbol{r_1}, \dots, \boldsymbol{r_N}) \tag{2.11}$$

Additionally, if the energy of the system is conserved ($dE/dt = 0$), the force acting on the i^{th} atom can be calculated as:

$$\boldsymbol{F_i} = -\boldsymbol{\nabla_i} U \tag{2.12}$$

As a consequence, the force can be computed from interatomic potentials that depend only on the atomic positions. The next step is solving this set of equations, which results in a very complex system of $6N$ first-order differential equations. These systems are challenging to be solved analytically. Therefore, numerical approaches are used to find the dynamics of the atoms. For instance, the Verlet algorithm[55] is based on a truncated Taylor expansion of the derivative of the positions:

$$r_i(t + \Delta t) \cong 2r_i(t) - r_i(r - \Delta t) + \frac{F_i(t)}{m_i}\Delta t^2 \tag{2.13}$$

where Δt (time step) has to be sufficiently small – in the order of *fs* (10^{-15} *s*) – to provide an accurate description of the trajectory of the atoms.

Another important approach to define the equations of motion is the Lagrangian (L), which is written in terms of the kinetic and potential energies as $L=K-U$. Thus, the systems of equations to be solved for each coordinate are:

$$\frac{d}{dt}\left(\frac{\partial L}{\partial v_i}\right) = \frac{\partial L}{\partial r_i} \tag{2.14}$$

One of the drawbacks of using classical MD is that it relies on the accuracy and availability of empirical interatomic potentials and force fields. Therefore, properties such as binding energies, electronic and magnetic structures are either challenging or cannot be obtained with this method. Fortunately, we could, in fact, calculate the potential energy of the atoms by using quantum mechanics or more precisely DFT. This concept is what is known as *ab initio* MD (AIMD) simulations.[56] Therefore the Lagrangian can be expressed as:

$$L = K - U = \frac{1}{2}\sum_{i=1}^{N} m_i \boldsymbol{v_i^2} - E[\phi(\boldsymbol{r_1}, \dots, \boldsymbol{r_N})] \tag{2.15}$$

where $\phi(\boldsymbol{r_1}, \dots, \boldsymbol{r_N})$ is the KS solution for the electronic ground state of the system. Here two implementations are the most common in the scientific community: the Born-Oppenheimer MD (BOMD)[56] and the Car-Parrinello MD (CPMD)[57]. These two methods work similarly to classical MD, the main difference is how the dynamics of the electrons are incorporated into the approach. In the BOMD approach, the positions of the nuclei are fixed to solve the KS equations using the algorithm in Figure 2.1, the electrostatic forces are then determined by the Hellmann-Feynman theorem discussed above, and finally, the atoms are moved via classical MD. This process is repeated until convergence is achieved. Alternatively, CPMD couples the electronic and ionic steps by variational minimization to find the electronic ground state, including a classical description of the electrons. This method seems to work well for semiconductors and insulator; however, trajectories may drift away from the potential energy surface for metals.[31] In this work, we use the BOMD

approach as implemented in the Vienna *ab initio* Simulation Package (VASP),[58-60] and it is referred to as AIMD unless stated otherwise.

2.3.1. Statistical Ensembles

In an MD simulation box, each atom behaves differently and new microstates are formed every time step. Nevertheless, after proper equilibration of the cell, it becomes a large set of possible configurations of the atoms known as an *ensemble* that yields macroscopic and thermodynamic properties such as number of particles *N*, volume *V*, temperature *T*, pressure P, and Energy *E*.[61] The *microcanonical* and *canonical* are two of the most commonly used ensembles in MD simulations. In the microcanonical ensemble, the energy of the system is conserved, i.e., the system is isolated, here N, V, and E are constant, the reason why this ensemble is referred sometimes as *NVE*. In the canonical ensemble or *NVT*, the system is allowed to exchange heat with its surroundings in order to keep the temperature constant. The isobaric-isothermal (*NPT*) and grand canonical (μVT, μ=chemical potential) ensembles are also used in some applications.

2.3.2. Radial Distribution Functions

One way to characterize the atom distribution with respect to other species in a trajectory or a single state of a simulation box is by calculating the radial distribution function (RDF), *g(r)*, similar to x-ray diffraction to characterize crystalline materials. RDFs can be computed from the summation of the atoms found within an interval Δr at a given radial distance *r*, N(r, Δr):

$$\mathrm{g}(r) = \frac{dN/N}{dV/V} = \frac{V}{N}\frac{\langle N(r,\Delta r)\rangle}{4\pi r^2 \Delta r} \tag{2.16}$$

where $4\pi r^2 \Delta r$ is the volume of the shell (r to $r+\Delta r$), see Figure 2.2a. An example of a typical RDF of AIMD simulation of a liquid is shown in Figure 2.2b. It must be noted that the *g(r)* of crystalline solids will exhibit sharp peaks due to the crystallinity of the material.

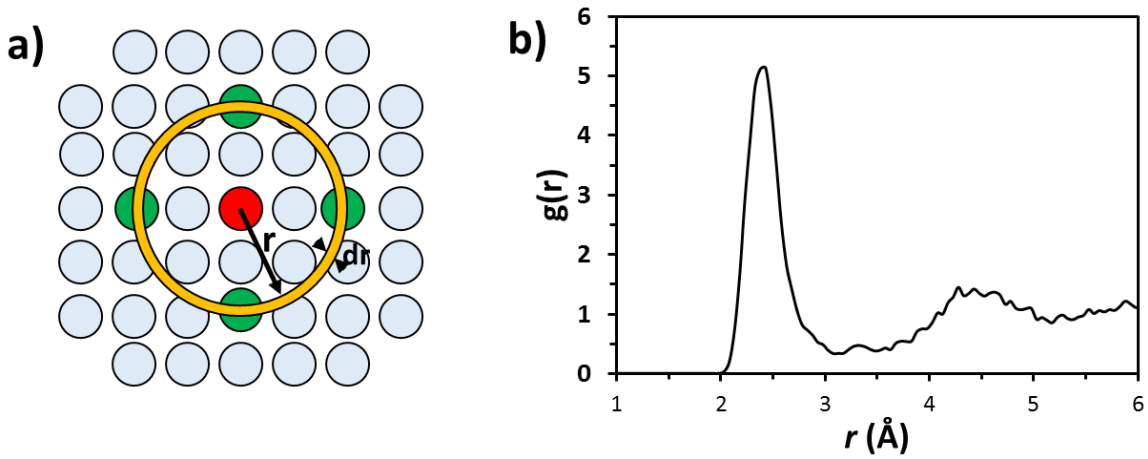

Figure 2.2 Radial Distribution Functions (RDF). a) Sketch of how to determine the RDF; b) *g(r)* of a Na^+ anion with respect to O-atoms. RDF was constructed from an AIMD simulation of a NaCl molecule solvated in water to illustrate the concept.

2.4. Bader Charge Analysis

In 1990, Richard F. Bader proposed a way to separate the atoms within a molecule based solely on the electronic charge density, he called it *the quantum theory of atoms in molecules*.[62] Bader's method states that the charge density finds a minimum between atoms and, therefore, it is a logical place to split atoms from each other. Consequently, the electronic charge assigned to each atom is defined by a zero flux surface. More recently, Henkelman *et al.*[63-65] developed a grid-based algorithm to partition the electronic density in Bader volumes or regions, which then allows the computation of electronic charge associated to that volume or, in other words, the partial atomic charges within a system.

3. REACTIVITY AT THE LITHIUM-METAL ANODE SURFACE*

3.1. Summary

Besides the redox reactions of Li species at the two electrodes, parasitic reactions of the electrolyte and soluble polysulfide (PS) species at the Li anode are the major reason behind severe capacity fading in Li-S batteries. In this chapter, interfacial reactions occurring at the surface of Li metal anodes due to electrochemical instability of the electrolyte components and PS species are investigated with a multimodal approach involving DFT-based computational methods and *in situ* XPS characterization. From AIMD simulations, it is found that the bis(trifluoromethane)sulfonimide lithium (LiTFSI) salt reacts very fast when in contact with the Li surface, and anion decomposition precedes salt dissociation. The anion decomposition mechanisms are fully elucidated. In addition, ether solvents used in Li-S technology are found stable during the entire simulation length, in contrast with the case of EC that is rapidly decomposed by sequential 2 or 4 electron mechanisms. On the other hand, the fast reactivity of the soluble PS species alters the side reactions because the PS totally decomposes before any of the electrolyte components forming Li_2S on the anode surface. Finally, by combining AIMD and *in situ* XPS

---

* Reprinted with permission from:

Luis E. Camacho-Forero, Taylor W. Smith, Samuel Bertolini, and Perla B. Balbuena. "Reactivity at the Lithium–Metal Anode Surface of Lithium-Sulfur Batteries." *The Journal of Physical Chemistry C*, 2015, **119** (48), 26828-26839. Copyright © 2015 American Chemical Society.

Manjula I. Nandasiri, Luis E. Camacho-Forero, Ashleigh M. Schwarz, Vaithiyalingam Shutthanandan, Suntharampillai Thevuthasan, Perla B. Balbuena, Karl T. Mueller, and Vijayakumar Murugesan. "In Situ Chemical Imaging of Solid-Electrolyte Interphase Layer Evolution in Li-S Batteries." *Chemistry of Materials*, 2017, **29** (11), 4728-4737. Copyright © 2017 American Chemical Society.

techniques, the SEI layer evolution mechanism is revealed. Three major stages are present: the formation of a primary composite mixture phase involving stable lithium compounds (Li_2S, LiF, Li_2O, etc.) and formation of a secondary matrix type phase due to cross interaction between reaction products and electrolyte components, which is followed by a highly dynamic mono-anionic polysulfide (i.e., LiS_5) fouling process.

3.2. Introduction

Despite being a promising alternative for next-generation energy storage devices, several limitations have kept Li-S batteries from mainstream adoption despite nearly half a century of research.[66] For instance, electrolyte stability is also crucial due to the high reactivity of the lithium surface. The electrode-electrolyte interface at the Li-metal anode is characterized by a combination of redox, decomposition, substitution, and coordination reactions of the electrolyte components, leading to the formation of the SEI layer.[18] As described in Chapter 1, the SEI properties are expected to play a role in controlling dendrite formation and passivating the surface. In addition, the shuttle of long-chain PS species from the cathode to the anode Li_2S_n ($4 \leq n \leq 8$)[5, 7] can also critically alter the properties of SEI layer since these species can undergo further reduction to eventually produce insoluble Li_2S_2 and Li_2S.[9-10] This complex chemistry creates a chemically and spatially inhomogeneous film at the anode, which could increase the interfacial resistance for the diffusion of Li-ion due to the deposition of a thick SEI layer of insulating and insoluble species on the active Li surface.[5] In order to control the complex reactivity at Li-anodes and improve the performance of Li-S batteries, it is important to elucidate the mechanisms of electrolyte degradation and subsequent formation of the SEI layer.

Although some recent efforts have been made to build *in situ* spectroscopic and microscopic capabilities for the analysis of Li-S batteries,[67-71] none of them could capture the entire set of reactions and identify all the components associated with SEI layer formation.[72-80] Therefore, the knowledge gap, which could provide a comprehensive understanding of SEI layer evolution at the Li-anode, remains and prevents the development of better electrolytes. To gain a comprehensive and molecular-level view of the parasitic reactions and subsequent SEI layer evolution, a first-of-its-kind *in situ* X-ray photoelectron spectroscopy (XPS) capability was developed. This apparatus can simultaneously provide spatially resolved chemical imaging as well as chemical speciation through high-resolution core-level spectroscopy of key elements.

Here we combine first-principle computational modeling and *in situ* XPS results to provide molecular-level insights regarding the distinct roles of transient species from parasitic reactions and the subsequent SEI layer evolution during cycling processes of Li-S batteries. The first part of this chapter, we use DFT and AIMD simulations to characterize surface reactions including reduction mechanisms of the various electrolyte components: solvent, salt, and polysulfide. The solvents studied were 1, 3-Dioxolane (DOL) and 1, 2-Dimethoxyethane (DME), which are commonly used in Li-S systems, and ethylene carbonate (EC), which is often found in conventional Li-ion batteries. LiTFSI was chosen as a salt due to its excellent electrochemical properties and ubiquity in Li-S systems. Then, we combine our previous AIMD simulations with *in situ* XPS results to provide a description of SEI layer evolution.

3.3. Methodology

3.3.1. Computational and System Details

3.3.1.1. Model of Lithium-Metal Surface and Electrolyte Components

A body-centered cubic Li-bulk system was optimized using DFT. The calculated optimum lattice parameter *a* is 3.442 Å, which shows good agreement with previous experimental and theoretical results.[81-82] Afterward, three surfaces with (100), (110) and (111) crystallographic planes were built from the optimized bulk crystal (Figure 3.1a). Surface energies were obtained from the DFT calculations using the following equation[35]:

$$\sigma = \frac{1}{A}[E_{Slab} - nE_{Bulk}] \tag{3.1}$$

where σ is the surface energy, A is the total area of the surface in the slab model, E_{Slab} is the total energy of the slab model for the surface, E_{Bulk} is the energy of one atom in the bulk, and *n* is the number of atoms in the slab model. Surface energies were converged by increasing the number of Li layers for each case. The calculated energies for the (100), (110), and (111) surfaces correspond to 0.029, 0.031, and 0.033 eV/Å^2, respectively. Thus, the crystal facet with the lowest surface energy is (100). These results are consistent with those reported in previous theoretical works.[82-83] Here, the most stable surface, (100), was used for our calculations.

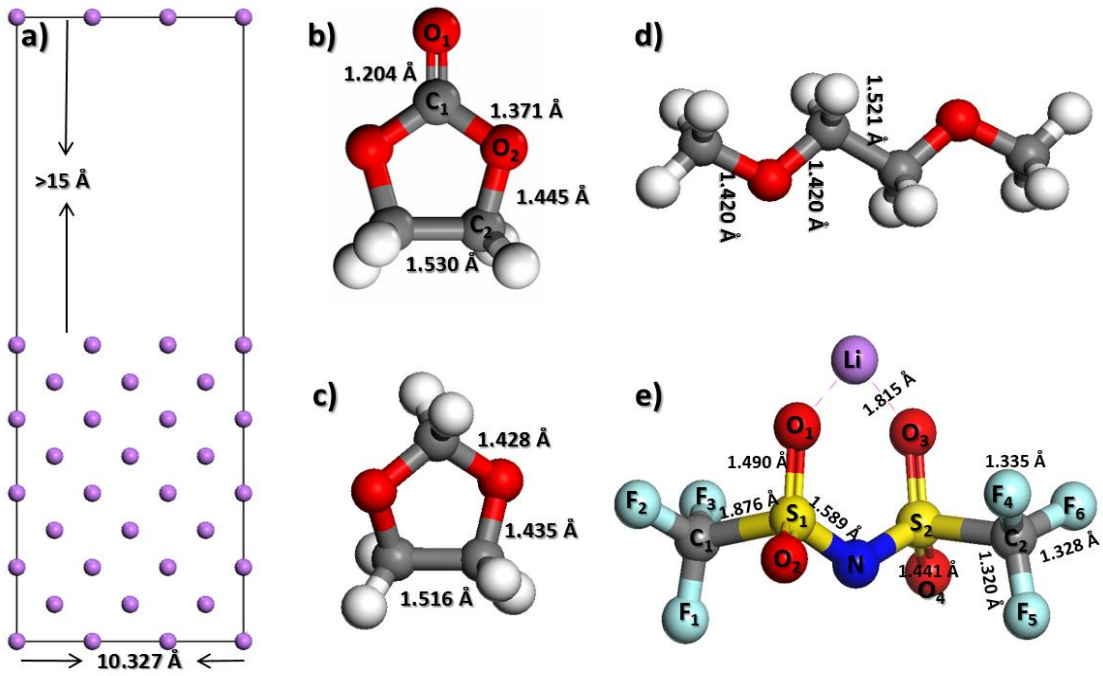

Figure 3.1 Model of Lithium-metal anode surface and electrolyte constituents used in the AIMD simulations. (a) Li-(100) surface. (b-e) optimized electrolyte molecules: EC (C_2 symmetry), DOL (C_1 symmetry), DME (C_{2h} symmetry), and LiTFSI (C_2 symmetry), respectively. Color code: Lithium, purple; Oxygen, red; Carbon, grey; Fluorine, light blue; Sulfur, yellow, Nitrogen, blue; Hydrogen, white.

Calculations were performed using VASP.[58-60] Electron-ion interactions were described by PAW pseudopotentials[50-51] as provided in the VASP databases. The Perdew-Burke-Ernzerhof generalized gradient approximation (GGA-PBE)[45] was selected as the exchange-correlation functional. The energy cut-off for the plane-wave basis expansion was chosen to be 400 eV. A conjugate-gradient algorithm was employed to relax the ions into their instantaneous ground state. A Gaussian smearing with a width of 0.05 eV was also utilized. For the surface Brillouin zone integration, a 4×4×1 Monkhorst-Pack[54] k-point mesh was used. The convergence criteria for electronic self-consistent iteration and ionic relaxation were set to 10^{-4} and 10^{-3} eV, respectively.

Optimized geometries of EC, DOL, DME, and LiTFSI salt molecules shown in Figure 3.1 were found to be in good agreement with previous experimental and theoretical reported bond lengths and symmetries.[84-88] EC, DOL, and DME solvent molecules (Figure 3.1b, c, d) were optimized using VASP. Here, similar DFT methodology as described above was employed. A Γ-centered k-point mesh was used in this case. The LiTFSI molecule (Figure 3.1e) was optimized using the Gaussian 09 (G09) package[89] with a hybrid functional B3PW91 and the 6-311++G(p,d) basis set.[46, 90] First, the anion $TFSI^-$ was optimized to the C_2 symmetry, which is been reported to be slightly more stable than the C_1 symmetry.[91-93] Next, the optimum Li-ion location in the salt was tested. It was found that Li is attached preferentially between two oxygen atoms (Figure 3.1e) rather than close to the nitrogen atom.

3.3.1.2. Solvent Stability at the Lithium-Metal Anode Surface

The stability of the solvent in contact with the lithium-metal anode was studied with AIMD simulations performed on the optimized model lithium-metal surface in contact with liquid-phase solvent in the *NVT* ensemble at 330 K using a time step of 1 femtosecond. The Nose thermostat was used to control the temperature oscillations during the simulation with a Nose-mass parameter of 0.5. The density of liquid-phase solvents was estimated by placing randomly 14, 13, and 9 molecules of EC (density = 1.32 g/cm^3), DOL (density = 1.06 g/cm^3), and DME (density = 0.87 g/cm^3) in contact with the model anode surface (Figure A.1, Appendix A), respectively. Subsequently, the solvent molecules (liquid-phase) were allowed to relax using a classical molecular mechanics minimization. For the minimization, the consistent valence force field (CVFF) with a

conjugate gradient algorithm as implemented in the Materials Studio software[94] was used. The maximum force among all the atoms in the system required for convergence was set to 0.005 kcal mol^{-1} $Å^{-1}$. Afterward, the minimized systems were allowed to run for 20 ps of AIMD simulation. Charge transfer was investigated by using the Bader charge analysis.[63-65] We remark that electronic charges are not observables and the results indicating fractional charges are an artifact of the method.

3.3.1.3. Solvent-Salt Mixtures

The salt decomposition and its effect on the model lithium-metal anode surface were evaluated by adding 1 M of the LiTFSI salt to the pure solvent system in contact with the model Li surface. Given the volume of the simulation cell, only one LiTFSI molecule was required to reach the 1 M concentration. Different initial configurations for the salt were selected: close to the surface or distant from it. In each case, binary mixtures (solvent/salt) were used to carry out AIMD simulations. In order to test the consistency of AIMD results regarding the salt decomposition, bond dissociation energies of the LiTFSI molecules were calculated under different conditions: in gas-phase, in solvent (EC and DME), and under Li radical attack (close to either an oxygen or nitrogen atom). Bond energies were calculated using G09 at the same level of theory aforementioned. In this case, the solvation effects were implicitly represented by the polarizable continuum model (PCM)[95] as implemented in the G09 software package.

3.3.1.4. Polysulfides and Solvent-Salt Mixtures at the Lithium-Metal Anode Surface

In order to investigate the effect of PS species present at the anode surface due to the shuttle effect, PS molecules were added to the model electrolyte. The lithiated PS

molecules were optimized using the G09 package software at the same level of theory above mentioned. In addition, the energy of a neutral Li_2S_8 molecule was first calculated, and subsequently, fragments and potential decomposition products were optimized to evaluate the most thermodynamically favorable reduction pathways. Li_2S_8 molecules were then added to the fresh solvents-salt mixtures, and the effect of the PS on the electrolyte and its decomposition on the lithium-metal anode were investigated during 20 ps of AIMD simulations at 330 K.

3.3.2. Experimental Details

The high vapor pressures of elemental sulfur (S_8) and aprotic electrolyte solvents such as DOL and DME are the central challenge in developing *in situ* XPS for Li-S batteries. To overcome this issue, we employed an ultrahigh vacuum (UHV) compatible ionic liquid (IL), 1-butyl-1-methylpyrrolidinium TFSI, i.e., $[bmpyr]^+[TFSI]^-$, as a cosolvent in the electrolyte. The $[bmpyr]^+[TFSI]^-$ ionic liquid used in this study has been reported as a compatible electrolyte for Li-S cells due to their high electrochemical stability.[96-97] Various ionic liquids have been used as electrolytes and are electrochemically stable in the voltage range (±2.2V) of Li-S batteries.[98-99] A solution of 1 M Li_2S_6 dissolved in a DOL and DME solvent mixture is prepared as reported earlier.[100] Subsequently, 20 wt % of the Li_2S_6 in DOL and DME solution is mixed with $[bmpyr]^+[TFSI]^-$ and used as the final electrolyte system for the *in situ* study. Apart from the vacuum compatibility, the specific choice of $[TFSI]^-$ counter anion containing IL is to ensure the electrolyte system represents the traditional LiTFSI salt widely used in the Li-S battery studies. In addition, this electrolyte solution resembles the typical Li-S battery

after the discharge cycle, where the lithium polysulfide (Li_2S_x) species are dissolved in DOL/DME solvent. In this case, however, the sulfur cathode is replaced with graphite foil and Li_2S_6 dissolved in the electrolyte solvent mixture is used as a sulfur source by initiating the redox process via the charging cycle, see Appendix A. Li-anode and graphite-cathode materials can be mounted on a Teflon base and subsequently connected with gold wires as an external electrical contact line to the electrochemical analyzer. The reservoir in between the anode and cathode is filled with electrolyte mixture such that it covers half of the electrode surfaces. The cell is fully charged and discharged at 2.2V for two consecutive cycles only due to the limited availability of active sulfur material. All measurements are performed on the Li-electrolyte interfacial region at the end of each charge/discharge cycle to avoid the charge-induced XPS peak shifts. The graphite cathode is fully covered by ionic liquid due to high surface wetting processes, see Appendix A.

XPS analysis was performed using a Kratos Axis Ultra DLD spectrometer, which consists of a high-performance Al Kα monochromatic X-ray source (1486.6 eV) and a high-resolution hemispherical mirror analyzer. The X-ray source was operated at 150 W, and emitted photoelectrons were collected at the analyzer entrance slit normal to sample surface. The data acquisition was carried out in a hybrid mode with an analysis area of 700 × 300 μm. The survey spectra were recorded at a pass energy of 160 eV with 0.5 eV step size and high-resolution spectra were recorded at a pass energy of 20 eV with step size of 0.1 eV. The pass energy of 20 eV in the 700 × 300 μm analysis area is referenced to the FWHM of 0.59 eV for Ag $3d_{5/2}$. A charge neutralizer with low energy electrons was used to exclude surface charging effects and the binding energy of C *1s* at 284.8 eV was

used as the charge reference. The elemental and chemical state maps were acquired using the imaging XPS capability in the Kratos Axis Ultra system. The maps were collected in a field of view of 800 μm with a spatial resolution of ~ 5 μm. The imaging XPS data were collected under a pass energy of 160 eV at each peak and background energy. The chamber pressure was maintained at $\leq 5 \times 10^{-9}$ Torr during all measurements. XPS data were analyzed using the CasaXPS software assuming Gaussian/Lorentzian (30% Lorentzian) line shapes and utilizing Shirley background correction. All the XPS binding energies reported here have an uncertainty of ±0.1 eV. The background subtraction and imaging data processing were accomplished using the CasaXPS software to obtain the elemental and chemical state XPS maps presented here.

3.4. Results and Discussion

3.4.1. Solvent Stability at the Lithium-Metal Anode Surface

Figure A.2 (Appendix A) shows the final configuration of the system for the three pure solvents. No reduction of the DOL or DME was observed during 20 ps of AIMD simulation. These observations are in agreement with the experimentally reported higher stability of the ether solvents on Li metal surfaces.[101-104] Furthermore, charge analyses (shown in Figure 3.2) indicate that when the anode is interacting with either DOL or DME, the lithium anode exhibits a low positive charge close to 0.024 and 0.020|e|/Li-atom, respectively. Solvent molecules are observed to be adsorbed on the surface, with O–Li being the predominant adsorption interaction. DOL and DME molecules close to the surface have an average charge of -0.24 and -0.29 |e|/molecule, respectively, whereas those relatively far from the surface only have an average charge of -0.01 and -0.03 |e|/molecule.

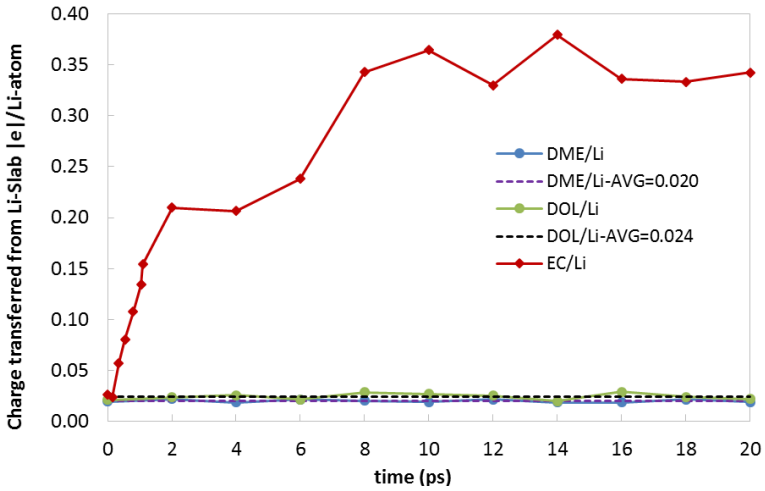

Figure 3.2 Net charge evolution of the lithium-metal anode in contact with pure solvents during 20 ps of simulation. Dotted lines represent the average transferred charge within the simulated time for DOL/Li and DME/Li.

On the other hand, a rapid transferal of charge is observed during the first 8 ps of simulation when EC is used as a solvent (Figure 3.2). This behavior is due to the fast reduction of EC which takes place on the lithium surface. After 8 ps, the net charge transferred from the surface to the electrolyte is stabilized. This suggests that the remaining adsorbed fragments, resulting from the reduction of EC, lower the reactivity of the surface. We note that we did not include extra Li ions that may be arriving at the anode during charge and would keep a highly reactive surface including dendrite formation. In pure liquid EC electrolytes, there is an attraction effect between their carbonyl oxygen atoms and the lithium surface, which causes the solvent molecules to orient in such a way as to maximize the proximity of the oxygen and lithium atoms. This typically results in the solvent aligning parallel to the metal surface. At 20 ps of simulated time, ~0.35 |e|/Li-atom were transferred from the anode to the electrolyte. Thus, seven (out of 14) EC

molecules decomposed following two reaction mechanisms. The first mechanism is described in Figure A.3, and it can be summarized in the following reactions:

$$\mathrm{EC_{(ads)}} + 2\mathrm{e^-} \rightarrow \mathrm{O(C_2H_4)OCO^{2-}_{(ads)}} \quad (3.2)$$

$$\mathrm{O(C_2H_4)OCO^{2-}_{(ads)}} + 2\mathrm{e^-} \rightarrow \mathrm{O(C_2H_4)O^{2-}_{(ads)}} + \mathrm{CO^{2-}_{(ads)}} \quad (3.3)$$

In this case, six out of seven EC are reduced by reaction 3.2. Afterward, five $\mathrm{O(C_2H_4)OCO^{2-}}$ species followed reaction 3.3. In contrast, only one EC molecule followed the sequential reduction path described in Figure A.4 and reactions 3.4 and 3.5. Both reduction mechanisms agree reasonably with previously reported studies of the decomposition of EC in contact with lithium-metal and Li_xSi_y surfaces.[105-106]

$$\mathrm{EC_{(ads)}} + 1\mathrm{e^-} \rightarrow \mathrm{EC^-_{(ads)}} \quad (3.4)$$

$$\mathrm{EC^-_{(ads)}} + 1\mathrm{e^-} \rightarrow \mathrm{C_2H_{4(ads)}} + \mathrm{CO_3{}^{2-}_{(ads)}} \quad (3.5)$$

Although no reduction of DOL or DME was observed during the AIMD simulated time, these results only indicate that DOL and DME are much more stable than EC when in contact with the lithium-metal anodes. Thus, such a relative stability of DOL and DME compared to EC is in agreement with experimental observations.[101]

3.4.2. Reactivity of Solvent-Salt Mixtures

Three initial configurations for the salt were tested with pure solvent in order to represent the randomness of the system, in which a salt molecule may be located close or far from the lithium anode (Figure A.5, Appendix A). In the case of the DME/LiTFSI electrolyte mixture, no reduction of DME was observed within the 20 ps of AIMD simulation in any of the three configurations. However, the LiTFSI salt did decompose in every case. Figure A.6 shows the configuration of the three systems of DME/LiTFSI in

contact with the anode at 20 ps. The salt was placed far from the surface in the initial configuration 1. Steps of the decomposition of the LiTFSI salt are shown in Figure 3.3. It was observed that the LiTFSI molecule remains stable in the liquid phase for about 5600 fs. Some femtoseconds later, a C-S bond is broken, resulting in the formation of $CF_3SO_2NSO_2^{2-}$ and CF_3^-. The same type of bond breaking was found by Sodeyama *et al.* using DFT-MD analyses of the TFSI anion decomposition.[107] Interestingly, the formed $CF_3SO_2NSO_2^{2-}$ group is attracted after a few hundreds of femtoseconds to the anode surface. It stayed adsorbed for the remaining simulated time via O–Li interaction. This type of interaction was observed by Budi *et al.*'s AIMD simulations[108] and it was followed by LiO and Li_2O formation. Charge analysis evolution of the system (Figure A.7a) suggests that although the LiTFSI salt is not that close to the surface, electron transfer from the anode is the reason for the LiTFSI reduction. To further investigate the electron transfer, we calculated the density of states (DOS) of snapshots obtained at different stages of the reaction depicted in Figure 3.3. The DOS of the total system and that of individual components is shown in Figure A.8. Considering the total system which includes the salt, solvent and surface atoms, the evolution of the DOS (Figure A.8) shows a clear increase in the population of the occupied states, particularly those near and at the Fermi level. This could contribute to the development of an instantaneous voltage favorable to the reaction as discussed by Leung.[109] The individual DOS of the fragments (TFSI anion, DME, CF_3, and $CF_3SO_2NSO_2$) are also illuminating (Figure A.8), clearly showing a trend of increasing population of the occupied states derived from the electron transfer in all the species.

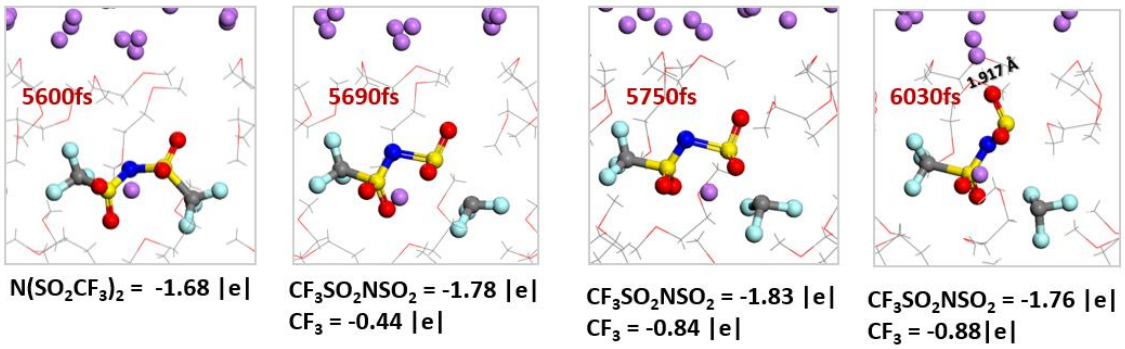

Figure 3.3 Sequence of TFSI anion decomposition obtained from AIMD simulations for DME/LiTFSI mixture where the salt was initially placed far from the surface. Li^+ from the salt remains near to the O atoms along the simulated time. Calculated Bader charges regarding the different species are also presented.

Alternatively, Figure 3.4 shows the LiTFSI decomposition sequence when the salt/DME mixture is situated close to the surface. In this case, similarly to Figure 3.3, the molecule is reduced (within one hundred femtoseconds), and a C-S bond breaks, yielding $CF_3SO_2NSO_2^{2-}$ and CF_3^-, which remain close to the surface. The CF_3^- decomposes into its constituents C and F in the next 300 fs. On the other hand, the $CF_3SO_2NSO_2^{2-}$ group remains adsorbed on the surface for 600 fs more until one of the N-S bonds is broken, forming SO_2^- (in liquid phase) which survives for the remaining 19 ps of simulation. The other $CF_3SO_2N^{2-}$ fragment is reduced and all the F-C bonds are broken by 1.8 ps of simulated time. Sequentially, the CSO_2N species loses the two oxygen atoms. Finally, a CSN anion with charge -4.53 |e| remains, together with the F^-, C^{4-}, and O^{2-} products of the LiTFSI decomposition, interacting with the Li-anode. After 20 ps, the Li-metal anode exhibited a very positive charge (+0.23 |e|/Li-atom, Figure A.7b) primarily due to the LiTFSI reduction. A third initial configuration for the salt (also close to the surface but different orientation) was evaluated. In this case, the decomposition of LiTFSI starts in

the first 100 fs with a rupture of an S-N bond. This type of bond breaking has been also suggested by theoretical investigations of TFSI anion decomposition.[108, 110] Similar to the previous case the salt was completely decomposed, and the decomposition products stay attached to the surface (Figure A.6). There, it is observed that CO species are formed from C and O constituents that were dissolved in the Li-anode. It is interesting that similar TFSI anion decomposition mechanisms have also been deduced from experimental analyses of Mg-ion batteries as well.[111]

Regarding the DOL/LiTFSI electrolyte mixture, no reduction of DOL was observed after 20 ps of AIMD simulation in any of the three configurations. However, as in the previous mixture (DME/LiTFSI), the LiTFSI salt decomposed in every case. DOL/LiTFSI in contact with the anode at 20 ps is shown in Figure A.9. As in the DME case, first, the case where the salt is placed far from the surface anode (Configuration 1) is analyzed (Figure 3.5). In the DOL/LiTFSI mixture, the reduction of the LiTFSI starts earlier (2500fs) compared to the DME/LiTFSI (5690fs) for the case where the salt is far from the Li-(100) anode surface. However, the same initial mechanism is followed; C-S bond breaking. The resulting CF_3^- and $CF_3SO_2NSO_2^{2-}$ remain stable in the liquid phase. After approximately 1.5 ps the negatively charged CF_3^- group is attracted by the surface; subsequently, it is gradually decomposed to C and F in the next 2 ps.

On the other hand, in the DOL/LiTFSI (close to the surface) mixture, the salt decomposition starts later in comparison with the DME/LiTFSI (Figure 3.6). In this case, the reduction of the salt takes place by breaking an N-S bond. As a result, $CF_3SO_2N^{2-}$ and $CF_3SO_2^{2-}$ are produced. The $CF_3SO_2N^{2-}$ remains adsorbed to the surface for the rest of the

simulation time, whereas the $CF_3SO_2^{2-}$ group reacts into CF_3 and SO_2 within the next 100 fs. At 2000fs, the CF_3 decomposes and forms CF_2, which remains adsorbed on the anode surface for more than 6 ps, when it is finally decomposed into C and F. Alternatively, at 2100 fs, the SO_2 is reduced by the lithium surface into its constituents S and O.

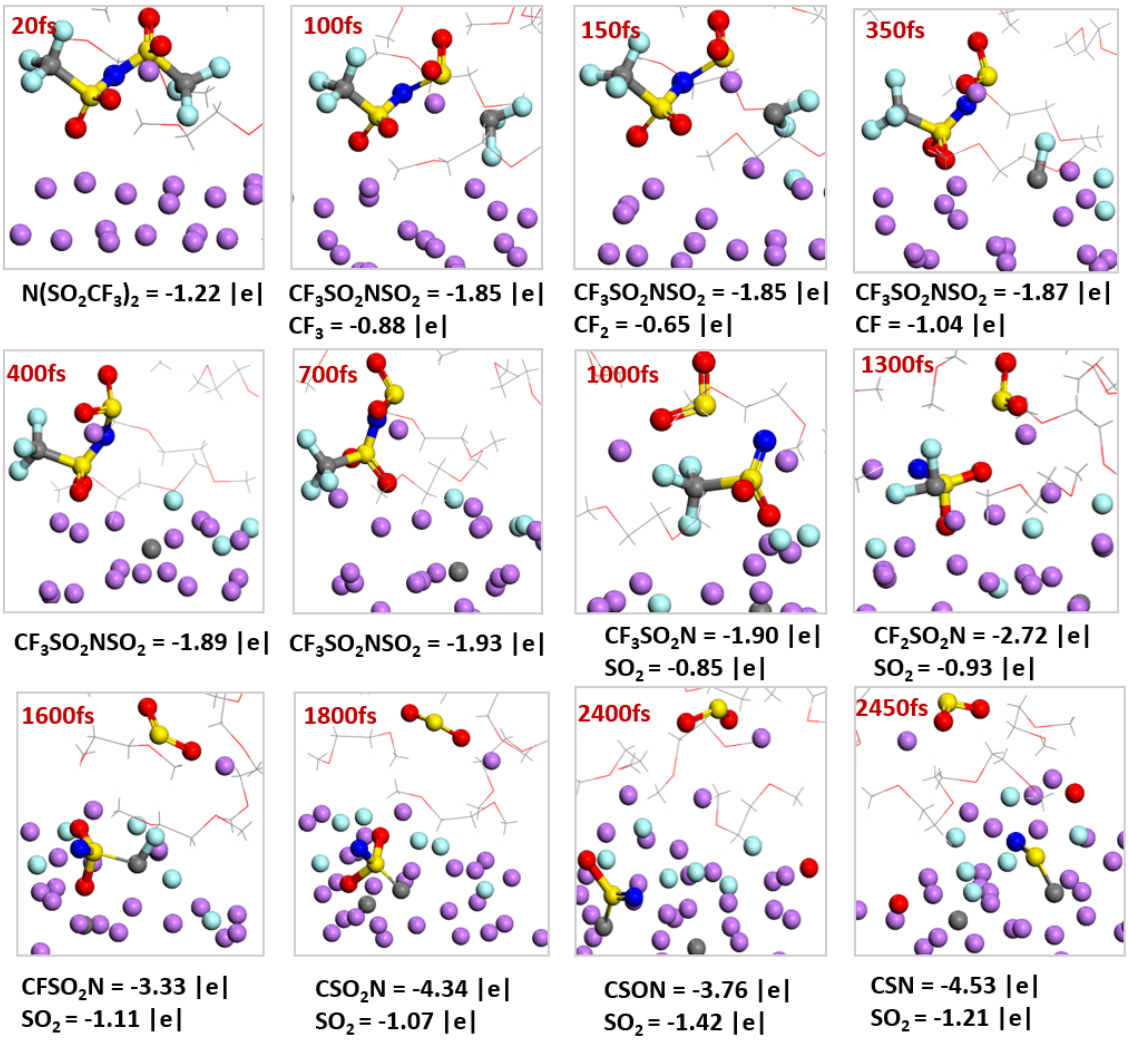

Figure 3.4 Complete sequence of TFSI anion decomposition obtained from AIMD simulations for DME/LiTFSI mixture, in which the salt was initially placed close to the surface. Li^+ from the salt remains near to one of the oxygen atoms. After 1.5 ps, the Li cation diffuses to the liquid-phase attached to the SO_2 group. Calculated Bader charges regarding the different species are also shown at the bottom of each panel.

Although it seems that somehow the DOL stabilizes the larger salt fragment better than DME, an initial alternative position of the LiTFSI, where the N is closer to the surface, revealed that the salt is decomposed by breaking an S-N bond as fast as it did when the DME was used as a solvent (final configuration after 20 ps of simulation is shown in Figure A.9 and Figure A.10 illustrates charge evolution of the surface during the reaction). Thus, this suggests that the decomposition rate of the salt may depend primarily on its location with respect to the surface which is supported by Leung's analysis of the voltage effect on this type of reactions.[109]

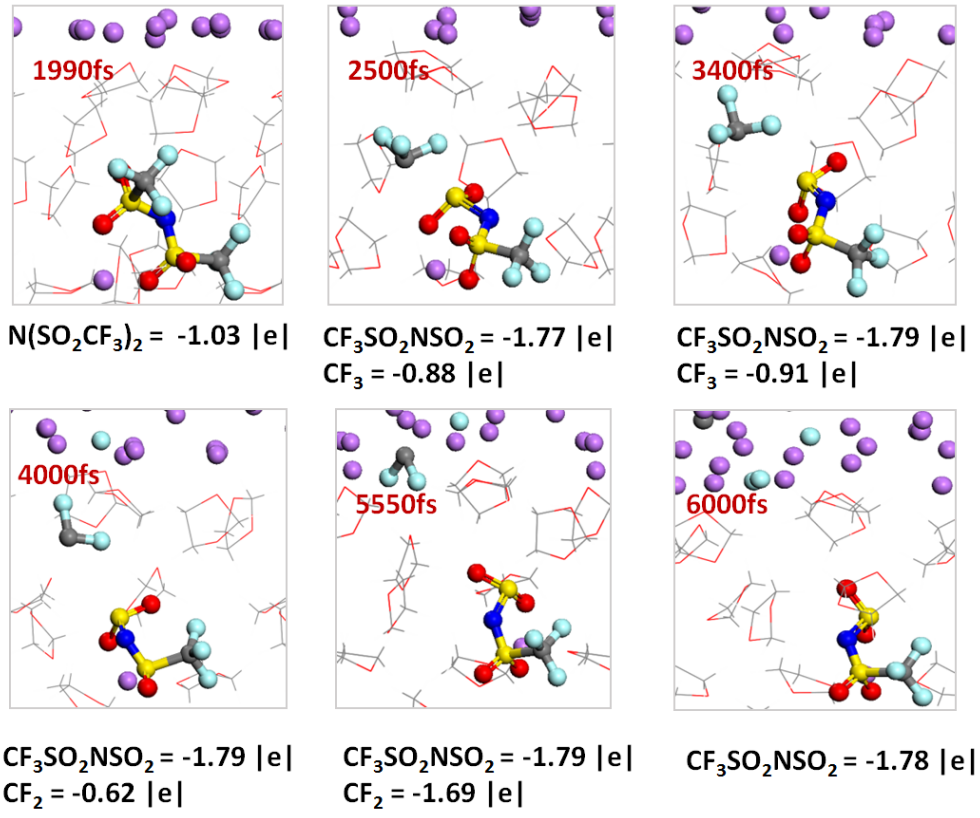

Figure 3.5 Sequence of TFSI anion decomposition obtained from AIMD simulations for DOL/LiTFSI mixture, in which the salt was initially placed far from the surface. Li cation from the salt remains bonded to the oxygen atoms during the simulated time. Calculated Bader charges regarding the different species are also shown at the bottom of each panel.

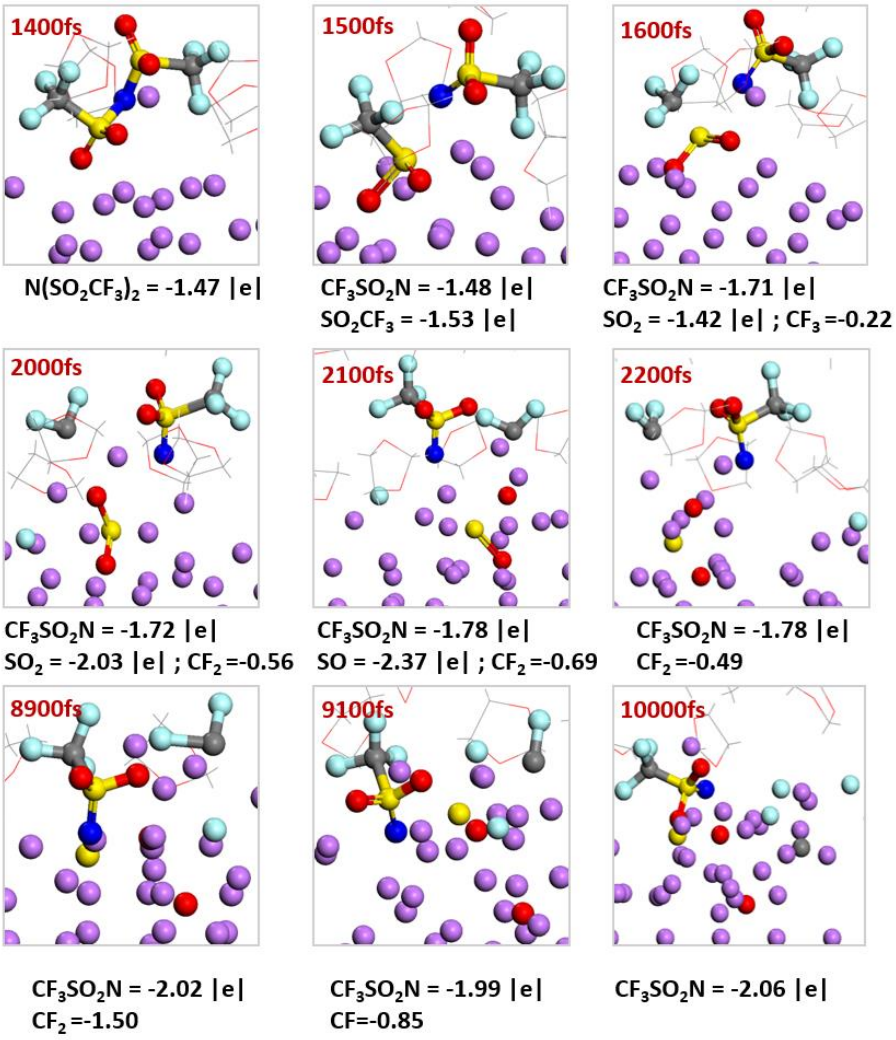

Figure 3.6 Sequence of TFSI anion decomposition obtained from AIMD simulations for DOL/LiTFSI mixture, where the salt was in close contact with the surface. Li^+ remains bonded to TFSI fragments until 9 ps. Then it keeps close to the surface. Calculated Bader charges regarding the different species are also shown.

In order to evaluate the energetics of the salt decomposition, bond dissociation energies for the LiTFSI were calculated under different conditions. Results are reported in Table 3.1. If the dissociation is carried out in gas-phase, none of the proposed reactions are thermodynamically favorable. The one that requires the lowest energy (2.34 eV) is the C-S breaking bond. However, it is still highly thermodynamically not favorable. In

contrast, the dissociation of LiTFSI to Li^+ and $TFSI^-$ in EC is possible as found in previous MD simulations.[112] However, the driving force (ΔG) is still low (-0.05 eV). Similar implicit solvent calculations for DME or DOL yielded significantly lower energy compared to the gas-phase reaction although still suggest that the process is not thermodynamically possible, in contrast to results of MD simulations.[113] Thus, explicit solvent simulations should be necessary to better characterize this process.

Table 3.1 Calculated bond dissociation energies for LiTFSI: Gas-Phase, in-solution (EC, and DME solvents) from B3PW91/6-311++G(p,d) calculations.

Reactions	**Bond Dissociation Energies (eV)**					
$(Li)N(SO_2CF_3)_2 \rightarrow$	**Gas-Phase**		**EC solvent**		**DME Solvent**	
	ΔE (0K)	**ΔG (298K)**	**ΔE (0K)**	**ΔG (298K)**	**ΔE (0K)**	**ΔG (298K)**
$Li^0 + [N(SO_2CF_3)_2]^0$	5.86	5.47	6.58	6.23	6.40	5.97
$Li^+ + [N(SO_2CF_3)_2]^-$	5.96	5.64	0.21	-0.05	0.75	0.43
$CF_3SO_2(Li)NSO_2 + CF_3$	2.34	1.75	2.32	1.78	2.32	1.74
$CF_3SO_2N(Li) + SO_2CF_3$	3.28	2.68	2.80	2.21	2.91	2.28
$CF_3SO_2(Li)NSO_2CF_2 + F$	4.98	4.58	4.98	4.63	4.97	4.52
$CF_3SO_2(Li)NSOCF_3 + O$	3.63	3.25	3.83	3.50	3.77	3.38

To emulate dissociation induced by electron transfer, a lithium radical was added to the system. This is a real situation because the Li-ion becomes reduced near the anode and is converted into a neutral Li atom ready to react; alternatively, plating may occur. Two radical attack positions were tested: near an oxygen atom in the salt (Li---O) and close to the nitrogen (Li---N). Thus, several reaction options were considered. Results are shown in Table 3.2. Interestingly, as observed with the AIMD simulations when the salt gets in contact with the surface, under either mode of radical attack (Li---O or Li---N),

dissociation is highly favorable when the C-S or N-S bond is broken. Rupture of the C-S bond is the most thermodynamically favorable path in both cases, in agreement with Sodeyama *et al.*'s work.[107] The results agree with our AIMD simulation results reported above, where cleavage of the C-S or N-S bond was the starting point for all of the LiTFSI reduction observed in agreement with previous experimental reports.[114-115] We note however that these reactions may be kinetically controlled as suggested earlier[108, 110] and the magnitude of the activation barrier would decide for the most favorable mechanism.

Table 3.2 B3PW91/6-311++G(p,d) calculated bond dissociation energies for LiTFSI under Li radical attack. Optimized geometries are provided in Figure A.11.

Reactions	**Bond Dissociation Energies (eV)**			
$[(\mathbf{Li})\mathbf{N}(\mathbf{SO_2CF_3})_2]\cdots\mathbf{Li(radical)}\rightarrow$	**Li···O**		**Li···N**	
	ΔE (0K)	**ΔG (298K)**	**ΔE (0K)**	**ΔG (298K)**
$\mathbf{Li^0 + Li\cdots[N(SO_2CF_3)_2]^0}$	0.63	0.33	0.62	0.32
$\mathbf{Li^+ + Li\cdots[N(SO_2CF_3)_2]^-}$	5.72	5.33	5.33	5.04
$\mathbf{[CF_3SO_2(Li)NSO_2]\cdots Li + CF_3}$	-1.75	-2.29	-2.12	-2.63
$\mathbf{[CF_3SO_2N(Li)]\cdots Li + SO_2CF_3}$	-0.26	-0.80	-0.80	-1.31
$\mathbf{CF_3SO_2N(Li) + [SO_2CF_3]\cdots Li}$	-0.68	-1.22	-1.04	-1.56
$\mathbf{CF_3SO_2N + (Li)[SO_2CF_3]\cdots Li}$	2.94	2.12	2.40	1.79
$\mathbf{[CF_3SO_2(Li)NSO_2CF_2]\cdots Li + F}$	1.57	1.22	1.16	0.77

3.4.3. Effect of PS Species on Electrolyte Reactivity on the Li Surface

As mentioned before, one of the most difficult aspects of the Li-S battery system to understand and therefore engineer is the process for the decomposition of the long-chain PS molecules which occurs during the discharge process.[100] Initially, sulfur from the cathode (S_8) reacts with dissolved lithium ions to form Li_2S_8.[116] Even upon successive cycles of charge and discharge, this species is typically not oxidized back into its elemental

components.[117] The traditional reaction mechanism for the lithium PS during discharge is as follows: $Li_2S_8 \rightarrow Li_2S_6 \rightarrow Li_2S_4 \rightarrow Li_2S_2 \rightarrow Li_2S$.[66] These last two species are of particular importance because both the Li_2S_2 and Li_2S are insoluble in the electrolyte and therefore deposit on the electrode, sterically impeding further lithiation of other PS species and removing themselves from the charge/discharge cycle.[118] Additionally, Li_2S is electronically insulating, which only serves to exacerbate the aforementioned issues.[11] Therefore, it is critical for us to better understand how PS decomposition occurs and how it may interfere with the other side reactions. A very complete study of the many potential reactions occurring at the cathode of Li-S batteries was recently presented by Assary *et al.*[119] Our work is mainly concerned with the solubility and potential dissociation of the PS species in the electrolyte and with their reaction in contact with the anode surface. Thus, in this discussion we refer to Assary *et al.*'s study and also investigate a few new reactions that are relevant to the PS decompositions at the anode.

To begin to understand how a PS molecule behaves inside an electrolyte medium and in an electrochemical environment, we must first understand its behavior in gas phase, or without solvent interactions or other effects that might influence its behavior. Then we add implicit solvents to determine how their properties influence the stability and favorability of the PS decomposition products and reactions. These results are summarized in Table 3.3. It should be noted that the Li_2S_8 molecule can take either a linear or ring form, with the lowest-energy configuration depending on the solvent environment. For simplicity's sake, the energies in Table 3.3 are calculated using the linear conformation of

the PS; the same trends are found for the ring Li_2S_8. In all cases, the lowest multiplicities are shown corresponding to the lowest-energy molecular structures.

Table 3.3 Calculated bond dissociation energies for PS from B3PW91/6-311++G(p,d) calculations.

Reactions	Bond Dissociation Energies (eV)					
	Gas-Phase		EC Solvent		DOL Solvent	
	ΔE (0K)	ΔG (298K)	ΔE (0K)	ΔG (298K)	ΔE (0K)	ΔG (298K)
$Li_2S_8 \rightarrow 2Li^+ + S_8^{-2}$	14.11	13.51	0.45	-0.15	1.74	1.14
$Li_2S_8 \rightarrow 2Li + S_8$	7.02	6.37	8.85	8.24	8.39	7.76
$Li_2S_8 \rightarrow LiS + LiS_7$	2.43	1.94	2.05	1.55	2.07	1.56
$Li_2S_8 \rightarrow LiS_2 + LiS_6$	0.99	0.48	1.20	0.65	1.15	0.61
$Li_2S_8 \rightarrow LiS_3 + LiS_5$	1.28	0.79	0.87	0.33	0.81	0.30
$Li_2S_8 \rightarrow 2LiS_4$	0.31	-0.24	0.78	0.29	0.68	0.16
$Li_2S_8 + 2Li \rightarrow Li_2S + Li_2S_7$	-3.56	-3.43	-5.53	-5.39	-5.18	-4.85
$Li_2S_8 + 2Li \rightarrow Li_2S_2 + Li_2S_6$	-5.63	-5.38	-6.02	-5.92	-5.64	-5.51
$Li_2S_8 + 2Li \rightarrow Li_2S_3 + Li_2S_5$	-5.32	-5.17	-6.19	-6.09	-5.78	-5.65
$Li_2S_8 + 2Li \rightarrow 2Li_2S_4$	-6.95	-6.69	-6.28	-6.14	-6.15	-5.98
$S_8^{-2} \rightarrow S_1^{-1} + S_7^{-1}$	0.48	0.10	2.06	1.71	1.91	1.54
$S_8^{-2} \rightarrow S_2^{-1} + S_6^{-1}$	-0.85	-1.32	1.11	0.66	0.88	0.41
$S_8^{-2} \rightarrow S_3^{-1} + S_5^{-1}$	-1.33	-1.87	0.78	0.24	0.52	-0.03
$S_8^{-2} \rightarrow 2S_4^{-1}$	-1.39	-1.93	0.57	0.05	0.34	-0.18

From the gas phase calculations, a variety of observations can be made. First, all of the decomposition products in gas phase are at their lowest energy state with a -1 charge (radical anions) instead of neutral or -2 (dianions) except the S_8 molecule, which prefers to be a dianion. This is interesting because the S_8^{-2} molecule actually favors decomposition in the gas phase, particularly by breaking of the middle sulfur bond. In solvent, however,

the reactions are less favorable (last three rows in Table 3.3), in agreement with Assary *et al.*'s work.[119] Originally, we assumed that the delithiation reaction occurred first, followed by subsequent polysulfide fragmentation, but in the gas phase, this is certainly not the case. And although this pathway has less of an energy barrier in solvent, AIMD simulations of a Li_2S_8 molecule in each of the three solvents discussed in this chapter produced no decomposition when the lithium metal surface was not included, even after over 20 picoseconds of simulation. Therefore, we can conclude that the primary method of Li_2S_8 fragmentation away from the anode surface does not involve delithiation.

For a PS molecule in the bulk solvent, with no direct interaction with additional lithium atoms, decomposition has still been observed in AIMD anode simulations, albeit at a much slower rate than at the lithium metal surface. While there is little precedent for this occurring in gas phase, the transfer of charge from the metal surface to the conductive electrolyte in anode simulations, which has been confirmed using Bader charge analysis, creates an environment conducive to PS dissociation. It is worth noting, however, that even using gas-phase data, the reduction of Li_2S_8 to Li_2S_6 ($Li_2S_8 \rightarrow Li_2S_6 + S_2$, which is the first step in the traditional decomposition progression, is thermodynamically favorable, with a ΔG_{rxn} of -0.28 eV. Additionally, cleaving of the middle sulfur bond is also viable, as per Table 3.3.

By far the most favorable pathway involves reaction of the lithiated polysulfide with additional lithium atoms. These reactions were not examined by Assary *et al.*,[119] although they did consider those of the dianions with Li-ions yielding similar products, and some of them were found to be favorable in solution although with lower ΔG_{rxn} values.

Gas-phase calculations indicate that cleaving by the middle sulfur bond is the most energetically favorable, but all of these reactions are very capable of occurring (Table 3.3). The formation of Li_2S_6 breaks the trend of increased favorability with increasing symmetry of the fragments, as both the enthalpy and free energy of the reaction are greater than the same values for Li_2S_5. A similar trend can be observed in the data for decomposition in the bulk solvent. This seems to indicate that this configuration is indeed one of the more stable for the lithiated polysulfides, which gives credence to the traditional reaction mechanism given at the beginning of this section ($Li_2S_8 \rightarrow Li_2S_6 \rightarrow Li_2S_4 \rightarrow Li_2S_2 \rightarrow Li_2S$). Results from Vijayakumar *et al.*[100] further support these assumptions, indicating via mass spectrometry the presence of Li_2S_4, Li_2S_6, and Li_2S_8, in addition to S_8^{-2} and even polysulfide clusters (containing more than two lithium atoms).

As shown in Table 3.3, when the lithiated PS molecule was simulated with an implicit solvent using dielectric properties consistent with that of EC, it is readily observed that ionic delithiation is much more likely to occur, particularly in the bulk solvent, while neutral delithiation remains highly unfavorable. This is due to the stabilizing effect of solvent in dissipating the charge of both species, which is the obvious difference between these results and those in the gas phase. At the anode surface, where additional lithium is present, Li_2S_8+2Li reactions are again extremely favorable (Table 3.3). In gas phase, there was a 95% increase in the reaction energies when breaking an "end" sulfur-sulfur bond versus a "middle," while the numbers from the EC simulation show only a 14% increase. Additionally, there is no evidence to suggest that a LiS_6 or Li_2S_6 molecule was unusually stable in solvent, and in AIMD anode simulations this has also been observed – there is

no clear transition to a Li_2S_6 species during the decomposition process. The similarities in the reaction energies of Li_2S_8+2Li shown in Table 3.3 are in agreement with the observations from AIMD simulations (Appendix A) that suggest that the point of rupture of the PS chain is random (any of the possible reactions are approximately equally favorable).

In the case of Li_2S_n species in EC, delithiation is thermodynamically favorable when *n* is greater than 2, i.e., Li_2S_3 will spontaneously go to Li^++LiS_3^{-1}. In fact, for all species of the form LiS_n, the dianion (-2) charge state is most favorable, meaning that even for shorter chain (*n* less than 8) lithiated polysulfides, delithiation is still likely to occur. Due to the very similar dielectric constant of both DOL and DME, the calculated reaction energies of PS species in both solvents were virtually the same. The values calculated in DME (not shown) were an average of 1% lower than the same results in DOL (Table 3.3). Both DOL and DME are stable in the presence of the lithium anode and the polysulfide, and the reaction energy calculations seem to confirm these observations. However, PS surface reactions are still favorable, and even a few Å farther from the surface, AIMD results indicate that the PS molecule still decomposes due to charge transfer from the metal surface to the electrolyte. The reduction potentials of the solvents tested (EC, DOL, and DME) are -1.46, -1.48, and -1.68 V, respectively.[120] Due to the small differences among them, there seems to be no correlation between the calculated results and the solvent reduction potentials.

To examine PS behavior at the anode surface, AIMD calculations were performed by adding a ring or linear Li_2S_8 molecule close to the Li surface and considering each salt-

solvent mixture described in the previous section. The configurations of the systems after 20 ps are shown in Figure A.12 (Appendix A). The PS is highly decomposed despite the solvent used or the PS initial geometry (ring or linear), resulting in the formation of a lithium-sulfur layer. In contrast, the solvents tested (DOL and DME) exhibited no reduction. PS bond lengths were tracked throughout the simulation in order to identify PS decomposition (Figure A.13). Reduction of PS was almost instantaneous (<10 fs) in every case, and no clear trend was observed regarding the decomposition mechanism. Regarding the SEI layer formed, atomic charge and coordination number analyses of S species along the AIMD trajectories suggest the formation of an amorphous Li_2S phase. Additionally, the salt was decomposed in each case following the same reduction mechanisms reported in the previous section.

3.4.4. Chemical Imaging of SEI Layer Evolution

In situ XPS and imaging XPS were carried out at the interfacial region between Li metal anode and IL/Li_2S_6 electrolyte before and after cycling process using the XPS sample holder developed for *in situ* battery analysis (Figure A.14). The high-resolution S 2p core-level XPS spectra of Li metal anode before cycling and after each charge/discharge cycles are shown in Figure 3.7. The S 2p spectra is a doublet comprised of closely spaced spin-orbit components (Δ=1.16eV, intensity ratio=0.511) arising from $2p_{3/2}$ and $2p_{1/2}$. Each sulfur compound shows the characteristic doublet, and only the high-intensity $2p_{3/2}$ will be discussed hereafter for simplicity. The sulfone group (R-SO_2-R) of TFSI anion is observed at 169 eV along with broad sulfide peaks encompassing 160-165 eV binding energy regime.[121-122] In addition, a low-intensity peak at 167.2 eV representing

sulfite (SO_3^{2-}) or thiosulfate ($S_2O_3^{2-}$) species is also observed.[123-124] Deconvolution of S 2p spectra under the broad sulfide region gave three unique components, namely sulfide dianion (S^{2-}) of Li_2S at 160.2 eV along with terminal sulfur (S_T^{1-}) and bridging sulfur (S_B^0) of lithium polysulfide (Li_2S_x with x>1) at 161.6 and 163.3 eV, respectively.[123, 125] Based on the evolution of different sulfide concentrations (Figure 3.7b and Table A.1) during the cycling process, we can analyze the polysulfide shuttling process and subsequent parasitic reaction with the Li-anode, which is widely believed to be a major cause for capacity loss in Li-S batteries. Similarly, the S 2p peak ratio between the bridging and terminal sulfur i.e. S_B^0/S_T^{1-} of the polysulfide species can be used as a qualitative indicator of polysulfide speciation.

Before cycling, the polysulfide components (S_T^{1-} and S_B^0) are about 22 at.% of total sulfur and the S_B^0/S_T^{1-} ratio is about 2.2 in accordance with our starting electrolyte mixture, which is predominantly Li_2S_6 (Figure 3.7d). After the first charge cycle, the total amount of polysulfide components increased to ~30 at.% whereas the lithium sulfide (S^{2-}) remains at the same concentration as before cycling (5 at.% of total sulfur). During the charging process, Li^+ cations move towards Li-anode and engage in the Li-plating process ($Li^+ + e^- \rightarrow Li^0$). Such an electrochemically driven process includes Li^+ cations, which are part of lithium polysulfide species, and initiates the polysulfide shuttling process. A significant increase in polysulfide components after the charging process clearly indicates that the polysulfide shuttling process mainly depends on the Li-S interaction strength relative to Li-solvent and Li-TFSI interactions. Such a Li^+ driven shuttling process will lead to accumulation of polysulfide species and starts the fouling process at Li-anode,

which is followed through increased concentrations of polysulfide components in the XPS spectra after a charge cycle. Interestingly, the S_B^0/S_T^{1-} ratio increases to ~3 indicating that the parent Li_2S_6 polysulfide species evolve into other types of polysulfide species during the fouling process.

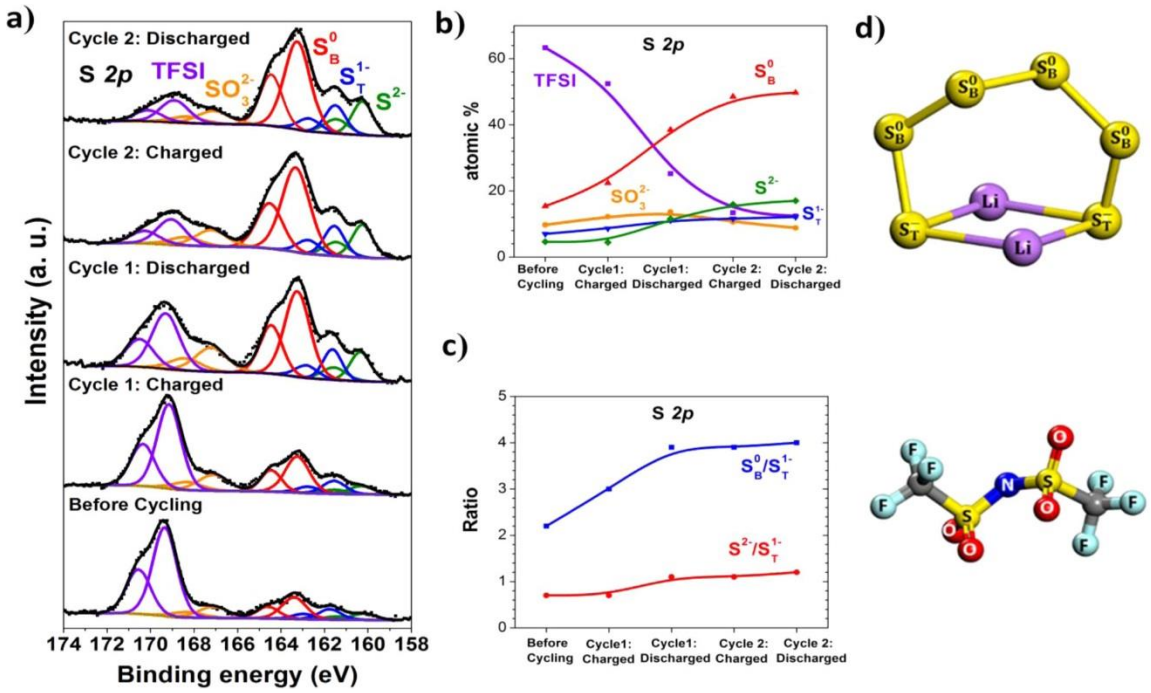

Figure 3.7 (a) Core level S 2p XPS spectra of the Li-electrolyte interfacial region with subsequent charge/discharge cycles. (b) Evolution of various sulfur-based species over charge/discharge cycles based on atomic concentration derived from S 2p peak areas. (c) The ratio between terminal sulfide and bridging sulfur atoms (S_B^0/S_T^{1-}) along with the disulfide and sulfide ratio (S^{2-}/S^{1-}) derived from S 2p peak areas. (d) Molecular structure of lithium polysulfide Li_2S_6 (top) and TFSI anion (bottom) with chemical labels used in the XPS analysis

During the discharge process, the Li-anode undergoes Li-stripping processes releasing Li^+ and electrons, which can reduce the accumulated long-chain polysulfides to lithium sulfide (S^{2-}). Evidently, the lithium sulfide (S^{2-}) concentration is nearly doubled (~10 at.%) after the first discharge cycle and further increases to 15 at.% of the total sulfur

concentrations during the second charge and discharge cycles. The significant increase in S^{2-} concentration during the discharge cycles indicates that the longer chain polysulfides accumulated at the Li-anode are being reduced to insoluble Li_2S and subsequently become irreversible parts of the SEI layer during the first discharge process.[119] This Li_2S formation covers the Li-anode surface and restricts further sulfide reduction during subsequent cycling process as noted by the similar S^{2-} concentration in the second charge and discharge cycles. Interestingly, the total amount of polysulfide components (S_T^{1-} and S_B^0) increases further to ~50 at.% and eventually reaches a plateau value of ~63 at.% during the second charge/discharge cycles (see Table A.1). It is expected that the polysulfide will shuttle back towards the cathode side during the discharge process based on Li^+ flow direction. However, we observed a continuous increase in polysulfide and Li_2S concentration at the Li-anode leading to loss of active materials (i.e., scarcity of polysulfide solute in IL electrolyte) and subsequently causing cell failure and preventing further cycling studies. This finding indicates that the fouling process is mostly irreversible and the polysulfide is chemically interacting with the other components of the SEI layer. We postulate that various components of SEI layers can strongly interact with polysulfide solutes in the electrolyte and cause continuous fouling processes that are supported by the increase in polysulfide concentration during the cycling process (see Figure 3.7b). This observation is in agreement with a previous AIMD analysis, which predicted the clustering of polysulfide chains near the Li_2S layer as part of SEI formation.[126] Nevertheless, the cluster formation is favored for lower-order polysulfide chains (Li_2S_x with $x<6$), which would require lower S_B^0/S_T^{1-} ratio (≤ 2).[100] In addition,

recent reports suggest the formation of insoluble Li_2S_2 from polysulfide reduction process at the Li-anode.[127] The observed increase in terminal polysulfide (S_T^{1-}) peak intensity with cycling initially seems to support the presence of Li_2S_2 species within the SEI layer (see Figure 3.7b). However, any such Li_2S_2 formation should significantly decrease the S_B^0/S_T^{1-} and S^{2-}/S_T^{1-} ratios. Conversely, we observed that these ratios increase with charge/discharge cycles (see Figure 3.7c), which strongly suggests that Li_2S_2 is not the dominant sulfide phase in the SEI layer.

Interestingly, the S_B^0/S_T^{1-} ratio of ~4 is even higher than the possible longer polysulfide chain (i.e. Li_2S_8 for which S_B^0/S_T^{1-} ratio is 3). Therefore, an increase in S_B^0/S_T^{1-} ratio could result from two possible scenarios: (a) the relative concentration of terminal sulfur within the polysulfide decreases possibly due to parasitic redox reactions; or (b) the presence of a new form of sulfur species which has the same binding energy (~163.5 eV) and overlaps with the S_B^0 peak. Previous studies of sulfur cathode materials have revealed that both pristine elemental sulfur (S_8) and carbon bonded sulfur (C-S^0 bond) can also register S 2p peaks at the same binding energy (~163.5 eV) as of the bridging sulfur (S_B^0) of the polysulfides.[128] Theoretical studies have predicted the formation of S_8 as a product of dissociation of polysulfide anions reactions in Li-S batteries,[119] via the reaction:

$$S_8^{2-} \rightarrow 2S_3^- + \frac{1}{4}S_8 \qquad \Delta G_{Soln}^{298K} = -0.17 \text{ eV} \qquad (3.6)$$

Nevertheless, our AIMD simulations (section 3.4.3) predicted that longer polysulfide chains are reduced very rapidly near to the Li anode.[126, 129] Thus, it is very unlikely to detect the formation of neutral S_8 on the bare surface of the Li-metal electrode. Hence, we

carried out new DFT simulations to provide more insight into the possible decomposition of the precursor Li_2S_6. In this case, the reaction energies were calculated using G09 at the B3PW91/6-311+G(3df,p) level of theory and the polarizable continuum model (PCM). The calculated Gibbs free energy in DME solvent reveals two possible reduction processes:

$$Li_2S_6 + 2Li^0 \rightarrow Li_2S + Li_2S_5 \qquad \Delta G_{Soln}^{298K} = -4.69 \text{ eV} \qquad (3.7)$$

$$Li_2S_6 + Li^0 \rightarrow Li_2S + LiS_5 \qquad \Delta G_{Soln}^{298K} = -1.29 \text{ eV} \qquad (3.8)$$

Our DFT results indicate that the reduction product of Li_2S_5 is energetically favorable (Equation 3.7) but represents a S_B^0/S_T^{1-} ratio of 1.5. Despite its favorable formation energy (ΔG_{soln}), the Li_2S_5 formation requires a higher concentration of Li^0 (i.e. prevalent access to Li-metal surface) relative to the LiS_5 formation process. This implies that, with restricted access to Li-metal, the reduction product of LiS_5 would be more probable (see Equations 3.7 and 3.8). Formation of LiS_5 ($S_B^0/S_T^{1-} = 4$) can account for the simultaneous increase of both Li_2S concentration and S_B^0/S_T^{1-} ratio (~3.9) observed in our *in situ* XPS results (see Figure 3.7c). Such a reduction process can occur at the terminal sulfur atom of polysulfide molecule (i.e. S_T^{1-} to S^{2-}), which will result in a significant increase in the S_B^0/S_T^{1-} ratio and S^{2-} concentration, agreeing with our observations (see Figure 3.7c). However, the long term stability of LiS_5 molecule within the SEI layer still needs to be evaluated further with other analytical techniques.

In addition to the polysulfide shuttling, the SEI layer formation would also depend on the TFSI anion decomposition process. The decomposition of the TFSI anion can be simultaneously monitored by the evolution of sulfone and sulfite peaks observed in the

higher binding energy regime (>166 eV) in the S 2p spectra (see Figure 3.7a). Before cycling, the sulfone peak from TFSI species represents ~63 at.% of total sulfur concentration on the Li-anode. During the first charge and discharge cycles, the amount of sulfone species drops to ~53 and 27 at.%, respectively. Subsequently, after the second charge and discharge cycles, it drops to about 20 at.%, relative to sulfide and polysulfide concentrations (see Figure 3.7c). Such a significant drop in the pristine TFSI anion concentration on the Li-anode indicates two possible mechanisms: (a) a set of redox reactions altering the sulfone group as part of TFSI decomposition, (b) displacement of some TFSI molecules by polysulfide species at the Li-anode surface due to the SEI layer formation process within the XPS analysis volume. Recently, Cui *et al.*[127] suggested that the sulfone group of TFSI anion can undergo oxidation processes at the Li-anode and produce sulfite (SO_3^{2-}) and sulfate (SO_4^{2-}) species based on XPS analysis. However, they did not consider the sulfur spin-orbit based doublet in their peak deconvolution and the reported (SO_4^{2-}) species peak (~ 170 eV) falls within the S $2p_{1/2}$ component of the sulfone group of a pristine TFSI molecule. Our results do not show the presence of any sulfate but only the sulfite (SO_3^{2-}) species, which shows minimal changes during the cycling process (~ 4 at.%) and fails to account for the significant drop in pristine TFSI concentration (see Figure 3.7c). Decomposition of the sulfone group and formation of $Li_2S_2O_4$ and Li_2SO_3 were proposed in the literature, and this mechanism can explain the low-intensity sulfite peak (~10 at.%) observed at ~167 eV during the cycling process.[22, 130] The other possibility would be the reduction of the sulfone group of the TFSI molecule to sulfur (S^0), which will fall in the sulfide regime of the XPS spectra and thereby increase the S_B^0 concentration

as observed in a higher S_B^0/S_T^{1-} ratio. However, unless the sulfone group of a TFSI anion undergoes multi-electron reduction (from S^{6+} to S^0) at the Li-metal anode, the decomposed products are expected to be at higher binding energy (>166 eV) similar to the sulfite/thiosulfate or sulfone regions. Since multi-electron reduction is less likely, we do not expect a significant increase in S^0 due to this mechanism. The second scenario would be the displacement of TFSI anions by the polysulfide fouling process discussed earlier. Typically, the TFSI anion can interact with the counterion from the IL (i.e. $[bmpyr]^+$), Li-anode, and Li^+ from the polysulfide species. During the cycling process, we observed that the polysulfide reduces to insoluble Li_2S, which can grow as a passivating film on the Li-anode surface.[126, 129] Such a Li_2S passivation layer can inhibit the Li^+-$TFSI^-$ interactions and enhance the $[bmpyr]^+$-$TFSI^-$ ion-pairing leading to ionic solute flux towards the electrolyte phase. However, it should be noted that the Li_2S passivation layer is unlikely to be uniform and the TFSI anion will compete for interactions with the exposed Li-anode surfaces (vide infra) and cause the TFSI decomposition process. The TFSI anion decomposition is a cascade process with many transient species including sulfone and fluoride groups, which can subsequently interact with lithium polysulfide molecules and the Li-anode.[129] This process supports our previous discussion regarding the polysulfide species interacting with other components of the SEI layer and causing continuous fouling processes on the Li-anode. This clustering process will be further justified a posteriori below using other elemental analysis.

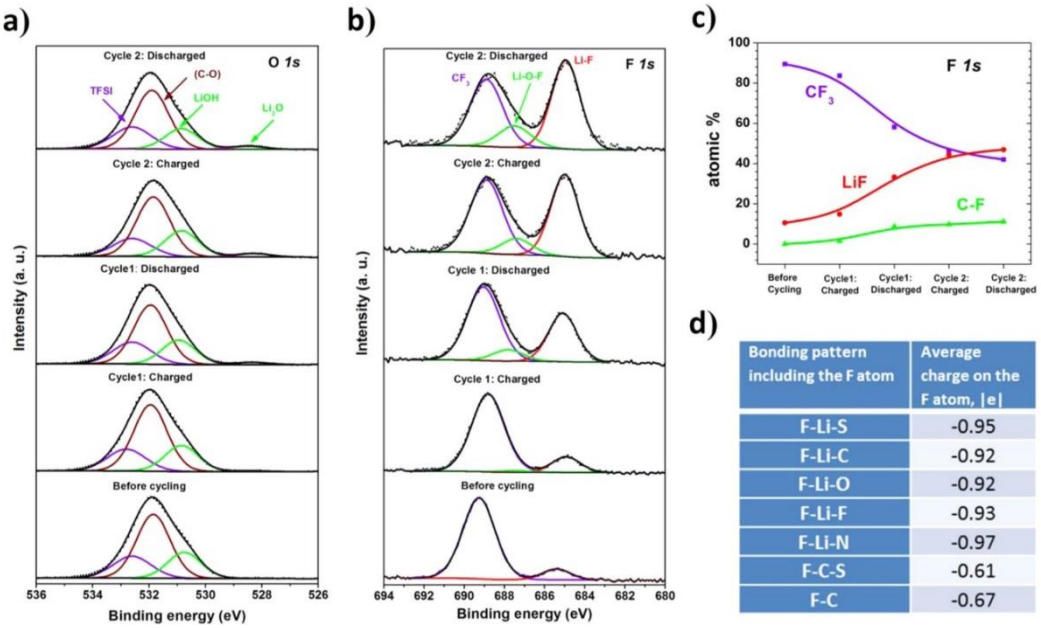

Bonding pattern including the F atom	Average charge on the F atom, |e|
F-Li-S	-0.95
F-Li-C	-0.92
F-Li-O	-0.92
F-Li-F	-0.93
F-Li-N	-0.97
F-C-S	-0.61
F-C	-0.67

Figure 3.8 (a) Core level O 1s XPS spectra of the Li-electrolyte interfacial region with subsequent charge/discharge cycles. (b) Core level F 1s XPS spectra of Li-electrolyte interfacial region with charge/discharge cycles. (c) Evolution of various fluorine-based species over charge/discharge cycles based on atomic concentration derived from respective F 1s peak areas. (d) The various fluoride based species from TFSI decomposition predicted from AIMD calculations along with their respective electronic charges.

The TFSI anion decomposition process at the Li-anode can be followed through O 1s and F 1s spectra for a deeper understanding of the SEI layer formation. The O 1s spectra is dominated by a broad peak centered around 532 eV, which can be assigned to C-O bonds within DOL/DME (electrolyte solvents) as well as lithium carbonate (Li-metal surface impurity) owing to their small chemical shift differences (see Figure 3.8a).[130-131] Deconvolution of the broad O 1s spectra revealed shoulder peaks at ~ 532.6 eV and 530.6 eV indicating the S-O bonds (sulfone and sulfite) and lithium hydroxide (Li-metal surface impurity), respectively.[131] There is no significant change in the concentration of these oxygen species during the cycling process. We also observe a low intensity (~3 at.%) peak at 528.5 eV with the cycling process indicating lithium oxide (Li_2O) formation at the

Li-anode as a result of TFSI decomposition. Although, the decomposition of the sulfone group can cause Li_2O formation,[129] the presence of carbonate and hydroxide native impurities at the Li-anode surface can also lead to lithium oxide. The main product of TFSI decomposition would be lithium fluoride (LiF) formation from C-F bond breaking at the Li-anode.[129] Such a decomposition process can be analyzed through F 1s spectra (see Figure 3.8b). The F 1s spectra show the dominant TFSI anion peak (CF_3) at 688.8 eV along with a low-intensity Li-F related species peak around 685 eV.[121, 130-131] The Li-F related species formation even before the cycling process demonstrates the instability of TFSI anions on the Li-metal anode. The concentration of Li-F species is about 11 at.% of total fluorine before cycling and increases to 15 at.% following the first charging cycle (see Table A.2). During the subsequent discharge cycle, the amount of this Li-F based species more than doubles to ~33 at.% (see Figure 3.8c). Such a substantial increase in the amount of Li-F species must correlate to accelerated decomposition of the TFSI anion during the discharge process. This peak at ~685 eV in the F 1s spectra is widely reported as evidence of LiF formation.[132-135] In addition, a new shoulder peak (~687.5 eV) arises near the parent CF_3 peak following the charge/discharge process, which is traditionally assigned to C-F intermediate species as part of TFSI decomposition.[129, 136] However, such a simplified peak assignment can hinder deeper understanding of the SEI layer evolution.

To clearly identify the possible fluoride species within the SEI layer, we analyzed various components of TFSI decomposition products predicted by our AIMD simulations in sections 3.4.2 and 3.4.3 (see Figure A.17 to Figure A.19). Since the charge state of an atomic site dictates the binding energy of XPS spectra, we analyzed the average electronic

charges of the F atom for various decomposition products and relevant fluoride atomic arrangements along with their average charge as shown in Figure 3.8d. These fluorine-containing species generally fall in two categories based on the charge at the F atom. The first category is fluorine directly bonding through Li where the F atom takes the highest negative charge (ionic bonding), and the second is fluorine directly bonding with C atoms in which a much lower negative charge is observed (covalent bonding). The F-C-S bond (when part of an otherwise pristine TFSI molecule) holds the lowest charge (-0.61 |e|) and is expected produce a signal at high binding energy (688.8 eV) in the F 1s spectra. The C-F bonding interaction, which may correspond to the different intermediates (radical and anions) formed during the TFSI decomposition such as CF, CF_2, and CF_3, holds a slightly elevated charge (-0.67 |e|) at the F atom and is observed as a shoulder peak at ~688 eV. However, it should be noted that the CF_3^- remaining intact after the C-S bond cleavage during TFSI decomposition has a longer life span and is more likely to represent the shoulder peak observed under cycling conditions.[129] Similarly, the lower binding energy (~685 eV) peak represents various species involving Li-F ionic bonding, such as F-Li-S, F-Li-O, and the traditional LiF phase. At the end of the initial charge cycle, the C-F species remains at very low concentration (~1 at.%) relative to total fluorine concentration, but increases to 9 at.% following the first discharge cycle. This suggests further decomposition of TFSI anion at the fully discharged state, which is typically initiated by C-S bond cleavage and subsequent breaking of the CF_3 bond to C-F and F-species and the formation of Li-F related species.[129] The decomposition of TFSI anion continued during the second charging cycle resulting in 33% and 11% increases in Li-F and C-F species, respectively,

relative to the fully discharged anode. However, both Li-F and C-F species reached a plateau after the second discharge cycle, which resembles the saturation of polysulfide fouling process (see Figure 3.7b). A similar trend observed for both TFSI decomposition and the polysulfide fouling process in the SEI layer evolution during the cycling process supports our previous deduction that the polysulfide molecules interact with various components of the SEI layer including the TFSI decomposition products. Our previous *in situ* NMR and our AIMD computational analysis (see section 3.4.3) have unveiled the presence of sulfide based transient radicals and reactive fluoride anions at the Li-anode participating in the SEI layer formation process.[77, 129] During the cycling process, the redox-based parasitic reaction can cause highly reactive transient species (such as sulfide radicals and fluoride anions) that can initiate clustering of nearby electrolyte components through polymerization and subsequently leading to precipitation-induced SEI layer formation on the Li-anode.[137] Although the high resolution *in situ* XPS analysis revealed the evolution of polysulfide and Li-F species as the major components, the growth mechanism of SEI layer formation is still elusive, mainly due to extreme complexity involving parasitic reaction rate, Li-anode surface chemistry and the concentration gradient of solutes. In particular, the concentration gradient of solutes at the interfacial regime can dictate the composition of the cluster and subsequent SEI layer nucleation and growth phenomena.[138]

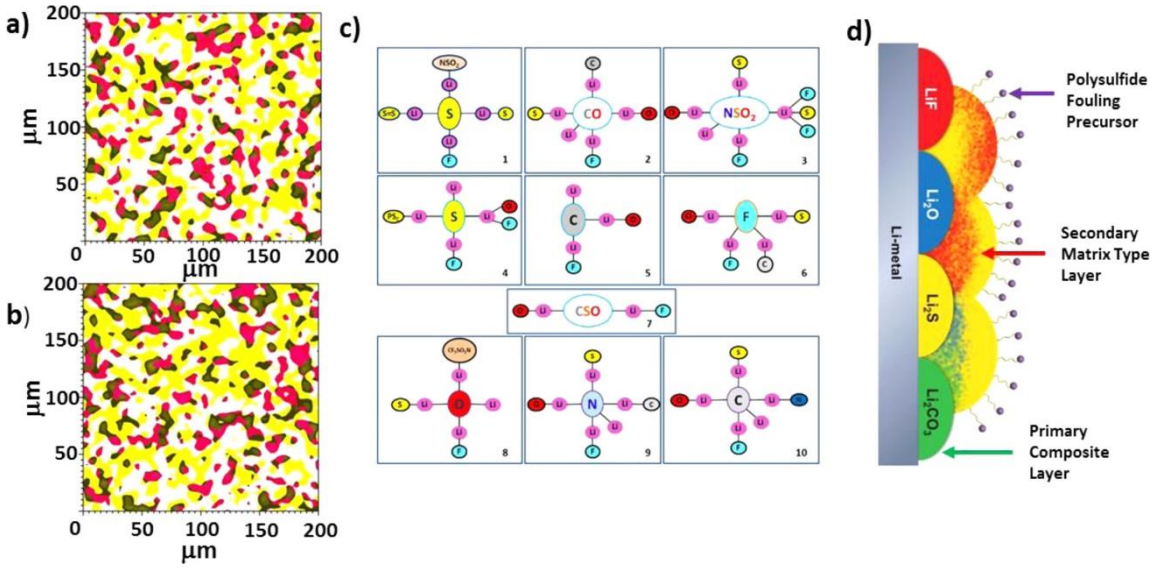

Figure 3.9 XPS chemical imaging of the Li-electrolyte interfacial region after (a) first charging cycle and (b) first discharging cycle. The Li-F species from F 1s spectra and S^0 polysulfide species from S 2p spectra are represented as yellow and red regions, respectively. The black region represents the overlapping regions of Li-F and S^0polysulfide species. (c) Schematic representation of various fluorine-based Li-F species predicted from AIMD calculations. (d) Cartoon representation of SEI layer growth mechanism based on the combined XPS and computational results (see text for details).

We also employed XPS spectromicroscopy to analyze the underlying growth mechanism of the SEI layer, which can provide realistic views of concentration gradients in the spatial domain.[139-140] Figure 3.9 shows a two-dimensional chemical imaging performed at the same spot on the Li-anode after the first charge/discharge process (see Figure A.20). The interfacial region (800x800 µm) is scanned at 685 eV (F 1s; Li-F species) and 163.3 eV (S 2p; S_B^0) binding energies to monitor the TFSI anion and polysulfide gradient with a spatial resolution of about 5 µm. The contour mapping of chemical imaging clearly shows the clustering of reactive solutes, polysulfide (blue) and Li-F related species (red), within the top layers of anode – electrolyte interfacial region, which can subsequently precipitate as an SEI layer (Figure 3.9a, b). Since the XPS imaging

is typically dominated by the concentration gradient of the top layer (< 5 nm) within the interfacial regime, the delimited white background represents SEI layers adjacent to the Li-anode surface with a relatively lower concentration of polysulfide and LiF. It should be noted that the discharge cycle has a higher concentration of polysulfide and Li-F species than during the charge cycle. The rise in polysulfide concentration after the discharge cycle simply reflects the expected polysulfide shuttling towards the Li-anode. Such clustering of polysulfide at the interfacial region can facilitate Li_2S precipitation as a SEI layer due to possible reduction reactions (see Equations 3.7 and 3.8). Similarly, the clustering of Li-F species can cause precipitation of lithium fluoride (LiF) phases within the SEI layer. The presence of well-separated clusters of polysulfide (blue) and Li-F (red) represents the nucleation seeds for Li_2S and LiF phases and evolve as a dominant part of SEI layer evolution. Intriguingly, the total Li-F species raises along with polysulfide from the shuttling process during the discharge cycle, indicating that the F^- anion from TFSI decomposition interacts with lithium polysulfide (see Figure 3.8b). The overlapped signal (black) in the imaging map indicates a possible cross-interaction between F^- anion and lithium polysulfides. This corroborates our a priori assumption that the reactive transient species involving polysulfide and fluoride anion can chemically interact and initiate clustering with various electrolyte components. For example, AIMD computational results predicted multiple types of Li-F species involving various electrolyte components (see Figure 3.9c and Appendix A), which could also be part of clustering phenomena that can initiate the precipitation as part of SEI layer.

Combining high-resolution XPS and chemical imaging analysis with AIMD computational modeling results, we can begin unraveling the SEI layer growth mechanism. The SEI layer is commonly viewed as a multiphase material with chemically distinctive phases (such as LiF, Li_2S, Li_2O, and Li_2CO_3) separated by well-defined boundaries (see Figure 3.9c). In fact, clearly distinguishable clustering of polysulfide (blue) and Li-F (red) species supports this multiphase structural view of the SEI layer. However, significant overlapping of polysulfide and Li-F regions (black) reveals the presence of a matrix type SEI layer with continuous phases and diffuse boundaries between the various sulfide and fluoride-based regimes (see Figure 3.9d). The simultaneous multiphase and continuous phase SEI layer formation can be explained by the Stranski-Krastanov (SK) growth model developed for thin film nucleation processes.[138] Based on this growth model, the SEI layer formation can be viewed as a two-step process where (a) the products of parasitic reactions at the Li-anode surface result in multiphase layers (such as Li_2S, Li_2O, and LiF), and (b) clustering of transient species from parasitic reactions, by strongly interacting with the electrolyte and other SEI components, leads to a matrix type precipitation. During the evolution of the first step, the parasitic products need to be adjacent to the Li-anode surface to gain expedited access to preferably unbound Li^+ ions that can facilitate an extended network of Li_2S and LiF solid multiphase layers. For example, clustering of polysulfide as part of the shuttling process on the Li-anode can cause the nucleation of Li_2S phases by accessing the Li stripping process during discharge cycles. With growth to critical thickness, this insoluble multiphase layer can significantly inhibit the access to unbound Li^+ from the Li-anode and

thereby activate the second stage of the SEI layer growth. With restricted access to the Li-metal surface and scarcity of unbound Li^+ ions, the parasitic reaction products will react with each other as well as with adjacent electrolyte components to initiate nucleation directly on the multiphase layer and produce a matrix type phase with diffused boundaries. In particular, the restricted access to Li-metal can cause partial polysulfide reduction processes (Equation 3.8) leading to a mono-anionic polysulfide (LiS_5) as a major component of the secondary layer that results in a high S_B^0/S_T^{1-} ratio ($\geq$3). This secondary SEI layer mainly consists of aggregated polysulfides and oligomeric reactive products and is comparable to the organic phase layer comprised of polymerized solvents reported in lithium-ion batteries.[22, 137, 141] Nevertheless, the major difference is that it involves polysulfides as a main component and also serves as an absorbent layer for the shuttling polysulfides, which leads to an exponential increase in polysulfides after the first charge/discharge cycle in high resolution *in situ* XPS (see Figure 3.7b). In addition, the adsorbed polysulfides can undergo association and disproportionation reactions causing oligomeric aggregates on top of the SEI layer, which is evident from the clustering of polysulfides detected via *in situ* imaging XPS analysis (see Figure 3.9b).[100] Unlike the primary multiphase layer containing inorganic solid phases, the constituents of the second stage matrix-type layer could be relatively soluble and hence subsequent polysulfide fouling will be a dynamic process depending on electrolyte composition and cycling current rate. In short, the oligomeric aggregation of polysulfides on the SEI layer entraps the active material on the Li-anode and manifests as the severe capacity fading that is widely reported in the Li-S battery literature.

3.5. Conclusions

The extreme reactivity of the Li-anode surface in contact with the electrolyte solution in Li-S batteries has been investigated using DFT-based and *in situ* XPS techniques. From DFT and AIMD simulations, we found that the salt LiTFSI is much more reactive than typical solvents such as DOL and DME. Cleavage of the C-S or N-S bond was found as the starting point for all of the LiTFSI reduction pathways, the first one being the most thermodynamically favorable. Eventually, the salt becomes decomposed into multiple fragments. One of the most important products is LiF but other charged radical anions are derived from C, SO_2, O, and CSN fragments that mostly become adsorbed onto the metal surface. None of the Li-S solvents tested (DOL and DME) were found to be decomposed during the entire simulation, whereas EC decomposes very quickly via sequential 4 or 2 electron mechanisms in agreement with previous analyses on lithiated silicon anodes and on pure Li surfaces. The primary method of Li_2S_8 fragmentation away from the anode surface does not involve delithiation; however, the most favorable pathway includes reaction of the lithiated PS with additional Li atoms, in gas phase or in presence of the solvent, with four different fragmentation modes found having similar (very favorable) ΔG*s* of reaction. In contact with the anode surface, the long-chain PS species is highly decomposed despite the solvent used or the PS initial geometry (ring or linear), resulting in the formation of a Li_2S layer.

In addition, the XPS core-level spectra of S 2p showed a gradual increase of sulfide dianion (S^{2-}) indicating the formation of Li_2S due to polysulfide reduction processes. Similarly, the F 1s spectra showed a significant increase in Li-F and C-F species with a

decrease in CF_3 due to $TFSI^-$ decomposition. Evolution of both Li_2S and Li-F species with cycling causes the precipitation of an inorganic multiphase layer as the primary SEI component. A simultaneous exponential increase of polysulfide species (S^0 and S^{1-}) suggests a continuous fouling process on the Li anode during both charge and discharge cycles. The high S_B^0/S_T^{1-} ratio (>3) observed for the polysulfide species indicates the formation of mono-anionic polysulfide (i.e. LiS_5) due to restricted access to Li-metal during the sulfide reduction process. With access to the Li-metal surface becoming restricted, the parasitic reaction products will engage in cross-interaction with adjacent electrolyte components and nucleate into a secondary matrix type SEI layer, which is visualized as clustering in XPS imaging and supported by AIMD analysis. The continuous increase in polysulfide concentration at the Li interface also suggests a facilitated fouling process due to its absorption on a matrix type SEI layer. Chemical entrapment of the dissolved polysulfides at the top of the matrix type layer on the Li-anode causes the fouling and subsequent continuous loss of active material. Therefore, controlling the role of SEI layer in Li-S batteries will require a multi-functional scaffold design, which can deflect the shuttling polysulfide as well as inhibit the electrolyte decomposition at the Li anodes.

4. EFFECTS OF HIGH AND LOW SALT CONCENTRATION IN ELECTROLYTES AT LITHIUM-METAL ANODE SURFACES[*]

4.1. Summary

The use of high concentration salts in electrolyte solutions of Li-S batteries has been shown beneficial for mitigating some effects such as polysulfide shuttle and dendrite growth at the Li metal anode. Such complex solutions have structural, dynamical, and reactivity associated issues that need to be analyzed for a better understanding of the reasons behind such beneficial effects. Here we investigate – using DFT and AIMD – the salt decomposition, solvation effects, interactions among intermediate products and other species, and potential components of the SEI layer as a function of chemical nature and concentration of the salt, for LiTFSI and LiFSI at 1M and 4M concentrations in DME. It is found that LiTFSI undergoes a less complete reduction and facilitates charge transfer from the anode, whereas LiFSI shows a more complete decomposition forming LiF as one of the main SEI products. In addition, the specific decomposition mechanisms of each salt clearly point to the initial SEI components and the potential main products derived from them. Very complex networks are found among the salt and solvent molecules in their attempt to maximize Li-ion solvation that is quantified through the determination of coordination numbers.

---

[*] Reprinted with permission from Luis E. Camacho-Forero, Taylor W. Smith, and Perla B. Balbuena. "Effects of High and Low Salt Concentration in Electrolytes at Lithium-Metal Anode Surfaces." *The Journal of Physical Chemistry C*, 2017, **121** (1), 182-194.

4.2. Introduction

One of the issues holding back the development of Li-S batteries is the need for an electrolyte which will allow for rapid cycling of lithium, exhibit stability even near the lithium anode, and, when decomposition does occur, decompose to products which will yield a SEI layer with beneficial properties for the cell.[14, 120, 142-143] Solvents such as DME and DOL have been shown to exhibit acceptable stability at the anode and are widely used in Li-S cells.[144-145] Common Li-S salts such as LiTFSI and $LiPF_6$, meanwhile, have higher reduction potentials than the aforementioned solvents, and both components of the electrolyte are prone to decomposition.[146-147] More importantly, this SEI also seems to hamper the cell's performance, as these salts and others can yield inefficient lithium cycling, and passivate the electrode.[148-149]

Theoretical methods have shown to yield insights into the makeup of the SEI formed and the mechanism by which it occurs, providing guidance for the formulation of new chemistries or alternative conditions (concentration, temperature of the cell, etc.). To this end, Qian *et al.*[101] discussed the use of the LiFSI salt to help mitigate the problems seen at the lithium anode, specifically at high concentrations (up to 4M) in DME. For these conditions, a Coulombic efficiency (CE) of over 99% was achieved while also eliminating dendrite growth, and a vast difference was seen in the performance of the LiTFSI and LiFSI salts, which the authors attributed to an increase in the coordination of the solvent and Li^+ availability. LiFSI also has a higher conductivity than other common Li-S salts such as $LiPF_6$, $LiClO_4$, and LiTFSI.[150] Kim *et al.*[151], on the other hand, showed that LiFSI-based electrolytes at high concentration (5M) yield similar CE and good cycle stability

attributed to protective layers formed at both electrodes resulting from LiFSI reduction. The use of high-molarity salts, especially LiTFSI, has been previously shown to dramatically reduce polysulfide dissolution, yielding similar results to those seen by Qian and leading to a significant reduction in overcharge.[152] For instance, Suo *et al.*[153] demonstrated exceptional results when using ultrahigh LiTFSI concentration (7M) in a solvent-in-salt electrolyte, where the salt comprised most of the electrolyte. This resulted in inhibited dendrite growth and polysulfide shuttle, as well as outstanding CE and rate capability. Furthermore, Yushin *et al.*[154] also reported enhanced cycle stability of Li_2S-based cathodes using high electrolyte molarity (up to 7M LiTFSI) without any electrolyte additives, where the superior performance was attributed to reduced polysulfide dissolution and favorable SEI formation on the Li surface.

Unfortunately, LiTFSI is, compared to the other materials in the typical Li-S cell, extremely expensive, and this is only worsened at higher molarities.[155] But perhaps through the use of alternative salts at these conditions (such as LiFSI), a more affordable electrolyte still possessing excellent electrochemical properties can be attained. Although there are other components that are present in the electrolyte such as PS species, in this chapter, we attempt to provide a theoretical basis for the structural, dynamical, and reactive behavior of high-molarity salt solutions by examining the differences between LiFSI and LiTFSI, and comparing the behavior of both species at both high (4M) and low (1M) concentrations at the anode, without including the presence of the PS species. The reaction pathways, structure and composition of the decomposed fragments, extent of decomposition, distribution of charge, and composition of the SEI are all examined in

detail in order to identify and explain the exceptional salt performance mentioned above, especially in the 4M LiFSI case.

4.3. Computational and System Details

4.3.1. Model of Lithium-Metal Surface and Electrolyte Components

In order to model the Lithium-metal anode, a BCC Li cell was optimized using DFT. Subsequently, the (100) Li crystallographic plane was cleaved from the optimized bulk structure. A 9-layer (3x3) supercell model was employed to represent the anode surface in this case as shown in Figure 4.1a. All calculations were performed using the VASP.[58-60] The PAW pseudopotentials[50-51] as provided in the VASP databases were used to describe electron-ion interactions. The Perdew-Burke-Ernzerhof generalized gradient approximation (GGA-PBE)[45] was chosen as the exchange-correlation functional. The energy cut-off of the plane-wave basis expansion was set to 400 eV, which corresponds to the optimum cut-off found for bulk Li with energy convergence within 1 meV. A conjugate-gradient algorithm was employed to relax the ions into their instantaneous ground state. The convergence criteria for electronic self-consistent iteration and ionic relaxation were set to 10^{-4} and 10^{-3} eV, respectively. A Gaussian smearing with a width of 0.05 eV was utilized to set the partial occupancies to each wavefunction. For the surface Brillouin zone integration, a 4×4×1 Monkhorst-Pack[54] k-point grid was used.

Optimized structures for DME and LiTFSI were taken from our previous work (Chapter 3).[129] The LiFSI salt molecule was optimized using the Gaussian 09 (G09) package[89] with a hybrid functional B3PW91 and the 6-311++G(p,d) basis set[46, 90]. FSI^- has been reported to be stable in two different configurations similar to LiTFSI: C_1 (*cis*)

and C_2 (*trans*).[156-158] In this work, the anion was optimized to the C_2 symmetry. Both bond lengths and angles for the optimized FSI^- were found in good agreement with previous theoretical studies.[156-157] Next, the cation Li^+ was located in the bridge position between two oxygen atoms. This site has been found preferentially rather than close to the nitrogen atom.[159] Comparative optimized geometries for both salts, LiFSI and LiTFSI, are shown in Figure B.1 (Appendix B).

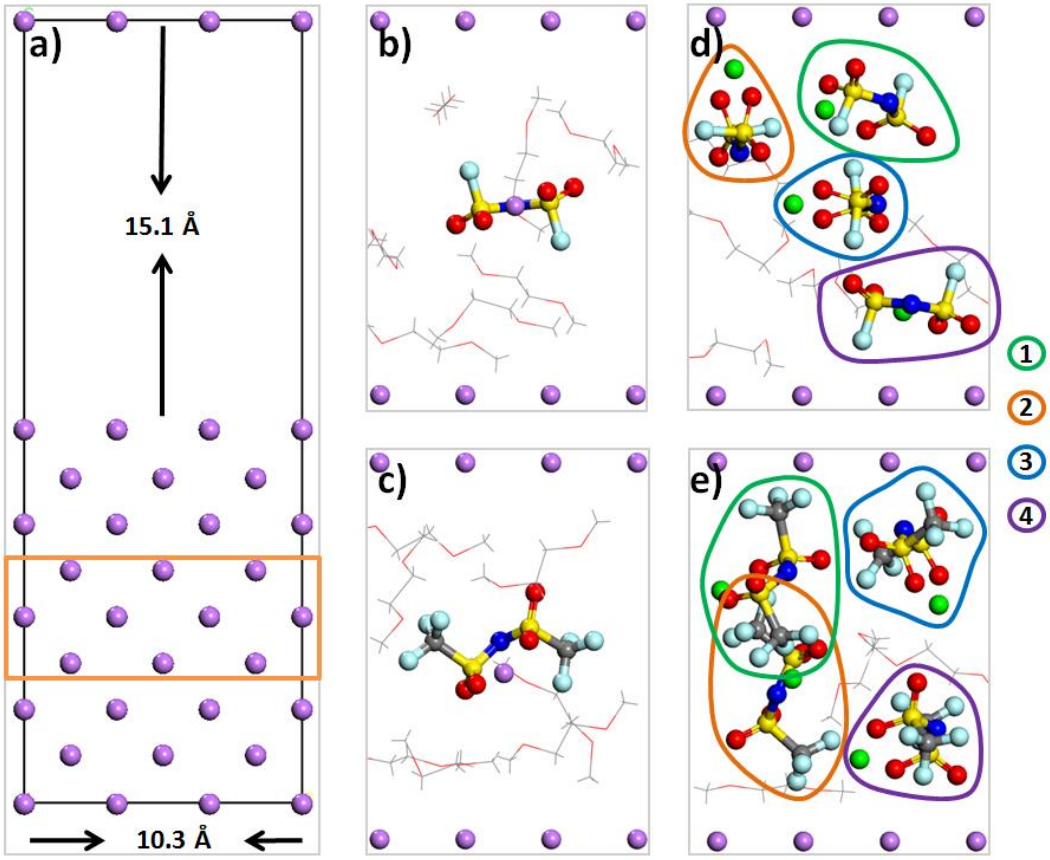

Figure 4.1 Model of the lithium-metal anode surface and initial electrolyte mixtures (salt/DME) used in the AIMD simulations. (a) Li-(100) surface. Orange rectangle indicates fixed Li layers. (b) 1M LiFSI, (c) 1M LiTFSI, (d) 4M LiFSI, and (e) 4M LiTFSI. Salt molecules (right) are identified according to colored shapes and numbered circles. Color code: lithium from the slab and salts in 1M (4M) solutions, purple (green); oxygen, red; carbon, gray; fluorine, light blue; sulfur, yellow, nitrogen, blue; hydrogen, white.

4.3.2. Effects of Salt Concentration on Reactivity at the Li-Metal Surface

The salt reactivity, stability, and concentration effect near the lithium-metal anode surface were studied using AIMD simulations carried out on the optimized anode surface in contact with a liquid-phase mixture containing DME as solvent and salt (LiTFSI or LiFSI). For this purpose, a *NVT* ensemble at 330 K was used. Tritium masses were replaced for protons to allow a time step of 1 femtosecond. The Nose thermostat was used to control the temperature oscillations during the simulation with a Nose-mass parameter of 0.5. In this case, a 2x2x1 k-point mesh was used. Both low (1M) and high (4M) salt concentration were investigated. Due to the volume of the simulation cell, one and four salt molecules were required to achieve the 1M and 4M concentration, respectively. The number of solvent molecules placed randomly in contact with the model anode surface was estimated by using the density of the liquid-phase DME (density = 0.87 g/cm^3). Afterward, the solvent molecules in the liquid-phase were allowed to relax using a classical molecular mechanics energy optimization. For this minimization, the consistent valence force field (CVFF) with a conjugate gradient algorithm as implemented in the Materials Studio software[94] was used. The maximum force among all the atoms in the system required for convergence was set to 0.005 kcal mol^{-1} $Å^{-1}$. The resulting electrolyte systems are shown in Figure 4.1b-c, and Figure 4.1d-e for 1M and 4M concentrations of each salt, respectively. Subsequently, the minimized systems were allowed to run for 16 ps of AIMD simulation. Charge transfer was studied by using the Bader charge analysis.[63-65] It is noteworthy that electronic charges are not observables and the results indicating fractional charges are an artifact of the method. Finally, in order to test the consistency of

AIMD results regarding the salt decomposition, bond dissociation energies for the LiFSI molecule and resulting fragments from the decomposition were calculated in solvent (DME) and under Li^0 radical attack. The solvation effects were implicitly represented by the polarizable continuum model (PCM)[95] as implemented in the G09 software package. Bond energies were calculated using G09 at the same level of theory abovementioned.

4.3.3. Structure and Dynamics of Salt Solutions in Bulk Electrolyte

In order to gain more insights about the behavior of the electrolyte under different salt concentrations, several electrolyte mixtures were investigated by using AIMD simulations at 330 K during 20 ps with the same simulation parameters used in the previous section. In this case, the electrolyte system was modeled using a periodic 15 Å x 10 Å x 10 Å cell. These dimensions are similar to those of the liquid-phase (not including the slab) in the previous section (4.3.2); however, here the model lithium anode was removed in order to study how the nature of the salt, its concentration, and the Li^+ concentration affect the structure of the electrolyte and solvation of Li ions in the bulk electrolyte (far from the electrodes). A total of twelve different mixtures were studied, divided into three main groups: 0M, 1M, and 4M, corresponding to the salt concentration. The first group (0M) was built with a pure solvent model electrolyte containing 1 and 3 Li^+. The second group (1M) was formed by mixtures of salt (either LiTFSI or LiFSI) and DME, where three systems per each salt were considered corresponding to the addition of 0, 1, and 3 Li ions to the 1M-salt electrolyte mixtures. In the last group (4M), 0 and 1 Li^+ were added to each 4M-salt solution. The locations of the added Li ions were assigned randomly and relatively far away from each other. The radial distribution functions (RDF)

g(r) were obtained using the Visual Molecular Dynamics (VMD)[160] program with a Δr of 0.05 Å.

4.4. Results

4.4.1. Salt Reactivity and Effect of Salt Concentration at the Li-Metal Surface

4.4.1.1. 1M Solutions

LiFSI has shown promising performance in Li-S systems as an alternative to the LiTFSI salt. Thus, to better understand its role and impact in Li-S batteries, the reactivity of 1M of LiFSI solution in DME is compared to the 1M LiTFSI counterpart. The salts are initially located slightly far away from the surface (~5 Å) as shown in Figure 4.1a and b for LiFSI and LiTFSI, respectively. The LiFSI reduction mechanism and instantaneous fragment charges are depicted in Figure 4.2. The fractional charges shown are an artifact of the model but provide an idea of the extent of charge transfer. It is found that the LiFSI salt molecule does not survive the duration of the simulation. At 2.8 ps, it partially dissociates, i.e., one of the two O-Li^+ ionic bonds (Figure B.1) in the molecule dissociates. The resulting configuration begins to defluorinate at 3.7 ps, where the F^- remains in the liquid-phase until a SO_2 group breaks and recombines with the F^- forming FSO_2^- at around 4 ps. The new anion retains the Li^+ and is stable for the next 7 ps when it breaks again producing $LiSO_2$ (being the only remaining stable fragment in the liquid-phase by the end of the simulation) and F^- that migrates toward the surface where LiF is formed. Regarding the $FNSO_2^{2-}$ fragment formed when SO_2 breaks, it defluorinates almost at the same time as it is formed and the NSO_2^- anion moves then to the surface where it initially gains two additional electrons and is reduced into its elemental constituents by the lithium anode. A

similar reduction mechanism has been reported for FSI^- anion decomposition in ionic liquids in contact with a lithium metal anode or lithiated silicon anodes.[108, 110, 161]

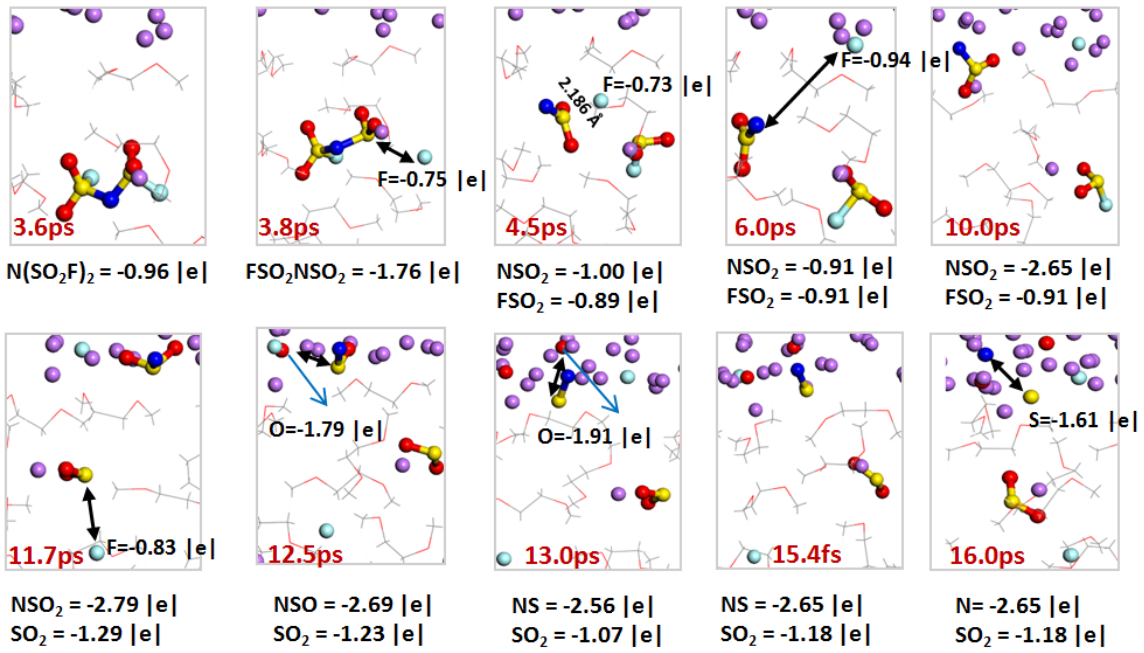

Figure 4.2 LiFSI reduction mechanism in a 1M solution. The average charge of Li (from LiFSI) is 0.87 (±0.01) |e| over the simulation time. Color code as in Figure 4.1.

On the other hand, Figure B.2 illustrates the reduction mechanism of LiTFSI. Here, the salt decomposes by the breaking of an S-C bond at 5.1 ps, but both fragments $(Li^+)CF_3SO_2N^{2-}$(adsorbed on the surface via O–Li) and CF_3^- (in liquid-phase) survive until the end of the simulation (no further reduction). Also, the LiTFSI salt is not observed to dissociate into anion and cation species, as was the case, at least partially, with the LiFSI system. These results suggest that there is a significant difference in the reactivity and reduction pathways between these two salt molecules. For this reason, both salts were tested in separate AIMD explicit solvent simulations in order to determine their stability

in DME (without the anode). Over 16 ps, however, the LiFSI did not decompose, and neither did the LiTFSI. This indicates that the presence of the lithium anode is a major factor driving the salt reduction. A charge analysis of Li-anode surfaces in both cases reveals that electron transfer from the anode towards the electrolyte drives the reactions to happen, as shown in Figure B.3. For LiFSI, an increasing charge transfer starts at around 3ps of simulation time, which coincides with the different decomposition events seen during the simulation. Conversely, a gain of 2 electrons is detected at 5 ps in the case of LiTFSI, which is when the S-C bond cleavage takes place. By the end of the simulations, the Li-slab exhibits a charge of +11 |e| and +3 |e| for the 1M-LiFSI and LiTFSI, respectively, where only about +1 |e| is associated to the interaction with the solvent. Although in this scenario (salt relatively far from anode) the LiTFSI molecule did not decompose to a great extent, it has been reported that when LiTFSI is initially located near the anode it may decompose close to its elemental constituents and $LiSO_2$; in that case the charge transferred to the salt is considerably higher (~17 |e|)[129]. Thus, both salts may decompose to the point where their elemental constituents interact with the lithium anode to form SEI layer components. Based on the number of F atoms one may speculate that the SEI layer formed from LiFSI may contain less LiF than in the case of LiTFSI, and in the latter, C-containing SEI components are expected to form. In addition, shorter remaining fragments from the salt decomposition may be produced from LiFSI in comparison with those from LiTFSI decomposition leading to relatively stable large fragments[129] such as $CF_3SO_2N^{2-}$. Thus, it is possible that the amount of LiF could be larger

for LiFSI in spite of the lower number of F atoms, while fluorinated polymers derived from fragments such as $CF_3SO_2N^{2-}$ may be expected in LiTFSI electrolytes.

4.4.1.2. 4M Solutions

To further explore salt behavior at the anode, high molarity (4M) salt simulations were carried out with both salts. To begin, we examine the 4M LiFSI solution by isolating the reaction mechanism of each molecule resulting from the AIMD simulations (there are 4 molecules in the simulation cell tagged according to Figure 4.1d). Figure 4.3 illustrates the reaction pathway followed by the molecule 1 (1-LiFSI). The 1-LiFSI molecule loses a fluorine atom within 120 fs, which is adsorbed on the lithium surface. The $F(SO_2)_2N^{2-}$ fragment dissociates into FSO_2N^{2-} and SO_2 within the next 200 fs. 300 fs later, the FSO_2N^{2-} group breaks and forms NSO and other elemental constituents that are adhered to the surface for the rest of the simulation time. On the other hand, SO_2 remains stable for more than 5 ps, when it is finally decomposed into S^{2-} and O^{2-}.

The reduction mechanisms of the 2-LiFSI and 3-LiFSI molecules are shown in Figure B.4 and Figure B.5, respectively. In these cases, the sets of reactions start later (1 and 4 ps for 2- and 3-LiFSI, respectively) than in the 1-LiFSI molecule, yet a similar mechanism to the one observed for 1-LiFSI was identified in both cases. The main observable difference is the extent of decomposition. Here, the FSI^- anion loses one fluorine atom. Interestingly, in the case of 3-LiFSI, the F^- forms a LiF neutral species with the cation of the salt. This is followed by the cleavage of an N-S bond which leads to the formation of the FSO_2N^{2-} and SO_2 fragments. The first fragment only defluorinates and the NSO_2^{3-} formed remains attached to the surface for the rest of the simulation. Regarding

the SO_2, for 2-LiFSI, it is reduced to its elemental constituents as in the first case. However, for 3-LiFSI, only one of the S-O bonds breaks, leaving a SO^{2-} fragment adsorbed on the lithium anode. In order to corroborate the degree of decomposition for these three salt molecules, the simulation was run for eight more picoseconds, giving a total simulation time equal to 24 ps. No further reactions were observed.

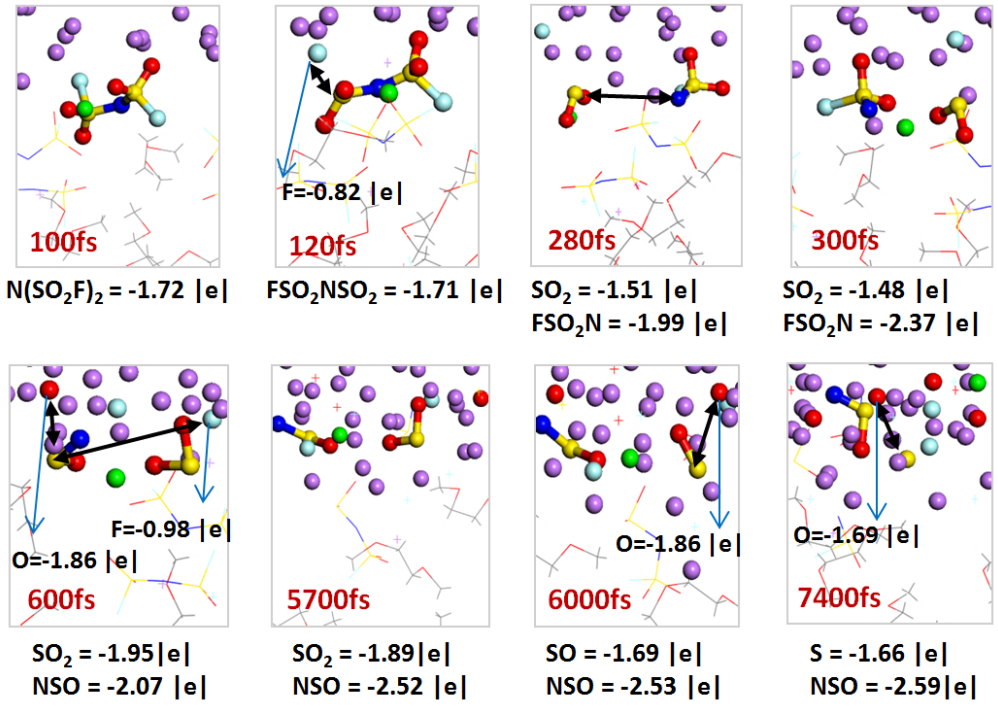

Figure 4.3 1-LiFSI reduction mechanism in a 4M-LiFSI/DME solution. The average charge of Li (from LiFSI) is 0.85 (±0.02) |e| over the simulation time. Color code as in Figure 4.1.

Although molecules 1 to 3 showed a similar reduction mechanism, this was not the case for the fourth molecule: 4-LiFSI. Interestingly, the 4-LiFSI molecule starts to decompose similarly to the other LiFSI molecules, by one S-F bond breaking. However, in this case, the second S-F bond is cleaved almost simultaneously with the first. The first

F^- forms a LiF neutral species resembling the one observed for 3-LiFSI, while the second fluorine atom is adsorbed on the surface. The remaining $(SO_2)_2N^{3-}$ fragment stays attached to the surface for the duration of the simulation (Figure 4.4).

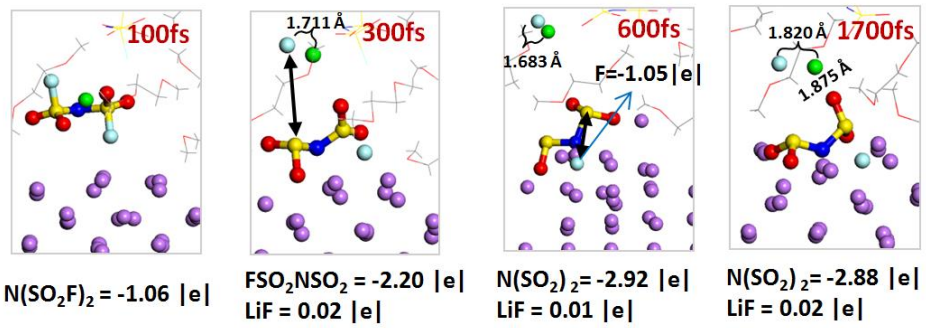

Figure 4.4 4-LiFSI reduction mechanism in a 4M-LiFSI/DME solution. Average charge of Li (from LiFSI) 0.87 (±0.01) |e| over the simulation time. Color code as in Figure 4.1.

The 4M-LiTFSI solution is also found to be very reactive and to begin decomposition almost immediately. We begin by considering the reduction of the 1-LiTFSI molecule shown in Figure B.6. The 1-LiTFSI molecule begins its decomposition by the breaking of the S-N bond at 1 ps resulting in $CF_3SO_2N^{2-}$ and $CF_3SO_2^-$. The $CF_3SO_2N^{2-}$ fragment is stable for the remainder of the simulation time. However, $CF_3SO_2^-$ decomposes sequentially into CSO, F, and O within the next 2 ps. The 2-LiTFSI molecule starts to decompose at 8 ps, as seen in Figure B.7. A C-S bond is initially broken, followed by the reduction of the CF_3^- group into its C and F elements within the next 5 ps. The $CF_3SO_2NSO_2^{2-}$ fragment did not undergo further reaction. Figure B.8 illustrates the fast reduction of the 3-LiTFSI molecule (at a time < 2 ps). In fact, this reaction pathway is similar to the one seen in the 1-LiTFSI molecule. Once the $CF_3SO_2N^{2-}$ and $CF_3SO_2^-$

fragments are formed due to the cleavage of one S-N bond, the $CF_3SO_2^-$ reacts immediately. The SO_2^{2-} group in contact with the anode is reduced into its elemental constituents, followed by the CF_3^- defluorination. Both S-N and C-S bonds breaking have been found in previous theoretical studies of $TFSI^-$ decomposition.[107-108, 129] In contrast, the decomposition of 4-LiTFSI follows an entirely different pathway (Figure B.9) and does not begin until 10 ps of simulation time have elapsed, being the last of the four salt molecules to react. The first bond to break is an S-O; 200 fs later a CF_3^- group is released, and by 14.6 ps of simulation it has been reduced to its elemental constituents. The CF_3SO_2NSO group then begins to defluorinate within the next picosecond, leaving a CSO_2NSO fragment with a charge of ~ -5 |e|. After an S-O and S-N bonds are broken in the next 500 fs, a CSO_2N fragment remains. The elemental C from the CF_3^- group decomposition then reacts with the CSO_2N group, removing the C to form a C-C group. Its charge (~ -2 |e|) and the fact that is surrounded by Li atoms from the anode suggest the formation of a molecule of lithium carbide (Li_2C_2). The remaining SO_2N^{3-} group loses its two oxygen atoms by the end of the simulation, leaving only a SN^{3-} group adhered to the lithium anode. To briefly summarize the 4M LiTFSI results: this high molarity salt electrolyte is very prone to salt decomposition, the fragments remain relatively large, and many fragments survive the duration of the simulation.

4.4.1.3. Bader Charge Analyses

In order to gain additional insights into the behavior of the high molarity salt electrolytes, Bader charge analysis was conducted on each salt molecule for both 4M solutions. Figure 4.5 shows the net charge transferred to each salt molecule over the

simulation time. First, let us consider the 4M-LiFSI case shown in Figure 4.5a. The 1-LiFSI molecule (in green) showed a great increase of charge within the first picosecond of simulation (~7 |e|), followed by a 3 |e| gain at about 6 ps corresponding to the reduction of the salt (into SO_2, NSO, F, and O) and decomposition of SO_2, respectively. Similarly, the 2-LiFSI molecule (in orange) exhibits a rapid increase of charge (~7 |e|) which is attributed to the fast decomposition of this salt as revealed in Figure B.4. Interestingly, the 3-LiFSI molecule (in blue) presented the slowest charge transfer mechanism, which can be related to its relatively larger distance from the surface compared to the other salt molecules. Here, a +~2 |e| step mechanism is observed at about 3.5, 7.2, 8.8, and 15.4 ps and corresponding to S-F, S-N, S-F, and S-O bond cleavages. Finally, the 4-LiFSI molecule (in purple) shows a sharp ~4 |e| charge increase attributable to the two +2 |e| S-F bond breaking mechanisms observed in Figure 4.4.

For the 4M-LiTFSI solution, the charges of the 1-LiTFSI and 3-LiTFSI molecules increase rapidly (about 8 and 12 |e|, respectively) due to their relatively fast decomposition (Figure 4.5b). The two reaction mechanisms are similar; however, in the 1-LiTFSI case, a CSO fragment is not reduced resulting in less charge transfer to this molecule compared to 3-LiTFSI. 2-LiTFSI and 4-LiTFSI molecules exhibit much slower charge transfer mechanisms. In fact, the net charge of the 4-LiTFSI molecule oscillates significantly within the first 8 ps, after which its charge is stabilized when the 2-LiTFSI molecule gains ~2 |e|. 1.6 ps later the 4-LiTFSI molecule starts to decompose following the above mentioned unusual S-O bond breaking. This reduction is carried out over the following 6 ps, requiring a progressive increase of charge up to about 17 |e| to take place. By the end

of the simulation, only a SN fragment survives. To clarify the possible reason for this new S-O bond cleavage mechanism, a 1M-LiTFSI solution using the same salt location was simulated using AIMD for 16 ps and, surprisingly, the salt decomposes following the C-S bond cleavage mechanism. This suggests a concentration effect led to the S-O bond-breaking first. The fact that the charge of the 4-LiTFSI molecule is stabilized once the 2-LiTFSI molecule is reduced also seems to indicate that there may be competitive charge transfer processes between the 2-LiTFSI and 4-LiTFSI molecules and the surface which leads to this new decomposition mechanism.

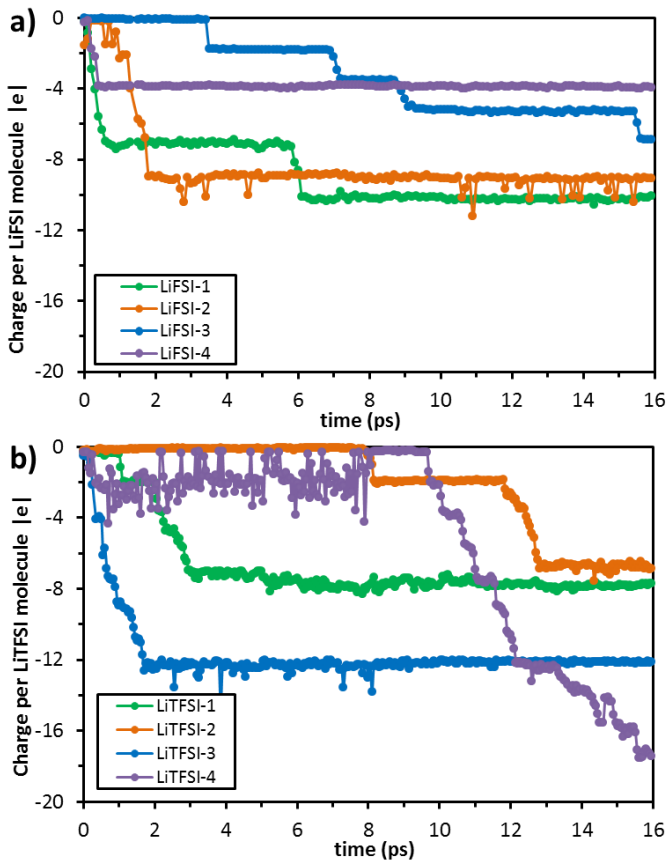

Figure 4.5 Charge transfer per molecule*. a) LiFSI and b) LiTFSI. *Charges were calculated based on the elements forming the molecule before reduction.

Further examination of the charge analysis reveals the net charge transferred from the Li-slab in both scenarios. According to Figure B.10a, both Li-anodes for the high salt concentration systems started with a charge of +2 |e| (initial solvation/interaction between surface lithium atoms and the electrolyte, see details in Figure B.10b). By the end of the simulation, the Li-slab in the 4M-LiFSI system had transferred over 30 electrons to the electrolyte, most of which were accepted by the salt molecules. In the 4M-LiTFSI system, the Li-slab had a net charge transfer of +44 |e|. Although the decomposition of LiTFSI is less extensive than that of LiFSI, the charge analysis reveals a higher electron transfer (14 electrons) for the LiTFSI case. Therefore, in order to investigate the origin of this significant difference, the net charge of the atoms making up the salt molecules was calculated and reported in Figure 4.6. It can be observed that while there is some change in the net charges of N, O, and F, this is minimal compared to those of S and C. The S atoms in the salt molecules accept around 23 and 17 electrons for 4M-LiFSI and 4M-LiTFSI, respectively. Hence, it is clear that the S atoms in the LiFSI system gain more charge from the lithium anode than in LiTFSI, which might be partly responsible for the lower extent of decomposition of LiTFSI. However, the main difference between the two salts is that the carbon atoms in the LiTFSI are able to accept additional electrons (-19 |e|), whereas carbon is not present in the LiFSI salt. This is also the primary reason the Li anode exhibits a greater net charge transferred in the high molarity LiTFSI system than in the LiFSI. The DME molecules are relatively stable, and no reactions have been observed during the timescale of these simulations. Moreover, Figure B.11 illustrates the average

charge per atomic species (complementing the data in Figure 4.6) and the DME. DME molecules gain only -0.07 |e| and -0.01 |e| per molecule by the end of the simulated time with LiFSI and LiTFSI, respectively.

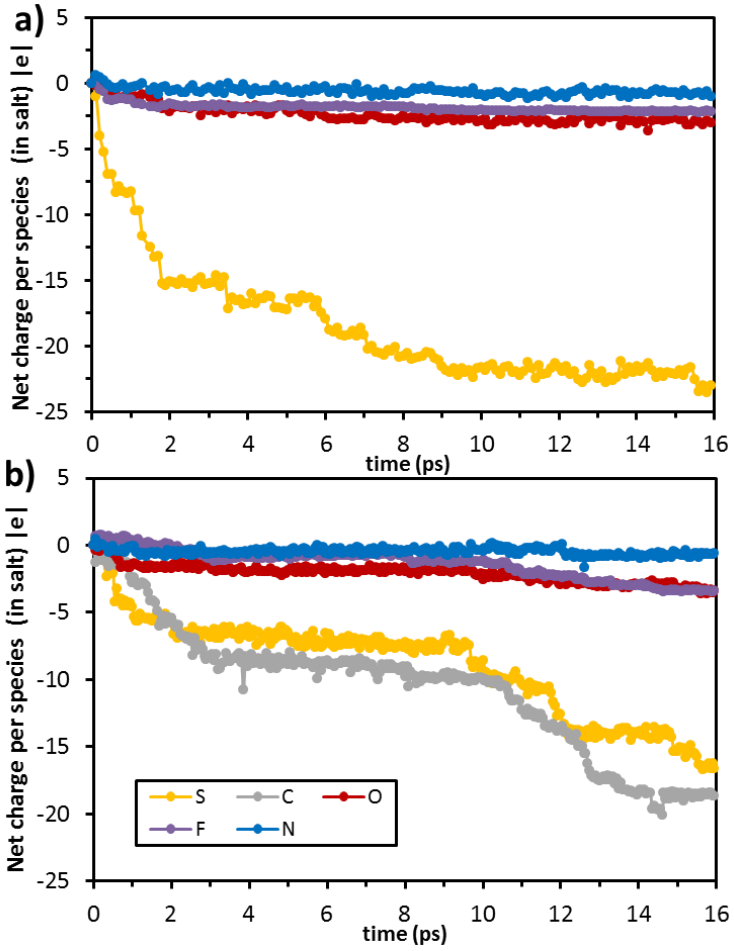

Figure 4.6 Net charge** transferred to the elemental species within the salts (S, C, O, F, and N). a) LiTFSI and b) LiFSI. **Charge corresponds to the summation of all the charges of each atomic species within the salts.

4.4.1.4. Characterization of SEI Components (4M solutions)

Figure 4.7 shows the two exposed surfaces (since our model is a symmetric slab) for each system at the end of the simulation. This figure allows us to identify the initial

components of the likely SEI layer formed due to salt decomposition at the anode in high molarity salt electrolytes. In both high-concentration electrolyte systems, 2-3 layers of Li from each exposed side of the slab (top and bottom) were involved in the reduction of the salts. Almost complete decomposition of the salt can be observed in three out of the four salt molecules in the 4M-LiFSI system, with the largest fragments being NSO_2 (bottom) and $N(SO_2)_2$ (top) (Figure 4.7a). Conversely, the 4M-LiTFSI case shown in Figure 4.7b illustrates a rougher surface due to the larger fragments that appears comparatively more stable at least in the first instants of interactions with the metal surface. Here we can identify that one of the four LiTFSI molecules almost completely decomposes. The remaining three molecules also decompose; however, large fragments are still present by the end of the simulation (CF_3SO_2N and $CF_3SO_2NSO_2$). In addition, the presence of reactive molecules containing carbon, such as LiTFSI, generates a distinct pathway in the formation and properties of the SEI layer. Another key difference between these two salts is with respect to the possible formation of LiF. For the LiFSI salt, no F atom stays adhered to any remaining fragment after 16 ps, while for the LiTFSI, several whole CF_3 groups remain attached. Thus, these results suggest that the LiFSI-based electrolyte may form a LiF SEI-layer more efficiently than LiTFSI, resulting in a protective mechanism for the Li-metal anode.

4.4.1.5. Thermodynamics of Reactions

According to the previously discussed reaction mechanisms, it appears that the orientation of the salt with respect to the anode surface may be causing some of the differences in the decomposition pathways. In order to establish a better understanding of

these reactions, DFT calculations were performed separately to establish reaction energies and thermodynamic favorability based on the direction of lithium attack on the salt molecule. Here, a Li^x (x=0, +1) was located near a neutral LiFSI (LiTFSI) salt in different positions: near an oxygen (Li^x--O), a nitrogen (Li^x--N), a fluorine (Li^x--F) atom or a Li^+ (Li^x--Li^+) as described in Figure B.12 in order to calculate the affinity towards charged or neutral Li. Furthermore, two more Li-salts commonly used in lithium batteries systems[120, 162] ($LiPF_6$ and $LiBF_4$) were tested to compare their behavior with these two salts.

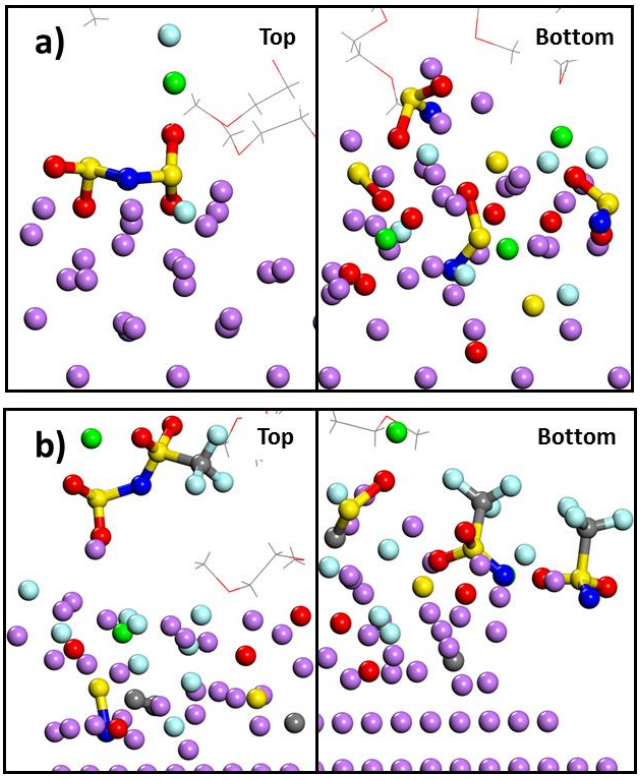

Figure 4.7 SEI-layer components resulting after 16 ps of Simulation time for 4M solutions. Fragments and atomic species, products of the salt decomposition remain adsorbed or forming the SEI on the Li-metal slab. No reduction products were observed in the liquid-phase in any case. a) LiFSI and b) LiTFSI. Color code as in Figure 4.1.

Table 4.1 Calculated interaction energies for different salts with various Li^x (x=0, +1) orientations from B3PW91/6-311++G(p,d) calculations. All energies are given in eV and were calculated using an implicit model to represent the DME. Final configurations for reacting systems are shown in Figure B.13. 1c, 2c, and 3c are the 1, 2, and 3-fold LiF coordination shown in Figure B.12. ΔE and ΔG are at 0 and 298 K, respectively.

Salt		Li^x--F				Li^x--N		Li^x--O		Li^x--Li^+	
		1c		2c/3c							
		Li^0--F	Li^+--F	Li^0--F	Li^+--F	Li^0--N	Li^+--N	Li^0--O	Li^+--O	Li^0--Li^+	Li^+--Li^+
LiFSI	**ΔE**	**-3.16**	-0.16	-	-	**-2.80**	-0.19	**-2.78**	-0.15	**-0.33**	-0.09
	ΔG	**-2.86**	0.17	-	-	**-2.52**	0.08	**-2.50**	0.18	**-0.13**	0.18
LiTFSI	**ΔE**	-	-	**-1.67**	-0.01	-0.08	-0.16	-0.13	-0.17	**-0.34**	-0.11
	ΔG	-	-	**-1.45**	0.27	0.23	0.19	0.16	0.15	**-0.16**	0.21
$LiPF_6$	**ΔE**	-0.09	-0.15	**-1.34**	-0.20	-	-	-	-	**-0.35**	-0.10
	ΔG	0.19	0.16	**-1.12**	0.11	-	-	-	-	**-0.14**	0.16
$LiBF_4$	**ΔE**	-0.20	-0.23	-0.07	-0.19	-	-	-	-	**-0.32**	-0.20
	ΔG	0.08	0.07	0.20	0.13	-	-	-	-	**-0.13**	0.09

The interaction energy resulting from these orientations are displayed in Table 4.1. Regarding LiFSI, the data suggests that the Li^0 attack from the position near the fluorine atom is the most favorable, followed closely by an attack on the N atom, O atom, and Li^+ (from salt), respectively. Interestingly, in the three first cases, a reaction has actually taken place – the same reaction detected in the AIMD simulations. The attacking lithium atom has induced a removal of a fluorine atom in all three scenarios. In fact, in the most favorable case, Li removes the F and LiF is formed. This reaction is extremely favorable ($\Delta E_r = -3.16\ eV$), as might be expected from the AIMD simulations in which LiFSI reacts rapidly in contact with Li metal and forms LiF. This data supports the results of the previous AIMD simulation: Li attack on the F atoms is highly thermodynamically favorable, while the Li^0 being near the Li^+ (from the salt) is much less so. This provides us a good theoretical explanation for the difference in stability of molecules 1-LiFSI and

2-LiFSI in the 4M LiFSI simulation; molecule 1 (F atom oriented towards the Li metal) reacts rapidly with the lithium surface (within 120 fs) and decomposes almost completely, while molecule 2 survives for nearly 10 times as long (1200 fs) and has a less complete decomposition. The LiTFSI seems to be more stable than the LiFSI, as only one C-S bond was affected when the Li^0 was initially placed near the fluorine atoms (3-fold coordinate, 3c). However, in this case, the energy was reduced almost by half compared to the Li^0--F previously discussed. With a reaction energy slightly lower than the LiTFSI salt, LiF is formed (as in LiFSI) due to a fluorine atom being removed by the Li^0 attack when the neutral lithium is located near two F atoms (2-fold coordinate, 2c) in $LiPF_6$ in agreement with earlier studies on lithiated silicon anodes[163], where PF_6^- decomposes in contact with Li active surface sites. Finally, for $LiBF_4$ no spontaneous reaction was observed regardless of the orientation of Li^0 or Li^+. In general, whenever the reaction is thermodynamically spontaneous ($\Delta G_r < 0$, highlighted in red and bold font in Table 4.1), the attack by neutral lithium is much more favorable than charged, i.e., higher interaction energy, even when near nucleophilic sites, such as in the configuration near the N or O, which explains the high reactivity only at the surface for all the salts tested. In addition, the Li^0--Li^+ energy of interaction is very consistent within all the salts tested: $\Delta E_r = -0.32\ to - 0.35$ eV and $\Delta G_r = -0.13\ to\ - 0.16$ eV.

It has been observed that, in different scenarios for 1M and 4M LiFSI systems, the Li^+ in the salt may play a role in the salt decomposition process. For instance, in the 1M case, partial dissociation was observed prior to decomposition. In the 4M solution, the decomposition of salts 3 and 4 show Li^+ forming a LiF with a fluorine atom that is released

from its salt. Therefore, the ionic dissociation energy was calculated for LiFSI in gas-phase and in-DME (implicit solvent) using G09 and comparing these results to those reported for LiTFSI.[129] The results (see Table B.1) show that for gas-phase, the dissociation is unlikely in any case (ΔEr's~6 eV). In-DME, there is a substantial reduction in the energy of reaction compared to gas-phase, as might be expected. However, the dissociation energies (free energies) of LiFSI and LiTFSI are 0.62 (0.31) and 0.75 (0.43) eV, with the LiFSI being more prone to dissociate, yet neither being favorable. This suggests that the impressive properties observed by Qian *et al.*[101] may arise from properties other than LiFSI's tendency to dissociate and supports the idea that the LiFSI is, in fact, stable far away from the anode surface, as is LiTFSI, and as was found in the explicit solvent results with DME. Additionally, energy calculations were made using an explicit solvent model within a periodic cell by using VASP (not shown). The final results in reaction energy between the implicit and explicit solvent calculations differed by only 5%, leading us to confirm the previous results.

In order to evaluate the energetics of the decomposition of LiFSI and some of the fragments observed during the AIMD simulations, bond dissociation energies were calculated. If the LiFSI decomposition is carried out in-solvent and without the presence of additional lithium atoms (Table 4.2), none of the proposed reactions is thermodynamically favorable. The one that requires the lowest energy (3.09 eV) is the N-S breaking bond. Similar results were observed when a FSI^- anion is used instead (Table B.2). Thus, these results coupled with the ionic dissociation data shown before allow us to infer that the real driving force in salt decomposition is the presence of the lithium

anode. In addition, the further decomposition of the fragments tested in this case (NS_2O_4F and SO_2F with varying charge allocation) is still not thermodynamically favorable even though the energy required in some of these cases is much lower than what is needed to break the salt molecule itself.

Table 4.2 B3PW91/6-311++G(p,d) calculated bond dissociation energies for LiFSI and fragments in solution (DME).

Reactions	Bond Dissociation Energies (eV)	
	ΔE (0K)	ΔG (298K)
$LiFSI \rightarrow F + LiNS_2O_4F$	3.77	3.39
$LiFSI \rightarrow F^- + LiNS_2O_4F^+$	3.40	3.02
$LiFSI \rightarrow LiNSO_2F + SO_2F$	3.09	2.49
$LiFSI \rightarrow NSO_2F + LiSO_2F$	3.61	3.01
$NS_2O_4F^- \rightarrow NSO_2^- + SO_2F$	1.96	1.43
$NS_2O_4F^- \rightarrow NSO_2 + SO_2F^-$	1.45	0.92
$NS_2O_4F \rightarrow NSO_2 + SO_2F$	2.17	1.61
$SO_2F^- \rightarrow F^- + SO_2$	1.09	0.77
$SO_2F^- \rightarrow F + SO_2^-$	3.89	3.53
$SO_2F \rightarrow F + SO_2$	1.43	1.10

To emulate the decomposition of LiFSI induced by the anode, one lithium radical was added to the system. Results are shown in Table 4.3. In contrast to the in-solvent only scenario, the presence of Li induces a very thermodynamically favorable reaction. Both S-F and N-S bonds are very likely to break, with cleavage of the S-F bond being the most favorable (-2.93 eV). These results are consistent with our AIMD simulations in which S-F was in every case observed as the initial bond cleavage in the decomposition process at both 1M and 4M concentrations. Decomposition by the N-S bond is also likely and agrees well with our molecular dynamics observation of this behavior after the S-F cleavage.

Additionally, NSO_2 and SO_2F fragments were also identified as common products in the AIMD results; these species were often further reduced, even to their elemental constituents in some cases. Accordingly, we have calculated the reaction energies corresponding to deoxygenation and defluorination of NSO_2 and SO_2F at different charges. These results indicate that the formation of LiO is highly favorable. The formation of LiO^-, however, is more complicated. When produced from NSO_2^- and neutral lithium, LiO^- is thermodynamically unfavorable (1.32 eV). But in the case of NSO_2^{-2}, the creation of both NSO^- and LiO^- anions is very favorable. Likewise, defluorination of SO_2F to form LiF and either SO_2 neutral or charged shows a tremendous driving force (-5.38 and -2.95 eV, respectively). This provides another example of the large propensity of LiFSI to form LiF when in contact with Li metal, which was also discussed in relation to the AIMD simulations for this salt.

Table 4.3 Calculated bond dissociation energies for LiFSI and fragments in-solution (DME) and under Li radical attack from B3PW91/6-311++G(p,d).

Reactions	Bond Dissociation Energies (eV)	
	ΔE (0K)	ΔG (298K)
$LiFSI+Li \rightarrow LiF+LiNS_2O_4F$	-2.93	-3.08
$LiFSI+Li \rightarrow Li_2NSO_2F+SO_2F$	-1.23	-1.52
$LiFSI+Li \rightarrow LiNSO_2F+LiSO_2F$	-2.64	-2.95
$Li+NSO_2 \rightarrow NSO+LiO$	-1.75	-1.89
$Li+NSO_2^- \rightarrow NSO^-+LiO$	-1.22	-1.36
$Li+NSO_2^- \rightarrow NSO+LiO^-$	1.32	1.18
$Li+NSO_2^{-2} \rightarrow NSO^-+LiO^-$	-2.00	-2.09
$SO_2F^-+Li \rightarrow LiF+SO_2^-$	-2.82	-2.95
$SO_2F+Li \rightarrow LiF+SO_2$	-5.28	-5.38

4.4.2. Structure and Dynamics of Salt Solutions in Bulk Electrolyte

In the previous section, our discussion was limited to events occurring at or near the lithium-metal anode and its electrical double-layer. We now turn our analysis toward the bulk electrolyte in order to study how the salts, their concentration, and the Li^+ concentration affect the structure of the electrolyte and the solvation of Li ions. The addition of Li^+ ions to the solution represents the flux of Li-ions through the bulk. Thus, the excess of 0, 1, or 3 Li^+ ions in the solution is equivalent to have infinite dilution, 0.008, or 0.023 g/cm^3 of Li^+, respectively. From these calculations, we observe that Li^+ ions may be solvated differently after 20 ps depending on the salt concentration. We first consider the case of 1M salt concentration, illustrated in Figure 4.8. Neither salt completely dissociates after 20 ps (i.e., only one of the two O—Li^+ bonds is broken), which agrees well with our prediction in the previous section regarding the dissociation energy of each salt. Interestingly, even when there is an excess of Li^+, the salts still partially dissociate, with the lone exception being when 3 Li^+ are added to a solution containing LiTFSI. In this case, the original cation keeps its two bonds to the O atoms from the salt. For both salts at 1M concentration with no Li-ion excess, the cation is solvated by two DME species, coordinating with one and two oxygen atoms in each case. The addition of one Li^+ to the solution does not affect the way the cation from the salt is solvated, and two clusters are formed: one containing the salt and the other the added Li-ion 4-fold coordinated by 3 and 2 DME molecules for LiFSI and LiTFSI mixtures, respectively. Further addition of lithium ions (+3Li^+) to the mixtures induces the creation of a more complex coordinated network near the salts. In the 1M-LiFSI solution, the salt shares two

cations (its own and an attracted one) with the solvent molecules and the remaining two added Li^+ form one cluster each coordinated by four oxygen atoms from two and three DME molecules. In contrast, for 1M-LiTFSI, a more complex cluster is formed surrounding the salt, but this salt also traps one of the added Li^+. The cation from the salt (in purple) is solvated by two oxygen atoms from two DME species; one of these two molecules solvates also one of the added Li^+. This lithium-ion is solvated by two additional DME molecules. One of the DME molecules solvates, simultaneously, one Li^+ which is attracted by the salt atoms, closing the complex structure.

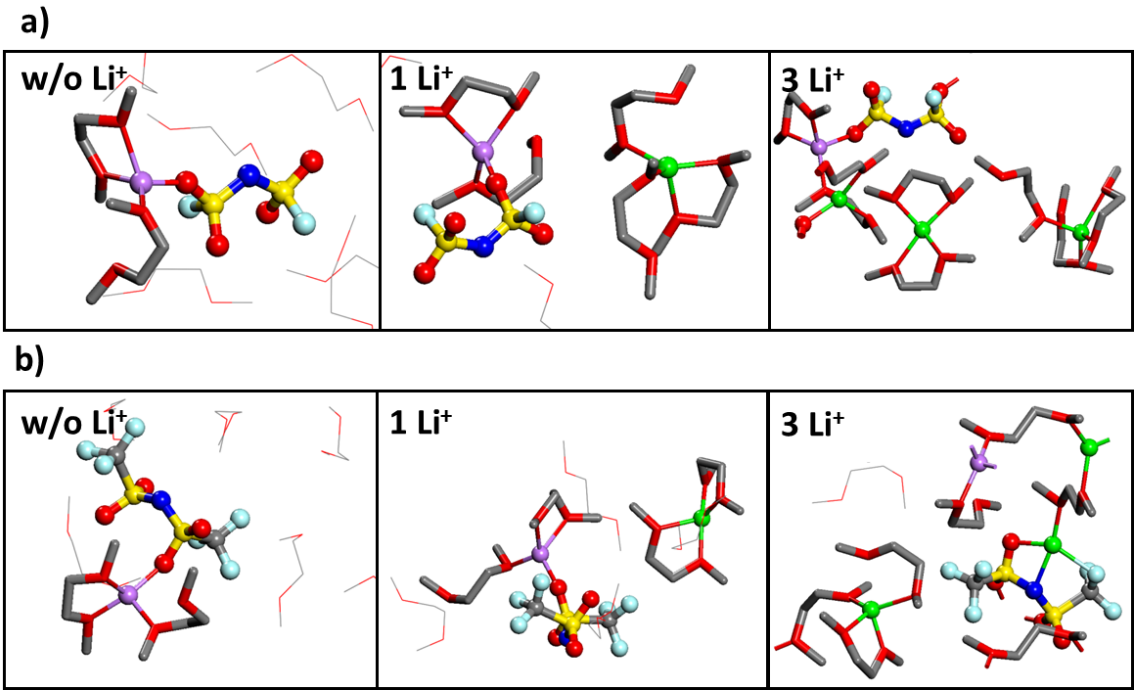

Figure 4.8 1M-salt electrolyte solutions after 20 ps of simulation time at 330K with different concentrations of Li-ions (see text). a) LiFSI and b) LiTFSI, respectively. Color code: lithium from salts (excess), purple (green); oxygen, red; carbon, gray; fluorine, light blue; sulfur, yellow, nitrogen, blue; hydrogen, white. Hydrogen atoms are not shown for clarity.

Figure B.14 shows the system configuration after 20 ps of simulation time for high molar concentration of LiFSI and LiTFSI with and without excess Li^+. For the stoichiometric amount of Li^+, both salts form a unique and more complex network than what is observed in the previous case (1M concentration). This network contains all the cations in the solution. Here all the Li^+ ions are shared between the salt and solvent molecules. Interestingly, in the case of 4M-LiFSI/DME mixture, the FSI^- anions are all interconnected by their counterions. On the other hand, the 4M-LiTFSI solution also forms a similar network but, in this case, one of the $TFSI^-$ anions is connected to the rest of the network by a DME species which solvates two Li ions (from two different salts). A remarkable difference between the 1M concentration and high molarity case is that no significant rotation was observed within the salts, i.e., the *trans*- structures remain unchanged, after the 20 ps simulation time in the 1M case. In the 4M case, the barriers associated with the change of chirality are overcome and some of the salts in both systems exhibit a more *cis*-like structure than *trans*-. Umebayashi *et al.*[164] and Yoon *et al*.[165] found a similar conformational change for the LiTFSI and LiFSI salts, respectively; however, in their analysis, the amount of the *cis*- conformer increases with increasing concentration of the lithium-ion instead of salt molarity. Regarding the scenario where an excess of Li ions is present (1 Li^+), comparable networks are formed. FSI^- species are connected by Li^+ ions and the added cation adheres to the network through solvent molecules that, at the same time, are sharing the Li^+ ions with the anions. The 4M-LiTFSI solution arranges to form a similar network to that found in the non-excess case, and again, one of the LiTFSI salts is found connected to the main network through DME solvating the cations. Finally, a

pure solvent electrolyte was tested by adding Li ions (see Figure B.15). Here it can be observed that each ion is solvated by four oxygen atoms from three DME molecules when one Li^+ is added or two DME's when 3 Li^+ are present. This behavior is also observed when the salt is present at low concentration and does not directly interact with the cations or their solvation of DME molecules. This suggests that these two structures may be the most probable solvation forms between DME and Li^+. $Li^+(DME)_2$ structures have been suggested previously.[166-167] By using DFT calculations, Liu *et al.*[166] showed that when one Li^+ is solvated by less than three DME molecules (both oxygen atoms interacting), stable complexes are formed. Although our results showed three DME molecules solvating one Li^+ on several occasions, our conclusion remains valid since the final coordination for Li–O is four (since two DME molecules are sharing only one oxygen atom each).

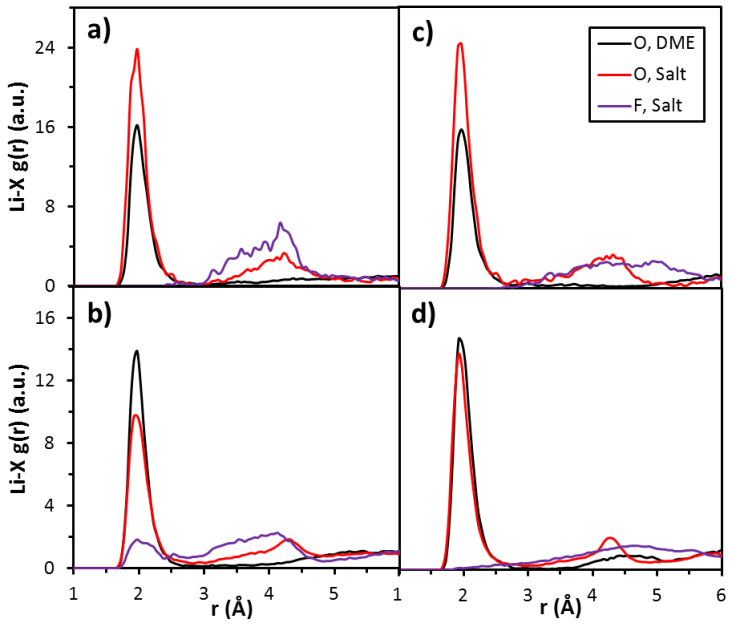

Figure 4.9 Radial distribution function for Li^+--X (X=O and F atoms) pairs for solutions with no additional ions. a) 1M-LiFSI, b) 4M-LiFSI, c) 1M-LiTFSI, and d) 4M-LiTFSI.

To gain a more quantitative understanding of the structure of the electrolyte at high and low salt concentration, RDFs for Li–X distances were evaluated over a 20 ps trajectory. Figure 4.9 shows the RDF for DME and salt oxygen and fluorine atoms for the case with no Li ions excess. The first solvation shell is well-defined by oxygen atoms from both salt and solvent molecules at 1.9-2.0 Å. It is quite remarkable that the concentration and the type of salt do not play a significant role here. In addition, a second peak coming from the salt oxygen atoms can be identified at 4.1-4.3 Å, and this time the oxygen atoms correspond to the ones facing opposite the cation of the salt (O_1 and O_3, see Figure B.1). In this case, a sharpened peak arises when the concentration of each salt increases (Figure 4.9b and d for LiFSI and LiTFSI, respectively). With respect to the Li-F pairs, no clear peak is observable for LiTFSI at low or high molarity. However, the LiFSI case shows a very broad peak with maximum at around 4.1 Å. This peak is present for both concentrations and can be identified as fluorine atoms from the cation of the same salt. Contrary to what is seen in LiTFSI, a peak at 2.0 Å develops when the salt concentration in the LiFSI/DME electrolyte mixture is increased, suggesting that Li is being coordinated by fluorine atoms in addition to the oxygen. Concerning the cases where there are additional Li^+ ions, similar behavior is observed in all the mixtures studied (see Figure B.16 and Figure B.17, Appendix B). However, the Li–F coordination is lost for high molarity LiFSI (peak around 2.0 Å disappears). In addition, the second peak for Li–O becomes narrower, suggesting a more interconnected network due to the presence of additional ions. If salt is not present in the electrolyte (pure DME, Figure B.18, the solvation shell for Li–O remains, albeit with the peak maximum slightly shifted to the left

(corresponding to a shorter distance) when the concentration of ions increases. This might be due to the adoption of a $Li^+(DME)_2$ configuration (Figure B.15) which makes the network more compact.

To complete our analysis of the electrolyte structures, averaged coordination numbers were calculated as a function of time (Figure B.19). It is observed that for 4M solutions, the Li–O coordination numbers take longer to reach an approximate equilibrium value (at least 2 ps). Accordingly, averaged coordination numbers (CNs) were computed over the total simulation length (from 2 to 20 ps) for Li–O and Li–F pairs (with the cutoff distance set to 2.3 Å). The complete results are shown in Table B.3 and summarized in Figure 4.10 for Li–O only. Negligible Li–F coordination is found in cases where LiFSI concentration is 1M. Likewise, non Li–F binding is noted when LiTFSI is used in low concentration unless the excess of lithium ions is high (3 Li^+) the CNs is equal to 0.04. Although this number is very small, it reveals that at least some Li–F coordination is being formed due to the increase of ion concentration. On the contrary, a higher coordination number is found for Li–F in 4M-LiFSI solutions and no extra ions added (CNs=0.21). This result explains the peak observed in Figure 4.9. When one cation is added to the 4M solutions a small fraction of Li^+ is coordinated to fluorine atoms over this span, with CNs=0.03 and 0.08 for LiFSI and LiTFSI, respectively. These results agree well with the lack of favorability shown in our previous DFT calculations of affinity between lithium ions and fluorine atoms from these two salts (Table 4.1), although small interactions may still be possible if the concentration of either salt or ions is high enough as seen here.

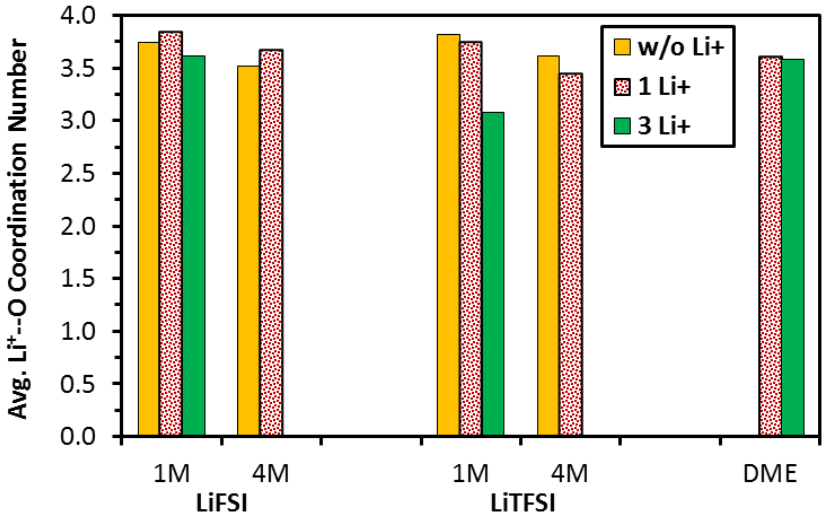

Figure 4.10 Li^+–O (total) coordination numbers averaged over 18 ps (2 to 20 ps) with and without additional ions in the simulation cell.

Li–O contributes to at least 93% of the CNs, making it primarily responsible for the solvation of Li ions. From Figure 4.10, we note that for the same number of Li-ions in each electrolyte system, the Li–O CNs decrease by 0.2-0.3 when the concentration is increased. For LiTFSI at a fixed concentration, the CNs decrease as the number of cations increases, whereas for LiFSI no clear trends are observed. Furthermore, comparing the two salts, when an excess of Li-ions is present, LiFSI exhibits a slightly higher Li–O coordination than LiTFSI at the same concentration. However, LiTFSI salt electrolytes show relatively higher CNs toward oxygen atoms than LiFSI when no extra cations are in the solution. In general, Li is mainly solvated by oxygen atoms from the DME and salts. The CNs for Li^+ are close to four, which is in agreement with previous studies where one Li^+ typically coordinates with four oxygen atoms to form the stable Li^+–O clusters.[166] It is noteworthy that no decomposition of either the salt or DME is observed during the

simulation and even in the presence of excess Li^+, which suggests the good stability of the two salts at different concentrations in the bulk electrolyte. None of the mixtures studied showed complete anion/cation dissociation; however, this has been observed experimentally,[168] leading us to conclude that additional studies using classical MD simulations would be valuable to achieve longer timescales.

4.5. Conclusions

In this chapter, two salts used in Li-S systems: LiTFSI and LiFSI at both low and high concentrations have been targeted for analysis, and the differences in reactivity, SEI products, and solvation structures have been explored in detail. The decomposition pathway for these two salts, when located near the anode, differs substantially and is also a function of their concentration. While LiTFSI undergoes less complete reduction, it also facilitates more charge transfer from the Li slab, and the carbon atoms in this salt are instrumental in accommodating this charge. LiFSI, on the other hand, shows a more complete decomposition and is found to be extremely efficient in LiF formation. In contrast, larger fragments are the initial SEI components derived from LiTFSI and some of them contain C atoms, which are absent from the LiFSI salt. DFT calculations for LiFSI showed the existence of highly thermodynamically favorable reaction pathways forming LiF. For both salts, neutral lithium attack is the primary cause of the salt fragmentation. Finally, coordination effects between the salt and solvent molecules in the bulk electrolyte were examined thoroughly. It was found that even in the presence of an excess of Li ions, the high concentration salts still partially dissociate. However, the excess of Li ions induces the formation of highly complex coordinated networks even in the 1M solution.

A remarkable difference between the low and high molarity effects is that the *trans* structures dominate the 1M solutions, whereas *cis* structures are observed in the 4M concentration. This structural change may also affect the structure of the complex solvation networks. The first solvation shell of Li ions that peaks at 1.9-2Å is always well-defined by the interactions with O atoms from DME or the salts, regardless of the type of salt or concentration. The coordination number of O atoms around Li ions is 4 in most of the cases, with the exception of the 1M solution of LiTFSI in presence of an excess of Li ions, where it decreases to 3. F atoms define a clear second shell around Li ions in LiFSI solutions independent of concentration, and even a small peak is observed in the first shell at 4M concentration, whereas only a broader second shell of F atoms is observed for LiTFSI.

5. ELUCIDATING ELECTROLYTE DECOMPOSITION UNDER ELECTRON-RICH ENVIRONMENTS AT THE LITHIUM-METAL ANODE*

5.1. Summary

In this chapter, using DFT and AIMD simulations, we investigate the effect of electron-rich environments on the decomposition mechanism of electrolyte species in pure DME solvent and 1M LiTFSI and LiFSI salt solutions. It is found that systems with pure DME require an average environment of at least ~0.9 |e|/molecule for a DME to decompose into CH_3O^- and $C_2H_4^{2-}$ via a 4-electron transfer. In the case of mixtures, the salts are very prone to react with any excess of electrons. In addition, DME dehydrogenation due to reactions with fragments coming from the salt decompositions was detected. Formation of oligomer anionic species from DME and salt fragments were also identified from the AIMD simulations. Finally, the thermodynamics and kinetics of the most relevant electrolyte decomposition reactions were characterized. DME decomposition reactions predicted from the AIMD simulations were found to be thermodynamically favorable under exposure to Li atoms and/or by reactions with salt fragments. In most cases, these reactions were shown to have low to moderate activation barriers.

---

* Reprinted with permission from Luis E. Camacho-Forero and Perla B. Balbuena. "Elucidating Electrolyte Decomposition under Electron-rich Environments at the Lithium-Metal Anode." *Physical Chemistry Chemical Physics*, 2017, **19**, 30861-30873.

5.2. Introduction

Improving the fundamental understanding of electrolyte decomposition is critical for controlling the properties of a protective SEI layer. Thus, significant efforts have gone into investigating reaction mechanisms of electrolyte decomposition and SEI formation, specifically for carbonates used in Li-ion batteries such as ethylene carbonate.[169-172] However, carbonate solvents are not stable against Li-metal anodes. Conversely, ether-based solvents such as DME and DOL have shown improved stability at the anode and are commonly used for battery systems with Li-metal electrodes.[120, 145] Furthermore, the addition of salts such as LiTFSI and LiFSI have shown to enhance coulombic efficiency and ionic conductivity, and mitigate dendrite growth.[101, 146] Unfortunately, solvent and salt decomposition still occurs and although some of the improvements are attributed to the SEI formed due to the salt reduction, the mechanisms are not well understood yet.

Theoretical methods have been proven to help elucidating the reaction mechanisms of electrolyte components and SEI formation, providing guidance for the exploration of new electrolyte additives that yield improved battery performance.[173-175] However, there are still some challenges associated with the modeling of electrochemical interfaces that need additional efforts to be overcome. For instance, modeling the electrified anode surface with first-principles simulations is, perhaps, one of the most important issues that remains under investigation, albeit a number of methods have been proposed[109, 176-179] including systems where an excess of electrons is added to the simulation cell.

Recently, Chen *et al.*[180] have successfully investigated the reduction mechanism of DOL and DME solvents in contact with a Li-metal surface and a Li-cluster using first-

principles atomistic simulations. In general, they found that DME is more stable than DOL and no reduction of DME is observed when in contact with the Li-(110) surface. Nevertheless, when the Li-cluster model is used, the cluster is dissolved and reduction of both DME and DOL is detected. Previously, we have considered a similar approach in which the Li-(100) surface is in contact with pure solvents or solvent/salt mixtures.[129, 181] However, it is noteworthy that, in these models, the electron transfer from the Li-anode to the electrolyte is uniquely given by the lithium atoms at the surface, leading the surface to become positively charged, i.e., there is not an external electron source – this model can be represented as shown in Figure 5.1a. Therefore, in this work, we attempt to model the electrified anode surface by considering only the electron-rich region near the electrode surface, as depicted in Figure 5.1b. Here the effect of electron excess on the decomposition mechanism of different electrolyte mixtures and conformations is presented as a result of the electrified interface, where DME is used as solvent and LiFSI and LiTFSI as salts. Thus, we aim to provide insights not only for the pure solvent decomposition but also for mixtures of it with additives such as salts, which can represent better the real cell.

Here we use DFT and AIMD simulations to examine and characterize in detail the dynamics, reaction pathways, structure of the products, charge distribution as well as to provide some insights on the thermodynamics and kinetics of the electrolyte decomposition reactions.

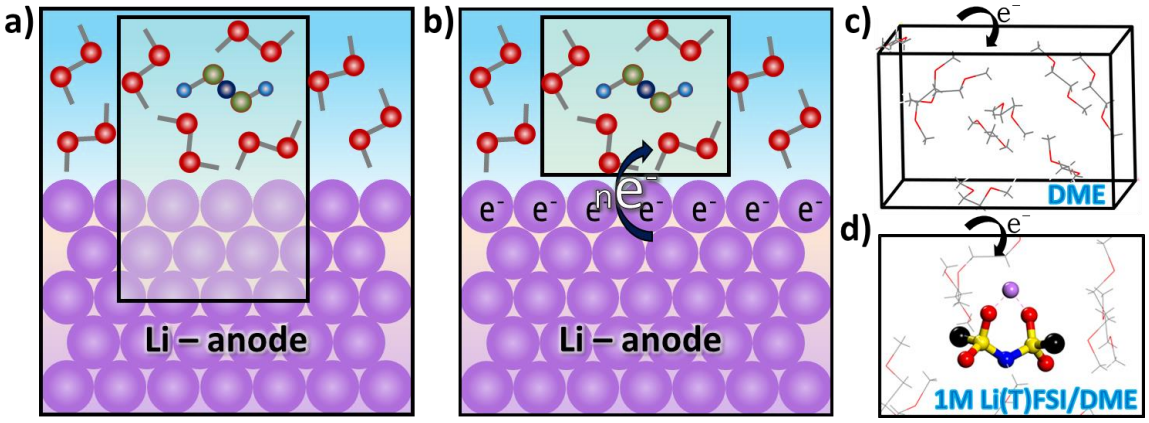

Figure 5.1 Model of the electrolyte and lithium-metal anode interface and initial configurations for electrolyte mixtures. (a) Scheme of electrolyte with Li-(100) surface with not excess electron, (b) Scheme of electrolyte with lithium anode incorporating the electrified interface, and initial configurations used in the AIMD simulations for (c) pure DME and (d) 1M salt/DME mixtures. The shaded boxes represent the simulated part of the system. Color code: lithium, purple; oxygen, red; carbon, gray; fluorine, light blue; sulfur, yellow, nitrogen, blue; hydrogen, white; CF_3 and F groups from LiTFSI and LiFSI, respectively, black.

5.3. Computational and System Details

5.3.1. Modeling the 'Electrified Interface'

In order to model the electrified interface, only the electron-rich region of the cell was simulated, as defined by the shaded area in Figure 5.1b. Therefore, a simulation cell representing the electrolyte system was modeled by a periodic 15 Å x 10 Å x 10 Å box. Previous works have adopted a similar methodology to investigate the decomposition mechanism of carbonate electrolytes in Li-ion batteries. They have considered the electron-rich conditions by including an excess of electrons in cluster-based DFT calculations in the gas phase and with an implicit solvent description[170, 182] as well as in periodic AIMD simulations in which the liquid environment is explicitly included.[169, 171] In this work, the simulation cells contain pure DME or DME mixtures with salts. All the structures for individual electrolyte components were taken for our previous reports.[129, 181]

Each constituent had been optimized to represent one of the most abundant conformers in the liquid phase, with the following symmetries: LiTFSI and LiFSI are C_2 (*trans*)[156-158] and DME is linear (TTT).[183] The optimizations were carried out using the Gaussian 09 (G09) simulation software[89] with a hybrid functional B3PW91 and the 6-311++G(p,d) basis set[46, 90] level of theory.

All AIMD simulations were performed within a *NVT* ensemble at 330 K using VASP[58-60] with the Perdew-Burke-Ernzerhof generalized gradient approximation (GGA-PBE)[45] functional. Electron-ion interactions were described by PAW pseudopotentials[50-51] as provided in the VASP databases. The energy cut-off of the plane-wave basis expansion was set to 400 eV with a Gaussian smearing width of 0.05 eV. The Brillouin zone was sampled using a 2×2×2 Monkhorst-Pack[54] k-point grid. A Nose thermostat with a Nose-mass parameter of 0.5 was used to control the temperature oscillations during the simulations. Tritium masses were replaced for protons in order to set a time step of 1 femtosecond. Finally, it must be noted that in order to simulate periodic systems with a non-zero net charge, a homogenous background-charge has to be assumed.

For the pure solvent and the 1M solution, the number of DME molecules randomly placed in the simulation box was nine and eight, respectively. These numbers were calculated based on the density of the liquid DME (0.87 g/cm^3). Due to the volume of the cell, one salt molecule was enough to achieve the desired salt concentration (1M). Subsequently, the solvent molecules in the cell were optimized using a classical molecular mechanics (MM) relaxation method. The consistent valence force field (CVFF) with a conjugate gradient algorithm as implemented in the Materials Studio software was

employed.[184] The convergence criteria was set such that the total force among the atoms was lower than $2x10^{-4}$ eV/Å. The resulting electrolyte systems are shown in Figure 5.1c-d. In addition, charge transfer was studied by using the Bader charge analysis.[63-65] Although the electronic charges are not observables and the results indicating fractional charges are an artifact of the method, this analysis is very useful to understand electron transfer and to characterize the reaction mechanisms.

Two methods were implemented to supply the excess of electrons to the simulation cell. In the first case, electrons were sequentially added one-by-one to the system every 2 ps until a total of 15 excess electrons, after which the simulations were allowed to run an additional time of 8 ps, bringing the total simulation time to 38 ps. The second method consisted of 10 ps simulations with a constant number of excess electrons. In this case, two initial configurations and a different number of initially added electrons (n_{eo}=1, 2, 3, 4, 5, 7, 9, 11, and 13) were studied. One set of initial configurations were the ones obtained after the MM relaxation (referred to as MM-relaxed). The second initial configuration set was obtained as a result of running the MM-relaxed systems for 20 ps of AIMD simulations with net charge equal to zero (referred to as AIMD-relaxed). The initial configurations for the mixtures are shown in Figure C.1 (Appendix C). The main difference between the two initial configurations is the conformation of the salt molecules. For the MM-relaxed case (see Figure C.1a and b), the salts are present in a perfect C_2 symmetry; meanwhile, for the AIMD-relaxed (see Figure C.1c and d), the salt molecules have been partially solvated by the solvent. Regarding the models with pure DME, different conformers are identified as seen in Figure 5.1c.

A more detailed model of the electrified interface should consider the effect of an external electric field and the formation of the electrical double layer. The effect of the electric field in the battery system would result in the electrode-electrolyte interface polarization and rearrangement of the charged species. As the electric field increases, the flow of electrons – from the metal electrode – will increase, and the polarization effects will also increase. Our model does not have a surface; therefore, the orientation effects of the molecule at the interface are not captured. However, the model incorporates a source of electrons that is increased in each simulation set, as if the metal would be under an electric field. Since the distribution of these electrons is only determined by the electrolyte molecules and not by the surface atoms, the effect of the excess electrons on the electrolyte molecules is definitely captured. Although the absence of the metal electrode does not allow the proper description of the electrical double layer, the addition of electrons to the simulation cell does provide us with a controlled environment to study the different degrees of electron transfer from the anode to the electrolyte, which cannot be achieved by using only the metal-slab model in contact with the electrolyte as previously reported.[129, 181] In this way, the study of the time evolution of the electrolyte under controlled electron-rich environments is very useful to determine potential decomposition products and SEI components under different stages of electrons transfer from the anode, albeit the surface is not explicitly included in the simulations.

5.3.2. Thermodynamics and Kinetics of Electrolyte Decomposition

Although AIMD simulations of net-charged electrolyte systems provide key information regarding the reaction mechanisms, the energies of reactions and kinetics

barriers cannot be computed using the same model since the total energies are not well-defined.[185] Thus, in order to gain a deeper fundamental understanding of the reaction mechanism of electrolyte components, the most relevant reaction mechanisms were identified from the AIMD simulations with an excess of electrons and the mechanisms were in parallel studied using a cluster-based DFT approach with implicit solvation effects described by a polarized continuum model (SMD).[95, 186] Reaction and Gibbs free energies were estimated using the G09 software at the same level of theory used to optimize the individual electrolyte components, B3PW91/6-311++G(p,d). Kinetic barriers and transition state structures were predicted using the Berny algorithm as implemented in G09.

5.4. Results

5.4.1. AIMD Simulations with Sequential Addition of Electrons

5.4.1.1. Pure DME

Although DME decomposition is observed upon battery cycling, DME has proven to have much better stability against decomposition induced by the Li-metal anode compared to other organic solvents such as cyclic ethers and carbonates. The DME molecule has two carbons that form the ethane group in the middle (C_m – middle carbon) and two more carbon atoms from the methoxy groups (C_t – terminal carbon), see the first panel in Figure 5.2. Thus, to gain a better understanding of the stability and reaction mechanisms of this solvent, a cell with pure liquid DME (containing nine molecules) is studied by adding one electron each 2 ps. Figure 5.3a illustrates the distribution of charge of DME molecules during the 38 ps of simulation. At times < 22 ps, DME molecules

exhibit similar charges (< -1.6 |e|). Afterward, the charge distribution becomes broader and two groups of charges can be identified; one between -0.5 and -2.0 |e| and another group between -3.0 and -4.0 |e|, corresponding to charges of *non-reacting* and reacting DME molecules, respectively.

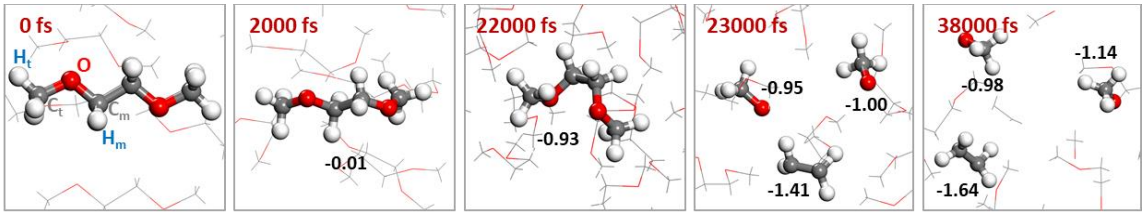

Figure 5.2 DME reaction mechanism with instantaneous charges from AIMD simulations of pure DME with the sequential addition of electrons. Charges are given in |e|. Color code as in Figure 5.1.

C–O bond lengths are monitored throughout the simulation to detect bond cleavages (Figure C.2a). During 22 ps of AIMD simulations (-10 |e|), no reactions were observed. Interestingly, after the addition of the 11th electron, one of the DME molecules decomposes by a 4-electron transfer simultaneously breaking the two C_m–O bonds and forming two CH_3O^- groups and one $C_2H_4^{2-}$. The DME reduction mechanism and instantaneous fragment charge are presented in Figure 5.2. This solvent molecule had almost no charge at the beginning of the simulation (2 ps). At 22 ps, immediately before the 11th electron is added, the molecule had gained a net charge of ~ -1 |e|. The decomposition reaction occurs when the total charge of the system is -11 |e| (22 – 24 ps). The last electron addition seems to trigger an additional 3-electron transfer to this molecule (see Figure C.2b for charge evolution of the fragments), which led to its decomposition. The decomposition is preceded by a conformational change in the

molecule (Figure 5.2, center image). The resulting fragments were stable for the remaining simulation time (~15 ps). Furthermore, two analogous reactions resulting in the same products were observed after the addition of the last electron (-15 |e|): the first one at 31 ps and the other at 33 ps (see Figure C.2c-d for charge evolution). Note that in this case there is an intermolecular electron transfer because the average charge of the non-reacting molecules decreases (Figure 5.3a). A similar reaction pathway was reported for DME in contact with a dissolved cluster of lithium.[180] However, in that case, ethylene was formed instead of the charged ethylene group observed in our simulations. The explicit addition of electrons to the simulation cell is probably the main reason for this difference.

5.4.1.2. 1M Solution

A key characteristic of the electrolyte decomposition is that neither the solvent, the salt nor any of its components react independently, on the contrary, they are influenced by the surrounding environment. Therefore, it is important to investigate solvent-salt mixtures in order to understand the complex reaction mechanisms taking place at the anode. To begin with, we examine the 1M LiFSI solution. Figure 5.4 shows the reaction mechanism coupled with the charge evolution of the different species resulting from the reduction of the salt. After the first electron is supplied to the simulation cell, the LiFSI molecule starts to decompose by one S−F bond cleavage, forming a LiF neutral species with the Li-ion from the salt. However, when the second electron is added no reaction was observed during 2 ps. Remarkably, the addition of the third electron leads to the second S−F bond breaking, resulting in the formation of the $N(SO_2)_2$ species. From the charge evolution, the LiFSI salt received approximately four electrons (at a time > 8 ps), which

were mostly transferred to the $N(SO_2)_2$ group (~3 |e|) whereas very little charge went to the fluorine atoms. No DME decomposition was observed in this case. However, Figure 5.3b shows that the charge distribution of DME molecules becomes more dispersed as electrons are added and it is likely that some of the DME molecules (with charges > -1.6 |e|) are close to decompose. In fact, the addition of an extra electron to the cell (not shown) can result in decomposition of a solvent molecule according to the aforementioned reaction mechanism.

The LiTFSI salt in the 1M solution is also found to be very reactive and to begin decomposing almost immediately after the first electron is added. The first panel in Figure 5.5 summarizes the reduction mechanism undergone by the LiTFSI molecule. It begins to decompose by breaking of the S–N bond at around 2 ps resulting in $CF_3SO_2N^-$ and $CF_3SO_2^-$. Subsequently, the addition of the third electron (~ 6 ps) leads the CF_3SO_2 fragment to react into CF_3 and SO_2 anions. The three species formed until this point are stable for the following 16 ps when the CF_3SO_2N fragment starts to defluorinate resulting in three fluorine ions and a CSO_2N^{3-} group. The initial bond cleavage and the final products of LiTFSI decomposition have been reported previously in different solutions containing LiTFSI in contact with Li-metal and Li_xSi anodes.[110, 175, 181]

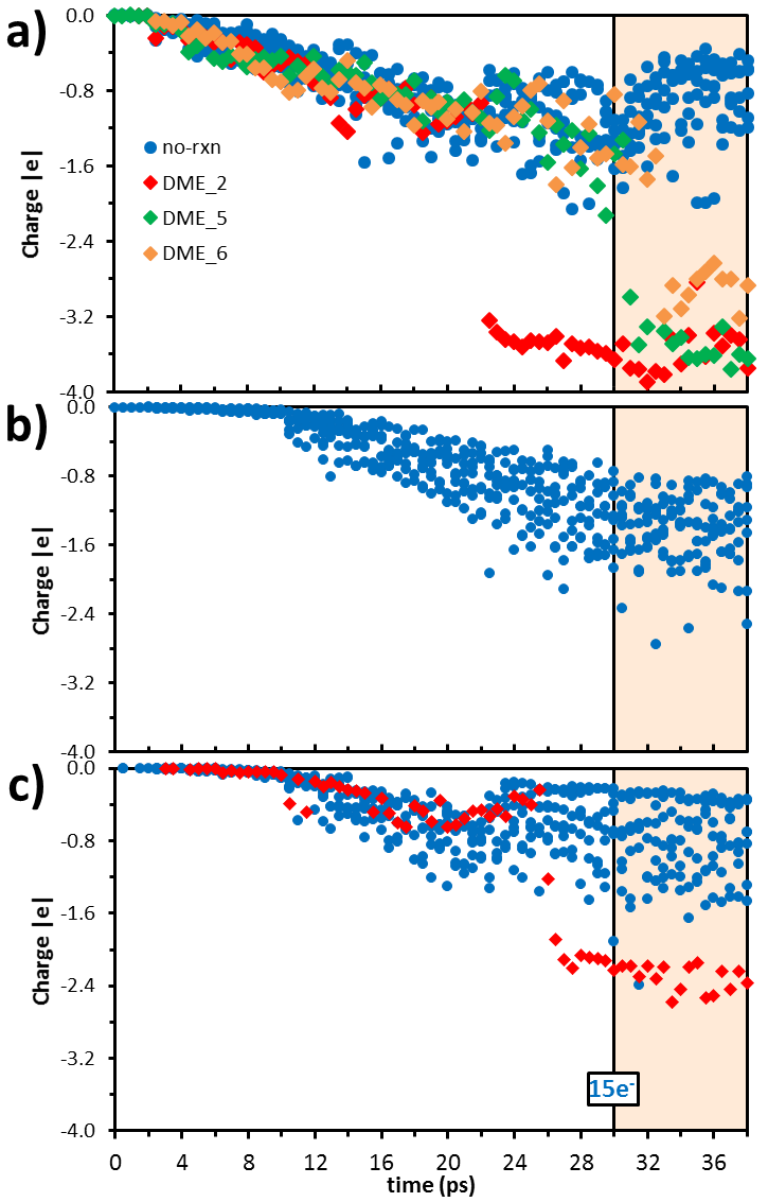

Figure 5.3 Charge evolution of individual DME molecules from AIMD simulations of three electrolyte systems with sequential addition of electrons: (a) Pure DME, (b) 1M LiFSI solution, and (c) 1M LiTFSI solution. The number in the labels indicates the reacting DME molecules.

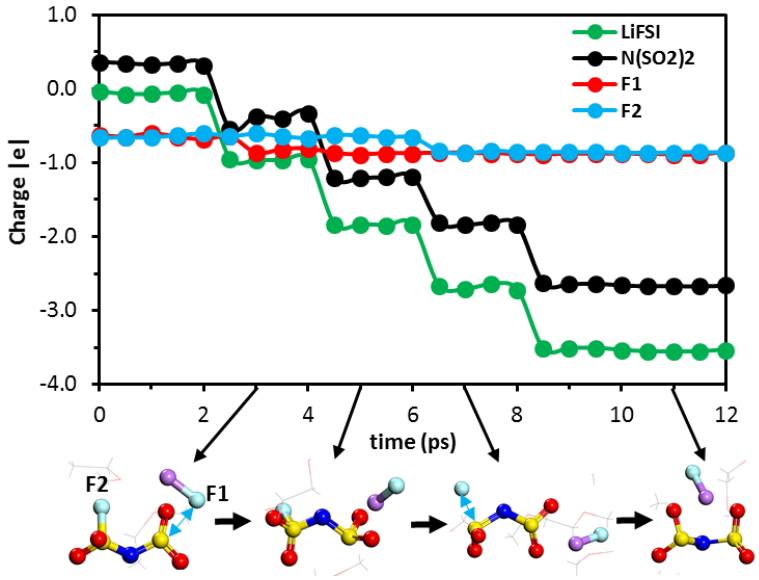

Figure 5.4 LiFSI reduction mechanism and charge evolution from AIMD simulations of 1M LiFSI solution with sequential addition of electrons. Color code as in Figure 5.1.

Something remarkable to highlight in Figure 5.5 is that the CSO_2N^{3-} species formed during the salt decomposition attacks one DME molecule and oxidizes it by removing one of the hydrogen atoms bonded to a C_m-atom resulting in $HCSO_2N^{2-}$ and DME(-H_m). Consecutively, DME(-H_m) also reacts to form a methoxy anion (CH_3O^-) and methyl vinyl ether (CH_3OCHCH_2). The CH_3OCHCH_2 and $HCSO_2N^{2-}$ fragments gain additional charge and combine via C-C bond to finally form the $CH_3OCHCH_2CHSO_2N$ species with a net charge around - 4 |e| (see last two panels in Figure 5.5). Interestingly, this oligomer anionic species is stable for the remainder of the simulation time. Finally, Figure 5.3c illustrates that the distribution of charge in the DME molecules becomes broader with increasing number of electrons, similar to the behavior observed in the previous two cases. After 26 ps, two groups of charges are identified: -0.2 to -1.6 |e| and -

2.0 to -3.0 |e| correlating with the *non-reacting* DME molecules and the one that decomposed, respectively.

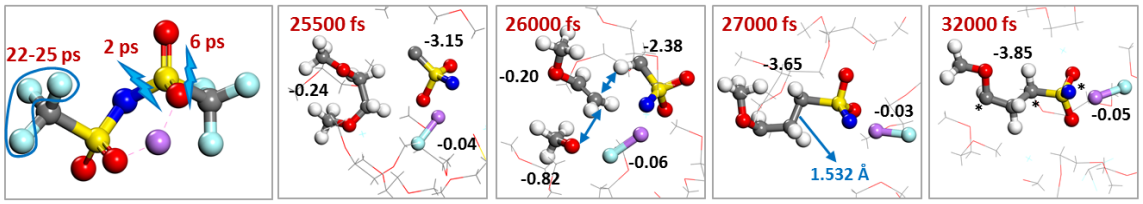

Figure 5.5 LiTFSI and DME redox reactions and instantaneous charges (in |e|) from AIMD simulations of 1M LiTFSI solution with sequential addition of electrons. Color code as in Figure 5.1.

5.4.1.3. Overall Charge Transfer

To further explore the behavior of the electrified system, a charge evolution analysis was carried out for the different species making the electrolyte. Figure 5.6a illustrates the total charge distribution among the solvent and the salt in the 1M solutions. The charge distribution is almost identical for the 1M solutions of both salts at times before 22 ps. At times < 10 ps (total charge $\leq$ -4 |e|), practically all the excess electrons are received by the salts in their respective solutions, which can be attributed as the main reason for their early decompositions. These results are also in agreement with our predicted values of electron affinity (EA) for the electrolyte components, in which it was found that the salts have a much larger EA (~-1.40 eV) than the DME (-0.25 eV) as shown in Table C.1. After 10 ps, the newly added electrons are accepted by DME molecules – clearly seen in the step-like function from 10-22 ps (Figure 5.6a). At that point, in the 1M LiFSI solution, any additional charge supplied to the cell is accepted by the DME molecules, which explains the stability of the $N(SO_2)_2$ fragment formed during the LiFSI

reduction. In contrast, a sharp charge transfer is observed toward the LiTFSI fragments between 22 to 25 ps in the 1M LiTFSI solution, which overlaps with depletion of charge on the electrolyte side for the same period. This behavior can be associated with the aforementioned defluorination of CF_3SO_2N that occurs during this time interval. Regarding the DME molecules in the 1M LiTFSI solution, the total charge starts to increase at 25 ps concurring with the redox reaction that one of the molecules undergoes (Figure 5.5). Afterward, the solvent accepts mostly any additional charge supplied to the cell, showing the stability of the fragments coming from the LiTFSI reduction and the complex anion formed with the DME fragment.

Finally, we analyzed the charge accepted by the *non-decomposed* DME molecules. Figure 5.6b shows the average charge for non-reacting solvent molecules in the three systems investigated. The main difference between the pure solvent system and the 1M solutions is that in the mixture the DME molecules start to gain electrons after the salts have already been reduced. In addition, once the DME molecules have started receiving charge, they only lose it when reactions take place. For instance, one DME molecule decomposes in the pure solvent at around 22 ps and the LiTFSI and DME molecules undergo a series of redox reactions observed after 22 ps in the 1M LiTFSI solution. In the pure DME system, two more molecules react after the final addition of electrons (>30ps) receiving intermolecular charge transfer from the molecules around them. Therefore, electron transfer between solvent and salt molecules may take place even at constant number of excess electrons.

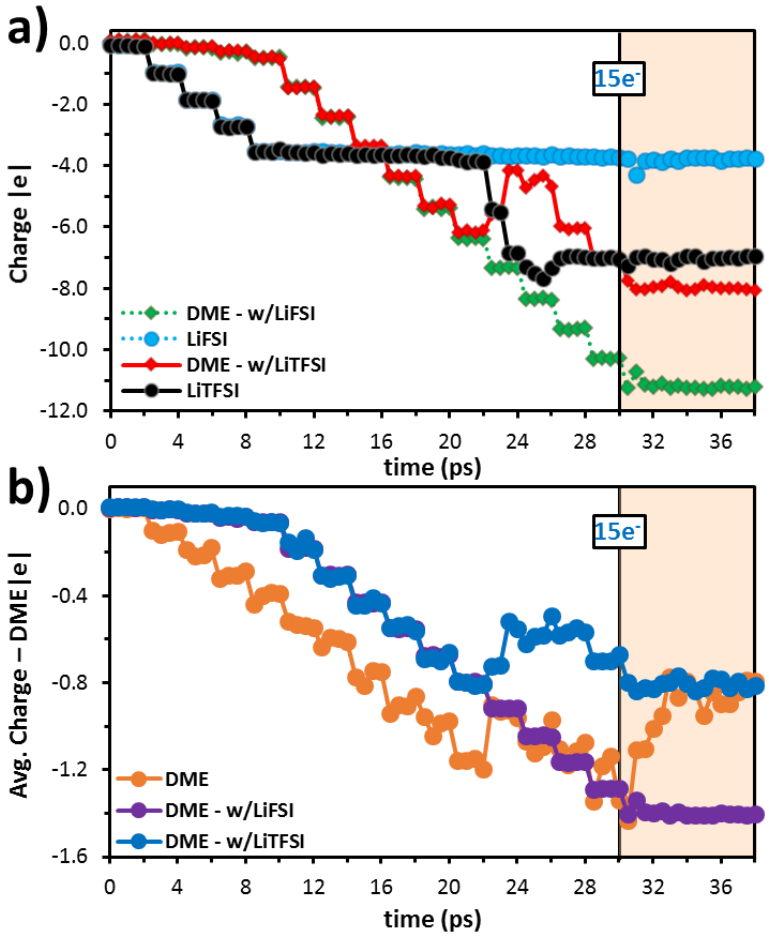

Figure 5.6 Charge evolution for different species from AIMD simulations of electrolyte solutions with sequential addition of electrons. (a) Time evolution of DME and salts total charge (and fragments formed from their decomposition). The total number of DME in both 1M solutions are the same. (b) Average charge of *non-reacting* DME molecules in pure solvent and mixtures with salt.

5.4.2. AIMD Simulations with Constant Excess of Electrons

In order to study the behavior of the electrolyte system under constant excess of electrons (n_{eo}), two initial sets of configurations were used as described previously in the methodology section: MM-relaxed and AIMD-relaxed. For each set, three solutions were investigated: pure DME, 1M LiFSI, and 1M LiTFSI.

5.4.2.1. MM–relaxed

First, we analyze the case in which the electrolyte is comprised only by the solvent. In this scenario, no DME decomposition was identified by the end of 10 ps of AIMD simulations with n_{eo} equal to 0, 1, 2, 3, 4, 5, 7, and 9. Interestingly, for initial charges of -11 and -13 |e|, one and three DME molecules reacted, respectively. All four molecules followed a similar decomposition pathway as shown in Figure 5.2. Figure C.3 illustrates the time evolution of C_m–O bond distances for the reacting molecules, which coincide with a rapid charge transfer toward the reacting molecules (Figure C.4a). For the solution with n_{eo} of 11 electrons, both C_m–O bonds break at around 2.6 ps of simulation. On the other hand, for an initial charge of -13 |e|, the three molecules decompose at around 1.3, 5.8, and 7.6 ps, respectively. Remarkably, two C_2H_4 fragments from the DME decomposition combine to form a dimer, $(C_2H_4)_2^{2-}$. DME decomposition and oligomer formation are fully characterized by instantaneous charges in Figure 5.7.

Alternatively, no DME decomposition reactions were found in 1M LiFSI solutions for any of the initial number of excess electrons during the 10 ps of AIMD simulation except for the model with a charge of -13 |e| in which two DME molecules decomposed following the reaction pathway described in Figure 5.2. On the other hand, the LiFSI salt did react in any system with non-zero net charge. The salt reduction reactions are carefully described in Figure C.5 and summarized in Table 5.1. Although each scenario has a different initial charge (which remains constant in each simulation, for 10 ps), a characteristic initial bond cleavage is always observed, S–F. For one and two additional electrons (n_{eo}=1 and 2), only one fluorine atom is removed resulting in the SO_2NSO_2F

species. For n_{eo}>2, the typical bond scission sequence is S-F, S-N, and S-F or double defluorination leading to SO_2 and NSO_2 or $N(SO_2)_2$, respectively. Concerning the fluorinated species, F^- and LiF are normally formed.

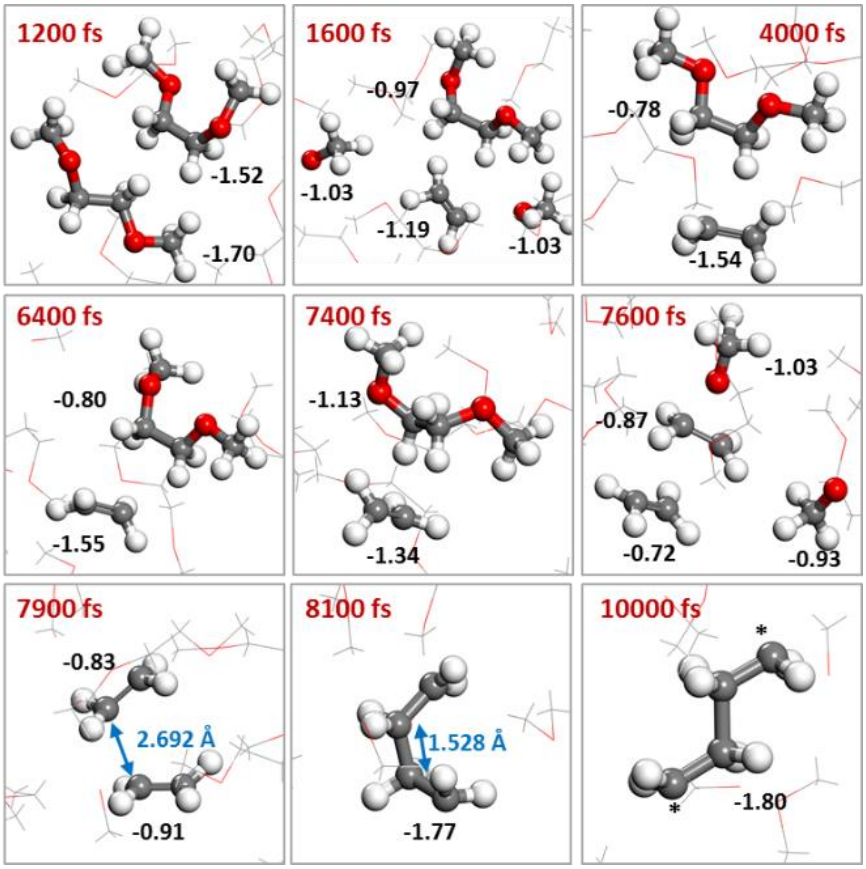

Figure 5.7 DME decomposition and $(C_2H_4)_2^{2-}$ formation in a pure DME system starting with the MM-relaxed configuration and n_{eo}=13 (constant number of excess electrons throughout the 10 ps of AIMD simulation). Charges are in |e|. Charge evolution of the oligomer can be found in Figure C.4b. Color code as in Figure 5.1.

Similar to the 1M LiFSI solution, the LiTFSI/DME electrolyte mixtures also exhibited salt decomposition even when a single electron is added to the simulation box as reported in Table 5.1 (see more details in Figure C.6). In this case, the S–N bond breakage starts the salt reduction in solutions initially charge with 1–9 electrons. In

contrast, in electrolytes with n_{eo} = 11 and 13, the LiTFSI decomposition starts with a C–S scission. Some of the most common fragments resulting from the reduction are CF_3SO_2, CF_xSO_2N, CF_x, SO_2, LiF, F^-, NSO_x, and OSC. Other species such as CO and O^{2-} can also be found as products of the salt disintegration. In fact, O^{2-} species play a crucial role in the oxidation of DME that was found in the two cases with the largest charges, -11 and -13 |e|. For instance, Figure 5.8a illustrates the rapid salt decomposition within 100 fs of simulation followed by the formation of a hydroxyl group as a consequence of a hydrogen removal from a DME molecule via oxygen radical attack to one of the hydrogen atoms bonded to a C_t-atom. The DME(-H_t) is stable for the remainder of the simulation with a charge of ~ -1 |e|. The OH^- ion, on the other hand, interacts closely with a LiF compound, which later dissociates and forms a LiOH, a compound that has been identified as a possible SEI component in Li-ion batteries.[187] Similarly, when n_{eo}=13, a hydrogen is removed from a C_m-atom in a DME molecule by an oxygen resulting from the LiTFSI decomposition. Conversely, in this case, the DME(-H_m) is reduced to form CH_3O^- and methyl vinyl ether. Similar behavior was previously observed when the addition of electrons was sequential in 1M LiTFSI mixtures (Figure 5.5). However, here the methyl vinyl ether losses one of the protons with NSO_2^{3-} to form $CH_2OCHCO_2^-$ and $HNSO_2^{2-}$ as depicted in the last panel in Figure 5.8b.

Figure 5.9a illustrates the average charge of non-reacting DME over the entire simulation time for each value of n_{eo}. In 1M salt/solvent electrolytes, the average charge for DME is very low for n_{eo}<5. After that, the average charge of DME in all three solutions continues to increase as a function of the initial total charge of the system except for those

systems where DME decomposition takes place in which charge is withdrawn from the non-reacting DME molecules – such systems are indicated with voided-circles in Figure 5.9a. Figure 5.9b shows that, overall, LiTFSI is able to accept more charge than LiFSI, mainly at higher number of excess electrons. It is remarkable that, although in the first case of study the electrons were added sequentially to the same system, comparable results could be obtained when analyzing independently different AIMD simulations at various constant electrified conditions, n_{eo}. Moreover, as further discussed below, the conclusions of this study are in agreement with those reported earlier, where the source of electrons was a Li slab.[129, 181]

Table 5.1 Summary of bond cleavage and fragments remaining after 10 ps of AIMD simulation in 1M solutions with MM-relaxed initial configurations. Structures in red are species neutrally charged. "Fragments w/ DME" alludes only to DME molecules decomposed due to a salt fragment.

number of electrons	LiFSI		LiTFSI		
	Initial Bond Cleavages	Salt fragments	Initial Bond Cleavages	Salt fragments	fragments w/ DME
1	S-F	SO_2NSO_2F, LiF	S-N	CF_3SO_2, CF_3SO_2N	-
2	S-F	SO_2NSO_2F, LiF	S-N	CF_3SO_2, CF_3SO_2N	-
3	S-F, S-N, S-F	SO_2, NSO_2, LiF, F^-	S-N, C-S	CF_3, SO_2, CF_3SO_2N	-
4	S-F, S-N, S-F	$N(SO_2)_2$, LiF, F-	S-N, C-S, C-F	LiF_2^-, NSO, CF_3SO_2, CO, F^-	-
5	S-F, S-N, S-F	SO_2, NSO_2, $2F^-$	S-N, C-S, C-F	CF_2, SO_2, CF_3SO_2N, LiF	-
7	S-F, S-F	$N(SO_2)_2$, LiF, F^-	S-N, C-S, C-F	CF_3, SO_2, CF_2SO_2N, F^-	-
9	S-F, S-F	$N(SO_2)_2$, $2F^-$	S-N, C-S, C-F	CF_3, SO_2, CF_2SO_2N, F^-	-
11	S-F, S-F	$N(SO_2)_2$, $2F^-$	C-S, C-F, S-N	CF_3, NSO_2, O--LiF, OSC, $2F^-$	HO--Li, $CH_3O(CH_2)_2OCH_2^-$
13	S-F, S-N, S-F	SO_2, NSO_2, $2F^-$	C-S, C-F, S-F	CF_3, NSO_2, O--LiF_2^-, OSC, F^-	HO--$LiFi_2^-$, $HNSO_2$, CH_3O^-, $CH_2OCHCH_2^-$

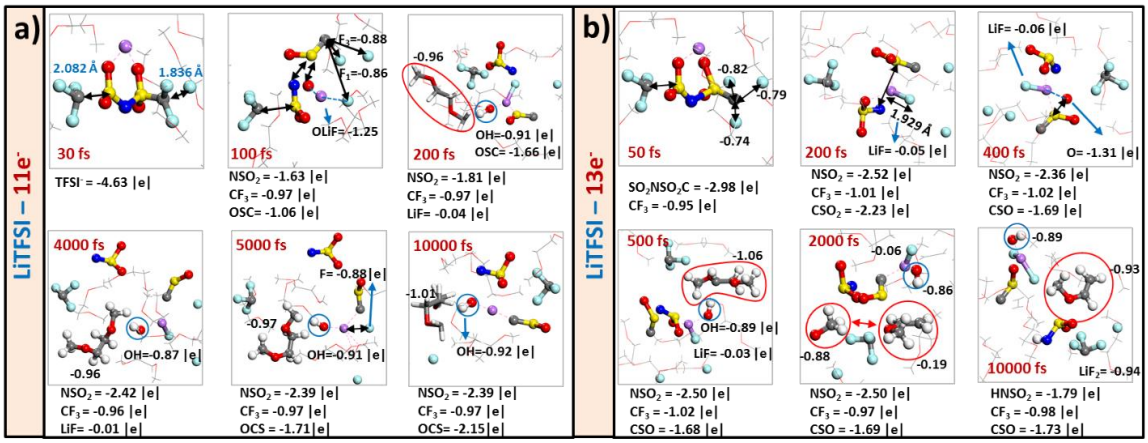

Figure 5.8 LiTFSI reduction involving DME redox reactions in 1M LiTFSI solutions with constant excess of electrons starting with the MM-relaxed configuration: n_{eo} equal to (a) 11 and (b) 13. Color code as in Figure 5.1.

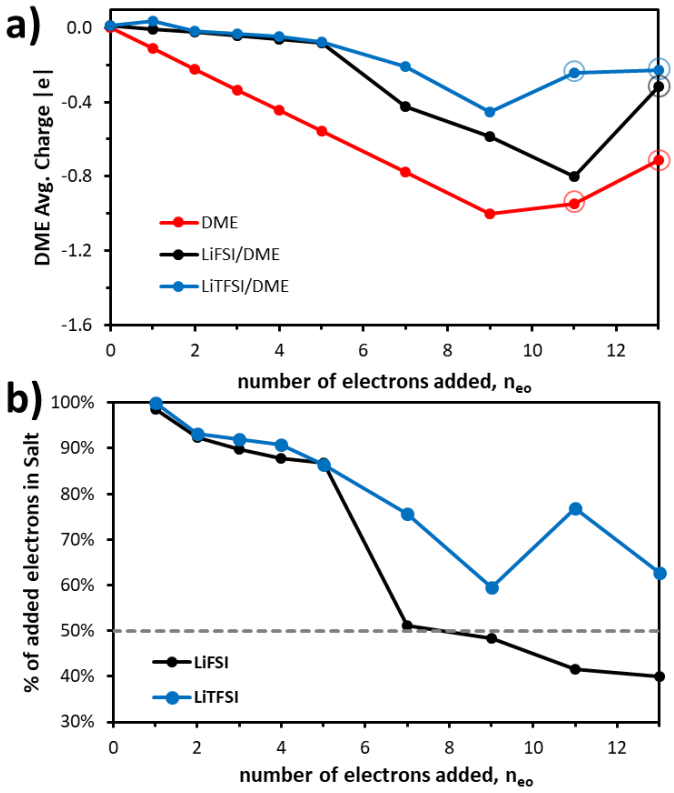

Figure 5.9 Average Charges over 10 ps of AIMD in solutions starting with MM-relaxed configuration (sampled every 1 ps) as a function of the initial number of excess electrons. (a) Average charges of non-reacting DME. Circles indicate systems where reactions took place. (b) Percentage of added electrons accepted by the salts. The dotted line depicts the 1:1 electron distribution between salt and solvent.

5.4.2.2. AIMD–relaxed

In this initial configuration, the pure DME system has an equivalent conformation to that obtained from the MM relaxation. In contrast, important structural changes can be observed for the molecular conformation of the mixture components. The main difference in that the salt molecules are partially dissociated, i.e., their Li-ion is being shared with two solvent molecules as shown in Figure C.1c-d, which can potentially lead to variations in the reaction mechanisms. For pure solvent, DME does not undergo any decomposition for $n_{eo}<11$, similar to the behavior observed in the MM-relaxed configuration. However, in systems with a charge equal to -11 and -13 |e|, two DME molecules reacted in each case following a comparable decomposition mechanism to the one described in Figure 5.2. Figure C.7 shows the calculated C_m–O bond distances for the reacting molecules. In the electrolyte with the highest electron-rich environment ($n_{eo}=13$), the same oligomer described in Figure 5.7, $(C_2H_4)_2^{2-}$, is formed resulting from the merge of two C_2H_4 fragments coming from breakup of DME molecules. The reacting DME molecules and the dimer charge evolution can be found in Figure C.8.

Regarding the 1M mixtures, a different initial configuration compared to the MM-relaxed structures yield some changes on the reaction mechanisms of the salt molecules (results are summarized in Table C.2). First, the initial bond cleavage for LiFSI is, for any value of n_{eo}, S–N instead of the S–F bond previously observed. Although the initial bond cleavage changed, some of the main products are essentially the same as those obtained from the MM-relaxed configurations (SO_2, NSO_2, LiF_x, and F^-) with the exception of $N(SO_2)_2$ which is not found in this case. Thus, this is the result of the different initial

configuration, which in the *MM-relaxed* structure has the Li-ion forming a bridge between two of the oxygen atoms offering additional stability to the S–N bonds, and exposing only the S–F bonds that are the initial bond cleavage in order to form the $N(SO_2)_2$ species. In contrast, in the *AIMD-relaxed* initial structure, the Li-ion is partially solvated by the solvent leaving the S–N bond prone to cleavage. Moreover, one DME molecule reacts in the solution containing nine electrons, see Figure 5.10a. DME losses one of the H_t-atoms to form a DME(-H_t) with charge ~ -1 |e|, similar to the pathway described in Figure 5.8a. However, in this case, the radical is not an O-atom but a NSO_2^{2-} resulting in the formation of the $HNSO_2^{2-}$ species, which had already been found in the 1M LiTFSI solution with starting MM-relaxed configuration and charge of -13 |e|. Again, no further decomposition is followed by the DME(-H_t). The detailed reaction pathways for the LiFSI in each initial electron-rich environment are reported in Figure C.9.

In the 1M LiTFSI/DME mixtures, the LiTFSI decomposition starts with the C–S bond scission in solutions with low electron-rich environment (n_{eo}<4). However, the initial cleavage of an S–N bond is observed exclusively when 4 or more electrons are added to the cell at the beginning of the simulation. Here similar fragments are formed from the LiTFSI reduction compared to the MM-relaxed initial configuration. A more complete description of this salt decomposition for each value of n_{eo} is reported in Figure C.10. With respect to the solvent reactions, one DME molecule breaks in each of the solutions containing 7, 11, and 13 electrons via the reduction pathway described in Figure 5.2. In addition, another DME molecule undergoes a redox reaction in the solution with n_{eo}=13, see Figure 5.10b. Similar to what occurred in the 1M LiTFSI solution with MM-relaxed

structure with the same amount of electron excess environment and when the electrons were being added sequentially, the DME losses one of the central hydrogens (H_m) to a CSO_2N^{3-} fragment forming in a $HCSO_2N^{3-}$ and a DME(-H_m). Consecutively, the DME(-H_m)$^-$ splits into CH_3O^- and methyl vinyl ether. Finally, an equivalent plot to Figure 5.9 is reported in Appendix C (Figure C.11).

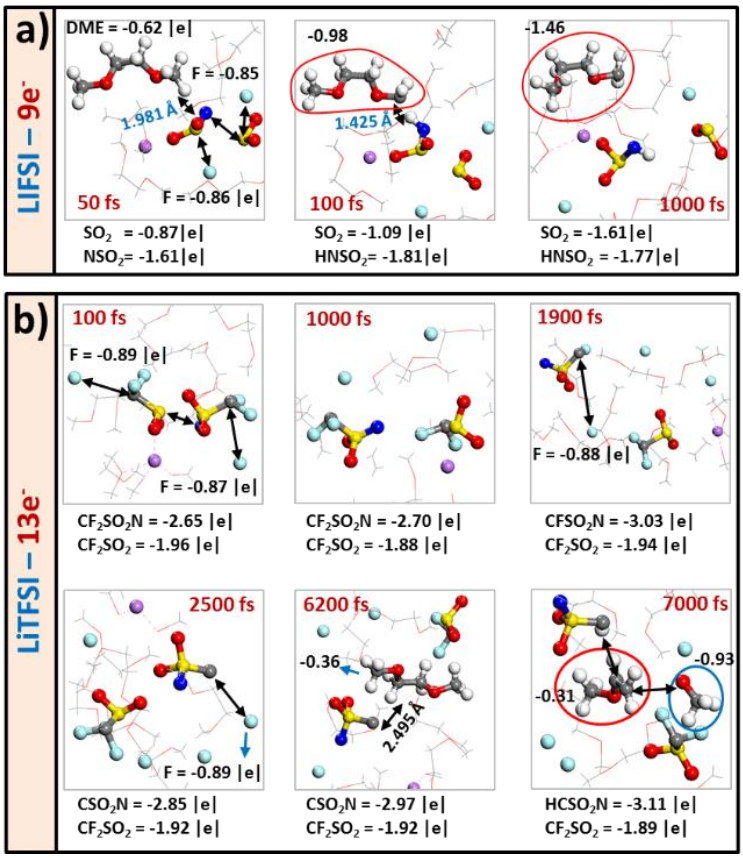

Figure 5.10 Salts reduction involving DME redox reactions in 1M solutions with constant excess of electrons starting with the AIMD-relaxed configuration: (a) 1M LiFSI with 11 |e| and (b) 1M LiTFSI with 13 |e|. Color code as in Figure 5.1.

To sum up the study of AIMD simulations under electron-rich environment, in the case of salt/DME mixtures, LiFSI and LiTFSI exhibit a similar decomposition behavior

than when in contact with the Li-metal surface. In the case of LiFSI, S–F and S–N bond cleavages have been found to initiate the reduction yielding similar SEI components such as SO_2, NSO_2, $N(SO_2)_2$, NSO_2F, SO_2F, and LiF_x species,[181, 188] which totally agrees with the findings in this work. For solutions containing LiTFSI, we have found that S–C and S–N bond scissions are responsible to start the decomposition resulting on reduction fragments such as CF_3SO_2, CF_xSO_2N, CF_x, SO_2, LiF_x, F^-, NSO_x, and CSO_x, which is also in good agreement with previous studies.[129, 161, 175, 183] Therefore, although the Li-metal surface is not explicitly present in our studies, the addition of excess electrons to emulate the electron-rich environment in a dynamic system successfully describes the salt reduction and, in addition, has allowed us to study further reactions involving the solvent as described below.

On the other hand, these simulations with excess electrons allowed us to observe DME decomposition for the first time. The redox reactions involving DME decomposition are summarized in the following equations:

$$\mathrm{DME} + 4e^- \rightarrow 2CH_3O^- + {C_2H_4}^{2-} \quad (5.1.1)$$

$${C_2H_4}^{2-} + \mathrm{DME} + 2e^- \rightarrow 2CH_3O^- + 2{C_2H_4}^- \quad (5.1.2)$$

$$2{C_2H_4}^- \rightarrow (C_2H_4)_2^{2-} \quad (5.1.3)$$

$$\mathrm{DME} + (\mathrm{frag.})^{x-} \rightarrow \mathrm{DME}(-H_t)^- + (H \cdot \mathrm{frag.})^{y-} \quad (5.2a.1)$$

$$\mathrm{DME} + (\mathrm{frag.})^{x-} \rightarrow \mathrm{DME}(-H_m)^- + (H \cdot \mathrm{frag.})^{y-} \quad (5.2b.1)$$

$$\mathrm{DME}(-H_m)^- \rightarrow CH_3O^- + CH_3OCHCH_2 \quad (5.2b.2)$$

$$CH_3OCHCH_2 + (\mathrm{frag.})^{x-} \rightarrow CH_2OCHCH_2{}^- + (H \cdot \mathrm{frag.})^{y-} \quad (5.2b.3)$$

where (frag.)$^{x-}$ could be any anion such as CSO_2N^{3-}, $O^{2-} \cdots LiF_x$, and $NSO_2{}^{3-}$. We must note that reactions given by equations 5.1.1–5.1.2 are electrochemical. However, the reactions involving salt fragments may be a combination of chemical and electrochemical reactions. Finally, we aim to provide some insights on the energetics for some of these reactions. Thus, in the following section, the reaction energies and kinetic barriers are calculated using a DFT-cluster model in which solvation effects are included implicitly in order to simplify our calculations.

5.4.3. Thermodynamics and Kinetics of the DME Decomposition

In this section, our goal is to characterize the energetic of the reactions involving solvent decomposition. Therefore, in order to achieve this, we consider the C–O bond cleavage, which is investigated under the presence of one or two lithium atoms. Moreover, hydrogen removal due to anion attack is also studied. However, before trying to predict the thermodynamics and kinetics of these reactions, we first calculate the bond dissociation energy of the DME in solvent phase as a comparative descriptor of its stability in the liquid phase. Results for bond dissociation energies of C_m-H_m, C_t-H_t, C_m-O, and C_t-O are presented in Table C.3. Reaction energies (ΔE_0) and Gibbs energies of reaction (ΔG_{298K}) were found to be higher than 4.30 and 4.20 eV, respectively in all the cases (no additional activation barriers were found in any case). Thus, the DME molecule is thermodynamically stable in solution.

5.4.3.1. Single Li Attack

Figure C.12 illustrates all possible DME decomposition mechanisms under a single Li attack yielding a C–O bond rupture. Reaction and activation energies are fully

characterized and reported in Table C.4. The thermodynamically favorable reaction pathways ($\Delta G_{298K} < 0$) are shown in Figure 5.11. Although both mechanisms C_m-O (α) and C_t-O (β) have similar reaction and activation energies, the initial C_m-O bond cleavage route leads to reactions with none or very low activation barriers ($\alpha_{1.3a}$ and $\alpha_{2.1a}$). These reactions in both cases yield the formation of $Li_2C_2H_4$ which is a lithium ethylene complex with most stable symmetry D_{2h},[189] and CH_3OLi. These compounds can be seen as the equivalent of the $C_2H_4^{2-}$ and CH_3O^- species commonly found in our AIMD simulations with electron excess. Regarding the other reaction pathway, β, once the first bond is broken the next splitting reactions have much higher activation energies (>0.90 eV) compared to the ones identified in the α-route (<0.04 eV). Formation of CH_3^- and $CH_3OCH_2CH_2O^-$ was only observed once for an electrolyte solution containing pure DME and an initial excess of 15 electrons (not shown) and no further reactions were detected in the simulation timescale due, possibly, to such activation energies. In general, our results are in good agreement with a similar DME initial reaction pathway reported in a recent study by Chen and co-workers.[180] However, in that case, the resulting products were CH_3OLi and ethylene. Thus, the possible formation of lithium ethylene complexes and/or charged ethylene groups were not considered.

5.4.3.2. Double Li Attack

Although the one-lithium attack model is useful to explain some of the compounds resulting from the electron-rich environment in the AIMD simulations, we are still not able to explain why the α-pathway is more commonly found in our simulation. From the AIMD simulations and charge analysis, it is found that the DME molecule undergoes

decomposition via a multi-electron mechanism. Therefore, a two-lithium attack is investigated in order to gain further understanding of the electrolyte decomposition reactions. Figure 5.12a illustrates a comparison between the two models (one- and two-lithium radical attack). In the first model, one-Li, similar reaction energies are predicted and a slightly higher activation energy is found for the C_m-O bond cleavage. However, when two-lithium atoms are included a significant difference is observed. First, the activation energy required to break the C_m-O is lower than for that of C_t-O. Importantly, the reaction energy is predicted to be more favorable by 1.08 eV toward the formation of CH_3OLi and its counterpart, $CH_3OCH_2CH_2Li$. Therefore, this can explain the more likely rupture of the C_m-O bond in the AIMD simulations.

5.4.3.3. Fragment Attack

As shown in the previous section, some of the DME splitting reactions might involve interaction with charged species. Here our goal is to characterize the energetics describing some of these reactions. In this case, we have opted to model the dehydrogenation process in equations 5.2a.1 and 5.2b.1 by using the $O^{2-} \cdots LiF$ anion. Nevertheless, it must be noted that other anions could also cause hydrogen removal as proven in section 5.4.2. In addition, similar oxidation mechanisms have been proposed for DME and other ethers due to interaction with Li_2O_2 (clusters and surfaces), and molecular oxygen in Li-O_2 (air) batteries[174, 190-192] as well as DME oxidation with Br^- anion in Li-S batteries. In fact, this oxidation process to form DME(-H) radicals is considered the first step towards the formation of DME-based oligomers.[173] According to Figure 5.12b and Table C.5, both C_t-H and C_m-H bond cleavages are thermodynamically

favorable. However, reaction and activation energies are predicted to be lower for dehydrogenation of C_m-atoms. Therefore, this reaction pathway was further explored and reactions given by equations 5.2b.2 and 5.2b.3 are considered for investigation. The C_m-O bond dissociation energy is favorable with a very small activation energy, which can explain the rapid reaction evidenced in the AIMD simulations to form CH_3O^- and methyl vinyl ether once the H_m was transferred to the radical anion. Finally, the dehydrogenation

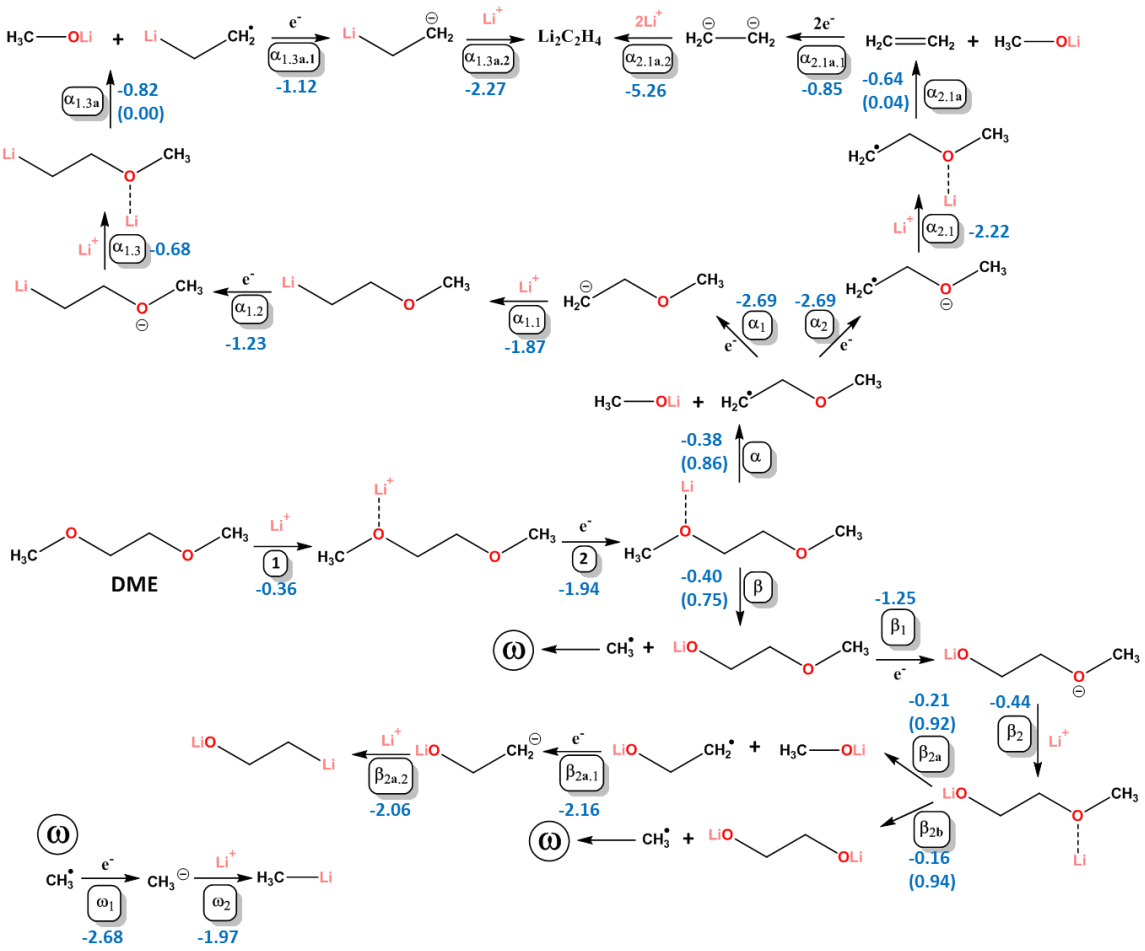

Figure 5.11 Thermodynamically favorable reaction pathway for DME decomposition under one Li-radical attack yielding C-O bond scission. Reaction energies (ΔE_0) and kinetic activation barriers (in parenthesis) (in eV) are calculated from B3PW91/6-311++G(p,d). Transition states structures are shown in Figure C.13.

of methyl vinyl ether is studied via NSO_2^{3-} attack. Here the reaction is, once again, thermodynamically possible. However, a high activation energy is predicted (0.67 eV). This relatively large activation energy might be the reason why this reaction is not observed in all the cases where the DME started to decompose via H_m-removal.

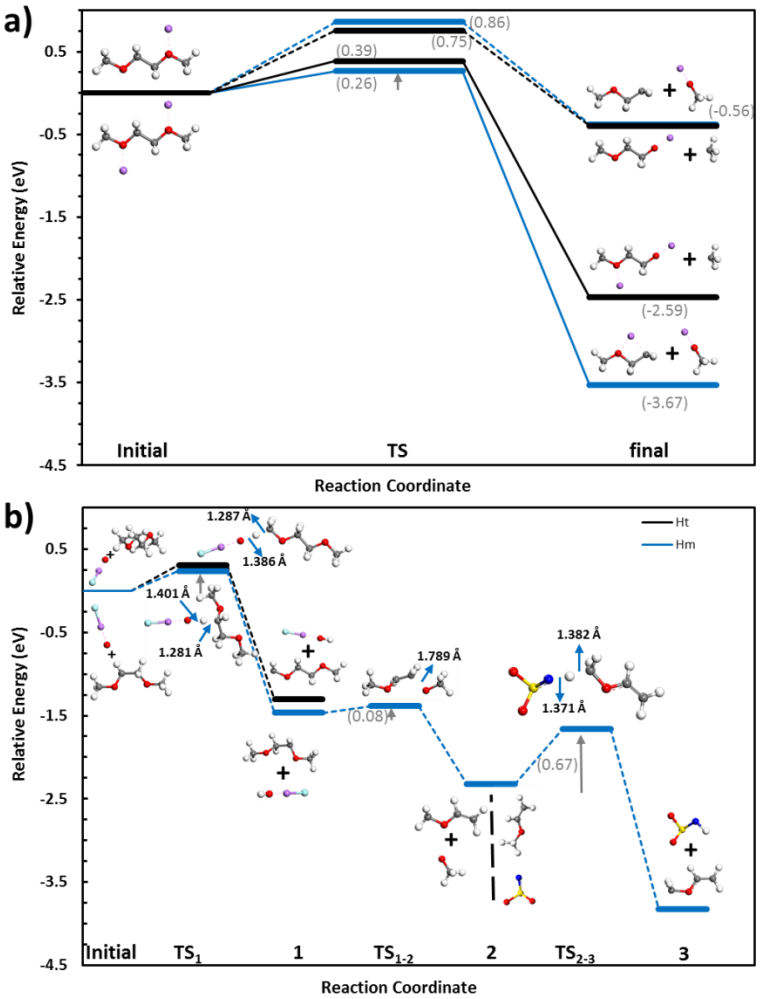

Figure 5.12 Reaction pathways for DME decomposition. (a) Single and double lithium radical attack and (b) DME decomposition via dehydrogenation. The relative energies and activation barriers are given in eV. Gibbs free energies (and activation barriers) in eV are shown in parenthesis.

5.5. Conclusions

The reaction mechanisms of electrolyte solutions used in Li-S batteries in electron-rich environments have been investigated using DFT and AIMD methods. In pure solvent, the DME molecule is reduced when the number of excess electrons in the cell is equal or larger than 11 – equivalent to an average charge of -0.9 |e| per surrounding DME molecule. It decomposes following a 4-electron mechanism via double C_m–O bond cleavage leading to the formation of CH_3O^- and $C_2H_4^{2-}$. Interestingly, the $C_2H_4^{2-}$ anion might also assist in the reduction of a different DME molecule which later combines with the newly formed C_2H_4 species to produce the $(C_2H_4)_2^{2-}$ oligomer. On the other hand, the LiFSI and LiTFSI salts are very prone to decomposition in any system with excess electrons. The LiFSI was found to start the reduction pathway with an S–F or S–N bond scission yielding the formation of SO_2, NSO_2 and $N(SO_2)_2$ radical anions. Alternatively, S–C or S–N bond cleavages were identified to begin the decomposition mechanism of the LiTFSI salt. Some of the most commonly detected fragments from LiTFSI decomposition are CF_3SO_2, CF_xSO_2N, CF_x, SO_2, LiF_x, F^-, NSO_x, OSC, CO and O. Remarkably, the presence of charged radical anions such as CSO_2N^{3-}, O^{2-}, and NSO_2^{3-} were found to trigger DME dehydrogenation from either the ethane or methoxy groups. However, when an H_t-atom is removed from the DME molecule no further reactions were observed. In contrast, the dehydrogenation from the ethane group further reduction was found, which yields the formation of CH_3O^- and methyl vinyl ether. The methyl vinyl ether may react with salt fragments. Finally, energetic of reactions involving the DME decompositions were examined thoroughly. It was found that the C_m–O and C_t–O bond cleavages of DME are

thermodynamically favorable under double Li-radical attack. However, C_m–O bond dissociation is more favorable and will probably occur faster due to a lower activation barrier. In addition, DME dehydrogenation from salt fragment attack was also found to be thermodynamically possible being slightly more favorable the removal of an H_t-atom. The short lifetime of DME(-H_t) was found to be related to the low activation energy and exothermic reaction to form CH_3O^- and methyl vinyl ether. Further decomposition of methyl vinyl ether is possible when reacting with NSO_2^{3-}; however, a relatively high activation barrier was found for this reaction.

It is worth mentioning that the presence of the surface may modify the structure of the electrical double layer and, in addition, it may allow the electron transfer to be more localized, which could lead to alternative decomposition pathways. However, although the metal electrode is not explicitly simulated, the time evolution of the electrolyte system under controlled electron-rich environments still provides new insights on the mechanistic description of electrolyte decomposition and the possible formation of SEI components under different stages of electron transfer from the anode. Finally, even when this study is very useful to elucidate the interfacial processes at the anode, it is not final and more elaborated methods are needed in order to have a model that captures the complex phenomena of the electrified interfaces.

6. EXPLORING INTERFACIAL STABILITY OF SOLID-STATE ELECTROLYTES AT THE LITHIUM-METAL ANODE SURFACE*

6.1. Summary

Solid-state electrolytes are promising materials to mitigate the issues derived from the extreme reactivity of the lithium metal anodes in Li-metal batteries. The main properties sought for this application are high ionic conductivity, low electronic conductivity, and high interfacial stability. Here we investigate a class of sulfides ($Li_{10}GeP_2S_{12}$, $Li_2P_2S_6$, β-Li_3PS_4, and $Li_7P_3S_{11}$) that have shown relatively good ionic conductivities. However, little is known regarding their interfacial stability. We use DFT and AIMD simulations to investigate the time evolution of the interfacial structure. We characterize atomic diffusion and reactions happening at the picosecond time scale, allowing us to identify the main interfacial products: Li_2S, Li_3P, and $Li_{17}Ge_4$. We then study how the reactivity changes when the Li metal surface is coated with a thin film of Li_2S.

6.2. Introduction

Sulfide-type materials are among the main solid electrolytes being investigated for use in battery systems due to their high ionic conductivity, good mechanical strength and flexibility, and low grain-boundary resistance.[24, 193] In particular, compounds such as β-

* Reprinted with permission from Luis E. Camacho-Forero and Perla B. Balbuena. "Exploring Interfacial Stability of Solid-State Electrolytes at the Lithium-Metal Anode Surface." *Journal of Power Sources*, 2018, **396**, 782-790. Copyright © 2018 Elsevier B.V.

Li_3PS_4, $Li_7P_3S_{11}$, and $Li_{10}GeP_2S_{12}$ (LGPS) have shown very promising ionic conductivities at room temperature: $8.9x10^{-7}$, $4.1x10^{-3}$, and $1.2x10^{-2}$ S cm^{-1}, respectively.[194-196] Recently, Liu *et al.*[194] showed that a nanoporous phase of β-Li_3PS_4 could lead to a higher ionic conductivity of $1.6x10^{-4}$ S cm^{-1}. In addition, other sulfides from the same family – lithium thiophosphates – are known to exhibit poor ionic conductivity, such as $Li_4P_2S_6$ and $Li_2P_2S_6$.[193]

High ionic conductivity and good interfacial stability are, perhaps, the most difficult challenges to be overcome for the implementation of SSEs in Li-batteries.[24, 26] Recent research efforts have focused on the study and design of materials with high ionic conductivity and the understanding of ion transport mechanisms via experimental and computational methods.[197-204] On the other hand, phase equilibria analyses from first-principles calculations have provided important insights on the chemical and electrochemical stability of SSEs against the electrodes and under biased potentials.[21, 205-207] While these studies are very useful and provide a remarkable amount of information regarding the stability of the SSEs at equilibrium conditions, the evolution of structure and composition of the electrolyte/electrode interfaces is still poorly understood. Recently, quantum mechanics-based methods and experimental tools have enabled the study of Li-metal/SSE interfaces.[208-210] Previously, similar approaches have been used to successfully studying the initial stages, and evolution of the solid-electrolyte interphase (SEI) formation for liquid electrolytes at the Li-metal anode.[175, 181, 211-212] In this work, we use DFT and AIMD simulations to learn more about the Li-metal/sulfide-type SSE interfacial chemistry. Here, we selected LGPS, $Li_2P_2S_6$, β-Li_3PS_4 (referred as Li_3PS_4), and $Li_7P_3S_{11}$

as representative materials of the sulfide family, which include a wide range of ionic conductivities (~10^{-11} to ~10^{-2} S cm^{-1}, see Table D.1).

6.3. Model and Computational Details

6.3.1. Computational Details

All the calculations were performed using VASP[58-60] with the GGA-PBE[45] functional. Electron-ion interactions were described by PAW pseudopotentials[50-51] as provided in the VASP databases. The energy cut-off of the plane-wave basis expansion was set to 500 eV with a Gaussian smearing width of 0.05 eV. Sampling of the Brillouin zone was done with the Monkhorst-Pack[54] k-point grid. The mesh was chosen based on the size of every system, see Table D.1 and Table D.2. Energy convergence during self-consistent cycles was ensured with an energy convergence threshold of 10^{-4} eV and the force convergence for ionic relaxations was set to $2x10^{-2}$ eV $Å^{-1}$. AIMD simulations were carried out using an *NVT* ensemble at 300 K with a time step of 1 fs. A Nose thermostat with a Nose-mass parameter of 0.5 was used to control the temperature oscillations during the simulations. For AIMD simulations, the energy cut-off was tested in order to improve the speed of the calculations. When a cut-off of 400 eV was used, the change in the total energy of each system was less than 1 meV per atom with respect to the case with 500 eV. Therefore, an energy cut-off of 400 eV was used for the AIMD simulations. Charges were calculated using the Bader analysis scheme.[63-65]

6.3.2. Modeling the Li-metal/SSE Interface

Our Li-metal/SSE models consist of a slab of each SSE deposited on top of a Li-metal surface. However, due to periodic boundary conditions, the SSE is allowed to

interact with the metallic surface not only at the top but also at bottom of the Li-slab, similar to a sandwich-like model: Li/SSE/Li. In order to build our systems, we use the following sequence of steps:

Table 6.1 Summary and characteristics of SSE systems investigated in this work. Units: the number of stoichiometric formulas contained in each SSE-slab; Supercell: MxN is the supercell size on the horizontal plane (*a*x*b*) and nL stands for the number of layers along the *c*-axis. The thickness of the SSE-slab is h. The (100)-Li-slab consists of 9 layers. Additional details of the model are provided in Appendix D, Table D.2. The final column lists the Li/SSE interfacial energies (γ).

SSE	Facet	Units	Supercell MxN-(nL)	h (Å)	γ (meV Å^{-2})
LGPS	(001)	8	2x2-(1L)	13	-62.55
	(100)	8	2x1-(2L)	17	-28.38
$Li_2P_2S_6$	(001)	12	1x2-(3L)	16	-111.44
	(100)	16	2x2-(2L)	19	-44.68
Li_3PS_4	(001)	24	1x2-(3L)	21	-16.42
	(100)	32	2x2-(2L)	28	-7.22
$Li_7P_3S_{11}$	(001)	8	2x1-(3L)	25	-23.99
	(100)	6	1x1-(2L)	20	-52.62

(*i*) The initial bulk crystalline structures for the SSEs were obtained from previous studies[193, 213] and were optimized at the PBE level of theory. One of the main characteristics of sulfide-type SSE materials is that they are comprised of anions surrounded by Li ions in a crystalline matrix. For instance, the anions for LGPS, $Li_2P_2S_6$, Li_3PS_4, and $Li_7P_3S_{11}$ systems are PS_4^{3-}/GeS_4^{4-}, $P_2S_6^{2-}$, PS_4^{3-}, and $PS_4^{3-}/P_2S_7^{4-}$, respectively. For details on the optimized lattice parameters and crystal structures, see Table D.1 and Figure D.1, respectively. The electronic band gap (E_g) for these materials were predicted to be 1.80, 2.14, 2.61, and 2.84 eV for $Li_2P_2S_6$, LGPS, $Li_7P_3S_{11}$, and Li_3PS_4. The same trend is found if the HSE06 functional is used; however, all the values were higher by ~1.1 eV (Table D.1), which agrees with previous calculations.[200, 213] (*ii*) Two low-index facets

– (001) and (100) – of the SSEs were selected to match with a (100)-Li surface. The size of the SSE slabs was chosen based on three criteria: (a) minimize the lattice mismatch with the Li-metal, (b) stoichiometric units with thickness > 13 Å, and (c) balance with computational resources. A summary of the model, size, and thickness of the SSEs studied are reported in Table 6.1. Figure D.2 shows the optimized surface slabs for the SSEs. In most cases, the anion groups in the SSE remained stable after the cleavage. However, in a couple of scenarios, the lack of coordination at the interface results in decomposition of some anions of the (100) surfaces of LGPS and Li_3PS_4. In the former, a GeS_4 group decomposes to form GeS_3 and S anions, whereas, in the latter, two PS_4 groups break into PS_3 and S, which might be an indication of poor surface stability of these facets. Surface energy (σ) calculation for the SSE facets and configurations under investigation (Table D.3) revealed that the (100) surfaces of LGPS and Li_3PS_4 exhibit the highest values of σ among the eight surfaces, which agrees with these findings. (*iii*) Once each of the surfaces (SSEs and Li-metal slabs) were optimized independently, an equilibrium distance between the SSE and the Li-anode was obtained by scanning the separation distance between one of the facets of every SSE and the Li-slab, see Figure D.3. The same separation distance was used for both sides of the Li-slab – bottom and top. (*iv*) A full geometry relaxation of the SSE/Li-metal systems was carried out. (*v*) Finally, AIMD simulations were performed for 20 ps using the optimized geometries obtained in the previous step as starting configurations, see Table D.2 for details on the cell parameters. The structures obtained from steps (*iii*), (*iv*), and (*v*) will be referred to as *initial*, *0 ps*, and *20 ps*, respectively, unless otherwise stated.

6.4. Results and Discussion

6.4.1. Characterization and Structural Evolution of the Li-metal/SSE Interface

The Li/SSE interfacial energies (γ) for our eight models were calculated as a measurement of the electrode-electrolyte affinity. The interfacial energy of two solids with lattice mismatch can be calculated according to the following equation[214]:

$$\gamma_{Li/SSE} = \frac{E_{Li/SSE} - n_{Li}E_{Li} - n_{SSE}E_{SSE} - E_{str}}{2A} \quad (6.1)$$

where A is the interfacial area, n_i is the number of *i* units, E_i is the bulk energy of species *i*, and E_{str} is the strain energy, which is defined as[215]:

$$E_{str} = \sum_{i=\mathrm{Li,\ SSE}} E^i(a_{str}) - E^i(a_0) \quad (6.2)$$

where $E^i(a_{str})$ and $E^i(a_0)$ are the energies of strained and pristine slabs of *i*, respectively. Table 6.1 shows that all the calculated γ values have a negative sign, which suggests that the adhesive forces at the interfaces are larger than the cohesive forces holding each material together and is probably an indicator of chemical instability of the interfaces.[214-215] Therefore, (001)-$Li_2P_2S_6$/Li and (100)-Li_3PS_4/Li seem to be the least and most chemically stable interfaces, respectively. In addition, the time evolution of γ is presented in Figure D.4. After 4 ps of AIMD simulation, a clear trend can be identified regarding the interfacial energy: $Li_3PS_4 > \mathrm{LGPS} > Li_7P_3S_{11} > Li_2P_2S_6$, which suggests that Li_3PS_4 ($Li_2P_2S_6$) possess the least (most) chemical active interfaces compared to the other three materials.

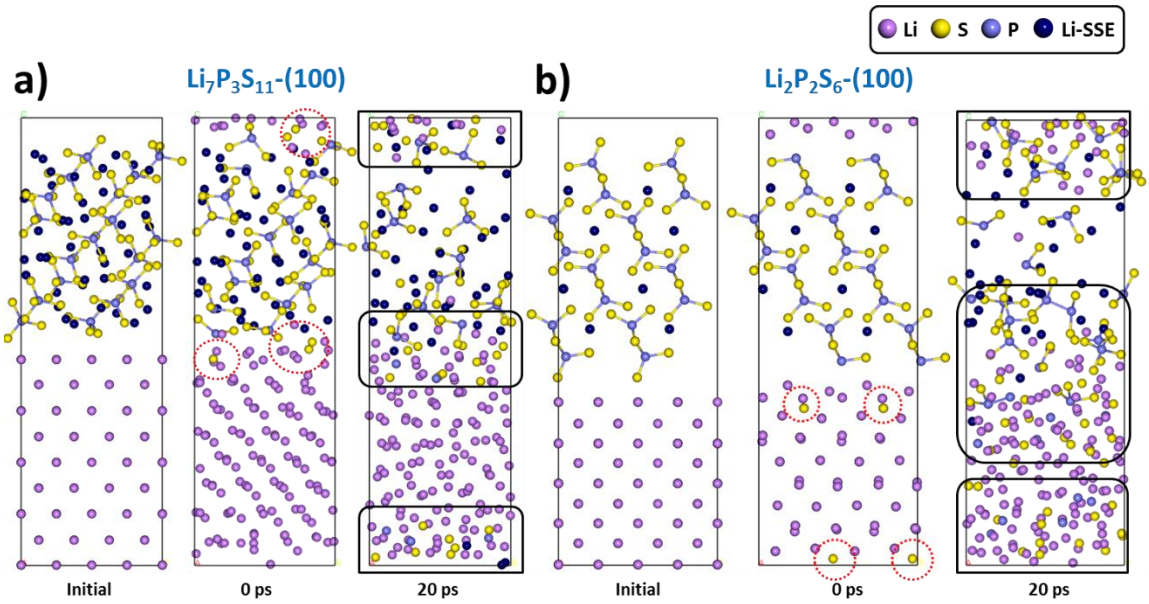

Figure 6.1 Illustration of structural changes of the SSE/Li models after optimization (0 ps) and AIMD simulations (20ps) compared with the initial configuration. For a complete list of structures, see Figure D.5. Red dotted ovals indicate decomposition after the structural optimization. Black rounded rectangles are included to show where the interface areas were initially located.

In each one of the eight models under investigation, anions that were close to the interface quickly decomposed during the DFT optimization (step *iv*), breaking S–P and S–Ge bonds depending on the anionic species, which can be clearly seen from Figure 6.1 and Figure D.5 (frames with the *0 ps* tag) and agrees well with our predictions of negative values of γ reported in Table 6.1. Although it is very remarkable that these events occur at such an early stage of the simulations, the results are in good agreement with previous *in situ* XPS observations of sulfide-type SSEs instability in contact with Li metal.[216-217] Figure 6.1 and Figure D.5 show further decomposition of the anions at the end of the AIMD simulations, to the point, that species comprising the anions – sulfur, phosphorous, and/or germanium – are no longer bonded and that atomic species are observed surrounded by Li ions. Figure 6.1 illustrates the evolution process of two of the studied systems:

$Li_7P_3S_{11}$-(100) and $Li_2P_2S_6$-(100) in contact with Li-metal. In both cases, there is significant decomposition at the interface after 20 ps of AIMD simulation. However, it is clear that for the $Li_7P_3S_{11}$-(100) system most of the reactions occur only at the interface level and there are several layers of Li-metal that remained intact, whereas the disintegration of the $Li_2P_2S_6$-(100) is far more advanced; practically no observable Li-metal layers are left after the 20 ps of dynamics and all the $P_2S_6^{2-}$ anions that originally were forming the SSE have reduced to other species.

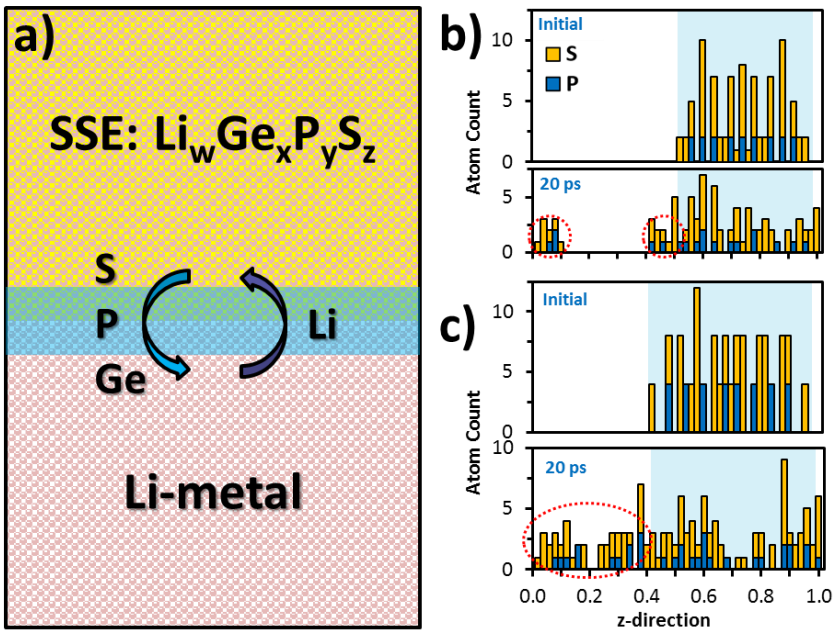

Figure 6.2 (a) Schematic representation of interfacial phenomena between the sulfide SSEs and the Li metal anode. Sulfur and phosphorus atom profiles along the z-direction for (b) $Li_7P_3S_{11}$-(100)/Li-slab and (c) $Li_2P_2S_6$-(100)/Li-slab. Light blue-shaded areas in (b) and (c) indicate the regions occupied by the SSE in the initial configuration. A complete list of z-direction atom profiles (including Li-atoms) can be found in Appendix D, see Figure D.6 to Figure D.9.

On the other hand, Figure 6.2a illustrates another important phenomenon that was identified from the AIMD simulations for all the systems: the diffusion of short fragments,

in most cases atomic species, inside the Li-metal, which is more evident in Figure 6.1b for the $Li_2P_2S_6$-(100) configuration. Likewise, some Li species that were part of the Li-metal diffuse toward the SSE side of the cells as ions. Atomic fraction compositions of the anode are reported in Figure 6.3, showing a decrease in Li content and increase of S, P, and Ge concentrations. In order to gain more insights on this diffusion phenomenon, atomic profiles in the z-direction were calculated at different instants for the SSE/Li systems (Figure D.6 to Figure D.9). Panels b and c in Figure 6.2 show the S and P atom profiles for the two systems shown in Figure 6.1, $Li_7P_3S_{11}$-(100) and $Li_2P_2S_6$-(100), respectively. At the initial configuration, P and S atoms are localized within the SSE region (shaded in light blue) as expected. However, at 20 ps, some peaks moved outside the SSE space, which means that some S and P atoms diffused to the Li-metal section. For the $Li_7P_3S_{11}$-(100) (Figure 6.2a), S and P atoms are only present at the SSE/Li interface. Conversely, in the $Li_2P_2S_6$-(100) configuration, S and P atoms are distributed along the entire simulation cell at the end of the dynamics. Overall, the distribution of fragments from the SSE decomposition through the cell might be used as an indicator of the stability of the SSEs against the Li-metal anode and the thickness of the interface layer that is formed since it is likely that the more reactions take place at the interface the more fragments will diffuse into the metal and consume the Li-anode. Therefore, the following trend is extracted from AIMD simulations at 20 ps regarding the fraction of Li-metal layers that remain intact, i.e., the ones that do not exhibit any interaction with S, P or Ge species: $Li_7P_3S_{11} - (100) > Li_3PS_4 - (001) > Li_3PS_4 - (100) > LGPS - (100) > LGPS - (001) > Li_7P_3S_{11} - (001) > Li_2P_2S_6 - (001) > Li_2P_2S_6 - (100)$. Therefore, $Li_2P_2S_6$-

(100) and $Li_7P_3S_{11}$-(100) correspond to the systems with the lowest and highest fraction of intact Li-metal layers after the 20 ps, respectively. Interestingly, Wenzel *et al.*[216] reported that the SEI formed between LGPS and Li-metal is thicker than the one between $Li_7P_3S_{11}$ and Li, which agrees with our results, at least for the (100) facet of $Li_7P_3S_{11}$ that has been predicted to be the most stable.[200] As a consequence of the diffusion and decomposition processes, some void regions were spotted to be localized in the SSE, see Figure D.10. Table D.4 shows the change in the free volume of each cell after the dynamics. In all the systems but the LGPS-(001), the voided volume increased by ~2–8%.

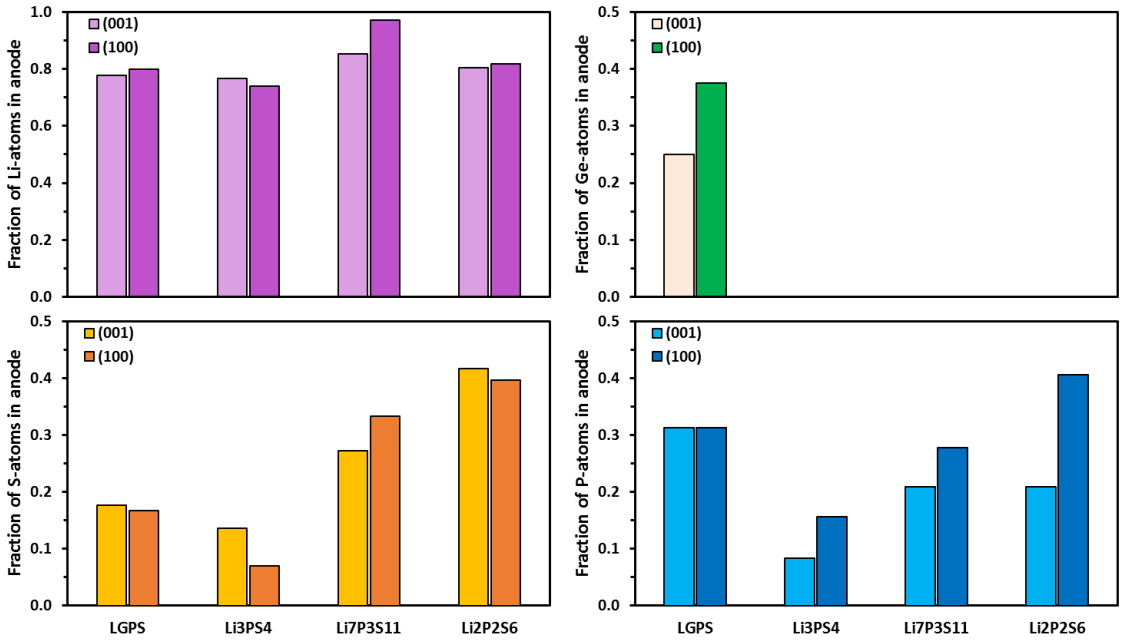

Figure 6.3 Anode atomic fractions after 20 ps of AIMD simulation. As anode, we referred the area of the cell that was comprised by the 9-layer Li-slab prior SSE/Li geometry optimization. Therefore, the fraction of Li corresponds to the Li-species that remains at the anode area after 20 ps, whereas the other fractions (S, Ge, and P) are the amount of such species that moved to the anode side during the relaxation/dynamic evolution.

Figure 6.4a shows the decomposition pathways from the different anions comprising the SSEs, which were obtained by analyzing the time evolution of each system. The PS_4^{3-} is a common anion that is present in almost of all the SSEs considered for this analysis: LGPS, Li_3PS_4, and $Li_7P_3S_{11}$. The PS_4 group decomposes sequentially by breaking each P–S bond. In most cases, the final decomposition species are S and P, however, some PS_x species might remain stable for long periods of time. The GeS_4 group from LGPS decomposes similarly to the PS_4 anion. The P_2S_7 anion (from $Li_7P_3S_{11}$) reduces to PS_3 and PS_4, which can further break into S and P. The P_2S_6 group from $Li_2P_2S_6$ has a very complex reaction mechanism, as described in Figure 6.4a. Remarkably, the transient species from the decomposition of this anion were the only ones that recombine to form P–P bonds which leads to the structures that are shown as "alternative products from recombination" in Figure 6.4: $S_2P–PS_x$ and P_3S, which can be the initial nuclei of polyphosphide compounds such as LiP, LiP_5, and LiP_7.[217] Furthermore, to characterize the phases/species that are formed, the coordination numbers (CNs) were calculated using the radii cut-off reported in Table D.5. The time-evolution average CNs are shown in Figure D.11 and summarized in Figure 6.4b. It is found that the CNs of P and Ge with respect to S decrease over time, while the lithium CNs of S, P, and Ge increase. This supports our earlier observation that the anions are decomposing (S-P and S-Ge bond cleavages) and suggests that Li_xS, Li_yP, and Li_zGe phases are being formed. Previously, experimental and computational studies have proposed the formation of $Li_{15}Ge_4$, Li_3P, and Li_2S from LGPS reduction reaction with the Li-metal; and Li_3P and Li_2S from Li_3PS_4 and $Li_7P_3S_{11}$ with Li-metal.[21, 216-217] In order to compare the structure of the phases obtained from AIMD

simulation and the ones reported, only the S, P, and Ge species product of the decomposition of the anions are considered for an average CN at 20 ps, see Table 6.2. The lithium CNs for S, P, and Ge from AIMD simulations are around 6, 7-8, and 8-9, whereas in the Li_2S, Li_3P, and $Li_{15}Ge_4$ crystalline phases are 8, 11, and 12, respectively. Although the CNs from our AIMD simulations are relatively smaller, this could represent the early stages of nucleation of those phases, where there are still many transient species.

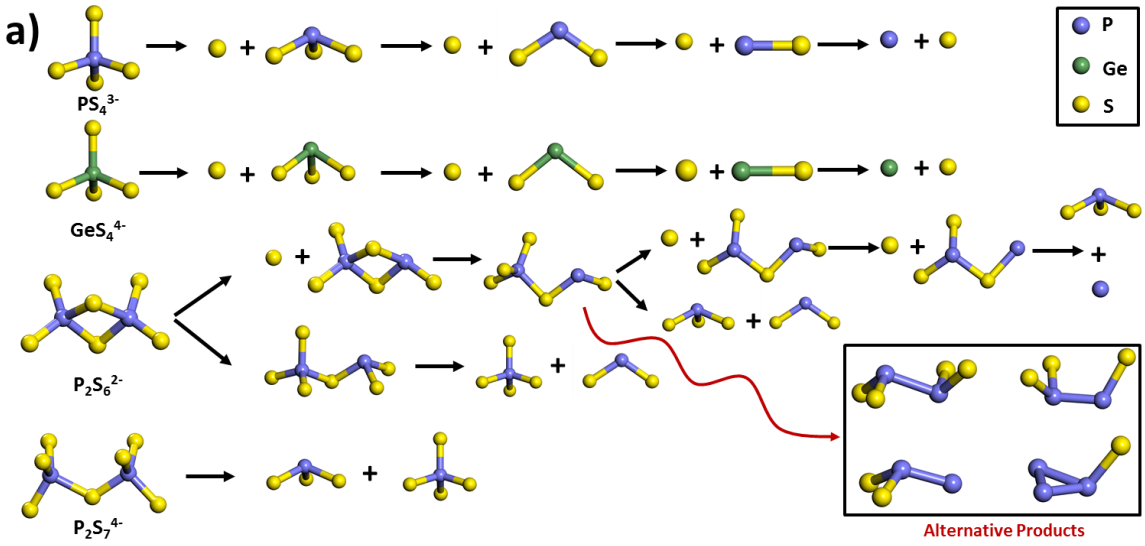

b)

SSE	Facet	Li-S		Li-P		Li-Ge		S-P		S-Ge	
		Initial	20 ps	Initial	20 ps	Initial	20 ps	Initial	20 ps	Initial	20 ps
LGPS	(001)	3.5	5.3	0.0	3.9	2.5	3.6	4.0	1.6	4.0	2.1
	(100)	3.3	4.9	0.1	3.3	1.8	3.6	4.0	2.2	3.8	1.9
$Li_2P_2S_6$	(001)	1.7	4.7	0.3	2.8	-	-	4.0	1.9	-	-
	(100)	1.4	4.3	0.0	3.4	-	-	4.0	2.0	-	-
Li_3PS_4	(001)	3.0	4.4	0.0	2.9	-	-	4.0	2.5	-	-
	(100)	2.9	4.1	0.3	2.1	-	-	4.0	2.9	-	-
$Li_7P_3S_{11}$	(001)	2.5	4.3	0.1	3.1	-	-	4.0	2.3	-	-
	(100)	2.5	4.2	0.0	2.8	-	-	4.0	2.4	-	-

CN in expected structures:	
$CN_S^{Li_2S}$	= 8
$CN_P^{Li_3P}$	= 11
$CN_{Ge}^{Li_{15}Ge_4}$	= 12
$CN_{Ge}^{Li_{17}Ge_4}$	= 9

Figure 6.4 (a) Anions decomposition mechanism from DFT optimizations and AIMD simulations. (b) (Left) average overall coordination number (CN) for the pre-optimized interface (initial) and the configuration after 20 ps of AIMD simulations. (Right) S, P, and Ge coordination number with respect to Li for expected (crystalline) products: Li_2S, Li_3P, and $Li_{15}Ge_4$ or $Li_{17}Ge_4$.

Table 6.2 Coordination number (CN) of atomic species (resulting from SSE's anions decomposition) at 20 ps and expected CN for crystalline bulk structures (highlighted in grey).

SSE	Facet	CN at 20 ps (atomic species)		
		Li-S	Li-P	Li-Ge
LGPS	(001)	5.9	7.2	9.0
	(100)	6.0	6.8	7.7
$Li_2P_2S_6$	(001)	6.0	8.3	-
	(100)	6.1	7.3	-
Li_3PS_4	(001)	6.0	7.2	-
	(100)	6.1	7.4	-
$Li_7P_3S_{11}$	(001)	5.9	7.4	-
	(100)	5.9	8.0	-
Li_2S		8	-	-
Li_3P		-	11	-
$Li_{15}Ge_4$		-	-	12

6.4.2. Bader Charge Analysis

To further explore the behavior of the SSE/Li interface, the time-evolution of the atomic charges in the anions were calculated, see Figure D.12. The S, P and Ge atoms gain charge throughout the 20 ps of the AIMD simulations, which confirms that reduction reactions are governing the SSE's anion decomposition. Additionally, Figure 6.5a shows how the total charge of the SSE materials changes as the dynamics evolves. During the first 8 ps of AIMD simulation, there is a rapid gain in charge for all the electrolytes, probably resulting from the quick decomposition of the SSE materials. More gain in charge (higher negative values) indicates larger reduction and more Li-metal consumption, which can be a measurement of the instability of the SSE. During the last 5 ps of the simulation, no major changes in charge are observed. This can be an indicator of potential passivation of the interface, which slows down the reduction of the solid electrolyte materials. At 20 ps, the following trend in net charge is obtained: $Li_7P_3S_{11} -$

$(100) < Li_3PS_4 - (100) < Li_3PS_4 - (001) < Li_7P_3S_{11} - (001) < LGPS - (100) \cong Li_2P_2S_6 - (001) < LGPS - (001) < Li_2P_2S_6 - (100)$.

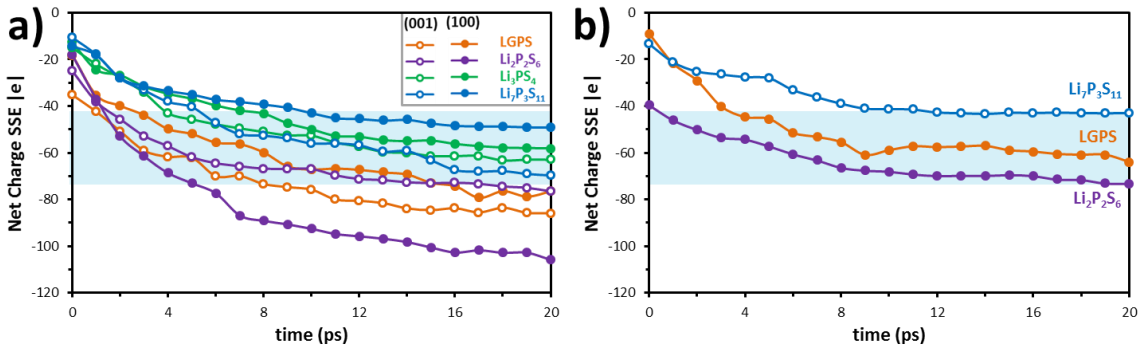

Figure 6.5 Net charge evolution of SSEs (a) without and (b) with a Li_2S thin-film interface (<1 nm).

The charges of all the atoms in each cell were calculated along the AIMD simulation (Figure 6.6a). Since Bader charges give fractional numbers, sometimes it is difficult to assign them to a particular oxidation state. Therefore, we calculated some Bader charge thresholds based on the charges of pure electrolytes (non-reduced species) and final products (totally reduced species) and assuming that $Li_{15}Ge_4$, Li_3P, and Li_2S are the final products, see details in Appendix D. As a result, three regions were obtained and are illustrated in Figure 6.6a: non-reduced (SSE), intermediates (inter), and totally reduced (red) for atoms that are in the pristine SSE, transient species (partially reduced), and final products, respectively. Figure 6.6b shows a distribution of atomic charges at 20 ps. Overall, a large number of sulfur atoms are assigned to the totally reduced species, ranging from 30 to 55% of the total atoms in each cell, being LGPS-(100) the largest and Li_3PS_4-(100) the lowest. A vast number of P atoms are also reduced, 40-100%, however, here the

transient species (partially reduced) govern the systems. Finally, it is found that all the Ge atoms in LGPS structures are reduced: ~30% totally reduced and ~70 partially reduced. Based on this distribution, the average charges of S, P, and Ge were computed across the simulation time (Figure 6.7). The charges for all the non-reduced atoms (SSE) and the totally reduced ones (red) across the eight systems studied were very consistent with low error bars in most cases, indicating that our method to distribute the atomic charges is accurate. Regarding the totally reduced atoms, a very good agreement was found for S and P in Li_2S and Li_3P, which confirm that early stages of Li_2S and Li_3P phases are being formed in our simulations as part of the SEI. However, it is worth mentioning that in the case of P-containing compounds a lot of transient products might be still present in our simulations. Regarding Ge, the computed charge from our simulations still deviates a lot from the ones obtained from a crystalline phase of the $Li_{15}Ge_4$ alloy. Therefore, it is possible that an alloy with higher lithium content is being formed at this stage of the interface formation. The charge of Ge in a $Li_{17}Ge_4$ alloy[218] is in better agreement with our calculations. In addition, the CN of Ge with respect to Li for this structure is 9. This coordination number is much closer to the ones reported in Table 6.2, 8-9. Consequently, it is very likely that the Ge atoms are mixing with Li to form the $Li_{17}Ge_4$ alloy.

From the previous analysis, we conclude that the interface is formed by a mixture of Li_2S, Li_3P (and $Li_{17}Ge_4$, in the case of LGPS) solid phases, and other transient species such as polyphosphides (in $Li_2P_2S_6$) and Ge-based compound (in LGPS). However, based on the number of atoms that are reduced and the atomic fraction in the systems studied (Figure 6.6b), the SSE/Li interfaces have a larger concentration of Li_2S phase followed by

Li_3P. The Li-Ge alloy in LGPS systems will be very low, but can also affect the interfacial resistance.[216] Li_3P have previously reported as a product of SSE decomposition such as LiPON and thiophosphate materials in contact with the Li-metal electrode.[208, 210] Earlier studies have suggested that Li_3P is a good ionic conductor (~10^{-2} S cm^{-1}),[219] however, the Li_2S crystalline bulk is known for being practically non-ionic conductor (~10^{-26} S cm^{-1}).[220] Nevertheless, these properties are expected to change at the interface.

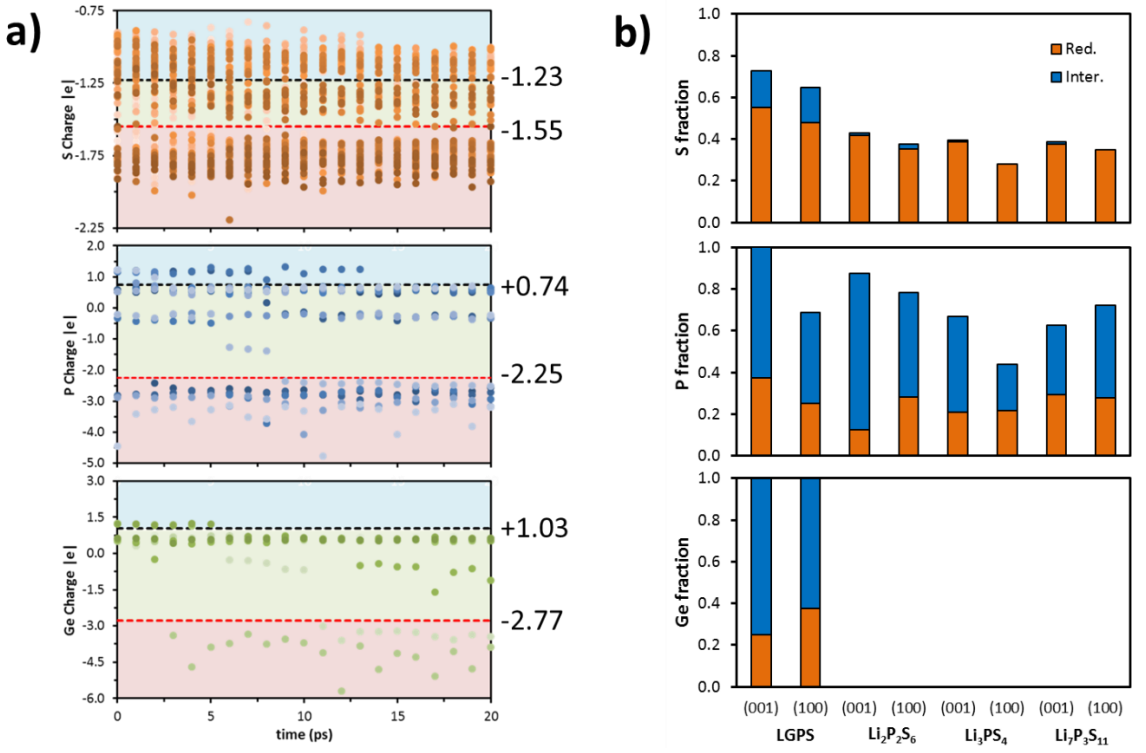

Figure 6.6 Charge Distribution. (a) Illustration of atomic charges evolution along the AIMD simulation distributed in three regions: (light blue) non-reduced - SSE, (green) partially reduced - Intermediate, and (red) totally reduced species - reduced. (b) Partially (Inter.) and totally (Red.) reduced fractions per atomic species at 20 ps.

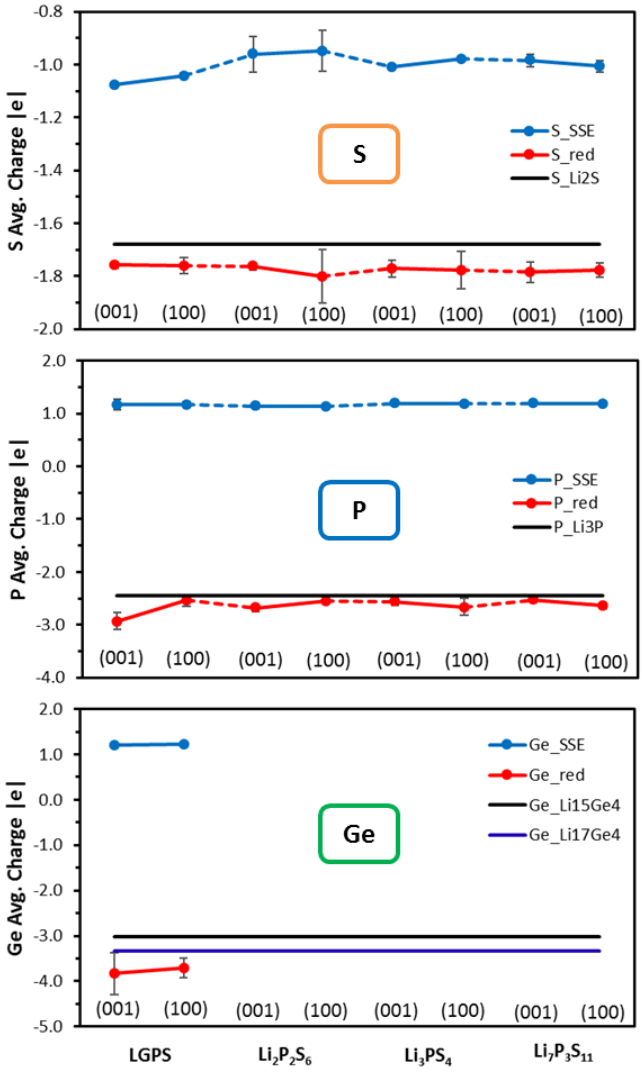

Figure 6.7 Atomic average charges for all non-reduced (i_SSE) and totally reduced (i_red) atomic species along the 20 ps of AIMD simulations – sampled every picosecond. The predicted Bader charges for each species in the expected reduced (crystalline) system are also included for comparison.

6.4.3. Incorporation of an Artificial Li_2S Thin-Film

To reach deeper insights into the SSE/Li-metal interfacial phenomena, we selected three of the worst systems (based on the trends abovementioned and different SSE nature) – $Li_7P_3S_{11}$-(001), LGPS-(100), and $Li_2P_2S_6$-(100) – and added a thin film of Li_2S (<1 nm)

between the Li-metal anode and the SSEs to emulate an artificially formed layer, so our sandwich-like model now is Li/SSE/Li_2S/Li. We found that most of the reduction (some desulfurization of anions) and rearrangement on the Li_2S side happened during the DFT optimization (Figure D.13). With the exception of the $Li_2P_2S_6$ where some Li diffused through the Li_2S and produce further reactions with the SSE, the Li_2S in the other two systems remained very stable even after the 20 ps of simulation time (Figure 6.8). On the other hand, the side with no artificial layer behaves similarly to the SSE/Li interfaces. Figure D.14a shows the calculated charge transfer evolution. Clearly, since one of the sides of the SSE is exposed to the Li-metal, some reduction reactions are expected. However, the charge transfer per species is much lower than the case with no Li_2S (Figure D.14b). An important result from this analysis is that most of the charge transfer occurs before 10 ps, then there is a plateau region, indicating some passivation of the interface. In the case with no Li_2S interface (Figure D.14b), on the contrary, no clear plateau is observed even near the end of the simulation. If we compare the net total charge transfer to the SSE for these three systems (Figure 6.5), we can conclude that their degree of reduction is comparable to the "best" systems without the additional interface, which means that there is a strong passivation effect at the interface due to the presence of Li_2S. However, the ionic transport kinetics through this layer must be investigated in the future in order to gain a complete knowledge of its effect.

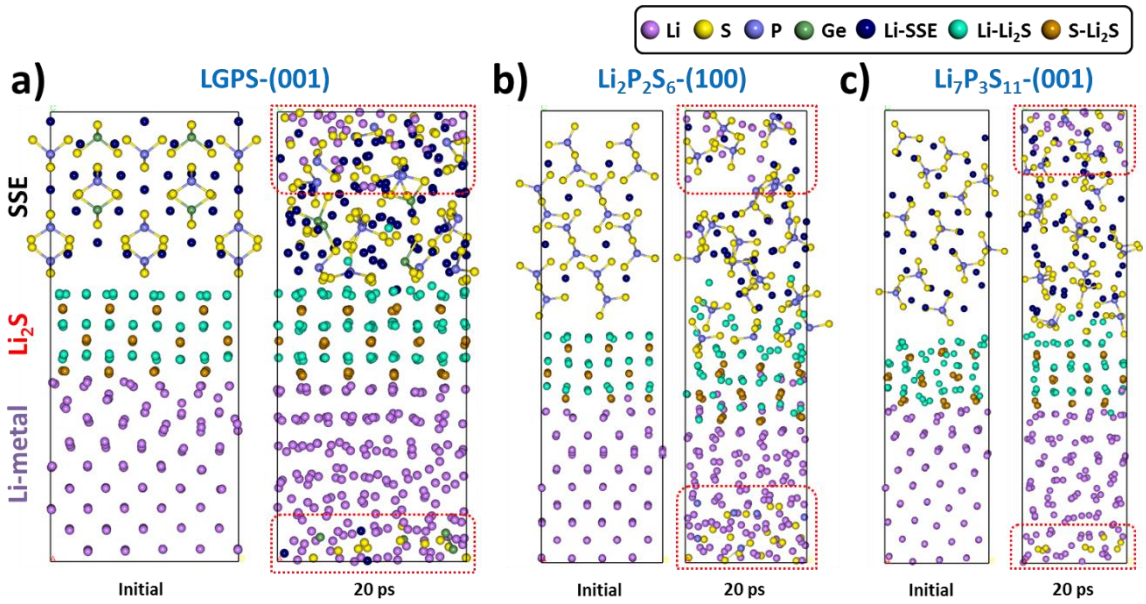

Figure 6.8 Structural changes of tested SSEs with Li_2S thin film (SSE/Li_2S/Li) after AIMD simulations.

6.4.4. Consistency Analysis

In order to test the consistency of our results at longer simulation times, we ran the facet (100) of $Li_2P_2S_6$ and $Li_7P_3S_{11}$ in contact with the Li surface up to 50 ps. As we might expect, it was found that longer simulation time leads to further decomposition of anions (Figure D.15) and electron transfer (Figure D.16a). However, the relative stability between the different interfaces and the reduction products at 20 and 50 ps are consistent, which validates the use of the 20 ps simulations for our analyses. For instance, Figure D.16b shows the fraction of S and P atoms partially and totally reduced after 20 and 50 ps of simulation. Although a slightly higher fraction of reduced atoms is observed in each case, the relative fraction between partially (inter) and totally (red) reduced S and P species is similar at 20 and 50 ps. Regarding the average coordination numbers (Table D.6) and S and P charges (Figure D.16c and d) remain almost unchanged.

6.5. Conclusions

We used DFT and AIMD simulations to predict the interfacial evolution of a set of sulfide-type SSE materials in contact with Li-metal. We find that, in general, the SSE/Li interface is very unstable and induces the formation of multiple solid phases such as Li_2S, Li_3P, $Li_{17}Ge_4$, transient Ge- and P-based compounds, and possibly some polyphosphide compounds in $Li_2P_2S_6$/Li interfaces. The compounds that are formed in the interface are likely to increase the ionic transport resistance. Although this study focuses on the (001) and (100) facets, the fast and strong interfacial reactivity behavior observed in these electrolytes should be valid for most exposed surfaces in contact with Li metal. As an attempt to further investigate the effect of these solid phases, we selected three systems with some of the worst stabilities and added a Li_2S thin film. A strong passivation effect was found at the interface due to the presence of the Li_2S. However, ionic transport kinetics studies of this and other thin-film layers are required in order to gain a more complete understanding of their effect on the overall performance of the batteries. Our study provides new insight into the complex transient phenomena at the SSE/Li interfaces using computational tools, showing the potential of *ab initio* methods in the understanding and design of materials for battery systems.

7. ELUCIDATING INTERFACIAL PHENOMENA BETWEEN SOLID-STATE ELECTROLYTES AND THE SULFUR-CATHODE

7.1. Summary

In this chapter, we use DFT and AIMD simulations to investigate the formation of the cathode-electrolyte interface at two limiting states of charge: S_8 and Li_2S. β-Li_3PS_4 and two lithium halide doped sulfides (Li_6PS_5Cl and $Li_7P_2S_8I$) were selected due to their Li-ion superionic conductivity and compatibility with sulfur electrodes. The work of adhesion and interfacial energy of the interfaces were calculated as descriptors of the interfacial properties, then the mechanisms of the interfacial reactions taking place were characterized. Finally, a charge transfer analysis is presented, suggesting that, overall, the S_8 electrode will oxidize the electrolyte, whereas the fully discharged Li_2S cathode will reduce it at different extents depending on the reactivity of the exposed facet. Introduction

7.2. Introduction

Among the inorganic SSEs currently under investigation as promising candidates for Li-S batteries, sulfide-type materials have drawn a lot of attention because of their high ionic conductivity at room temperature (RT) (>10^{-4} S cm^{-1}), low grain-boundary resistance, easy processability, and potential compatibility with sulfur-based electrodes.[24, 28] For instance, β-Li_3PS_4 and $Li_7P_3S_{11}$ have demonstrated to be lithium superionic conductors with conductivities of $1.6x10^{-4}$ and $4.1x10^{-3}$ S cm^{-1}, respectively.[194, 196] More recently, it has been reported that chemical doping with lithium halides LiX (Cl, Br, and I) improve the electrochemical stability of sulfide SSEs. In addition, the use of non-

electroactive species (lithium halides) leads to high Li-ion conductivities (~10^{-2} to 10^{-3} S cm^{-1} at RT) and enhanced compatibility with Li-metal anodes.[221-223]

Besides the bulk properties of electrolyte and electrode materials, the interfacial properties between the electrolyte and the electrodes are crucial for the adequate performance of the Li-S battery. Due to the high reactivity of the Li anode, which results in the formation of the solid-electrolyte interphase (SEI), research efforts have mainly been devoted on understanding interfaces between liquid or solid electrolytes and Li-metal anodes.[19, 22, 175, 224] Although some studies have attempted to address interfacial properties between electrolytes and other cathode chemistries (i.e., $LiCoO_2$, $LiMn_2O_4$, and NCM),[207, 225-229] sulfur-based cathode/electrolyte interfaces are not well understood yet. Therefore, in order to overcome the interfacial challenges facing this battery technology, fundamental understanding of the interfacial behavior of cathode/electrolyte using both experimental and computational approaches is imperative.[228, 230]

With the advances of high-performance computing, quantum mechanics-based methods have proven to be an effective and reliable approach to elucidate electrode/electrolyte interfacial behavior for both cathodes and anodes. For instance, these methods have extensively been used to study the SEI formation from solid or liquid electrolytes on the metallic Li metal anode.[181, 210, 231-232] Recently, Arneson *et al.*[233] studied the interfacial de-/lithiation at sulfur cathodes in contact with liquid electrolytes by employing AIMD simulations. In this work, we use ground state DFT and AIMD simulations to explore the formation and S-cathode/SSE interfacial behavior. Here, we selected β-Li_3PS_4 as a sulfide material representative of this group of electrolytes as well

as two of its doped structures with lithium halides (LiI and LiCl) – Li_6PS_5Cl and $Li_7P_2S_8I$ – because of the common interest in their promising ion conductivities and electrochemical stability.

7.3. Computational and Model Details

7.3.1. Computational Details

All the calculations were performed using VASP.[58-60] The exchange-correlation functional was described within the generalized gradient approximation parametrized by Perdew-Burke-Ernzerhof (PBE).[45] PAW pseudopotentials[50-51] were utilized to model the electron-ion interactions as provided in the VASP database. The Brillouin Zone was sampled using a Monkhorst-Pack k-point grid.[54] The mesh size was chosen according to the magnitude of the lattice vectors of each system. The energy cut-off of the plane-wave basis expansion was set to 500 eV with a Gaussian smearing width of 0.05 eV. However, the energy cut-off was reduced to 400 eV to reduce the computational cost during the AIMD simulations. The reduction of cut-off only led to changes of ~1 meV/atom in the total energy of each system, which is a good balance between accuracy and supercomputing time. Convergence during self-consistent field was achieved when the energy change was less than 10^{-4} eV and the convergence criterion for ionic relaxations was set to atomic forces lower than 0.02 eV $Å^{-1}$. AIMD simulations were performed within an *NVT* ensemble at 300 K and a time step of 1 fs unless otherwise stated. The temperature oscillations during the simulations were controlled by a Nose thermostat with a Nose-mass parameter of 0.5. Charge analysis was carried out within the Bader analysis scheme.[63-65] Visualization of structures was obtained by combining the use of several software

packages: VESTA (Visualization for Electronic and Structure Analysis)[234], Materials Studio[184], and OVITO (Open Visualization Tool)[235]. Finally, radial distribution functions (RDF) g(r) were evaluated using the Visual Molecular Dynamics (VMD)[160] program with a Δr of 0.01 Å.

7.3.2. Model of Bulk Solid-Electrolyte

The initial crystalline structures for the bulk SSEs were obtained from a previous computational study ($Li_7P_2S_8I$)[221] and the Materials Project Database (β-Li_3PS_4 and Li_6PS_5Cl)[213]. These geometries were further optimized using DFT (at PBE level of theory). The relative deviations of the lattice parameters with respect to the reported structures were less than 1%, see Table 7.1 for optimized lattice parameters. One of the main features of these three electrolytes (see Figure E.1) is the different anionic groups that comprise the material with the common characteristic that each of them possess the PS_4^{3-} tetrahedral anion – typical in sulfide materials. Hence, the different anionic groups for β-Li_3PS_4, Li_6PS_5Cl, and $Li_7P_2S_8I$ (hereinafter referred to as LPS, LPSCl, and LPSI for simplicity) are PS_4^{3-}, $S^{2-}/Cl^-/PS_4^{3-}$, and $S^{2-}/I^-/PS_3I^{2-}/PS_4^{3-}$, respectively. The predicted electronic band gaps from Density of States (DOS) – calculated using HSE06 hybrid functional[236] – are also shown in Table 7.1. LPS, LPSCl, and LPSI exhibit moderate band gaps of 3.98, 3.55, and 2.54 eV, respectively. These values decrease slightly over 1 eV when the PBE functional was used. These results are in good agreement with previous reports.[221, 237-238] More interestingly, the band gap of LPSI is significantly lower (by more than 1 eV) than the other two materials. This is the result of the PS_2I^{2-} anion mixing group, which leads to the formation of new band states in the conduction band, see Figure E.2.

Table 7.1 Simulation k-points, optimized crystallographic parameters, and predicted electronic band gap (E_g) for the studied SSEs. The DOS is reported in Figure E.2. [a]E_g values were calculated using double the number of k-points shown in this table.

SSE	K-points	Crystallography							E_g (eV)[a]	
		Space Group	a (Å)	b (Å)	c (Å)	α (°)	β (°)	γ (°)	PBE	HSE06
β-Li_3PS_4	2x4x4	*Pnma*	13.073	8.112	6.253	90	90	90	2.84	3.98
Li_6PS_5Cl	2x2x2	*F-43m*	10.258	10.258	10.258	90	90	90	2.29	3.55
$Li_7P_2S_8I$	3x3x2	*Pm*	9.431	7.820	11.748	90	75	90	1.53	2.54

To provide a more complete description of the SSEs considered in this study, the transport properties of Li ions in bulk were also calculated from AIMD simulations. The simulations were run using an *NVT* ensemble during 100 ps with a time step of 2 fs at temperatures (T) from 600 to 1300 K (100 K step). This methodology has commonly been used to successfully estimate diffusion coefficients of SSEs.[237, 239-240] First, the diffusivity (D) of Li ions was determined at each temperature from the Einstein relation:

$$\mathrm{D} = \frac{1}{2n}\frac{\mathrm{MSD}(\Delta \mathrm{t})}{\Delta \mathrm{t}} \tag{7.1}$$

where n=3 is the dimension of the system, MSD(Δt) is the mean squared displacement of Li ions over time interval Δt. The MSD was computed using the *nMoldyn* 3 software[241]. Regarding the bounds of the time interval, the lower bound was set to 1 ps since for Δt > 1 ps, the local derivative $dMSD/d\Delta t$ reaches a plateau. The upper bound was set to 90 ps to avoid deviations from linearity at the end of the MSD curve. The diffusivities of LPS, LPSCl, and LPSI as a function of the temperature are reported in Figure E.3, where a linear behavior between the *log D* and *1/T* is clearly evidenced as described by the Arrhenius relation:

$$D = D_0 \exp\left(-\frac{E_a}{kT}\right) \tag{7.2}$$

where k is the Boltzmann constant, and the activation energy E_a can be calculated by the fitting of the data to this equation. Furthermore, the fitted Arrhenius relation can be used to extrapolate the D to other temperatures. Finally, the ionic conductivity (σ_{Li^+}) is computed based on the diffusivity and the Nernst-Einstein relation:

$$\sigma_{Li^+} = \frac{Nq^2}{VkT} D \tag{7.3}$$

where N, q, and V are the number of ions, the charge of the mobile-ion species, and the volume of the system, respectively.

Table 7.2 Activation energy E_a and extrapolated Li-ion diffusivity and conductivity at 300 K from fitting the Arrhenius equation.

SSE	E_a (eV)	D ($cm^2 s^{-1}$)	σ_{Li^+} ($mS\ cm^{-1}$)
LPS	0.28	4.18×10^{-8}	4.69
LPSCl	0.37	1.20×10^{-9}	0.17
LPSI	0.27	5.85×10^{-8}	6.07

The activation energies E_a obtained from the fitted Arrhenius relation and the extrapolated the D and σ_{Li^+} at 300 K are presented in Table 7.2. These predicted transport properties for Li-ions in bulk LPS, LPSCl, and LPSI are comparable with values previously reported, which are summarized in Table E.1 for comparison. For instance, Yamamoto *et al.*[242] recently reported activation energies at RT of 0.32 and 0.27 eV for LPS and LPSI, respectively. Additionally, Rao *et al.*[243] found the activation energy of LPSCl to be 0.38 eV. Regarding the Li-ion diffusivity, the predicted value for LPS

($4.18x10^{-8}$ cm^2 s^{-1}) falls within the range of diffusivities of Li^+ in LPS found from Pulsed-gradient spin-echo (PGSE) ^{7}Li NMR, 1.4-$7.2x10^{-8}$ cm^2 s^{-1}.[244] In the case of LPSCl, the D_{Li+} was found to be $7.7x10^{-8}$ cm^2 s^{-1} at 313 K[245] in an earlier study, which is almost two orders of magnitude larger than the value extrapolated at 300 K, $1.20x10^{-9}$ cm^2 s^{-1}. Nonetheless, the Li^+ conductivity in LPSCl (0.17 mS cm^{-1}) is very close to the one obtained from experimental measurements by Boulineau *et al.*[246] (0.20 mS cm^{-1}). The diffusivities of LPS and LPSI – 4.69 and 6.07 mS cm^{-1}, respectively – are overestimated by c.a. one order of magnitude with respect to previous works: 0.50[247] and 0.63[222] mS cm^{-1}, respectively. In the case of LPSI, these variations could be related to chemical and structural changes occurred at high temperatures due to dehalogenation of the anion mixing group PS_3I^{2-} and association with another anion PS_4^{3-} to form $P_2S_7^{4-}$ and I^- at T between 600 and 1000 K, and further reactions, yielding the formation of PS_x (x=2, 3, and 5) and I^- anion species, at higher temperatures.

7.3.3. Model of Surface SSEs

In order to select the proper surfaces of the SSEs to be considered, the surface energies (σ) of five low-index facets – (001), (010), (100), (110), and (111) – were calculated using the following equation[35]:

$$\sigma = \frac{1}{2A}\left(E_{SSE-slab} - n_{SSE-slab}E_{SSE-bulk}\right) \quad (7.4)$$

where $E_{SSE\text{-}slab}$, $E_{SSE\text{-}bulk}$, $n_{SSE\text{-}slab}$, and A are the energy of the slab, the energy of one unit of SSE in bulk, number of SSE units in the surface slab, and area, respectively. The surface terminations and thickness of each facet were chosen to fulfill the following conditions: the slabs had to *i)* keep the stoichiometry of the material, *ii)* have at least two

stoichiometric layers, and *iii)* have a reasonable thickness *h* (15 Å< h <25 Å) without compromising computational resources. The surface energies for the optimized facets considered are reported in Table 7.3. Final optimized structures of LPS, LPSCl, and LPSI facets are shown in Figure E.4, Figure E.5, and Figure E.6, respectively. Although the surface anions of SSEs lose coordination, for LPS and LPSCl, the anions remained stable in most cases, except for LPSCl-(110), where one of the PS_4 groups seems to have stretched one of the P-S bonds to form PS_3 and S species, see Figure E.5. In contrast, the PS_3I mixing anions in LPSI facets exhibit a less stable behavior, see Figure E.6. For (010) and (111) facets, for example, this anion decomposes into PS_3 and I at the sub-surface and surface. On the other hand, one of the P-S bonds is stretched due to lack of coordination at the surface of LPSI-(100), resulting in the formation of PS_2I and S species.

Table 7.3 Surface energy (σ) for the SSE facets and configurations shown in Figure E.4 to Figure E.6. Italic and underlined values indicate slabs that have at least one of the lattice angles different to 90º, *i.e.*, non-orthorhombic cells.

SSE	Surface Energy σ (meV Å^{-2})				
	(001)	**(100)**	**(010)**	**(110)**	**(111)**
LPS	27	49	28	27	*24*
LPSCl	1	1	1	10	*25*
LPSI	16	35	*12*	*11*	*10*

From the calculated surface energy, the most stable facets for the reported configurations are (111), (001), and (111) for LPS, LPSCl, and LPSI. In the case of LPSCl, all three low-index facets (001), (010), and (001) exhibit the same surface energy and this is due to the symmetry of the face-centered space group (*F-43m*) of this SSE, which results

in equivalent surfaces. In the case of LPS and LPSI, the most stable facets are not orthorhombic cells, which, from a practical point of view, represents a challenge to match with the S-based electrode model and it will result in large strains and, potentially, disruption of the crystallinity of the SSE. Therefore, in this study, we considered one of the most stable facets with an orthorhombic cell for each SSE, *i.e.*, the (001) plane. In addition, a second facet with the largest surface energy among the fundamental planes of the electrolyte crystals was also considered in order to provide a further description of more reactive surfaces that might be in contact with the sulfur particles in the electrode. For LPS and LPSI, such facet is the (100), whereas, in the case of LPSCl, no additional facets were included since they are equivalent and will exhibit the same reactivity of the (001) surface.

7.3.4. Model of S-based Cathode Surface

Sulfur cathode materials are typically made of a mixture between sulfur nanoparticles of a few hundred nanometers in diameter and hierarchical carbon materials including mesoporous carbon, reduced graphene oxide, carbon nanofibers, and carbon nanotubes, which role is to enhance the electronic conductivity of sulfur-based electrode materials.[248] Although recent studies have attempted to characterize and understand the actual structure of S/C materials using reactive classical molecular dynamics,[249] this is still a formidable task to be addressed from first-principles calculations such as DFT. Therefore, in this work, we focus only on the interface formed between the active material, *i.e.*, sulfur and the solid electrolyte, and model the electrode using a slab, similar to previous studies[233]. In addition, three cathode surface models are used to represent the

active material at two limiting states of charge corresponding to a fully charged (delithiated: S_8) or discharged (lithiated: Li_2S) Li-S battery. To build the surfaces, we started from the bulk structures of the two limiting case materials. In the charged case, the elemental sulfur was represented by an orthorhombic crystalline sulfur (α-S) structure, whereas the discharged state was considered using a Li_2S crystalline structure; see Table E.2 for details of the bulk optimized lattice parameters. Moreover, van der Waals interactions within the DFT-D3 parametrization[250] were considered for every system containing the cyclo-octa sulfur rings (S_8).

For α-S, previous DFT-based calculations have suggested that multiple facets – where no S-S bonds are broken – exhibit low and similar surface energies. For instance, the surfaces (001) and (100) show the lowest energies: 12 and 11 meV $Å^{-2}$,[233] which are very close to our predicted values of 8 and 9 meV $Å^{-2}$. In both cases, the relative difference in the surface energy between these two facets is within 1 meV $Å^{-2}$. However, Park *et al.*[251] reported the equilibrium shape of α-S based on the Wulff construction and surface energies. They found that 30.3% of the area fraction corresponds to the (001) surface and 23.2% to the (100). Therefore, due to the small differences in surface energy and this previously reported findings, we opted to model the α-S (001) – referred as S-(001) – as a representative surface of the charged cathode material. In the case of Li_2S, two scenarios are considered: the most stable surface (111) – which is more likely to be in abundance – and one that exhibits a large surface energy (001) to account for high reactive areas of the lithiated interfaces. The calculated surfaces energies for Li_2S (001) and (111) are 138 and 20 meV $Å^{-2}$, which are in good agreement with earlier reports: 148 and 23 meV $Å^{-2}$,[11]

respectively. In the case of Li_2S-(111), the simulation cell is hexagonal. However, for simplicity to match with the SSEs interfaces, it was transformed into an orthorhombic cell, see Figure E.7 for details. The geometry optimized slab models are shown in Figure E.8. The S-(001) is formed by 4 layers of cyclo-octa sulfur rings (~25 Å). Regarding the Li_2S (~15 Å), the surface (001) has 6 Li-S stacked layers with one Li- and one S-terminated faces of the slab surface, while the (111) is defined by 5 Li-S-Li sandwich-like stoichiometric layers, resulting in Li species exposed on both sides of the slab. Additionally, the charge difference between atomic species in the slab *vs.* the bulk were computed (see Figure E.9), and remarkably, there is a large charge polarization in the Li_2S-(001) surface, resulting from the rupture of the coordination of the S species at the top of the slab, which are charge-depleted. The depleted charge is localized among the Li and S species at the bottom layer of the slab. This charge localization could result in a reductive/oxidative behavior of the slab towards the SSE interfaces. On the contrary, no significant charge differences are observed for S-(001) and Li_2S-(111) surfaces.

7.3.5. Modeling the S-Cathode/SSE interfaces

Supercells of the surfaces (SSEs and electrode model) were built to minimize the mismatch between the two solid materials; SSE and electrode surface slabs, while keeping the total size of the interface systems at around 300 atoms. Details of the supercells are provided in Table E.3 in Appendix E. New lattice parameters *a* and *b* were then calculated as an average between those of the two solids. In addition, the strains induced along the *a* and *b* directions for each system are tabulated in Table E.4. Although the induced strains were attempted to be kept below 10% in either direction, slightly higher values were

allowed for the interfaces between SSEs and S-(001) due to the size of the S-(001) unit cell model (~10 x 12 Å), which did not allow much flexibility. Once each of the surfaces (with the new lattices) were built and re-optimized independently, they were placed at an equilibrium distance between 2.0 to 2.2 Å in a sandwich-like model were both solid are in contact with each other at the bottom and top of the simulation cell due to periodic boundary conditions along the vertical *c*-axis, yielding a total of 15 interfaces (3 electrodes *vs.* 5 SSE surfaces). These initial structures are referred to as *Initial* hereafter. Subsequently, a full geometry relaxation (no atoms were fixed) of the SSE/S-based electrode systems was carried out (referred as *Opt* or 0 ps). Finally, AIMD simulations were performed at 300 K during 20 ps using the *Opt* geometries as starting configurations. The DFT-optimized interfaces are reported in Figure E.10 to Figure E.12, where some interfacial reactions are already detected and are discussed later. The simulation cell parameters are summarized in Table 7.4.

7.4. Results and Discussion

7.4.1. Work of Adhesion and Interfacial Energy for the S-Cathode/SSE interface

The works of adhesion (W_{adh}) for the fifteen interfaces were calculated as a descriptor of the binding strength between the two solid surfaces according to the following equation[252]:

$$W_{adh} = \frac{E_{SSE-slab} + E_{Cath-slab} - E_{SSE/Cath}}{2A} \quad (7.5)$$

where A is the interfacial area, and $E_{SSE/Cath}$, $E_{SSE\text{-}slab}$, and $E_{Cath\text{-}slab}$ are the energies of the two surfaces in contact (optimized), the SSE slab, and the cathode slab model, respectively. Table 7.4 summarizes the results for the calculated work of adhesion and

shows that all the values are positive, which suggests some degree of affinity between the S-based electrode and these sulfide materials. In addition, for every SSE facet considered, the Li_2S-(001) exhibits the strongest interactions (70 to 107 meV $Å^{-2}$), with the strongest being for the LPSI-(001) among all the SSE facets. Conversely, the interaction between the same LPSI facet and Li_2S-(111) is considerably weaker (10.95 meV $Å^{-2}$). Additionally, the S-(001)/LPSCl-(001) interface displayed the weakest interaction by far among all the systems, 2.86 meV $Å^{-2}$. Overall, the work of adhesion of Li_2S-(111) and S-(001) was found to be substantially lower than those of Li_2S-(001), which could be explained by the higher surface energy and charge localization of the Li- and S-terminated Li_2S-(001) surfaces as discussed in the previous section.

Table 7.4 Simulation lattice parameters, work of adhesion (W_{adh}), and interfacial energy (γ) of the fifteen interfaces considered in this study. *All the simulation cells are orthorhombic, *i.e.*, angle parameters are 90°. Simulations were run using a fine k-point mesh of 2x2x1 in each case.

Cathode	Electrolyte		Lattice Parameters* (Å)			Units – meV $Å^{-2}$	
	SSE	Facet	a	b	c	W_{adh}	γ
S-(001)	**LPS**	(001)	12.841	9.183	47.840	17.47	25.18
		(100)	12.557	9.183	54.180	20.74	42.18
	LPSCl	(001)	10.256	11.434	46.419	2.86	19.07
	LPSI	(001)	9.842	14.124	50.294	26.73	2.68
		(100)	11.001	14.124	45.943	44.19	15.45
Li_2S-(001)	**LPS**	(001)	12.598	8.097	40.192	69.57	88.62
		(100)	12.314	8.097	47.653	72.33	110.63
	LPSCl	(001)	11.191	11.191	38.377	89.69	73.74
	LPSI	(001)	8.757	15.902	42.372	107.23	36.26
		(100)	15.902	11.936	37.886	83.30	90.52
Li_2S-(111)	**LPS**	(001)	12.598	7.556	39.649	9.13	39.37
		(100)	12.314	7.556	47.018	19.85	52.41
	LPSCl	(001)	7.668	14.254	37.608	10.76	11.16
	LPSI	(001)	8.756	14.820	42.085	10.95	25.16
		(100)	14.820	11.935	36.970	30.64	25.16

The S-Cathode/SSE interfacial energy (γ) is defined as the excess energy (per unit area) of a system due to the formation of such interface. In other words, it can be used to evaluate the thermodynamic stability of the interface.[253] The interfacial energy of two solids with lattice mismatch can be expressed as[214]:

$$\gamma_{Cath/SSE} = \frac{E_{Cath/SSE} - n_{Cath}E_{Cath} - n_{SSE}E_{SSE} - E_{str}}{2A} \quad (7.6)$$

where n_i is the number of i units, E_i is the bulk energy of species i, and E_{str} is the strain energy, defined as: $E_{str} = \sum_{i=\text{Cath, SSE}} E^i(a_{str}) - E^i(a_0)$, where $E^i(a_{str})$ and $E^i(a_0)$ are the energies of the strained and pristine slabs of i, respectively. Table 7.4 shows that, contrary to what is observed for Li-metal/sulfide-based solid materials; where $\gamma < 0$ due to the instability of the interface[214, 232], all the interfacial energies for the DFT-optimized cathode-electrolyte interfaces are positive. Among them, the Li_2S-(001)/SSE exhibited the highest interfacial energies, except Li_2S-(001)/LPSI-(001), which contrary to the work of adhesion, its interfacial energy (36.26 meV $Å^{-2}$) is considerably lower than half of the other interfaces considered in this study. Furthermore, the γ was calculated every picosecond over the 20 ps of AIMD simulation, see Figure E.13. It can be observed that the interfacial energy remains almost unchanged after 5 ps. Therefore, a time-averaged γ was calculated over the final 15 ps of the dynamic simulation and reported in Figure 7.1. From this graph, it is evident that there is a dependence of the interfacial energy with respect to the charge state of the electrode. For instance, if any of the SSE materials and facets are considered, the interfacial energy follows this trend: S-(001) < Li_2S-(111) < Li_2S-(001), suggesting better stability for Li_2S, but superior wettability for the charged electrode, S-(001).[254] In addition, if any facet of the sulfide solid electrolytes are compared

at the same cathode model, LPS interfaces exhibit higher interfacial than the lithium halide doped SSE compounds. In contrast, LPSCl-(001) displays the lowest interfacial energy when in contact with S-(001) and Li_2S-(111), whereas LPSI-(001) shows the lowest among the interfaces with Li_2S-(001).

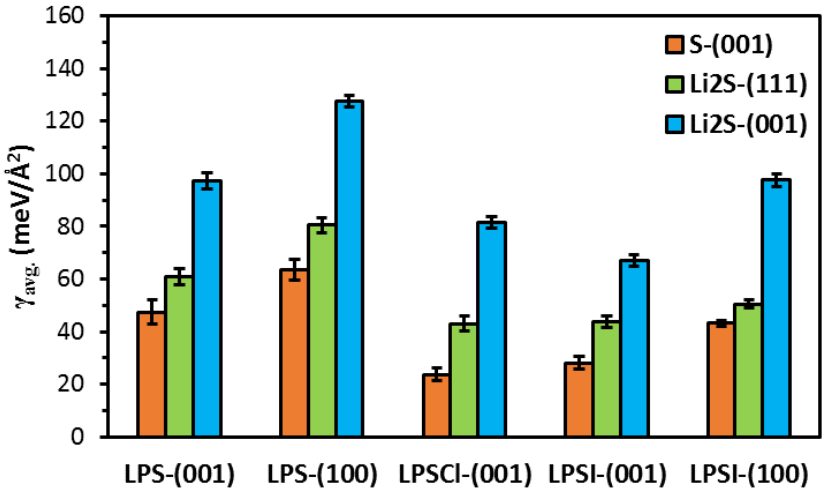

Figure 7.1 Averaged interfacial energies between 5 to 20 ps for the cathode/SSE interfaces. Sampled every picosecond. Error bars show the standard deviation, which is calculated from the energies of the sampled configurations.

7.4.2. Characterization and Structural Evolution of the S-Cathode/SSE Interface

To gain a more detailed understanding of the cathode-electrolyte interlayer structures, radial distribution functions (RDFs) for all the combinations of atomic species between the two solid components were calculated over the 20 ps of AIMD trajectory. Figure E.14 through Figure E.16 display every possible combination of pairs between the electrode and the electrolyte atomic components. The overall RDFs are shown in Figure 7.2(a-c), where the pairs are defined as *all* the atoms forming the cathode and SSE slabs.

Therefore, it will depict the coordination, if any, at the interface of two solids. The S-(001)/LPSI-(001) displays a unique peak around 2.07 Å (due solely to S-S pairs, Figure 7.2d), which coincides with the S-S bond length of elemental sulfur (2.06 Å), as we will see later, this is the result of the bond formed between a S anion from the SSE and a terminal sulfur of an opened S_8 ring at the interface. In addition, all S-(001) interfaces show two characteristic broad peaks below 4.0 Å. The first peak is centered on 2.66 Å and corresponds to the coordination of Li and S atoms from the electrolyte and cathode, respectively. Furthermore, longer-range S—S and S—X (X=Cl or I) coordination pairs contribute to the formation of the second peak, which is located between 3.5 and 4.0 Å.

On the other hand, Li_2S-(001) interfaces exhibit two well-defined peaks below 3 Å. The first peak at ~ 2.1 Å corresponds, again, to the formation of S-S bonds in the interlayer (except for the interface with LPSCl, see Figure 7.2e). The contributions to the second peak (~2.4 Å) are mostly due to Li—S coordination either from Li (cathode) – S (SSE) or Li (SSE) – S (cathode), and S—I and Li—Cl in the case of facets (001) of LPSI and LPSCl, respectively; see Figure 7.2e and Figure E.15. Similarly, the facets (100) of the SSEs and Li_2S-(111) interfaces have the same two peaks corresponding to Li—S and Li—Cl contributions alike. The S—I g(r) does not display a strong interaction for the LPSI electrolytes in this case. Although SSE (001) facets do not show the first peak, the second peak is present. Remarkably in all cases, the second peak seems to have a shoulder at ~ 3.0 Å. In this case, the shoulder peak is attributed to Li—Li and Li—I pairs. This behavior is illustrated in Figure 7.2f, where the RDFs of several atomic pairs for the Li_2S-(111)/LPS-(001) interface are shown. In summary, the S-cathode/SSE interfaces will

mostly be formed by Li—S and S—S interactions, and also Li—X in the case of the lithium halide containing solid electrolytes. In the following subsections, the interfacial models are discussed in more detail and the reaction mechanisms taking place across the two-solid interlayers are characterized.

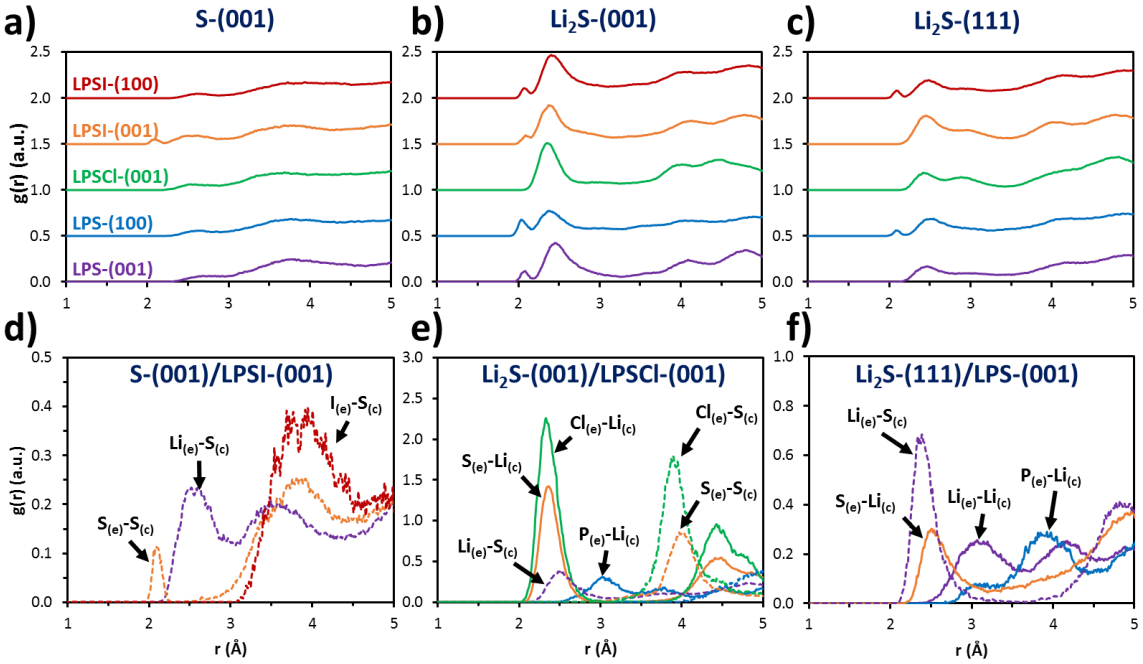

Figure 7.2 (Top) Relative radial distribution functions (RDFs) g(r) for all cathode-electrode pairs: a) S-(001)/SSE; b) Li_2S-(001)/SSE; and c) Li_2S-(111)/SSE interfaces. (Bottom) Illustration of the g(r) of specific pairs for three systems: d) S-(001)/LPSI-(001); Li_2S-(001)/LPSCl-(001); and Li_2S-(111)/LPS-(001). A complete list of RDFs for all possible atomic pairs can be found in Appendix E (Figure E.14 to Figure E.16). (e) and (c) subscripts indicate whether the atom is from the electrolyte or cathode, respectively.

7.4.2.1. S-(001)/SSE Interfaces

The pre-optimized (initial) and final (20 ps) structures of the S-(001)/SSE interfaces are presented in Figure 7.3 and Figure E.17. Although the sulfur rings within the charged cathode model seemed to undergo some structural reorganization, RDFs in Figure E.18 shows that the three main peaks (~2.1, 3.4, and 4.5 Å), concerning the short-

range structural coordination, remained after 20 ps for the interfaces with all five SSE models. In addition, interfaces between LPS-(001) and LPSCl-(001), and the S-(001) electrode did not exhibit any decomposition/recombination reactions across the two-solid interlayers. On the other hand, LPS-(100) and LPSI electrolytes displayed some reactions at the interface, which are highlighted with red dotted ovals. Reaction mechanisms are summarized in Figure E.19 (Appendix E). For instance, three PS_4 anions reacted at the S-(001)/LPS-(100) interface. First, one of them breaks into a tetrahedral PS_3 ($PS_{3(t)}$) and S anions during the optimization of the interface probably due to excess charge available from Li species lacking coordination at the top of the unit cell. Instead, one of the other two PS_4 anions seems to have a depleted charge (-2.11 |e|) at the other side of the slab at the initial configuration, which further oxidizes during the optimization (-1.94 |e|) and finally reacts with one PS_4 anion of the SSE subsurface at 0.4 ps of the AIMD simulation to form the $(PS_4)_2^{4-}$ dimer *via* a S-S bond, which remains stable for the remaining simulation time. Similarly, two of these dimers are also found at the S-(001)/LPSI-(100) interface, following a similar reaction mechanism. In addition, two of the PS_3I^{2-} mixing anions that initially have one P-S bond stretched (2.970 Å) form $PS_{3(t)}^{3-}$ and I^- species. In the case of the S-(001)/LPSI-(001) system, Figure 7.3 shows that two reactions have occurred at the end of the 20 ps. The first reaction is an interfacial reaction between a S_8^0 ring and a S^{2-} from the cathode and SSE, respectively, which takes place during the geometry relaxation to form a S_9^{2-} polysulfide. On the other hand, the second reaction did not occur at the interface, but at the inner region of the LPSI electrolyte at 6.2 ps of the AIMD simulation. Here a PS_4^{3-} and a PS_3I^{2-} chemically reacted among them to form the

$P_2S_7^{4-}$ and iodide (I^-) anions. The $P_2S_7^{4-}$ anion is characteristic of $Li_7P_3S_{11}$, a thiophosphate material with superionic conductivity (4.1 mS cm^{-1} at RT)[196], which has shown promising properties as a solid-state electrolyte for battery applications.

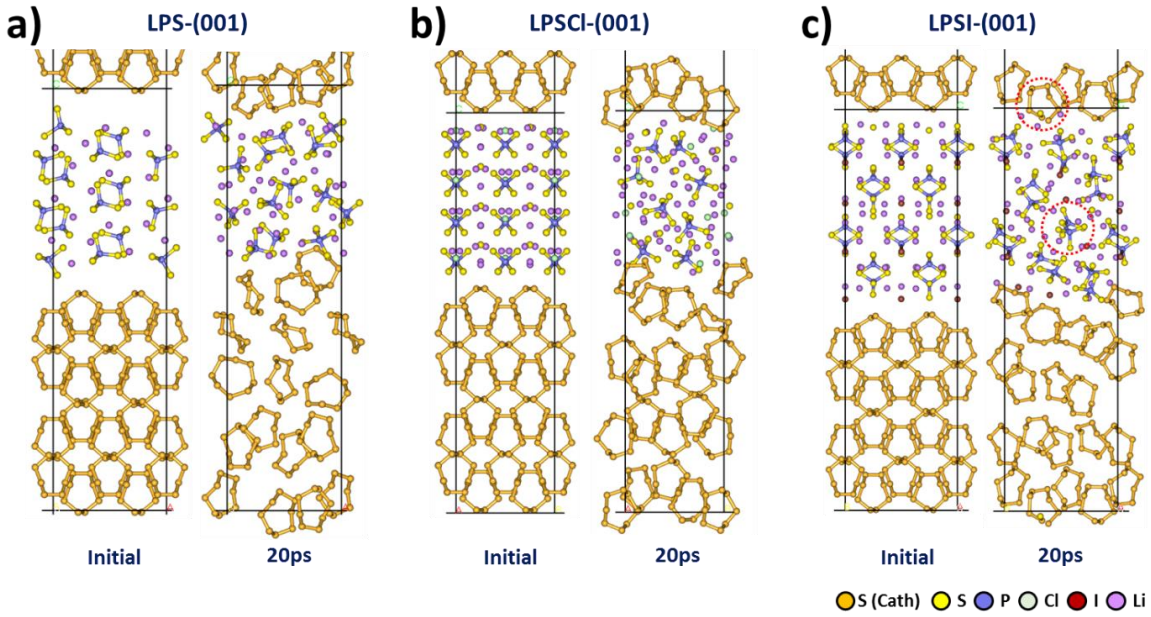

Figure 7.3 Structural changes of selected S-(001)/SSE models after AIMD simulations (20 ps) compared with the initial configuration (not optimized). For a complete list of structures, see Figure E.17. Red dotted ovals indicate places were reactions occurred.

7.4.2.2. Li_2S-(001)/SSE Interfaces

Among the three cathode electrode models considered in this study, the Li_2S-(001) is the most reactive, which could be attributed to the high surface energy of this Li_2S facet making it highly chemically active. The top and middle of the simulation cell in Figure 7.4 and Figure E.20 corresponds to the Li- and S- terminated facets of the Li_2S-(001). Here each one of the interfaces with SSE materials resulted in interfacial reactions, see Figure E.21 for details of these reactions. For instance, in Li_2S-(001)/LPS-(001) interface, the

three PS_4^{3-} anions close to the Li-exposed facet are decomposed and reduced to $PS_{3(t)}^{3-}$ and S^{2-}; two of them during optimization and the other one along the AIMD simulation, the S-anions are deposited on the Li-layer. On the other hand, a PS_4 – on the other side of the LPS slab – combines during the interfacial ground-state relaxation with two charge-depleted S ions (~-1 |e|) from the S-exposed layer to form a $S_3P\text{-}S_3^{3-}$ species, which then forms a bond with another S from the interface *via* one of the sulfurs from the S_3 group and simultaneously breaks into a planar PS_3 ($PS_{3(p)}^-$) and a four-member polysulfide S_4^{2-} during the AIMD simulation (0.39 ps). Furthermore, the Li_2S-(001)/LPS-(100) interface shows similar reactivity; again, the three PS_4^{3-} anions close to the Li-exposed facet reduced to $PS_{3(t)}^{3-}$ and S^{2-}. In this case, however, one of the $PS_{3(t)}$ anions further reduces (1 ps of AIMD simulation) to PS_2 and S^{2-}. On the S-exposed Li_2S surface, two $S_3P\text{-}S_3$ groups are also formed during the interface optimization. Remarkably, one of them splits into $PS_{3(p)}^-$ and S_3^{2-} during the optimization stage and the second one remains stable even after 20 ps of dynamic simulation. Figure 7.4b shows the reduction of two PS_4 groups into two PS_2^{3-} and four S^{2-} at the Li-exposed surface of the Li_2S-(001)/LPSCl-(001) interface. A very crystalline-like layer is formed below the Li-exposed surface with S-anions coming from these reactions, and S^{2-} and Cl^- from the LPSCl. In addition, three charge-depleted sulfur anions on the S-exposed surface are oxidized to form S_3^{2-}. It is noteworthy that, in this particular case, two S_2^{2-} species were already formed at the Li_2S slab due to the depletion of charge of S ions (Figure E.9) and the strain applied to the simulation cell due to the lattice mismatch between the two solids.

Figure 7.4c and Figure E.20b also show the reactivity of both faces of the Li_2S-(001) slab toward the LPSI electrolyte, where most of the reactions take place during the structural relaxation of the interfaces, see Figure E.11 and Figure E.21. For example, the L_2S-(001)/LPSI-(001) interface shows several reactions at both interfaces; at the top (i.e., the Li-exposed Li_2S surface), two PS_4^{3-} and PS_3I^{2-} anions are reduced to $PS_{3(t)}^{3-}/S^{2-}$ and $PS_{3(t)}^{3-}/I^-$ species, respectively. Similarly to the other two SSEs (LPS and LPSCl), PS_4^{3-} thiophosphates combine with sulfur species from the Li_2S surface at the S-exposed interface. In this case, two PS_4 reacted to form S-S bonds with one S each forming two $S_3P\text{-}S_2^{3-}$ anions. Moreover, charge-depleted I and S ions from LPSI and L_2S, respectively, also associate to form two SI^- anions, resulting in a well-interconnected interface. This could be the reason that this system, in particular, showed the strongest work of adhesion (per unit area) among the fifteen interfaces considered in this study (107.23 meV $Å^{-2}$). Finally, the Li_2S-(001)/LPSI-(100) interface also displays the same reactions observed with the other LPSI facet, except the formation of the SI anions. Additionally, a few more reactions were observed in this case, mostly formed during the DFT optimization of the interface. For instance, two PS_2I^- groups decomposed into PS_2^{3-} and I^-; the first one during the relaxation and the other at 2 ps of the AIMD simulation. The latter, then, combines with a PS_4 anion (P-S bond) at 7.3 ps to form a $(S_3P\text{-}S\text{-}P\text{-}S)^{4-}$ species and releasing a S^{2-} anion.

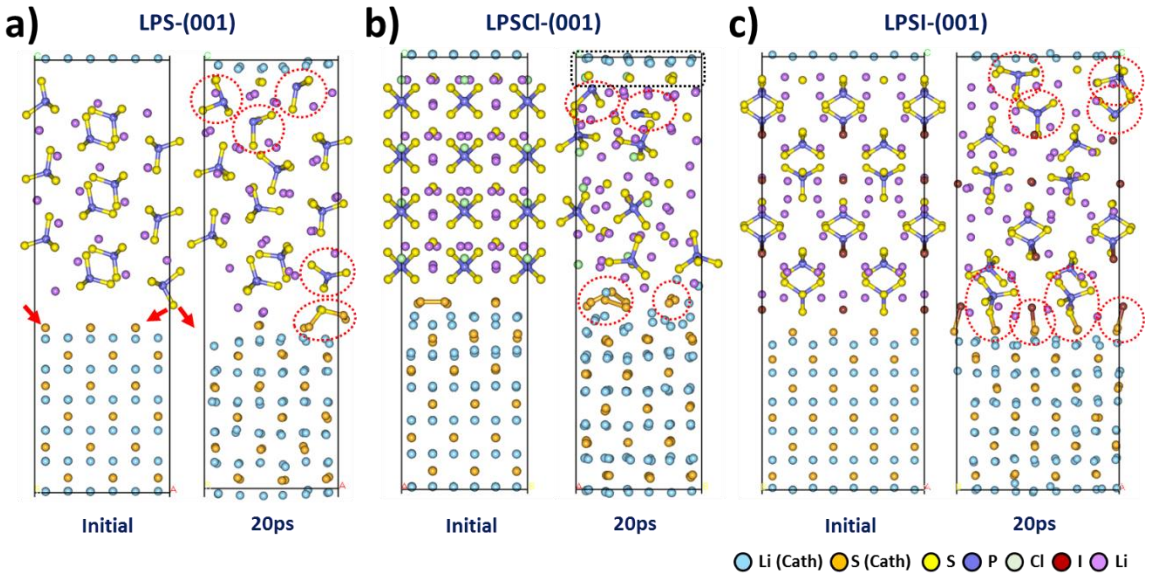

Figure 7.4 Structural changes of selected Li_2S-(001)/SSE interfaces after AIMD simulations (20 ps) compared with the initial configuration (not optimized). For a complete list of structures, see Figure E.20. Red dotted ovals indicate places were reactions occurred.

7.4.2.3. Li_2S-(111)/SSE Interfaces

Although the Li_2S-(111) electrode facet is not as chemically active as the Li_2S-(001), similar reactions could still be expected at different extent, as could be evidenced in Figure 7.5. The Li_2S-(111) facet is formed by fully coordinated S-anions within the Li-S-Li tri-layers, which decreases the surface reactivity. A complete description and evolution of the reactions can be found in Figure E.23 of Appendix E. In fact, LPS-(001), LPSCl-(001), LPSI-(001) did not display any chemical changes of their anions at the interfaces when they come into contact with Li_2S-(111), see Figure 7.5a and b. In the case of the Li_2S-(111)/LPSI-(001) interface, however, the P-I bond, from one of the PS_3I^{2-} anions in the LPSI subsurface, is stretched leading to the formation of a $PS_{3(p)}^{-}$ and a charge-depleted iodide anion (-0.50 |e|) during the AIMD simulation. Likewise, the Li_2S-(111)/LPSI-(100) system (Figure E.22b) also displays two similar reactions, but, in this

case, the iodide species were fully reduced to the expected Bader charge of ~ -0.85 |e| along the DFT-optimization. In addition, two of the PS_3I^{2-} mixing anions (with one P-S bond stretched at 3 Å) form $PS3_{(t)}^{3-}$ and I^- species during the interface relaxation, analogous to the behavior of this facet when it was in contact with the charged electrode, *i.e.*, S-(001). Finally, two PS_4 anions with charge depletion from the lack of coordination at the surface with their Li-ions binds with S^{2-} species from the discharged electrode, resulting in $S_3P\text{-}S_2^{3-}$ anions, which have been observed across other Li_2S/SSE interfaces in the previous subsections. As shown in Figure E.22a, the same reaction takes place at the Li_2S-(111)/LPS-(100) interface. In addition, one PS_4^{3-} with some excess charge (-3.25 |e|) breaks into $PS_{3(t)}^{3-}$ and S^{2-} at the other surface-surface region formed at the top of this electrode-electrolyte model.

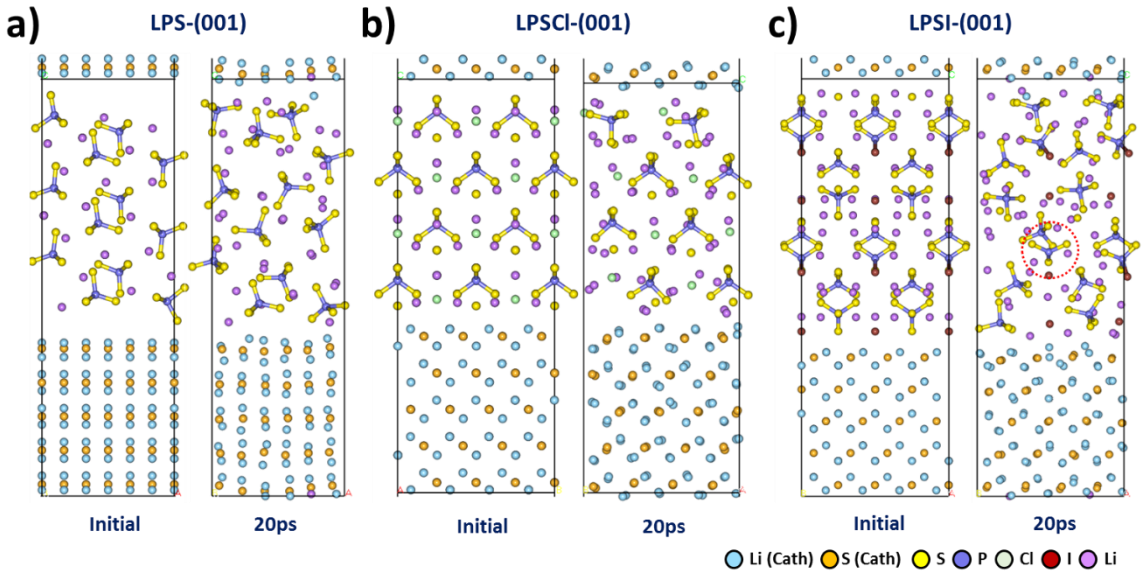

Figure 7.5 Structural changes of selected Li_2S-(001)/SSE interfaces after AIMD simulations (20 ps) compared with the initial configuration (not optimized). For a complete list of structures, see Figure E.22. Red dotted oval indicates places were reactions occurred.

7.4.2.4. Summary of Reactions

It is well-known that the decomposition and degradation of the SSE may have a negative effect on electrode charge transfer resistance and cell impedance.[255] Thus, the main electro-/chemical reactions taking place at the cathode/SSE interface are summarized in Figure 7.6a to provide some clear insights on the SSE degradation. In reaction (1), where the PS_4^{3-} thiophosphate is reduced to $PS_{3(t)}^{3-}$ or PS_2^{3-} and S^{2-} anions, is one of the most common electrochemical reactions that were found in this study. Although this reaction is characteristic during the reduction of the sulfide SSEs with Li metal,[232] previously reported XPS observations of Li_6PS_5Cl-C electrodes have also shown that S and P species can undergo reduction during the discharge process of the battery.[255] Reaction (2) describes the oxidation reactions between a PS_4^{3-} and sulfur (S_n) anions from the cathode/SSE interfaces, resulting in the formation of $S_3P\text{-}S_{n+1}^{3-}$ or PS_{4+n}^{3-}. Remarkably, Nagai *et al.*[256] recently reported XPS and Raman spectra of sulfide SSE-electrode interfaces, showing evidence of S-S bonds, which were assigned to the formation of $(PS_{4+n})^{3-}$ anions. Such S-S bonds are formed during the delithiation of the cathode composite. This anion is very similar to polysulfidophosphates P_2S_{5+x} found during the discharge of sulfide-based all-solid-state batteries.[257] In the case of the interfaces of this study, these anions were found to further react to form planar $PS_{3(p)}^{-}$ anions and polysulfides such as S_3^{2-} and S_4^{2-}.

It has been suggested that one plausible degradation mechanism for sulfide-based SSEs could start with the polymerization or oligomerization of the anions, which could lead to the formation of anions with the $P\text{-}[S]_n\text{-}P$ group. This mechanism has been

confirmed by XPS, NMR and UV-VIS spectroscopy analyses of $Li_{10}SnP_2S_{12}$ interfaces.[258] Our predicted reaction mechanisms – see reactions (2), (7.2), and (8) – are in excellent agreement with these findings. The formation of $(S_3P\text{-}S\text{-}S\text{-}PS_3)^{4-}$, in particular, which results from the S-S bridged PS_4^{3-} anions has been proposed as a product or intermediate of the oxidation of sulfide SSEs. Based on *in situ* XPS measurements[259], this anion could also undergo a disproportionation reaction to form the $P_2S_7^{4-}$ anion and S^0. If the oxidation persists, the $P_2S_7^{4-}$ can then be oxidized to $P_2S_6^{2-}$ and S^0. Additionally, two PS_4^{3-} tetrahedrons could alternatively reduce to $P_2S_7^{4-}$ and S^{2-}.

Reactions (4) and (5) in Figure 7.6 show the formation of additional polysulfide species. It has also been reported that Li_3PS_4 can open the sulfur ring to form lithium polysulfidophosphates.[260] However, in this case, it was a S^{2-} from LPSI that led to the opening of the ring to form the S_9^{2-} polysulfide chain, which could be the initial stage of the a $^{-}S\text{-}[S^0]_n\text{-}S^{-}$ oligomer chain. Reaction (5) shows the association of charge-depleted sulfur anions at the interface of Li_2S-(001), leading to the formation of short polysulfide chains (S_2^{2-} and S_3^{2-}) at the cathode/SSE interface. The iodide-based reactions are shown in reactions (6) through (9), where the P-I is found to be the weakest bond of the PS_3I^{2-} mixing anion. In addition, S and I species at the interface can also oxidize to form SI^{-}. Furthermore, Figure 7.6b shows both sides of Li_2S-(001)/LPSCl-(001) as an illustration of the interfacial phenomena occurring at the cathode-electrolyte interlayer. As discussed in the previous subsection, the LPSCl is reduced on the Li-exposed surface of Li_2S. On the other hand, the S anions at the S-exposed Li_2S surface are oxidized to polysulfide species. Finally, an interesting observation can be made from these results, that is, the

sulfide-based SSE can act as active material in conjunction with sulfur, which allows us to provide a clear explanation for reported specific capacities above the theoretical value of the S-cathode in all-solid-state Li-S batteries.[28]

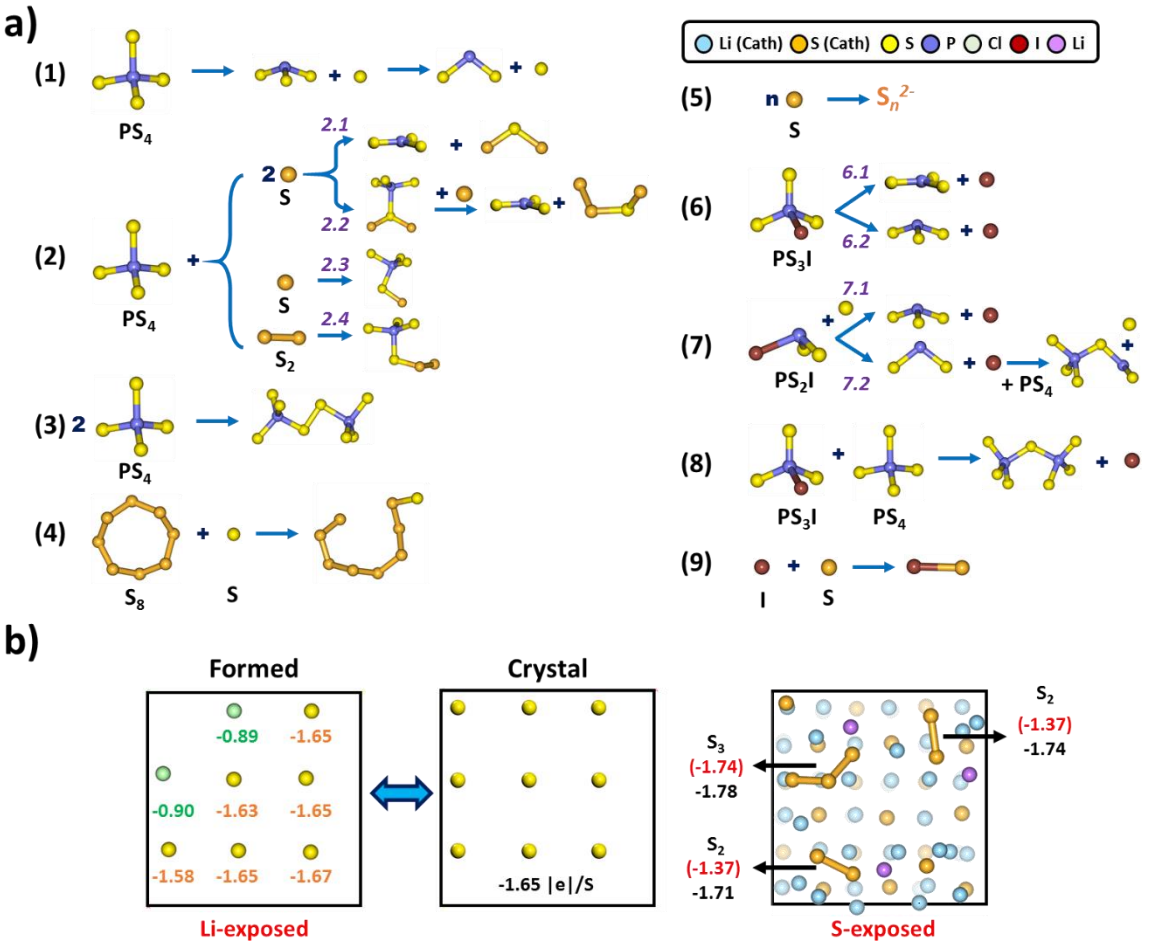

Figure 7.6 a) Summary of anions reaction mechanisms predicted from DFT ground-state optimizations and AIMD simulations; b) Final structural configuration of the interfaces of Li_2S-(001)/LPSCl-(001): (left) Formation of a mixed Cl^- and S^{2-} anion layer on the Li-exposed surface of Li_2S-(001) compared with the S-layer of the crystalline Li_2S (001) facet; (right) Formation of S_x^{2-} polysulfides due to the oxidation of the S-exposed surface of Li_2S-(001). Numbers (numbers in parenthesis and in red) indicate the net charge (in |e|) of the species after the AIMD simulation (DFT optimization of the interface).

In this section, the reactions taking place at the cathode-electrode interfaces were characterized in detail, and although good agreement was found with available literature, it is worth mentioning that two pieces were not considered in this study and should be incorporated in future studies for a better description of the interface model: (1) intermediate states of charge (lithiation) to mimic the charge/discharge process; and (2) the presence of carbon composites, which could modify the interfacial reactions due to the reactive carbon atoms at the edges of the carbonaceous structures.

7.4.3. Charge Analysis

In the previous section, the reaction mechanisms that could take place at the interface of a S-based cathode and sulfide solid electrolytes were discussed. It is clear that many of the reactions occurred during the DFT ground-state structural relaxation of the interface. Therefore, to further explore the behavior of these interfaces, a comparative analysis between the net charges associated to the SSE materials was performed at the initial, optimized (0 ps), and a post-AIMD simulations (20 ps). Figure E.24 (Appendix E) shows that, indeed, for most of the studied interfaces (11 out of 15), a large fraction (at least 65%) of the total charge transferred between the two solids during the interface formation relaxation, which agrees with the extent of reactions happening at this stage. Therefore, these results suggest low charge transfer during the dynamics simulation, which is corroborated by the SSE charge time-evolution along the 20 ps of AIMD simulations for all the interfaces, see Figure E.25. In every case, the SSE charge seems to remain around a constant value after 5 ps. Consequently, the time-averaged SSEs charges (per unit area) were calculated and are presented in Figure 7.7. We can split the plot into

two parts; the first part corresponds to interfaces formed between a fully charged S-cathode (in yellow) and the sulfide solid electrolytes and the second part, where the two facets of Li_2S are shown in light pink. Interestingly, it can be inferred that the sulfide SSEs will partially be oxidized when in contact with the pristine sulfur nanoparticles of the S-cathode. Additionally, the electrolytes could be reduced during the lithiation process of the cathode, *i.e.*, discharge, since the formation of any interface with either of the Li_2S facets yields an electron-transfer from the cathode to the electrolytes. However, the extent of reduction depends on the reactivity of the exposed lithiated facet: Li_2S-(001) > Li_2S-(111).

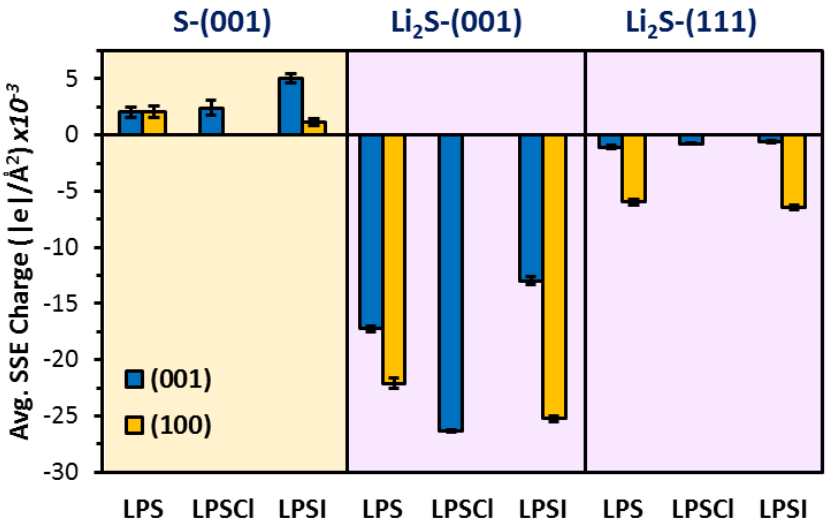

Figure 7.7 Time-averaged (from 5 to 20 ps of the AIMD simulations) of the net charge (per unit of area) of the SSEs due to the formation of the interface with the three S-cathode models. The charges were sampled every picosecond. Error bars show the standard deviation obtained from the charge transferred calculated at each sampled configuration.

In order to provide additional insights on the charge redistribution due to the formation of the cathode-electrolyte interface, the average charges of atomic species in

the SSE materials, before (SSE slab in vacuum) and after the interfaces were built (20 ps), were computed (Figure E.26). Based on these results, the relative charge changes of SSE atomic species for all the interfaces were obtained and are plotted in Figure 7.8. Overall, no significant charge differences are observed (less than ±2%) for Li species (in SSE). Moreover, S atoms are slightly oxidized for S-(001)/SSE interfaces; however, they are partially reduced when the interfaces with Li_2S are formed. This could be mostly related to the PS_4^{3-} reduction to $PS_{3(t)}^{3-}$ and S^{2-}. Phosphorus atoms are, in every case, one of the species that changed the most charge relative to other species within the same electrode-electrolyte system. Such behavior can be attributed to the P-I and P-S bond cleavages in PS_3I and PS_4 anions, respectively, which resulted in the formation of new anions such as PS_2, $PS_{3(t)}$, and $PS_{3(p)}$. Similar to the case of S atoms, the Li_2S-(001)/SSE interfaces led to a significant extent of reduction of the P atoms (larger than 10%). Regarding the halide species, there is no considerable change in the charge of the chloride anions, which agrees with the unchanged Cl 2p XPS signal obtained from the study of interfaces in a Li-In | LPSCl | NMC/LPSCl battery cell, suggesting no evident ongoing reactions involving Cl species during cycling.[261] In contrast, iodides exhibited the most reduction (relative change) among the components of the SSE after 20 ps of AIMD simulation in every case except Li_2S-(001)/LPSI-(001) where S-I bonds are formed at the interface, resulting in the oxidation of I and S atoms to form SI^-. In the other systems, the greater extent of reduction observed is a consequence of the change of iodine bond character (from covalent- to ionic-like) in the reduction of the PS_xI anion to PS_x and iodide (I^-) anions. Regarding the cathode materials, the gained charge is expected to be localized at both surfaces of the S-(001)

slab. In the case of the Li_2S electrodes (Figure E.27), S species are oxidized (~ 2-3% in most cases), whereas changes in charge of Li species in Li_2S-(111) are minimal, however, they are more prominent in the (001) facet.

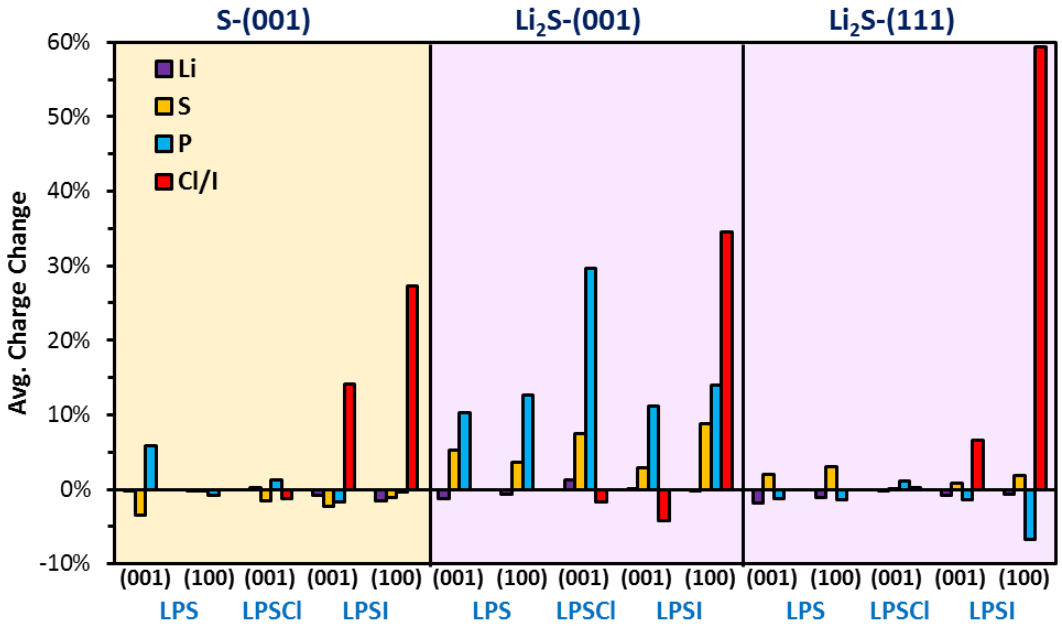

Figure 7.8 Relative charge change of the SSEs atomic components at 20 ps of AIMD simulations with respect to their charge in the (strained) DFT-optimized slab. Positive percentages mean that the species gained electrons (more negative charge), and the opposite if they are negative.

7.4.4. Comments on the LPSI Crystalline Structure and Consistency Analysis

7.4.4.1. LPSI

As it has been discussed in the previous sections, the mixing anion PS_3I^{2-} tends to dissociate into PS_3 and iodide anions. If the P-I bond cleavages are checked at the 20 ps of AIMD simulation (at 300 K), at least 25% of these bonds in the (001) facets are broken, and the percentage increases for the (100) facet; at least 50%, see Figure E.28. To provide some additional insights into the structural stability of the crystal phase of LPSI used in

this work, which was obtained from a XRD and DFT-based approach in a previous study[221], a 2x2x1 supercell was run during 50 ps of AIMD simulation using a *NVT* ensemble at 300 K (1 fs of time step), surprisingly, 50% of the P-I bonds were broken, resulting in the formation of two $PS_{3(p)}^-$ and I^- anions, similarly to what was observed for some interfaces, the $PS_{3(p)}^-$ could later combine with another PS_4^{3-} to form $P_2S_7^{4-}$ as seen in the LPSI-(001)/S-(001) interface. Hence, it might be possible that a mixture of crystalline phases is present for LPSI electrolytes with this stoichiometry. Therefore, more efforts on the characterization of the full crystalline structure of this promising electrolyte are needed to generate more accurate models in the future.

Inspired by the structural changes of LPSI observed from high-temperature AIMD simulation of the bulk, an AIMD simulation of the unit cell was run during 100 ps at 600 K. Remarkably, the structure obtained contains the $P_2S_7^{4-}$ group above mentioned and iodide, see Figure E.29a. All the atoms within the structure were then tightly relaxed using DFT ground-state optimization. The total energy of the resulting structure (Figure E.29b) is lower by 0.29 eV/unit than the previously reported configuration. In addition, the new structure has a wider electronic band gap (predicted with the HSE06 functional) of 3.69 eV compared to the 2.54 eV of the reported configuration, which results from the lack of the anion mixing PS_3I^{2-} that created new states at the conduction band, see Figure E.29c. This could have positive consequences when modeling the electrochemical stability window of this material. Finally, it is important to mention that this new structure obtained from high-temperature AIMD simulation may not be the most stable crystalline structure of the $Li_7P_2S_8I$ electrolyte. The simulations carried out in this subsection are for

comparative purposes only and further research still needs to be done in order to generate a more accurate representation of the crystallographic parameters of this solid electrolyte.

7.4.4.2. Consistency Analysis

In order to test the validity of the results of the interfaces at longer simulation times, the S-(001)/LPSI-(001), Li_2S-(001)/LPSCl-(001), and Li_2S-(111)/LPS-(001) interfaces were run during an additional time of 30 ps of AIMD, resulting in a total simulation time of 50 ps. With regards to the reactivity of the interfaces (not shown), no additional reactions are observed after 50 ps. In the case of the S-(001)/LPSI-(001) interface, the $P_2S_7^{4-}$ and S_9^{2-} anions formed earlier remained stable. In addition, same happened for the S_3^{2-} and PS_2^{3-} species at the Li_2S-(001)/LPSCl-(001) system. Moreover, the two interfaces shown in Figure 7.6b are still present at the end of the simulation. Similarly to what was observed up to 20 ps, no recombination or decomposition reactions took place after running the Li_2S-(111)/LPS-(001) interface for 50 ps. Figure E.30 shows the interfacial energy and charge transfer evolution over the 50 ps. It is found that both properties remain almost unchanged after 20 ps. These findings suggest that our 20 ps-simulations are consistent with longer times and provide enough description of the earlier stages of interface formation at the cathode of Li-S batteries.

7.5. Conclusions

We used DFT ground-state optimizations and AIMD simulations to study the initial stages of the interface formation between sulfide-based SSE and the S-cathode. All the interfaces showed some degree of affinity between the electrode and electrolyte as shown by the work of adhesion. Despite the SSE material, the interfacial energy exhibited

positive value and followed this trend: S-(001) < Li_2S-(111) < Li_2S-(001), which was correlated with the reactivity of the cathode surfaces. The interfaces were found to be rather stable during the AIMD simulations; nonetheless, several interfacial reactions took place during the DFT-optimization. All the reactions were fully characterized. It was found that $PS_{4(t)}$ typically reduces to PS_3^{3-} and S^{2-}. In addition, the PS_4^{3-} tetrahedron can also react with S or other thiophosphate anions to form polysulfidophosphate-type anions $(PS_{4+n})^{3-}$ or P-$[S]_n$-P-type oligomers, respectively. Moreover, polysulfide chains were also identified as an important part of the formation of the interfaces. Finally, charge transfer analysis showed that a charged electrode, S-(001), could partially oxidize the SSE. In contrast, Li_2S could lead to the reduction of the solid electrolyte material.

In summary, this study provides new insights on the cathode-solid electrolyte interfacial behavior at two limiting stages of the Li-S battery operation. The fundamental understanding of these interfaces is critical in order to overcome the interfacial challenges facing this battery technology. In addition, we also show the potential of using computational tools such as DFT-based methods to accelerate the understanding and design of the next generation of battery materials.

8. CONCLUSIONS AND RECOMMENDATIONS

One of the effective mechanisms that has been proposed – and, in some cases, proven – over the last decades to control the reactivity of battery anode materials is by tailoring the properties of the solid-electrolyte *interphase* – which is formed due to a set of redox, decomposition, recombination, and substitution reactions of electrolyte components with the solid electrode. Therefore, the properties and composition of this interfacial layer will depend on the formulation of the electrolyte. In Li-S batteries, for example, the lithium metal anode is highly reactive, which leads to an uncontrolled SEI formation. Typically, the SEI layer is chemically and topologically non-uniform which may exacerbate the nucleation of dendritic lithium and increase the resistance to Li-ion diffusion. In addition, there are many knowledge gaps with respect to the mechanism of electrolyte degradation and subsequent SEI formation. Thus, the present study was set out to elucidate how the nature and composition of the electrolyte affect the nascent SEI as well as other interfacial phenomena in Li-S batteries.

In presence of the Li-metal surface, the LiTFSI salt was found much more reactive than typical solvents such as DOL and DME. Cleavage of the C–S or N–S bond is predicted to be the most thermodynamically favorable starting point for all of the LiTFSI reduction pathways. The salt is reduced into multiple fragments, where LiF is one of the most important decomposition products. In addition, other charged radical anions are derived from CF_x, SO_2, O, and CSN fragments that mostly become adsorbed onto the metal surface. At this time-scale, neither DOL nor DME decomposition is not observed,

whereas EC is reduced very quickly *via* sequential 4- or 2-electron mechanisms. Furthermore, the Li_2S_8 polysulfide fragmentation is found to be thermodynamically driven by the presence of Li^0 species. Long-chain PS species are highly decomposed despite the solvent used or the PS initial geometry (ring or linear), resulting in the formation of a deposited Li_2S layer on the anode surface. *In situ* XPS measurements confirm the formation of Li_2S, LiF, and CF_x components due to the reduction of PS and TFSI-anion. Finally, a SEI layer evolution mechanism was proposed by combining XPS imaging and AIMD analysis. Here three major stages are present: (*i*) formation of a primary composite mixture phase involving stable lithium compounds (Li_2S, LiF, Li_2O, etc.), (*ii*) formation of a secondary matrix-type phase (cross-interaction between reaction products), and (*iii*) adsorption of a highly dynamic mono-anionic polysulfide (i.e., LiS_5), which acts as precursor of a continuous fouling process.

At the anode-electrolyte interface, the decomposition pathways of LiFSI and LiTFSI salts at the Li anode differ substantially and are also a function of their *concentration*. LiTFSI undergoes less complete reduction (larger fragments), it also facilitates more charge transfer from the Li surface due to the reduction of C-based constituents from the salt. LiFSI, on the other hand, shows a more complete decomposition and is found to be extremely efficient in LiF formation *via* S-F bond scission. The rupture of S-F bonds in LiFSI is a highly thermodynamically favorable reaction in presence of Li^0. In the bulk electrolyte, both 1M and 4M salt solutions are stable. It was found that even in the presence of an excess of Li ions, the high concentration salts still partially dissociate. However, the excess of Li ions induces the formation of highly complex coordinated

networks even in 1M solutions. One key observation is that *trans* salt structures dominate the 1M solutions, whereas *cis* structures are observed in the 4M concentration. This structural change may also affect the structure of the complex solvation networks. Regardless of the type of salt or concentration, the first solvation shell of Li^+ (1.9-2Å) is always well-defined by a (3 or 4-fold) coordination with O atoms from DME and the salts. On the other hand, F atoms define a clear second shell around Li ions in LiFSI solutions independent of concentration, whereas only a broader peak of F atoms is observed for LiTFSI.

Up to this point, no solvent (DME) decomposition had been observed from our AIMD simulations. In contrast, under electron-rich environments (with no slab), DME molecules (in pure solvent) are reduced when the number of excess electrons in the cell is equal or larger to an average charge of -0.9 |e| per surrounding DME molecule. It decomposes following a 4-electron mechanism *via* double C_m–O bond cleavage leading to the formation of CH_3O^- and $C_2H_4^{2-}$. Interestingly, the $C_2H_4^{2-}$ anion might also assist in the reduction of a different DME molecule to produce $(C_2H_4)_2^{2-}$ oligomers. In 1M salt solutions – similarly to our studies in Chapters 3 and 4, where the electrolytes were exposed to the Li anode with no external charge – the LiFSI and LiTFSI salts are very prone to decomposition in any system with excess electrons. The LiFSI was found to start the reduction pathway with an S–F or S–N bond scission, whereas S–C or S–N bond cleavages were identified to initiate the decomposition mechanism of the LiTFSI salt. Some of the most commonly detected fragments from salt decomposition are $N(SO_2)_2$, CF_3SO_2, CF_xSO_2N, CF_x, SO_2, LiF_x, F^-, NSO_x, OSC, CO, and O. Remarkably, the presence

of charged radical anions such as CSO_2N^{3-}, O^{2-}, and NSO_2^{3-} were found to trigger DME dehydrogenation from either the ethane or methoxy groups. Finally, the C_m–O and C_t–O bond cleavages of DME are predicted to be thermodynamically favorable under double Li-radical attack. However, C_m–O bond dissociation is more favorable and will probably occur faster due to a lower activation barrier. In addition, DME dehydrogenation from salt fragment attack was also found to be thermodynamically possible being slightly more favorable the removal of a hydrogen from the methoxy groups.

Chapters 3 to 5 were focused on understanding the liquid-solid interfaces that are formed from using organic-based electrolytes. In the following chapters, we turned our attention to sulfide-based solid-state electrolytes. In general, the SSE-Li interface was found to be, as expected, very unstable and SEI is comprised by multiple solid phases such as Li_2S, Li_3P, $Li_{17}Ge_4$, transient Ge- and P-based compounds, and possibly some polyphosphide constituents. The compounds that are formed at the interface are likely to increase the ionic transport resistance. In addition, the effect of the nascent solid phases on the reactivity of Li metal was considered by incorporating a Li_2S thin film (< 1 nm) at the SSE-Li interfaces of systems with some of the worst stabilities. Remarkably, a strong passivation effect was found at the interface due to the presence of such a film.

Due to the interconnected chemistry in Li-S batteries, using SSE materials inherently brings several challenges regarding the solid-solid interfaces at both electrodes. Therefore, the formation of SSE and S-cathode interfaces were investigated in Chapter 7. The work of adhesion between the electrode and electrolyte showed that all interfaces exhibited some degree of affinity. Regardless of the SSE material used, the interfacial

energy exhibited positive value and followed this trend: S-(001) < Li_2S-(111) < Li_2S-(001), which was correlated with the reactivity of the cathode surfaces. Although the interfaces were found to be rather stable (compared to the Li electrode), several interfacial reactions still took place. It was found that $PS_{4(t)}$ can: (*i*) be reduced to PS_3^{3-} and S^{2-}, or (*ii*) react with S or other thiophosphate anions to form polysulfidophosphate-type anions $(PS_{4+n})^{3-}$ or P-$[S]_n$-P-type oligomers, respectively. Although PS species are commonly observed in Li-S batteries with liquid electrolytes, polysulfide chains were also identified as a vital part of the formation of the solid-solid interfaces. Finally, the fully charged electrode (S) could partially oxidize the SSE, whereas the completely discharged electrode (Li_2S) could lead to the reduction of the solid electrolyte material.

By using quantum mechanics based methods, here we provided a fundamental and molecular-level description of electrochemical phenomena governing the electrode-electrolyte interfaces. Such a comprehensive understanding is critical to better engineer electrolyte materials and formulations and, hence, SEI layers to control the reactivity of lithium metal. Moreover, this study also shows the potential of using computational tools such as DFT-based methods to accelerate the understanding and design of next-generation battery materials.

Finally, considering the new insights presented in this dissertation, a few aspects still need to be addressed in the future in order to provide a more accurate and complete description of the SEI formation in Li-S batteries. Some specific points to guide future work are outlined as follows:

- In a battery, an electric field is formed in the cell due to the external potential that is applied when cycling. The electric field is, to some extent, responsible for the migration of Li-ions from one electrode to the other. However, current implementations of DFT-based methods are not very efficient incorporating the effect of the electric field and other biased potentials. Therefore, in none of the simulations presented in this dissertation the effect of biased potentials is explicitly introduced. Instead, in most cases, the reactivity of the systems was treated with the inherent potentials of the electrode interfaces. Hence, it is recommended the development of new or more efficient ways to incorporate external potentials (e.g., electric fields, constant electrochemical potentials, electrified interfaces, etc.) into the dynamic simulation of the cells in order to provide a more complete description of the electrolyte decomposition and SEI formation under applied biases.
- It is clear that the development of a comprehensive understanding of complex electrochemical systems such as the formation of the SEI layer studied in this work would require joint efforts from computational modeling and experimental techniques. In Chapter 3, for example, the reaction mechanisms of some electrolyte components and the SEI layer evolution for a model system were elucidated by using a combined approach including DFT-based methods and *in situ* XPS. Thus, the development of *in situ* experimental techniques and advanced methods is critical. More importantly, future studies should use this combined approach not only for validation of either side but as a synergistic framework to accelerate the understanding and discovery of materials for next-generation batteries.

- In this dissertation, the lithium metal anode was modeled as a perfect crystal with its most stable facet exposed to the electrolyte. However, grain boundaries with different facets should also be considered as part of the model since they might be present in real anode surfaces. For instance, grain boundaries could serve as hot spots of reactivity, resulting in a less homogeneous formation of the SEI layer.
- As suggested by the SEI evolution model proposed in Chapter 3, some SEI components such as Li_2S, Li_2O, and LiF will nucleate in the presence of abundant lithium. Therefore, a detailed study of the nucleation process of SEI components is recommended. Here a multiscale approach combining DFT-based and reactive classical molecular dynamics simulations could be used to explore how the nascent fragments of electrolyte decomposition agglomerate to form well-defined phases. This task would also imply the further development of reactive force fields (e.g., ReaxFF) to provide a more precise picture of the chemically and structurally evolving interfaces.
- Throughout this dissertation, new insights on the decomposition products and the structure of the nascent SEI layer were provided. Therefore, this information could be used to build SEI models to evaluate not only their effect on passivating the reactivity of different facets of the lithium anode but also to study the transport kinetics of Li-ions through them. For instance, block-type SEI models (thin films) of multiple constituents (e.g., Li_2S, LiF, and Li_2O in liquid electrolyte; or Li_3P, Li_2S, and LiGe-alloys in sulfide SSEs) could be studied considering both single crystals and ground boundaries between facets of the same or different SEI components.

- Following the previous idea, the effect of different SEI components (e.g., Li_3N, Li_2S, LiF, and Li_2O) and structures (e.g., well-defined deposited phases, matrix-type complexes, and composite boundaries) on the dynamic process of Li deposition is also a key point to be investigated due to the non-uniform plating of Li, leading to the formation of dendrites. Here a dual computational approach could be used, in which DFT-based calculations are used to provide parameters for a kinetic Monte Carlo model.[262] The use of the latter would allow the exploration of longer simulation times. In addition to computational modeling, this task will also require the use of advanced *in situ* microscopic techniques such as *operando*/*in situ* cryogenic electron microscopy (cryo-EM)[263].
- In Chapter 5, the effect of electron-rich environments on the decomposition of electrolyte constituents was considered using a slab-free cell model. Therefore, future studies should include the Li metal slab since the presence of the surface may modify the structure of the electrical double layer and, in addition, it may allow the electron transfer to be more localized, which could lead to alternative decomposition pathways.
- Carbon-based frameworks play a critical role in the S-cathode, especially in regards of the electric conductivity and retention of polysulfide species; however, carbon was excluded from the analyses of cathode-SSE interfacial phenomena that are presented in Chapter 7. It is possible that – in addition to the reactions observed in this study – alternative interfacial reactions and interactions involving unsaturated carbons are present. Thus, models of the S-based cathode including a carbonaceous structure are recommended in future investigations.

- Finally, although combining computational physical chemistry methods and experiments is crucial to improve materials for energy storage such as Li-S batteries. Developing model systems that would permit the gathering of important battery descriptors – e.g., electrochemical performance, electrolyte stability, redox potentials, and interfacial resistance – could be quite beneficial to achieve battery improvements. These descriptors could then be used in machine learning algorithms to accelerate the screening and understanding of new materials or devise ways for future development.

REFERENCES

1. Sharon, D.; Salama, M.; Attias, R.; Aurbach, D., Electrolyte Solutions for "Beyond Li-Ion Batteries": Li-S, Li-O2, and Mg Batteries. *The Electrochemical Society Interface* **2019,** *28* (2), 71-77.

2. Thackeray, M. M.; Wolverton, C.; Isaacs, E. D., Electrical energy storage for transportation-approaching the limits of, and going beyond, lithium-ion batteries. *Energy & Environmental Science* **2012,** *5* (7), 7854-7863.

3. Tarascon, J. M.; Armand, M., Issues and challenges facing rechargeable lithium batteries. *Nature* **2001,** *414* (6861), 359-367.

4. Lv, D.; Zheng, J.; Li, Q.; Xie, X.; Ferrara, S.; Nie, Z.; Mehdi, L. B.; Browning, N. D.; Zhang, J.-G.; Graff, G. L.; Liu, J.; Xiao, J., High Energy Density Lithium–Sulfur Batteries: Challenges of Thick Sulfur Cathodes. *Advanced Energy Materials* **2015,** *5* (16), 1402290.

5. Bruce, P. G.; Freunberger, S. A.; Hardwick, L. J.; Tarascon, J.-M., Li-O2 and Li-S batteries with high energy storage. *Nature Materials* **2012,** *11* (1), 19-29.

6. Manthiram, A.; Fu, Y.; Su, Y.-S., Challenges and Prospects of Lithium–Sulfur Batteries. *Accounts of Chemical Research* **2013,** *46* (5), 1125-1134.

7. Scheers, J.; Fantini, S.; Johansson, P., A review of electrolytes for lithium-sulphur batteries. *Journal of Power Sources* **2014,** *255*, 204-218.

8. Cuisinier, M.; Cabelguen, P.-E.; Evers, S.; He, G.; Kolbeck, M.; Garsuch, A.; Bolin, T.; Balasubramanian, M.; Nazar, L. F., Sulfur Speciation in Li-S Batteries Determined by Operando X-ray Absorption Spectroscopy. *The Journal of Physical Chemistry Letters* **2013,** *4* (19), 3227-3232.

9. Weng, W.; Pol, V. G.; Amine, K., Ultrasound Assisted Design of Sulfur/Carbon Cathodes with Partially Fluorinated Ether Electrolytes for Highly Efficient Li/S Batteries. *Advanced Materials* **2013,** *25* (11), 1608-1615.

10. Diao, Y.; Xie, K.; Xiong, S.; Hong, X., Insights into Li-S Battery Cathode Capacity Fading Mechanisms: Irreversible Oxidation of Active Mass during Cycling. *Journal of The Electrochemical Society* **2012,** *159* (11), A1816-A1821.

11. Chen, Y.-X.; Kaghazchi, P., Metalization of Li2S particle surfaces in Li-S batteries. *Nanoscale* **2014,** *6* (22), 13391-13395.

12. Yang, Y.; Zheng, G.; Cui, Y., Nanostructured sulfur cathodes. *Chemical Society Reviews* **2013,** *42* (7), 3018-3032.

13. Choi, J.-H.; Lee, C.-L.; Park, K.-S.; Jo, S.-M.; Lim, D.-S.; Kim, I.-D., Sulfur-impregnated MWCNT microball cathode for Li-S batteries. *RSC Advances* **2014,** *4* (31), 16062-16066.

14. Huang, C.; Xiao, J.; Shao, Y.; Zheng, J.; Bennett, W. D.; Lu, D.; Saraf, L. V.; Engelhard, M.; Ji, L.; Zhang, J.; Li, X.; Graff, G. L.; Liu, J., Manipulating surface reactions in lithium-sulphur batteries using hybrid anode structures. *Nature Communications* **2014,** *5*.

15. Hencz, L.; Chen, H.; Ling, H. Y.; Wang, Y.; Lai, C.; Zhao, H.; Zhang, S., Housing Sulfur in Polymer Composite Frameworks for Li–S Batteries. *Nano-Micro Letters* **2019,** *11* (1), 17.

16. Peng, H. J.; Huang, J. Q.; Cheng, X. B.; Zhang, Q., Lithium-Sulfur Batteries: Review on High-Loading and High-Energy Lithium–Sulfur Batteries (Adv. Energy Mater. 24/2017). *Advanced Energy Materials* **2017,** *7* (24), 1770141.

17. Aurbach, D.; Pollak, E.; Elazari, R.; Salitra, G.; Kelley, C. S.; Affinito, J., On the Surface Chemical Aspects of Very High Energy Density, Rechargeable Li-Sulfur Batteries. *Journal of The Electrochemical Society* **2009,** *156* (8), A694-A702.

18. Peled, E., Lithium Stability and Film Formation in Organic and Inorganic Electrolyte for Lithium Battery Systems. In *Lithium Batteries*, Gabano, J. P., Ed. Academic Press: 1983.

19. Wang, A.; Kadam, S.; Li, H.; Shi, S.; Qi, Y., Review on modeling of the anode solid electrolyte interphase (SEI) for lithium-ion batteries. *npj Computational Materials* **2018,** *4* (1), 15.

20. Goodenough, J. B.; Kim, Y., Challenges for Rechargeable Li Batteries. *Chemistry of Materials* **2010,** *22* (3), 587-603.

21. Zhu, Y.; He, X.; Mo, Y., Origin of Outstanding Stability in the Lithium Solid Electrolyte Materials: Insights from Thermodynamic Analyses Based on First-Principles Calculations. *ACS Applied Materials & Interfaces* **2015,** *7* (42), 23685-23693.

22. Cheng, X.-B.; Zhang, R.; Zhao, C.-Z.; Wei, F.; Zhang, J.-G.; Zhang, Q., A Review of Solid Electrolyte Interphases on Lithium Metal Anode. *Advanced Science* **2016,** *3* (3), 1500213.

23. Zhang, K.; Lee, G.-H.; Park, M.; Li, W.; Kang, Y.-M., Recent Developments of the Lithium Metal Anode for Rechargeable Non-Aqueous Batteries. *Advanced Energy Materials* **2016,** *6* (20), 1600811.

24. Manthiram, A.; Yu, X.; Wang, S., Lithium battery chemistries enabled by solid-state electrolytes. *Nature Reviews Materials* **2017,** *2*, 16103.

25. Wang, Y.; Richards, W. D.; Ong, S. P.; Miara, L. J.; Kim, J. C.; Mo, Y.; Ceder, G., Design principles for solid-state lithium superionic conductors. *Nature Materials* **2015,** *14*, 1026.

26. Gao, Z.; Sun, H.; Fu, L.; Ye, F.; Zhang, Y.; Luo, W.; Huang, Y., Promises, Challenges, and Recent Progress of Inorganic Solid-State Electrolytes for All-Solid-State Lithium Batteries. *Advanced Materials* **2018**, 1705702.

27. Famprikis, T.; Canepa, P.; Dawson, J. A.; Islam, M. S.; Masquelier, C., Fundamentals of inorganic solid-state electrolytes for batteries. *Nature Materials* **2019**.

28. Wang, S.; Zhang, Y.; Zhang, X.; Liu, T.; Lin, Y.-H.; Shen, Y.; Li, L.; Nan, C.-W., High-Conductivity Argyrodite Li6PS5Cl Solid Electrolytes Prepared via Optimized Sintering Processes for All-Solid-State Lithium–Sulfur Batteries. *ACS Applied Materials & Interfaces* **2018,** *10* (49), 42279-42285.

29. Xia, S.; Wu, X.; Zhang, Z.; Cui, Y.; Liu, W., Practical Challenges and Future Perspectives of All-Solid-State Lithium-Metal Batteries. *Chem* **2019,** *5* (4), 753-785.

30. Medicus, H. A., Fifty years of matter waves. *Physics Today* **1974,** *27* (2), 38-45.

31. Lee, J. G., *Computational materials science : an introduction*. Taylor & Francis: 2012.

32. Schrödinger, E., Quantisierung als Eigenwertproblem. *Annalen der Physik* **1926,** *384* (4), 361-376.

33. Jensen, F., *Introduction to Computational Chemistry*. 3rd Edition ed.; Wiley: 2017.

34. Born, M.; Oppenheimer, R., Zur Quantentheorie der Molekeln. *Annalen der Physik* **1927,** *389* (20), 457-484.

35. Sholl, D.; Steckel, J. A., *Density Functional Theory: A Practical Introduction*. Wiley: 2009.

36. Fock, V., Näherungsmethode zur Lösung des quantenmechanischen Mehrkörperproblems. *Zeitschrift für Physik* **1930,** *61* (1), 126-148.

37. Kohn, W.; Sham, L. J., Self-Consistent Equations Including Exchange and Correlation Effects. *Physical Review* **1965,** *140* (4A), A1133-A1138.

38. Hohenberg, P.; Kohn, W., Inhomogeneous Electron Gas. *Physical Review* **1964,** *136* (3B), B864-B871.

39. Feynman, R. P., Forces in Molecules. *Physical Review* **1939,** *56* (4), 340-343.

40. Hafner, J., Ab-initio simulations of materials using VASP: Density-functional theory and beyond. *Journal of Computational Chemistry* **2008,** *29* (13), 2044-2078.

41. Ceperley, D. M.; Alder, B. J., Ground State of the Electron Gas by a Stochastic Method. *Physical Review Letters* **1980,** *45* (7), 566-569.

42. Wang, Y.; Perdew, J. P., Spin scaling of the electron-gas correlation energy in the high-density limit. *Physical Review B* **1991,** *43* (11), 8911-8916.

43. Becke, A. D., Density-functional exchange-energy approximation with correct asymptotic behavior. *Physical Review A* **1988,** *38* (6), 3098-3100.

44. Lee, C.; Yang, W.; Parr, R. G., Development of the Colle-Salvetti correlation-energy formula into a functional of the electron density. *Physical Review B* **1988,** *37* (2), 785-789.

45. Perdew, J. P.; Burke, K.; Ernzerhof, M., Generalized Gradient Approximation Made Simple. *Physical Review Letters* **1996,** *77* (18), 3865-3868.

46. Becke, A. D., Density-functional thermochemistry. III. The role of exact exchange. *The Journal of Chemical Physics* **1993,** *98* (7), 5648-5652.

47. Adamo, C.; Barone, V., Toward reliable density functional methods without adjustable parameters: The PBE0 model. *The Journal of Chemical Physics* **1999,** *110* (13), 6158-6170.

48. Heyd, J.; Scuseria, G. E.; Ernzerhof, M., Hybrid functionals based on a screened Coulomb potential. *The Journal of Chemical Physics* **2003,** *118* (18), 8207-8215.

49. Vanderbilt, D., Soft self-consistent pseudopotentials in a generalized eigenvalue formalism. *Physical Review B* **1990,** *41* (11), 7892-7895.

50. Kresse, G.; Joubert, D., From ultrasoft pseudopotentials to the projector augmented-wave method. *Physical Review B* **1999,** *59* (3), 1758-1775.

51. Blöchl, P. E., Projector augmented-wave method. *Physical Review B* **1994,** *50* (24), 17953-17979.

52. Foresman, J. B.; Frisch, A. E.; Gaussian, I., *Exploring chemistry with electronic structure methods*. Gaussian, Inc.: 1996.

53. Bloch, F., Über die Quantenmechanik der Elektronen in Kristallgittern. *Zeitschrift für Physik* **1929,** *52* (7), 555-600.

54. Monkhorst, H. J.; Pack, J. D., Special Points for Brillouin-Zone Integrations. *Physical Review B* **1976,** *13* (12), 5188-5192.

55. Verlet, L., Computer "Experiments" on Classical Fluids. I. Thermodynamical Properties of Lennard-Jones Molecules. *Physical Review* **1967,** *159* (1), 98-103.

56. Marx, D.; Hutter, J., *Ab Initio Molecular Dynamics: Basic Theory and Advanced Methods*. Cambridge University Press: 2009.

57. Car, R.; Parrinello, M., Unified Approach for Molecular Dynamics and Density-Functional Theory. *Physical Review Letters* **1985,** *55* (22), 2471-2474.

58. Kresse, G.; Furthmuller, J., Efficiency of ab-initio total energy calculations for metals and semiconductors using a plane-wave basis set. *Computational Materials Science* **1996,** *6* (1), 15-50.

59. Kresse, G.; Hafner, J., Ab initio molecular dynamics for liquid metals. *Physical Review B* **1993,** *47* (1), 558-561.

60. Kresse, G.; Hafner, J., Ab initio molecular-dynamics simulation of the liquid-metalamorphous-semiconductor transition in germanium. *Physical Review B* **1994,** *49* (20), 14251-14269.

61. Sandler, S. I., *An Introduction to Applied Statistical Thermodynamics*. Wiley: 2010.

62. Bader, R. F. W.; Bader, R. F., *Atoms in Molecules: A Quantum Theory*. Clarendon Press: 1990.

63. Henkelman, G.; Arnaldsson, A.; Jónsson, H., A fast and robust algorithm for Bader decomposition of charge density. *Computational Materials Science* **2006,** *36* (3), 354-360.

64. Sanville, E.; Kenny, S. D.; Smith, R.; Henkelman, G., Improved grid-based algorithm for Bader charge allocation. *Journal of Computational Chemistry* **2007,** *28* (5), 899-908.

65. Tang, W.; Sanville, E.; Henkelman, G., A grid-based Bader analysis algorithm without lattice bias. *Journal of Physics Condensed Matter* **2009,** *21* (8).

66. Zheng, J.; Gu, M.; Wang, C.; Zuo, P.; Koech, P. K.; Zhang, J.-G.; Liu, J.; Xiao, J., Controlled Nucleation and Growth Process of Li2S2/Li2S in Lithium-Sulfur Batteries. *Journal of the Electrochemical Society* **2013,** *160* (11), A1992-A1996.

67. Gauthier, M.; Carney, T. J.; Grimaud, A.; Giordano, L.; Pour, N.; Chang, H.-H.; Fenning, D. P.; Lux, S. F.; Paschos, O.; Bauer, C.; Maglia, F.; Lupart, S.; Lamp, P.; Shao-Horn, Y., Electrode–Electrolyte Interface in Li-Ion Batteries: Current Understanding and New Insights. *The Journal of Physical Chemistry Letters* **2015,** *6* (22), 4653-4672.

68. Harks, P. P. R. M. L.; Mulder, F. M.; Notten, P. H. L., In situ methods for Li-ion battery research: A review of recent developments. *Journal of Power Sources* **2015,** *288*, 92-105.

69. Hagen, M.; Schiffels, P.; Hammer, M.; Dörfler, S.; Tübke, J.; Hoffmann, M. J.; Althues, H.; Kaskel, S., In-Situ Raman Investigation of Polysulfide Formation in Li-S Cells. *Journal of The Electrochemical Society* **2013,** *160* (8), A1205-A1214.

70. Patel, M. U. M.; Demir-Cakan, R.; Morcrette, M.; Tarascon, J.-M.; Gaberscek, M.; Dominko, R., Li-S Battery Analyzed by UV/Vis in Operando Mode. *ChemSusChem* **2013,** *6* (7), 1177-1181.

71. Patel, M. U. M.; Dominko, R., Application of In Operando UV/Vis Spectroscopy in Lithium–Sulfur Batteries. *ChemSusChem* **2014,** *7* (8), 2167-2175.

72. Wang, Q.; Zheng, J.; Walter, E.; Pan, H.; Lv, D.; Zuo, P.; Chen, H.; Deng, Z. D.; Liaw, B. Y.; Yu, X.; Yang, X.; Zhang, J.-G.; Liu, J.; Xiao, J., Direct Observation of Sulfur Radicals as Reaction Media in Lithium Sulfur Batteries. *Journal of The Electrochemical Society* **2015,** *162* (3), A474-A478.

73. Lowe, M. A.; Gao, J.; Abruna, H. D., Mechanistic insights into operational lithium-sulfur batteries by in situ X-ray diffraction and absorption spectroscopy. *RSC Advances* **2014,** *4* (35), 18347-18353.

74. Patel, M. U. M.; Arčon, I.; Aquilanti, G.; Stievano, L.; Mali, G.; Dominko, R., X-ray Absorption Near-Edge Structure and Nuclear Magnetic Resonance Study of the Lithium–Sulfur Battery and its Components. *ChemPhysChem* **2014,** *15* (5), 894-904.

75. Wujcik, K. H.; Pascal, T. A.; Pemmaraju, C. D.; Devaux, D.; Stolte, W. C.; Balsara, N. P.; Prendergast, D., Characterization of Polysulfide Radicals Present in an Ether-Based Electrolyte of a Lithium–Sulfur Battery During Initial Discharge Using In Situ X-Ray Absorption Spectroscopy Experiments and First-Principles Calculations. *Advanced Energy Materials* **2015,** *5* (16), n/a-n/a.

76. See, K. A.; Leskes, M.; Griffin, J. M.; Britto, S.; Matthews, P. D.; Emly, A.; Van der Ven, A.; Wright, D. S.; Morris, A. J.; Grey, C. P.; Seshadri, R., Ab Initio Structure Search and in Situ 7Li NMR Studies of Discharge Products in the Li–S Battery System. *Journal of the American Chemical Society* **2014,** *136* (46), 16368-16377.

77. Xiao, J.; Hu, J. Z.; Chen, H.; Vijayakumar, M.; Zheng, J.; Pan, H.; Walter, E. D.; Hu, M.; Deng, X.; Feng, J.; Liaw, B. Y.; Gu, M.; Deng, Z. D.; Lu, D.; Xu, S.; Wang, C.; Liu, J., Following the Transient Reactions in Lithium–Sulfur Batteries Using an In Situ Nuclear Magnetic Resonance Technique. *Nano Letters* **2015,** *15* (5), 3309-3316.

78. Lin, C.-N.; Chen, W.-C.; Song, Y.-F.; Wang, C.-C.; Tsai, L.-D.; Wu, N.-L., Understanding dynamics of polysulfide dissolution and re-deposition in working lithium–sulfur battery by in-operando transmission X-ray microscopy. *Journal of Power Sources* **2014,** *263*, 98-103.

79. Nelson, J.; Misra, S.; Yang, Y.; Jackson, A.; Liu, Y.; Wang, H.; Dai, H.; Andrews, J. C.; Cui, Y.; Toney, M. F., In Operando X-ray Diffraction and Transmission X-ray Microscopy of Lithium Sulfur Batteries. *Journal of the American Chemical Society* **2012,** *134* (14), 6337-6343.

80. Yu, X.; Pan, H.; Zhou, Y.; Northrup, P.; Xiao, J.; Bak, S.; Liu, M.; Nam, K.-W.; Qu, D.; Liu, J.; Wu, T.; Yang, X.-Q., Direct Observation of the Redistribution of Sulfur and Polysufides in Li–S Batteries During the First Cycle by In Situ X-Ray Fluorescence Microscopy. *Advanced Energy Materials* **2015,** *5* (16), n/a-n/a.

81. Anderson, M. S.; Swenson, C. A., Experimental equations of state for cesium and lithium metals to 20 kbar and the high-pressure behavior of the alkali metals. *Physical Review B* **1985,** *31* (2), 668-680.

82. Doll, K.; Harrison, N. M.; Saunders, V. R., A density functional study of lithium bulk and surfaces. *Journal of Physics: Condensed Matter* **1999,** *11* (26), 5007.

83. Valencia, H.; Kohyama, M.; Tanaka, S.; Matsumoto, H., Ab initio study of EMIM-BF_4 molecule adsorption on Li surfaces as a model for ionic liquid/Li interfaces in Li-ion batteries. *Physical Review B* **2008,** *78* (20), 205402.

84. Andersson, M.; Karlstrom, G., Conformational structure of 1,2-dimethoxyethane in water and other dipolar solvents, studied by quantum chemical, reaction field, and statistical mechanical techniques. *The Journal of Physical Chemistry* **1985,** *89* (23), 4957-4962.

85. Li, X. Y.; Nie, J., Density Functional Theory Study on Metal Bis(trifluoromethylsulfonyl)imides: Electronic Structures, Energies, Catalysis, and Predictions. *The Journal of Physical Chemistry A* **2003,** *107* (31), 6007-6013.

86. Makarewicz, J.; Ha, T.-K., Ab initio study of the pseudorotation in 1,3-dioxolane. *Journal of Molecular Structure* **2001,** *599* (1–3), 271-278.

87. Nowinski, J. L.; Lightfoot, P.; Bruce, P. G., Structure of LiN(CF3SO2)2, a novel salt for electrochemistry. *Journal of Materials Chemistry* **1994,** *4* (10), 1579-1580.

88. Soetens, J.-C.; Millot, C.; Maigret, B.; Bakó, I., Molecular dynamics simulation and X—ray diffraction studies of ethylene carbonate, propylene carbonate and dimethyl carbonate in liquid phase. *Journal of Molecular Liquids* **2001,** *92* (3), 201-216.

89. Frisch, M. J.; Trucks, G. W.; Schlegel, H. B.; Scuseria, G. E.; Robb, M. A.; Cheeseman, J. R.; Scalmani, G.; Barone, V.; Mennucci, B.; Petersson, G. A.; Nakatsuji, H.; Caricato, M.; Li, X.; Hratchian, H. P.; Izmaylov, A. F.; Bloino, J.; Zheng, G.; Sonnenberg, J. L.; Hada, M.; Ehara, M.; Toyota, K.; Fukuda, R.; Hasegawa, J.; Ishida, M.; Nakajima, T.; Honda, Y.; Kitao, O.; Nakai, H.; Vreven, T.; Montgomery Jr., J. A.; Peralta, J. E.; Ogliaro, F. o.; Bearpark, M. J.; Heyd, J.; Brothers, E. N.; Kudin, K. N.; Staroverov, V. N.; Kobayashi, R.; Normand, J.; Raghavachari, K.; Rendell, A. P.; Burant, J. C.; Iyengar, S. S.; Tomasi, J.; Cossi, M.; Rega, N.; Millam, N. J.; Klene, M.; Knox, J. E.; Cross, J. B.; Bakken, V.; Adamo, C.; Jaramillo, J.; Gomperts, R.; Stratmann, R. E.; Yazyev, O.; Austin, A. J.; Cammi, R.; Pomelli, C.; Ochterski, J. W.; Martin, R. L.; Morokuma, K.; Zakrzewski, V. G.; Voth, G. A.; Salvador, P.; Dannenberg, J. J.; Dapprich, S.;

Daniels, A. D.; Farkas, Ã. d. n.; Foresman, J. B.; Ortiz, J. V.; Cioslowski, J.; Fox, D. J. *Gaussian 09*, Gaussian, Inc.: Wallingford, CT, USA, 2009.

90. Perdew, J. P.; Chevary, J. A.; Vosko, S. H.; Jackson, K. A.; Pederson, M. R.; Singh, D. J.; Fiolhais, C., Atoms, molecules, solids, and surfaces: Applications of the generalized gradient approximation for exchange and correlation. *Physical Review B* **1992,** *46* (11), 6671-6687.

91. Gejji, S. P.; Suresh, C. H.; Babu, K.; Gadre, S. R., Ab initio structure and vibrational frequencies of (CF3SO2)(2)N-Li+ ion pairs. *The Journal of Physical Chemistry A* **1999,** *103* (37), 7474-7480.

92. Rey, I.; Johansson, P.; Lindgren, J.; Lassegues, J. C.; Grondin, J.; Servant, L., Spectroscopic and theoretical study of (CF3SO2)(2)N- (TFSI-) and (CF3SO2)(2)NH (HTFSI). *The Journal of Physical Chemistry A* **1998,** *102* (19), 3249-3258.

93. Bauschlicher, C. W.; Haskins, J. B.; Bucholz, E. W.; Lawson, J. W.; Borodin, O., Structure and Energetics of Li^+-$(BF4-)_n$, Li^+-$(FSI-)_n$, and Li^+-$(TFSI-)_n$: Ab Initio and Polarizable Force Field Approaches. *The Journal of Physical Chemistry B* **2014,** *118* (36), 10785-10794.

94. *Materials Studio 8*, Accelrys Sofware Inc: 2011.

95. Tomasi, J.; Mennucci, B.; Cammi, R., Quantum Mechanical Continuum Solvation Models. *Chemical Reviews* **2005,** *105* (8), 2999-3094.

96. Barghamadi, M.; Best, A. S.; Bhatt, A. I.; Hollenkamp, A. F.; Mahon, P. J.; Musameh, M.; Rüther, T., Effect of Anion on Behaviour of Li-S Battery Electrolyte Solutions Based on N-Methyl-N-Butyl-Pyrrolidinium Ionic Liquids. *Electrochimica Acta* **2015,** *180*, 636-644.

97. Vranes, M.; Dozic, S.; Djeric, V.; Gadzuric, S., Physicochemical Characterization of 1-Butyl-3-methylimidazolium and 1-Butyl-1-methylpyrrolidinium Bis(trifluoromethylsulfonyl)imide. *Journal of Chemical & Engineering Data* **2012,** *57* (4), 1072-1077.

98. Höfft, O.; Krischok, S., Vacuum Electrochemistry in Ionic Liquids. *Electrochemical Society Interface* **2014**, 53.

99. Paulechka, Y. U.; Zaitsau, D. H.; Kabo, G. J.; Strechan, A. A., Vapor pressure and thermal stability of ionic liquid 1-butyl-3-methylimidazolium

Bis(trifluoromethylsulfonyl)amide. *Thermochimica Acta* **2005,** *439* (1–2), 158-160.

100. Vijayakumar, M.; Govind, N.; Walter, E.; Burton, S. D.; Shukla, A.; Devaraj, A.; Xiao, J.; Liu, J.; Wang, C.; Karim, A.; Thevuthasan, S., Molecular structure and stability of dissolved lithium polysulfide species. *Physical Chemistry Chemical Physics* **2014,** *16* (22), 10923-10932.

101. Qian, J. F.; Henderson, W. A.; Xu, W.; Bhattacharya, P.; Engelhard, M.; Borodin, O.; Zhang, J. G., High rate and stable cycling of lithium metal anode. *Nature Communications* **2015,** *6*.

102. Aurbach, D.; Youngman, O.; Dan, P., The Electrochemical Behavior of 1,3-Dioxolane-LiClO4 Solutions 2: Contaminated Solutions. *Electrochimica Acta* **1990,** *35* (3), 639-655.

103. Aurbach, D.; Youngman, O.; Gofer, Y.; Meitav, A., The Electrochemical Behavior of 1,3-Dioxolane-LiClO4 Solutions 1: Uncontaminated Solutions. *Electrochimica Acta* **1990,** *35* (3), 625-638.

104. Gofer, Y.; Ely, Y. E.; Aurbach, D., Surface-Chemistry of Lithium in 1,3-Dioxolane. *Electrochimica Acta* **1992,** *37* (10), 1897-1899.

105. Leung, K., Electronic Structure Modeling of Electrochemical Reactions at Electrode/Electrolyte Interfaces in Lithium Ion Batteries. *The Journal of Physical Chemistry C* **2013,** *117* (4), 1539-1547.

106. Martinez de la Hoz, J. M.; Leung, K.; Balbuena, P. B., Reduction Mechanisms of Ethylene Carbonate on Si Anodes of Lithium-Ion Batteries: Effects of Degree of Lithiation and Nature of Exposed Surface. *ACS Applied Materials & Interfaces* **2013,** *5* (24), 13457-13465.

107. Sodeyama, K.; Yamada, Y.; Aikawa, K.; Yamada, A.; Tateyama, Y., Sacrificial Anion Reduction Mechanism for Electrochemical Stability Improvement in Highly Concentrated Li-Salt Electrolyte. *The Journal of Physical Chemistry C* **2014,** *118* (26), 14091-14097.

108. Budi, A.; Basile, A.; Opletal, G.; Hollenkamp, A. F.; Best, A. S.; Rees, R. J.; Bhatt, A. I.; O'Mullane, A. P.; Russo, S. P., Study of the Initial Stage of Solid Electrolyte Interphase Formation upon Chemical Reaction of Lithium Metal and N-Methyl-N-Propyl-Pyrrolidinium-Bis(Fluorosulfonyl)Imide. *The Journal of Physical Chemistry C* **2012,** *116* (37), 19789-19797.

109. Leung, K., Predicting the voltage dependence of interfacial electrochemical processes at lithium-intercalated graphite edge planes. *Physical Chemistry Chemical Physics* **2015,** *17*, 1637-1643.

110. Piper, D. M.; Evans, T.; Leung, K.; Watkins, T.; Olson, J.; Kim, S. C.; Han, S. S.; Bhat, V.; Oh, K. H.; Buttry, D. A.; Lee, S.-H., Stable silicon-ionic liquid interface for next-generation lithium-ion batteries. *Nature Communications* **2015,** *6*.

111. Shterenberg, I.; Salama, M.; Yoo, H. D.; Yosef Gofer; Jin-Bum Park; Sun, Y.-K.; Aurbach, D., Evaluation of (CF3SO2)2N− (TFSI) Based Electrolyte Solutions for Mg Batteries. *Journal of The Electrochemical Society* **2015,** *162* (13), A7118-A7128.

112. Borodin, O.; Smith, G. D., LiTFSI structure and transport in ethylene carbonate from molecular dynamics simulations. *The Journal of Physical Chemistry B* **2006,** *110* (10), 4971-4977.

113. Borodin, O.; Smith, G. D., Development of many-body polarizable force fields for Li-battery applications: 2. LiTFSI-doped oligoether, polyether, and carbonate-based electrolytes. *The Journal of Physical Chemistry B* **2006,** *110* (12), 6293-6299.

114. Howlett, P. C.; Izgorodina, E. I.; Forsyth, M.; MacFarlane, D. R., Electrochemistry at negative potentials in bis(trifluoromethanesulfonyl) amide ionic liquids. *Zeitschrift fur Physikalische Chemie* **2006,** *220* (10-11), 1483-1498.

115. Markevich, E.; Sharabi, R.; Borgel, V.; Gottlieb, H.; Salitra, G.; Aurbach, D.; Semrau, G.; Schmidt, M. A., In situ FTIR study of the decomposition of N-butyl-N-methylpyrrolidinium bis(trifluoromethanesulfonyl)amide ionic liquid during cathodic polarization of lithium and graphite electrodes. *Electrochimica Acta* **2010,** *55* (8), 2687-2696.

116. Barchasz, C.; Molton, F.; Duboc, C.; Lepretre, J.-C.; Patoux, S.; Alloin, F., Lithium/Sulfur Cell Discharge Mechanism: An Original Approach for Intermediate Species Identification. *Analytical Chemistry* **2012,** *84* (9), 3973-3980.

117. Mikhaylik, Y. V.; Akridge, J. R., Polysulfide shuttle study in the Li/S battery system. *Journal of The Electrochemical Society* **2004,** *151* (11), A1969-A1976.

118. Moy, D.; Manivannan, A.; Narayanan, S. R., Direct Measurement of Polysulfide Shuttle Current: A Window into Understanding the Performance of Lithium-Sulfur Cells. *Journal of The Electrochemical Society* **2015,** *162* (1), A1-A7.

119. Assary, R. S.; Curtiss, L. A.; Moore, J. S., Toward a Molecular Understanding of Energetics in Li-S Batteries Using Nonaqueous Electrolytes: A High-Level Quantum Chemical Study. *The Journal of Physical Chemistry C* **2014,** *118* (22), 11545-11558.

120. Park, M. S.; Ma, S. B.; Lee, D. J.; Im, D.; Doo, S.-G.; Yamamoto, O., A Highly Reversible Lithium Metal Anode. *Scientific Reports* **2014,** *4*.

121. Men, S.; Lovelock, K. R. J.; Licence, P., X-ray photoelectron spectroscopy of pyrrolidinium-based ionic liquids: cation-anion interactions and a comparison to imidazolium-based analogues. *Physical Chemistry Chemical Physics* **2011,** *13* (33), 15244-15255.

122. Smart, R. S. C.; Skinner, W. M.; Gerson, A. R., XPS of sulphide mineral surfaces: metal-deficient, polysulphides, defects and elemental sulphur. *Surface and Interface Analysis* **1999,** *28* (1), 101-105.

123. Liang, X.; Hart, C.; Pang, Q.; Garsuch, A.; Weiss, T.; Nazar, L. F., A highly efficient polysulfide mediator for lithium–sulfur batteries. *Nature Communications* **2015,** *6*.

124. Turner, N. H.; Murday, J. S.; Ramaker, D. E., Quantitative determination of surface composition of sulfur bearing anion mixtures by Auger electron spectroscopy. *Analytical Chemistry* **1980,** *52* (1), 84-92.

125. Fantauzzi, M.; Elsener, B.; Atzei, D.; Rigoldi, A.; Rossi, A., Exploiting XPS for the identification of sulfides and polysulfides. *RSC Advances* **2015,** *5* (93), 75953-75963.

126. Liu, Z.; Bertolini, S.; Balbuena, P. B.; Mukherjee, P. P., Li2S Film Formation on Lithium Anode Surface of Li–S batteries. *ACS Applied Materials & Interfaces* **2016,** *8* (7), 4700-4708.

127. Li, W.; Yao, H.; Yan, K.; Zheng, G.; Liang, Z.; Chiang, Y.-M.; Cui, Y., The synergetic effect of lithium polysulfide and lithium nitrate to prevent lithium dendrite growth. *Nature Communications* **2015,** *6*, 7436.

128. Bhattacharya, P.; Nandasiri, M. I.; Lv, D.; Schwarz, A. M.; Darsell, J. T.; Henderson, W. A.; Tomalia, D. A.; Liu, J.; Zhang, J.-G.; Xiao, J., Polyamidoamine dendrimer-based binders for high-loading lithium–sulfur battery cathodes. *Nano Energy* **2016,** *19*, 176-186.

129. Camacho-Forero, L. E.; Smith, T. W.; Bertolini, S.; Balbuena, P. B., Reactivity at the Lithium–Metal Anode Surface of Lithium–Sulfur Batteries. *The Journal of Physical Chemistry C* **2015,** *119* (48), 26828-26839.

130. Howlett, P. C.; Brack, N.; Hollenkamp, A. F.; Forsyth, M.; MacFarlane, D. R., Characterization of the Lithium Surface in N-Methyl-N-alkylpyrrolidinium Bis(trifluoromethanesulfonyl)amide Room-Temperature Ionic Liquid Electrolytes. *Journal of The Electrochemical Society* **2006,** *153* (3), A595-A606.

131. Xu, C.; Sun, B.; Gustafsson, T.; Edstrom, K.; Brandell, D.; Hahlin, M., Interface layer formation in solid polymer electrolyte lithium batteries: an XPS study. *Journal of Materials Chemistry A* **2014,** *2* (20), 7256-7264.

132. Chan, C. K.; Ruffo, R.; Hong, S. S.; Cui, Y., Surface chemistry and morphology of the solid electrolyte interphase on silicon nanowire lithium-ion battery anodes. *Journal of Power Sources* **2009,** *189* (2), 1132-1140.

133. Schroder, K. W.; Celio, H.; Webb, L. J.; Stevenson, K. J., Examining Solid Electrolyte Interphase Formation on Crystalline Silicon Electrodes: Influence of Electrochemical Preparation and Ambient Exposure Conditions. *The Journal of Physical Chemistry C* **2012,** *116* (37), 19737-19747.

134. Leroy, S.; Martinez, H.; Dedryvère, R.; Lemordant, D.; Gonbeau, D., Influence of the lithium salt nature over the surface film formation on a graphite electrode in Li-ion batteries: An XPS study. *Applied Surface Science* **2007,** *253* (11), 4895-4905.

135. Song, J.; Noh, H.; Lee, H.; Lee, J.-N.; Lee, D. J.; Lee, Y.; Kim, C. H.; Lee, Y. M.; Park, J.-K.; Kim, H.-T., Polysulfide rejection layer from alpha-lipoic acid for high performance lithium-sulfur battery. *Journal of Materials Chemistry A* **2015,** *3* (1), 323-330.

136. Nguyen, C. C.; Woo, S.-W.; Song, S.-W., Understanding the Interfacial Processes at Silicon–Copper Electrodes in Ionic Liquid Battery Electrolyte. *The Journal of Physical Chemistry C* **2012,** *116* (28), 14764-14771.

137. Soto, F. A.; Ma, Y.; Martinez de la Hoz, J. M.; Seminario, J. M.; Balbuena, P. B., Formation and Growth Mechanisms of Solid-Electrolyte Interphase Layers in Rechargeable Batteries. *Chemistry of Materials* **2015,** *27* (23), 7990-8000.

138. Venables, J. A.; Spiller, G. D. T.; Hanbucken, M., Nucleation and growth of thin films. *Reports on Progress in Physics* **1984,** *47* (4), 399.

139. Gurker, N.; Ebel, M. F.; Ebel, H.; Mantler, M.; Hedrich, H.; Schön, P., Imaging XPS—a new technique. 2—Experimental verification. *Surface and Interface Analysis* **1987,** *10* (5), 242-249.

140. Gurker, N.; Ebel, M. F.; Ebel, H., Imaging XPS—A new technique, I—principles. *Surface and Interface Analysis* **1983,** *5* (1), 13-19.

141. An, S. J.; Li, J.; Daniel, C.; Mohanty, D.; Nagpure, S.; Wood Iii, D. L., The state of understanding of the lithium-ion-battery graphite solid electrolyte interphase (SEI) and its relationship to formation cycling. *Carbon* **2016,** *105*, 52-76.

142. Aurbach, D.; Zinigrad, E.; Cohen, Y.; Teller, H., A short review of failure mechanisms of lithium metal and lithiated graphite anodes in liquid electrolyte solutions. *Solid State Ionics* **2002,** *148* (3-4), 405-416.

143. Peled, E., The Electrochemical Behavior of Alkali and Alkaline Earth Metals in Nonaqueous Battery Systems—The Solid Electrolyte Interphase Model. *Journal of The Electrochemical Society* **1979,** *126* (12), 2047.

144. Mikhaylik, Y. V.; Akridge, J. R., Low temperature performance of Li/S batteries. *Journal of The Electrochemical Society* **2003,** *150* (3), A306-A311.

145. Agostini, M.; Scrosati, B.; Hassoun, J., An Advanced Lithium-Ion Sulfur Battery for High Energy Storage. *Advanced Energy Materials* **2015,** *5* (16).

146. Delp, S. A.; Borodin, O.; Olguin, M.; Eisner, C. G.; Allen, J. L.; Jow, T. R., Importance of Reduction and Oxidation Stability of High Voltage Electrolytes and Additives. *Electrochimica Acta* **2016,** *209*, 498-510.

147. Nasybulin, E.; Xu, W.; Engelhard, M. H.; Nie, Z. M.; Burton, S. D.; Cosimbescu, L.; Gross, M. E.; Zhang, J. G., Effects of Electrolyte Salts on the Performance of Li-O-2 Batteries. *The Journal of Physical Chemistry C* **2013,** *117* (6), 2635-2645.

148. Ding, F.; Xu, W.; Chen, X.; Zhang, J.; Engelhard, M. H.; Zhang, Y.; Johnson, B. R.; Crum, J. V.; Blake, T. A.; Liu, X.; Zhang, J.-G., Effects of Carbonate Solvents and Lithium Salts on Morphology and Coulombic Efficiency of Lithium Electrode. *Journal of The Electrochemical Society* **2013,** *160* (10), A1894-A1901.

149. Markus, I. M.; Jones, G.; Garcia, J. M., Investigation of Electrolyte Concentration Effects on the Performance of Lithium-Oxygen Batteries. *The Journal of Physical Chemistry C* **2016,** *120* (11), 5949-5957.

150. Han, H. B.; Zhou, S. S.; Zhang, D. J.; Feng, S. W.; Li, L. F.; Liu, K.; Feng, W. F.; Nie, J.; Li, H.; Huang, X. J.; Armand, M.; Zhou, Z. B., Lithium bis(fluorosulfonyl)imide (LiFSI) as conducting salt for nonaqueous liquid electrolytes for lithium-ion batteries: Physicochemical and electrochemical properties. *Journal of Power Sources* **2011,** *196* (7), 3623-3632.

151. Kim, H.; Wu, F.; Lee, J. T.; Nitta, N.; Lin, H.-T.; Oschatz, M.; Cho, W. I.; Kaskel, S.; Borodin, O.; Yushin, G., In Situ Formation of Protective Coatings on Sulfur Cathodes in Lithium Batteries with LiFSI-Based Organic Electrolytes. *Advanced Energy Materials* **2015,** *5* (6), 1401792-n/a.

152. Shin, E. S.; Kim, K.; Oh, S. H.; Il Cho, W., Polysulfide dissolution control: the common ion effect. *ChemComm* **2013,** *49* (20), 2004-2006.

153. Suo, L.; Hu, Y.-S.; Li, H.; Armand, M.; Chen, L., A new class of Solvent-in-Salt electrolyte for high-energy rechargeable metallic lithium batteries. *Nature Communications* **2013,** *4*, 1481.

154. Wu, F.; Lee, J. T.; Magasinski, A.; Kim, H.; Yushin, G., Solution-Based Processing of Graphene–Li2S Composite Cathodes for Lithium-Ion and Lithium–Sulfur Batteries. *Particle & Particle Systems Characterization* **2014,** *31* (6), 639-644.

155. Hagen, M.; Doerfler, S.; Fanz, P.; Berger, T.; Speck, R.; Tuebke, J.; Althues, H.; Hoffmann, M. J.; Scherr, C.; Kaskel, S., Development and costs calculation of lithium-sulfur cells with high sulfur load and binder free electrodes. *Journal of Power Sources* **2013,** *224*, 260-268.

156. Fujii, K.; Seki, S.; Fukuda, S.; Kanzaki, R.; Takamuku, T.; Umebayashi, Y.; Ishiguro, S.-i., Anion Conformation of Low-Viscosity Room-Temperature Ionic Liquid 1-Ethyl-3-methylimidazolium Bis(fluorosulfonyl) Imide. *The Journal of Physical Chemistry B* **2007,** *111* (44), 12829-12833.

157. Canongia Lopes, J. N.; Shimizu, K.; Pádua, A. A.; Umebayashi, Y.; Fukuda, S.; Fujii, K.; Ishiguro, S.-i., Potential energy landscape of bis (fluorosulfonyl) amide. *The Journal of Physical Chemistry B* **2008,** *112* (31), 9449-9455.

158. Yoshida, K.; Nakamura, M.; Kazue, Y.; Tachikawa, N.; Tsuzuki, S.; Seki, S.; Dokko, K.; Watanabe, M., Oxidative-Stability Enhancement and Charge Transport Mechanism in Glyme–Lithium Salt Equimolar Complexes. *Journal of the American Chemical Society* **2011,** *133* (33), 13121-13129.

159. Han, S.-D.; Borodin, O.; Seo, D. M.; Zhou, Z.-B.; Henderson, W. A., Electrolyte solvation and ionic association V. Acetonitrile-lithium bis (fluorosulfonyl) imide (LiFSI) mixtures. *Journal of The Electrochemical Society* **2014,** *161* (14), A2042-A2053.

160. Humphrey, W.; Dalke, A.; Schulten, K., VMD: visual molecular dynamics. *Journal of Molecular Graphics* **1996,** *14* (1), 33-38.

161. Shkrob, I. A.; Marin, T. W.; Zhu, Y.; Abraham, D. P., Why Bis(fluorosulfonyl)imide Is a "Magic Anion" for Electrochemistry. *The Journal of Physical Chemistry C* **2014,** *118* (34), 19661-19671.

162. Younesi, R.; Veith, G. M.; Johansson, P.; Edstrom, K.; Vegge, T., Lithium salts for advanced lithium batteries: Li-metal, Li-O2, and Li-S. *Energy & Environmental Science* **2015,** *8* (7), 1905-1922.

163. Martinez de la Hoz, J. M.; Soto, F. A.; Balbuena, P. B., Effect of the Electrolyte Composition on SEI Reactions at Si Anodes of Li-Ion Batteries. *The Journal of Physical Chemistry C* **2015,** *119* (13), 7060-7068.

164. Umebayashi, Y.; Mitsugi, T.; Fukuda, S.; Fujimori, T.; Fujii, K.; Kanzaki, R.; Takeuchi, M.; Ishiguro, S.-I., Lithium Ion Solvation in Room-Temperature Ionic Liquids Involving Bis(trifluoromethanesulfonyl) Imide Anion Studied by Raman Spectroscopy and DFT Calculations. *The Journal of Physical Chemistry B* **2007,** *111* (45), 13028-13032.

165. Yoon, H.; Best, A. S.; Forsyth, M.; MacFarlane, D. R.; Howlett, P. C., Physical properties of high Li-ion content N-propyl-N-methylpyrrolidinium bis(fluorosulfonyl)imide based ionic liquid electrolytes. *Physical Chemistry Chemical Physics* **2015,** *17* (6), 4656-4663.

166. Liu, B.; Xu, W.; Yan, P.; Sun, X.; Bowden, M. E.; Read, J.; Qian, J.; Mei, D.; Wang, C.-M.; Zhang, J.-G., Enhanced Cycling Stability of Rechargeable Li–O2 Batteries Using High-Concentration Electrolytes. *Advanced Energy Materials* **2016,** *26* (4), 605-613.

167. Hayamizu, K.; Aihara, Y.; Arai, S.; Martinez, C. G., Pulse-Gradient Spin-Echo 1H, 7Li, and 19F NMR Diffusion and Ionic Conductivity Measurements of 14 Organic Electrolytes Containing LiN(SO2CF3)2. *The Journal of Physical Chemistry B* **1999,** *103* (3), 519-524.

168. Hayamizu, K.; Aihara, Y., Ion and solvent diffusion and ion conduction of PC-DEC and PC-DME binary solvent electrolytes of LiN(SO2CF3)2. *Electrochimica Acta* **2004,** *49* (20), 3397-3402.

169. Yu, J.; Balbuena, P. B.; Budzien, J.; Leung, K., Hybrid DFT Functional-Based Static and Molecular Dynamics Studies of Excess Electron in Liquid Ethylene Carbonate. *Journal of The Electrochemical Society* **2011,** *158* (4), A400-A410.

170. Wang, Y.; Nakamura, S.; Ue, M.; Balbuena, P. B., Theoretical Studies To Understand Surface Chemistry on Carbon Anodes for Lithium-Ion Batteries: Reduction Mechanisms of Ethylene Carbonate. *Journal of the American Chemical Society* **2001,** *123* (47), 11708-11718.

171. Leung, K.; Budzien, J. L., Ab initio molecular dynamics simulations of the initial stages of solid-electrolyte interphase formation on lithium ion battery graphitic anodes. *Physical Chemistry Chemical Physics* **2010,** *12* (25), 6583-6586.

172. Aurbach, D.; Ein-Ely, Y.; Zaban, A., The Surface Chemistry of Lithium Electrodes in Alkyl Carbonate Solutions. *Journal of The Electrochemical Society* **1994,** *141* (1), L1-L3.

173. Wu, F.; Thieme, S.; Ramanujapuram, A.; Zhao, E.; Weller, C.; Althues, H.; Kaskel, S.; Borodin, O.; Yushin, G., Toward In-Situ Protected Sulfur Cathodes by Using Lithium Bromide and Pre-Charge. *Nano Energy* **2017**.

174. Bryantsev, V. S.; Faglioni, F., Predicting Autoxidation Stability of Ether- and Amide-Based Electrolyte Solvents for Li–Air Batteries. *The Journal of Physical Chemistry A* **2012,** *116* (26), 7128-7138.

175. Nandasiri, M. I.; Camacho-Forero, L. E.; Schwarz, A. M.; Shutthanandan, V.; Thevuthasan, S.; Balbuena, P. B.; Mueller, K. T.; Murugesan, V., In Situ Chemical Imaging of Solid-Electrolyte Interphase Layer Evolution in Li–S Batteries. *Chemistry of Materials* **2017,** *29* (11), 4728-4737.

176. Leung, K.; Leenheer, A., How Voltage Drops Are Manifested by Lithium Ion Configurations at Interfaces and in Thin Films on Battery Electrodes. *The Journal of Physical Chemistry C* **2015,** *119* (19), 10234-10246.

177. Rossmeisl, J.; Skúlason, E.; Björketun, M. E.; Tripkovic, V.; Nørskov, J. K., Modeling the electrified solid–liquid interface. *Chemical Physics Letters* **2008,** *466* (1), 68-71.

178. Bonnet, N.; Morishita, T.; Sugino, O.; Otani, M., First-Principles Molecular Dynamics at a Constant Electrode Potential. *Physical Review Letters* **2012,** *109* (26), 266101.

179. Cheng, J.; Sprik, M., Alignment of electronic energy levels at electrochemical interfaces. *Physical Chemistry Chemical Physics* **2012,** *14* (32), 11245-11267.

180. Chen, X.; Hou, T.-Z.; Li, B.; Yan, C.; Zhu, L.; Guan, C.; Cheng, X.-B.; Peng, H.-J.; Huang, J.-Q.; Zhang, Q., Towards stable lithium-sulfur batteries: Mechanistic insights into electrolyte decomposition on lithium metal anode. *Energy Storage Materials* **2017,** *8*, 194-201.

181. Camacho-Forero, L. E.; Smith, T. W.; Balbuena, P. B., Effects of High and Low Salt Concentration in Electrolytes at Lithium–Metal Anode Surfaces. *The Journal of Physical Chemistry C* **2017,** *121* (1), 182-194.

182. Arora, P.; White, R. E.; Doyle, M., Capacity Fade Mechanisms and Side Reactions in Lithium-Ion Batteries. *Journal of The Electrochemical Society* **1998,** *145* (10), 3647-3667.

183. Salama, M.; Shterenberg, I.; Gizbar, H.; Eliaz, N. N.; Kosa, M.; Keinan-Adamsky, K.; Afri, M.; Shimon, L. J. W.; Gottlieb, H. E.; Major, D. T.; Gofer, Y.; Aurbach, D., Unique Behavior of Dimethoxyethane (DME)/Mg(N(SO2CF3)2)2 Solutions. *The Journal of Physical Chemistry C* **2016,** *120* (35), 19586-19594.

184. *BIOVIA Materials Studio 2016*, 16.1.0.21; Dassault Systèmes BIOVIA: San Diego, 2015.

185. Leung, K.; Tenney, C. M., Toward First Principles Prediction of Voltage Dependences of Electrolyte/Electrolyte Interfacial Processes in Lithium Ion Batteries. *The Journal of Physical Chemistry C* **2013,** *117* (46), 24224-24235.

186. Marenich, A. V.; Cramer, C. J.; Truhlar, D. G., Universal Solvation Model Based on Solute Electron Density and on a Continuum Model of the Solvent Defined by the Bulk Dielectric Constant and Atomic Surface Tensions. *The Journal of Physical Chemistry B* **2009,** *113* (18), 6378-6396.

187. Aurbach, D., Review of selected electrode–solution interactions which determine the performance of Li and Li ion batteries. *Journal of Power Sources* **2000,** *89* (2), 206-218.

188. Shterenberg, I.; Salama, M.; Gofer, Y.; Aurbach, D., X-ray Photodecomposition of Bis(trifluoromethanesulfonyl)imide, Bis(fluorosulfonyl)imide, and

Hexafluorophosphate. *The Journal of Physical Chemistry C* **2017,** *121* (7), 3744-3751.

189. Ping So, S., Structures and bonding of lithium ethylene complexes. *Journal of Organometallic Chemistry* **1989,** *361* (3), 283-288.

190. Assary, R. S.; Lau, K. C.; Amine, K.; Sun, Y.-K.; Curtiss, L. A., Interactions of Dimethoxy Ethane with Li2O2 Clusters and Likely Decomposition Mechanisms for Li–O2 Batteries. *The Journal of Physical Chemistry C* **2013,** *117* (16), 8041-8049.

191. García, J. M.; Horn, H. W.; Rice, J. E., Dominant Decomposition Pathways for Ethereal Solvents in Li–O2 Batteries. *The Journal of Physical Chemistry Letters* **2015,** *6* (10), 1795-1799.

192. Kumar, N.; Radin, M. D.; Wood, B. C.; Ogitsu, T.; Siegel, D. J., Surface-Mediated Solvent Decomposition in Li–Air Batteries: Impact of Peroxide and Superoxide Surface Terminations. *The Journal of Physical Chemistry C* **2015,** *119* (17), 9050-9060.

193. Dietrich, C.; Weber, D. A.; Culver, S.; Senyshyn, A.; Sedlmaier, S. J.; Indris, S.; Janek, J.; Zeier, W. G., Synthesis, Structural Characterization, and Lithium Ion Conductivity of the Lithium Thiophosphate Li2P2S6. *Inorganic Chemistry* **2017,** *56* (11), 6681-6687.

194. Liu, Z.; Fu, W.; Payzant, E. A.; Yu, X.; Wu, Z.; Dudney, N. J.; Kiggans, J.; Hong, K.; Rondinone, A. J.; Liang, C., Anomalous High Ionic Conductivity of Nanoporous β-Li3PS4. *Journal of the American Chemical Society* **2013,** *135* (3), 975-978.

195. Kamaya, N.; Homma, K.; Yamakawa, Y.; Hirayama, M.; Kanno, R.; Yonemura, M.; Kamiyama, T.; Kato, Y.; Hama, S.; Kawamoto, K.; Mitsui, A., A lithium superionic conductor. *Nature Materials* **2011,** *10*, 682.

196. Minami, K.; Hayashi, A.; Tatsumisago, M., Preparation and characterization of superionic conducting $Li_7P_3S_{11}$ crystal from glassy liquids. *Journal of the Ceramic Society of Japan* **2010,** *118* (1376), 305-308.

197. Zhu, Z.; Chu, I.-H.; Ong, S. P., Li3Y(PS4)2 and Li5PS4Cl2: New Lithium Superionic Conductors Predicted from Silver Thiophosphates using Efficiently Tiered Ab Initio Molecular Dynamics Simulations. *Chemistry of Materials* **2017,** *29* (6), 2474-2484.

198. Yang, Y.; Wu, Q.; Cui, Y.; Chen, Y.; Shi, S.; Wang, R.-Z.; Yan, H., Elastic Properties, Defect Thermodynamics, Electrochemical Window, Phase Stability, and Li+ Mobility of Li3PS4: Insights from First-Principles Calculations. *ACS Applied Materials & Interfaces* **2016,** *8* (38), 25229-25242.

199. Mo, Y.; Ong, S. P.; Ceder, G., First Principles Study of the Li10GeP2S12 Lithium Super Ionic Conductor Material. *Chemistry of Materials* **2012,** *24* (1), 15-17.

200. Chu, I.-H.; Nguyen, H.; Hy, S.; Lin, Y.-C.; Wang, Z.; Xu, Z.; Deng, Z.; Meng, Y. S.; Ong, S. P., Insights into the Performance Limits of the Li7P3S11 Superionic Conductor: A Combined First-Principles and Experimental Study. *ACS Applied Materials & Interfaces* **2016,** *8* (12), 7843-7853.

201. Tatsumisago, M.; Hayashi, A., Sulfide Glass-Ceramic Electrolytes for All-Solid-State Lithium and Sodium Batteries. *International Journal of Applied Glass Science* **2014,** *5* (3), 226-235.

202. He, X.; Zhu, Y.; Mo, Y., Origin of fast ion diffusion in super-ionic conductors. *Nature Communications* **2017,** *8*, 15893.

203. Krauskopf, T.; Culver, S. P.; Zeier, W. G., Bottleneck of Diffusion and Inductive Effects in Li10Ge1–xSnxP2S12. *Chemistry of Materials* **2018,** *30* (5), 1791-1798.

204. Hu, C. H.; Wang, Z. Q.; Sun, Z. Y.; Ouyang, C. Y., Insights into structural stability and Li superionic conductivity of Li10GeP2S12 from first-principles calculations. *Chemical Physics Letters* **2014,** *591*, 16-20.

205. Richards, W. D.; Miara, L. J.; Wang, Y.; Kim, J. C.; Ceder, G., Interface Stability in Solid-State Batteries. *Chemistry of Materials* **2016,** *28* (1), 266-273.

206. Zhu, Y.; He, X.; Mo, Y., Strategies Based on Nitride Materials Chemistry to Stabilize Li Metal Anode. *Advanced Science* **2017,** *4* (8), 1600517-n/a.

207. Zhu, Y.; He, X.; Mo, Y., First principles study on electrochemical and chemical stability of solid electrolyte-electrode interfaces in all-solid-state Li-ion batteries. *Journal of Materials Chemistry A* **2016,** *4* (9), 3253-3266.

208. Cheng, T.; Merinov, B. V.; Morozov, S.; Goddard, W. A., Quantum Mechanics Reactive Dynamics Study of Solid Li-Electrode/Li6PS5Cl-Electrolyte Interface. *ACS Energy Letters* **2017,** *2* (6), 1454-1459.

209. Luo, W.; Gong, Y.; Zhu, Y.; Fu, K. K.; Dai, J.; Lacey, S. D.; Wang, C.; Liu, B.; Han, X.; Mo, Y.; Wachsman, E. D.; Hu, L., Transition from Superlithiophobicity

to Superlithiophilicity of Garnet Solid-State Electrolyte. *Journal of the American Chemical Society* **2016,** *138* (37), 12258-12262.

210. Sicolo, S.; Fingerle, M.; Hausbrand, R.; Albe, K., Interfacial instability of amorphous LiPON against lithium: A combined Density Functional Theory and spectroscopic study. *Journal of Power Sources* **2017,** *354*, 124-133.

211. Camacho-Forero, L. E.; Balbuena, P. B., Elucidating electrolyte decomposition under electron-rich environments at the lithium-metal anode. *Physical Chemistry Chemical Physics* **2017,** *19* (45), 30861-30873.

212. Bertolini, S.; Balbuena, P. B., Effect of solid electrolyte interphase on the reactivity of polysulfide over lithium-metal anode. *Electrochimica Acta* **2017,** *258*, 1320-1328.

213. Jain, A.; Ong, S. P.; Hautier, G.; Chen, W.; Richards, W. D.; Dacek, S.; Cholia, S.; Gunter, D.; Skinner, D.; Ceder, G.; Persson, K. A., Commentary: The Materials Project: A materials genome approach to accelerating materials innovation. *APL Materials* **2013,** *1* (1), 011002.

214. Lepley, N. D.; Holzwarth, N. A. W., Modeling interfaces between solids: Application to Li battery materials. *Physical Review B* **2015,** *92* (21), 214201.

215. Lazar, P.; Redinger, J.; Podloucky, R., Density functional theory applied to VN/TiN multilayers. *Physical Review B* **2007,** *76* (17), 174112.

216. Wenzel, S.; Randau, S.; Leichtweiß, T.; Weber, D. A.; Sann, J.; Zeier, W. G.; Janek, J., Direct Observation of the Interfacial Instability of the Fast Ionic Conductor Li10GeP2S12 at the Lithium Metal Anode. *Chemistry of Materials* **2016,** *28* (7), 2400-2407.

217. Wenzel, S.; Weber, D. A.; Leichtweiss, T.; Busche, M. R.; Sann, J.; Janek, J., Interphase formation and degradation of charge transfer kinetics between a lithium metal anode and highly crystalline Li7P3S11 solid electrolyte. *Solid State Ionics* **2016,** *286*, 24-33.

218. Zeilinger, M.; Fassler, T. F., Structural and thermodynamic similarities of phases in the Li-Tt (Tt = Si, Ge) systems: redetermination of the lithium-rich side of the Li-Ge phase diagram and crystal structures of Li17Si4.0-xGex for x = 2.3, 3.1, 3.5, and 4 as well as Li4.1Ge. *Dalton Transactions* **2014,** *43* (40), 14959-14970.

219. Nazri, G. A.; Julien, C.; Mavi, H. S., Structure of Li3X (X = N, P, As) superionic conductors: X-ray diffraction and FTIR studies. *Solid State Ionics* **1994,** *70-71*, 137-143.

220. Kim, B. S. D.-H.; Lee, M. S. B.; Park, K.-Y.; Kang, K., First-principles Study on the Charge Transport Mechanism of Lithium Sulfide (Li2S) in Lithium-Sulfur Batteries. *Chemistry – An Asian Journal* **2016,** *11* (8), 1288-1292.

221. Kang, J.; Han, B., First-Principles Characterization of the Unknown Crystal Structure and Ionic Conductivity of Li7P2S8I as a Solid Electrolyte for High-Voltage Li Ion Batteries. *The Journal of Physical Chemistry Letters* **2016,** *7* (14), 2671-2675.

222. Rangasamy, E.; Liu, Z.; Gobet, M.; Pilar, K.; Sahu, G.; Zhou, W.; Wu, H.; Greenbaum, S.; Liang, C., An Iodide-Based Li7P2S8I Superionic Conductor. *Journal of the American Chemical Society* **2015,** *137* (4), 1384-1387.

223. Yu, C.; van Eijck, L.; Ganapathy, S.; Wagemaker, M., Synthesis, structure and electrochemical performance of the argyrodite Li6PS5Cl solid electrolyte for Li-ion solid state batteries. *Electrochimica Acta* **2016,** *215*, 93-99.

224. Kamphaus, E. P.; Angarita-Gomez, S.; Qin, X.; Shao, M.; Engelhard, M.; Mueller, K. T.; Murugesan, V.; Balbuena, P. B., Role of Inorganic Surface Layer on Solid Electrolyte Interphase Evolution at Li-Metal Anodes. *ACS Applied Materials & Interfaces* **2019**.

225. Duncan, H.; Abu-Lebdeh, Y.; Davidson, I. J., Study of the Cathode–Electrolyte Interface of LiMn1.5Ni0.5O4 Synthesized by a Sol–Gel Method for Li-Ion Batteries. *Journal of The Electrochemical Society* **2010,** *157* (4), A528-A535.

226. Qin, X.; Balbuena, P. B.; Shao, M., First-Principles Study on the Initial Oxidative Decompositions of Ethylene Carbonate on Layered Cathode Surfaces of Lithium-Ion Batteries. *The Journal of Physical Chemistry C* **2019,** *123* (23), 14449-14458.

227. Liu, S.; Liu, D.; Wang, S.; Cai, X.; Qian, K.; Kang, F.; Li, B., Understanding the cathode electrolyte interface formation in aqueous electrolyte by scanning electrochemical microscopy. *Journal of Materials Chemistry A* **2019,** *7* (21), 12993-12996.

228. Yu, X.; Manthiram, A., Electrode–Electrolyte Interfaces in Lithium–Sulfur Batteries with Liquid or Inorganic Solid Electrolytes. *Accounts of Chemical Research* **2017,** *50* (11), 2653-2660.

229. Haruyama, J.; Sodeyama, K.; Han, L.; Takada, K.; Tateyama, Y., Space–Charge Layer Effect at Interface between Oxide Cathode and Sulfide Electrolyte in All-Solid-State Lithium-Ion Battery. *Chemistry of Materials* **2014,** *26* (14), 4248-4255.

230. Tian, Y.; Shi, T.; Richards, W. D.; Li, J.; Kim, J. C.; Bo, S.-H.; Ceder, G., Compatibility issues between electrodes and electrolytes in solid-state batteries. *Energy & Environmental Science* **2017,** *10* (5), 1150-1166.

231. Galvez-Aranda, D. E.; Seminario, J. M., Ab Initio Study of the Interface of the Solid-State Electrolyte Li9N2Cl3 with a Li-Metal Electrode. *Journal of The Electrochemical Society* **2019,** *166* (10), A2048-A2057.

232. Camacho-Forero, L. E.; Balbuena, P. B., Exploring interfacial stability of solid-state electrolytes at the lithium-metal anode surface. *Journal of Power Sources* **2018,** *396*, 782-790.

233. Arneson, C.; Wawrzyniakowski, Z. D.; Postlewaite, J. T.; Ma, Y., Lithiation and Delithiation Processes in Lithium–Sulfur Batteries from Ab Initio Molecular Dynamics Simulations. *The Journal of Physical Chemistry C* **2018,** *122* (16), 8769-8779.

234. Momma, K.; Izumi, F., VESTA 3 for three-dimensional visualization of crystal, volumetric and morphology data. *Journal of Applied Crystallography* **2011,** *44* (6), 1272-1276.

235. Stukowski, A., Visualization and analysis of atomistic simulation data with OVITO–the Open Visualization Tool. *Modelling and Simulation in Materials Science and Engineering* **2009,** *18* (1), 015012.

236. Krukau, A. V.; Vydrov, O. A.; Izmaylov, A. F.; Scuseria, G. E., Influence of the exchange screening parameter on the performance of screened hybrid functionals. *The Journal of Chemical Physics* **2006,** *125* (22), 224106.

237. Wang, Z.; Shao, G., Theoretical design of solid electrolytes with superb ionic conductivity: alloying effect on Li+ transportation in cubic Li6PA5X chalcogenides. *Journal of Materials Chemistry A* **2017,** *5* (41), 21846-21857.

238. Yang, J.; Tse, J. S., First-principles molecular simulations of Li diffusion in solid electrolytes Li3PS4. *Computational Materials Science* **2015,** *107*, 134-138.

239. Deng, Z.; Zhu, Z.; Chu, I.-H.; Ong, S. P., Data-Driven First-Principles Methods for the Study and Design of Alkali Superionic Conductors. *Chemistry of Materials* **2017,** *29* (1), 281-288.

240. He, X.; Zhu, Y.; Epstein, A.; Mo, Y., Statistical variances of diffusional properties from ab initio molecular dynamics simulations. *npj Computational Materials* **2018,** *4* (1), 18.

241. Hinsen, K.; Pellegrini, E.; Stachura, S.; Kneller, G. R., nMoldyn 3: Using task farming for a parallel spectroscopy-oriented analysis of molecular dynamics simulations. *Journal of Computational Chemistry* **2012,** *33* (25), 2043-2048.

242. Yamamoto, T.; Phuc, N. H. H.; Muto, H.; Matsuda, A., Preparation of Li7P2S8I Solid Electrolyte and Its Application in All-Solid-State Lithium-Ion Batteries with Graphite Anode. *Electronic Materials Letters* **2019,** *15* (4), 409-414.

243. Rao, R. P.; Adams, S., Studies of lithium argyrodite solid electrolytes for all-solid-state batteries. *Physica Status Solidi (A)* **2011,** *208* (8), 1804-1807.

244. Hayamizu, K.; Aihara, Y.; Watanabe, T.; Yamada, T.; Ito, S.; Machida, N., NMR studies on lithium ion migration in sulfide-based conductors, amorphous and crystalline Li3PS4. *Solid State Ionics* **2016,** *285*, 51-58.

245. Deiseroth, H.-J.; Maier, J.; Weichert, K.; Nickel, V.; Kong, S.-T.; Reiner, C., Li7PS6 and Li6PS5X (X: Cl, Br, I): Possible Three-dimensional Diffusion Pathways for Lithium Ions and Temperature Dependence of the Ionic Conductivity by Impedance Measurements. *Zeitschrift für anorganische und allgemeine Chemie* **2011,** *637* (10), 1287-1294.

246. Boulineau, S.; Courty, M.; Tarascon, J.-M.; Viallet, V., Mechanochemical synthesis of Li-argyrodite Li6PS5X (X=Cl, Br, I) as sulfur-based solid electrolytes for all solid state batteries application. *Solid State Ionics* **2012,** *221*, 1-5.

247. Xie, D.; Chen, S.; Zhang, Z.; Ren, J.; Yao, L.; Wu, L.; Yao, X.; Xu, X., High ion conductive Sb2O5-doped β-Li3PS4 with excellent stability against Li for all-solid-state lithium batteries. *Journal of Power Sources* **2018,** *389*, 140-147.

248. Cao, Y.; Zuo, P.; Lou, S.; Sun, Z.; Li, Q.; Huo, H.; Ma, Y.; Du, C.; Gao, Y.; Yin, G., A quasi-solid-state Li–S battery with high energy density, superior stability and safety. *Journal of Materials Chemistry A* **2019,** *7* (11), 6533-6542.

249. Perez Beltran, S.; Balbuena, P. B., Formation of Multilayer Graphene Domains with Strong Sulfur–Carbon Interaction and Enhanced Sulfur Reduction Zones for Lithium–Sulfur Battery Cathodes. *ChemSusChem* **2018,** *11* (12), 1970-1980.

250. Grimme, S.; Ehrlich, S.; Goerigk, L., Effect of the damping function in dispersion corrected density functional theory. *Journal of Computational Chemistry* **2011,** *32* (7), 1456-1465.

251. Park, H.; Koh, H. S.; Siegel, D. J., First-Principles Study of Redox End Members in Lithium–Sulfur Batteries. *The Journal of Physical Chemistry C* **2015,** *119* (9), 4675-4683.

252. Finnis, M. W., The theory of metal - ceramic interfaces. *Journal of Physics: Condensed Matter* **1996,** *8* (32), 5811-5836.

253. He, C.; Cheng, M.; Zhang, M.; Zhang, W. X., Interfacial Stability and Electronic Properties of Ag/M (M = Ni, Cu, W, and Pd) and Cu/Cr Interfaces. *The Journal of Physical Chemistry C* **2018,** *122* (31), 17928-17935.

254. Fan, X.; Ji, X.; Han, F.; Yue, J.; Chen, J.; Chen, L.; Deng, T.; Jiang, J.; Wang, C., Fluorinated solid electrolyte interphase enables highly reversible solid-state Li metal battery. *Science Advances* **2018,** *4* (12), eaau9245.

255. Tan, D. H. S.; Wu, E. A.; Nguyen, H.; Chen, Z.; Marple, M. A. T.; Doux, J.-M.; Wang, X.; Yang, H.; Banerjee, A.; Meng, Y. S., Elucidating Reversible Electrochemical Redox of Li6PS5Cl Solid Electrolyte. *ACS Energy Letters* **2019**.

256. Nagai, E.; Arthur, T. S.; Bonnick, P.; Suto, K.; Muldoon, J., The Discharge Mechanism for Solid-State Lithium-Sulfur Batteries. *MRS Advances* **2019**, 1-8.

257. Lin, Z.; Liu, Z.; Fu, W.; Dudney, N. J.; Liang, C., Lithium Polysulfidophosphates: A Family of Lithium-Conducting Sulfur-Rich Compounds for Lithium–Sulfur Batteries. *Angewandte Chemie International Edition* **2013,** *52* (29), 7460-7463.

258. Riphaus, N.; Stiaszny, B.; Beyer, H.; Indris, S.; Gasteiger, H. A.; Sedlmaier, S. J., Editors' Choice—Understanding Chemical Stability Issues between Different Solid Electrolytes in All-Solid-State Batteries. *Journal of The Electrochemical Society* **2019,** *166* (6), A975-A983.

259. Koerver, R.; Walther, F.; Aygün, I.; Sann, J.; Dietrich, C.; Zeier, W. G.; Janek, J., Redox-active cathode interphases in solid-state batteries. *Journal of Materials Chemistry A* **2017,** *5* (43), 22750-22760.

260. Yue, J.; Yan, M.; Yin, Y.-X.; Guo, Y.-G., Progress of the Interface Design in All-Solid-State Li–S Batteries. *Advanced Functional Materials* **2018,** *28* (38), 1707533.

261. Walther, F.; Koerver, R.; Fuchs, T.; Ohno, S.; Sann, J.; Rohnke, M.; Zeier, W. G.; Janek, J., Visualization of the Interfacial Decomposition of Composite Cathodes in Argyrodite-Based All-Solid-State Batteries Using Time-of-Flight Secondary-Ion Mass Spectrometry. *Chemistry of Materials* **2019,** *31* (10), 3745-3755.

262. Xiao, P.; Henkelman, G., Kinetic Monte Carlo Study of Li Intercalation in LiFePO4. *ACS Nano* **2018,** *12* (1), 844-851.

263. Fang, C.; Wang, X.; Meng, Y. S., Key Issues Hindering a Practical Lithium-Metal Anode. *Trends in Chemistry* **2019,** *1* (2), 152-158.

264. Lim, M.-S.; Jhi, S.-H., First-principles study of lithium-ion diffusion in β-Li3PS4 for solid-state electrolytes. *Current Applied Physics* **2018,** *18* (5), 541-545.

265. de Klerk, N. J. J.; van der Maas, E.; Wagemaker, M., Analysis of Diffusion in Solid-State Electrolytes through MD Simulations, Improvement of the Li-Ion Conductivity in β-Li3PS4 as an Example. *ACS Applied Energy Materials* **2018,** *1* (7), 3230-3242.

266. Rao, R. P.; Sharma, N.; Peterson, V. K.; Adams, S., Formation and conductivity studies of lithium argyrodite solid electrolytes using in-situ neutron diffraction. *Solid State Ionics* **2013,** *230*, 72-76.

267. Yu, C.; Ganapathy, S.; de Klerk, N. J. J.; Roslon, I.; van Eck, E. R. H.; Kentgens, A. P. M.; Wagemaker, M., Unravelling Li-Ion Transport from Picoseconds to Seconds: Bulk versus Interfaces in an Argyrodite Li6PS5Cl–Li2S All-Solid-State Li-Ion Battery. *Journal of the American Chemical Society* **2016,** *138* (35), 11192-11201.

268. Choi, S.-J.; Lee, S.-H.; Ha, Y.-C.; Yu, J.-H.; Doh, C.-H.; Lee, Y.; Park, J.-W.; Lee, S.-M.; Shin, H.-C., Synthesis and Electrochemical Characterization of a Glass-Ceramic Li7P2S8I Solid Electrolyte for All-Solid-State Li-Ion Batteries. *Journal of The Electrochemical Society* **2018,** *165* (5), A957-A962.

APPENDIX A

SUPPORTING INFORMATION FOR CHAPTER 3*

A.1 Supporting Computational Details

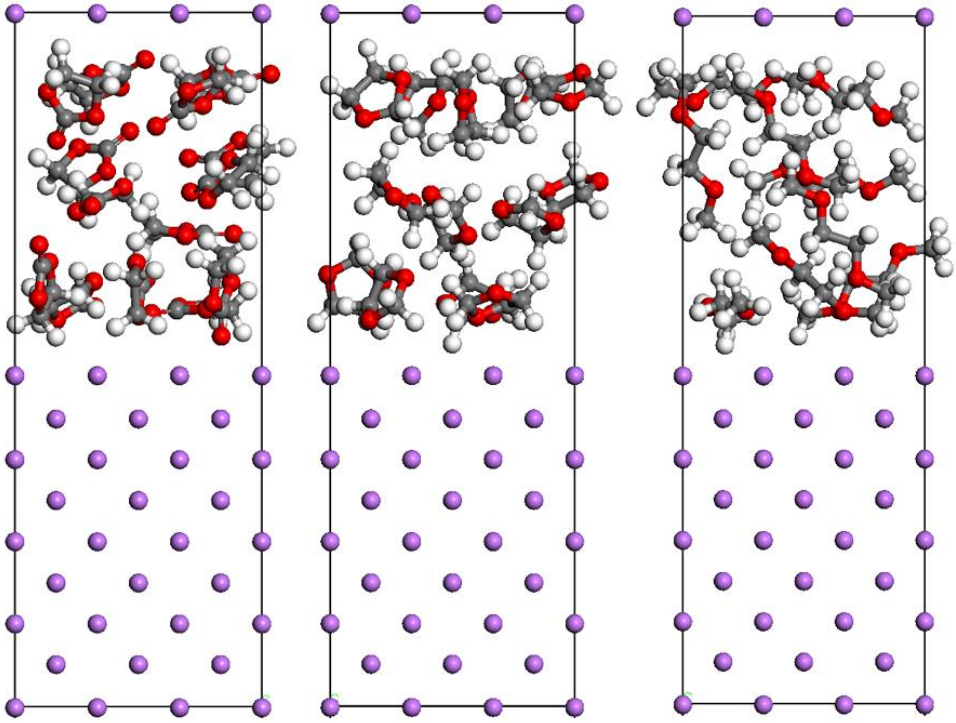

Figure A.1 Initial configurations used for AIMD simulations of pure solvents. Left: EC/Li(100); middle: DOL/Li(100); Right: DME/Li(100).

* Supporting Information reprinted with permission from:

Luis E. Camacho-Forero, Taylor W. Smith, Samuel Bertolini, and Perla B. Balbuena. "Reactivity at the Lithium-Metal Anode Surface of Lithium-Sulfur Batteries." *The Journal of Physical Chemistry C*, 2015, **119** (48), 26828-26839. Copyright © 2015 American Chemical Society.

Manjula I. Nandasiri, Luis E. Camacho-Forero, Ashleigh M. Schwarz, Vaithiyalingam Shutthanandan, Suntharampillai Thevuthasan, Perla B. Balbuena, Karl T. Mueller, and Vijayakumar Murugesan. "In Situ Chemical Imaging of Solid-Electrolyte Interphase Layer Evolution in Li-S Batteries." *Chemistry of Materials*, 2017, **29** (11), 4728-4737. Copyright © 2017 American Chemical Society.

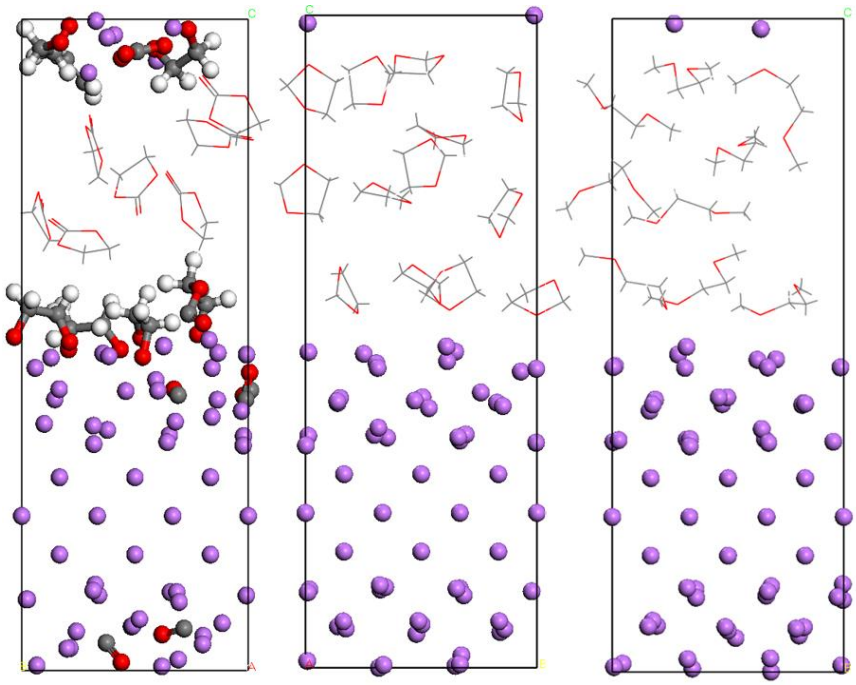

Figure A.2 Final configurations after 20ps of AIMD simulations of pure solvents. Left: EC/Li(100); middle: DOL/Li(100); Right: DME/Li(100). Lines figures illustrate non-reduced molecules. Balls and sticks depict fragments of reduced EC.

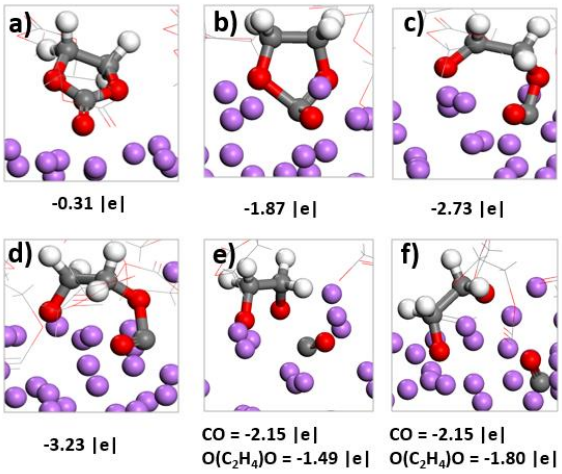

Figure A.3 Decomposition of an EC molecule on the lithium surface, following reactions 2 and 3. (a) Initially, EC is adsorbed via Li-O interaction. (b, c) Two electrons are transferred from the surface leading a C_1-O_2 bond to break, forming $\mathbf{O(C_2H_4)OCO^{2-}}$. (d-f) A few hundred femtoseconds later, two more electrons are transferred to the $\mathbf{O(C_2H_4)OCO^{2-}}$, forming $\mathbf{O(C_2H_4)O^{2-}}$ and $\mathbf{CO^{2-}}$ which remain strongly adsorbed on the surface for the rest of the simulated time. Interestingly, the formed CO^{2-} seems to diffuse into the lithium surface anode. Calculated Bader charges for the different species are also shown below each panel.

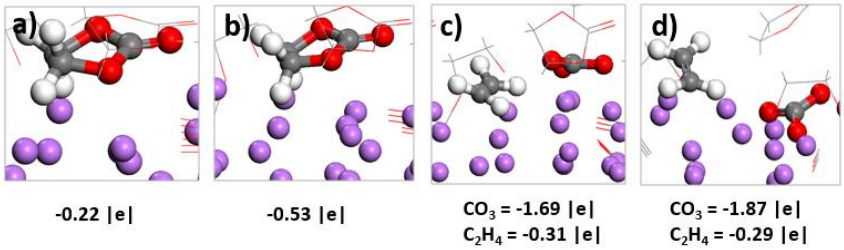

Figure A.4 Decomposition of an EC molecule on the lithium surface, following the reactions 4 and 5. (a, b) Initially, one single electron is transferred from the surface to the EC. (c, d) A second electron is transferred leading to break both O_2-C_2 bonds. The charge analysis suggests that the formed C_2H_4 and CO_3^{2-} remain adsorbed on the surface.

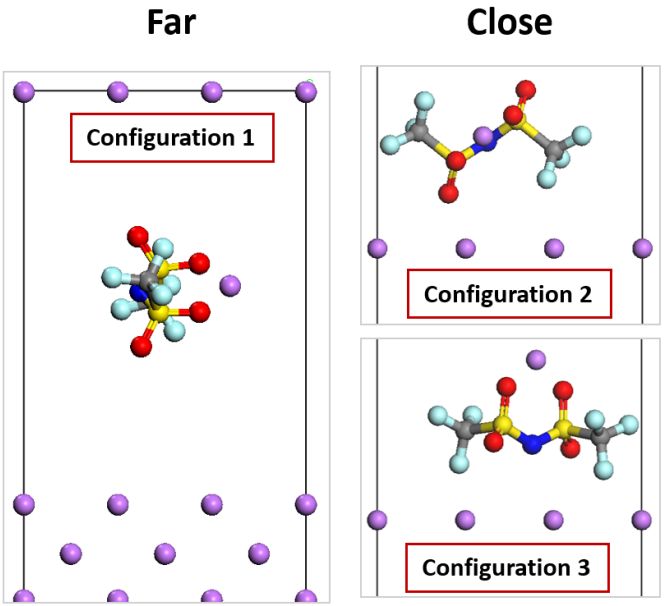

Figure A.5 Initial LiTFSI configurations used for AIMD simulations of mixtures solvent/salt. Right: close to Li anode; Left: far from it.

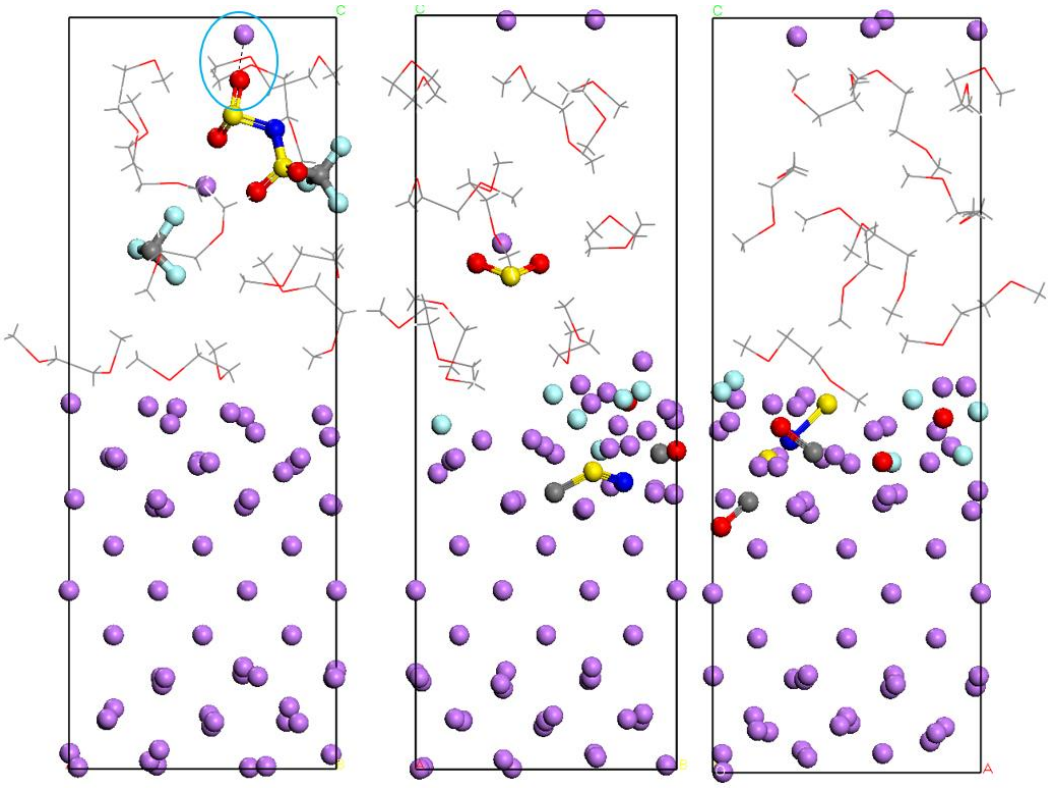

Figure A.6 Configuration of the system after 20ps of AIMD simulation of mixtures DME/LiTFSI. Left: configuration 1; Middle: configuration 2; Right: configuration 3. Lines figures illustrate non-reduced molecules. Balls and sticks depict fragments of reduced LiTFSI.

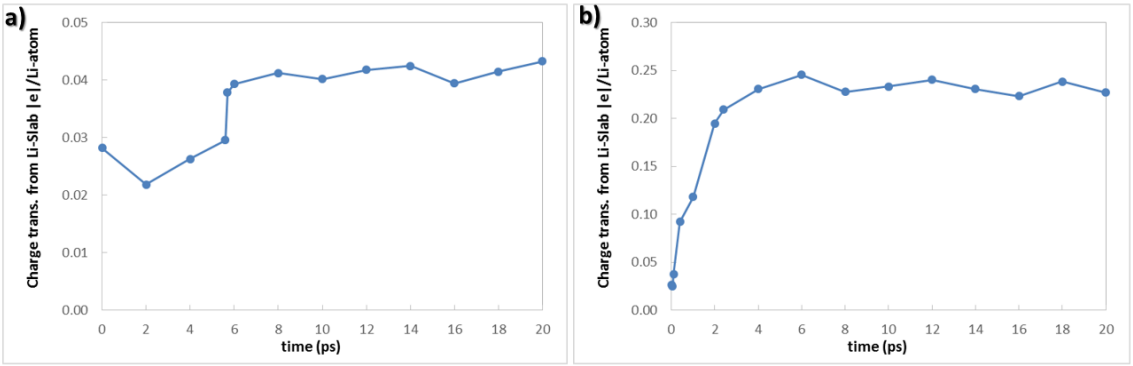

Figure A.7 Net charge evolution of the lithium-metal anode interacting with the DME/LiTFSI electrolyte during 20 ps of simulation, in which the salt is (a) initially far from the surface and (b) close to it.

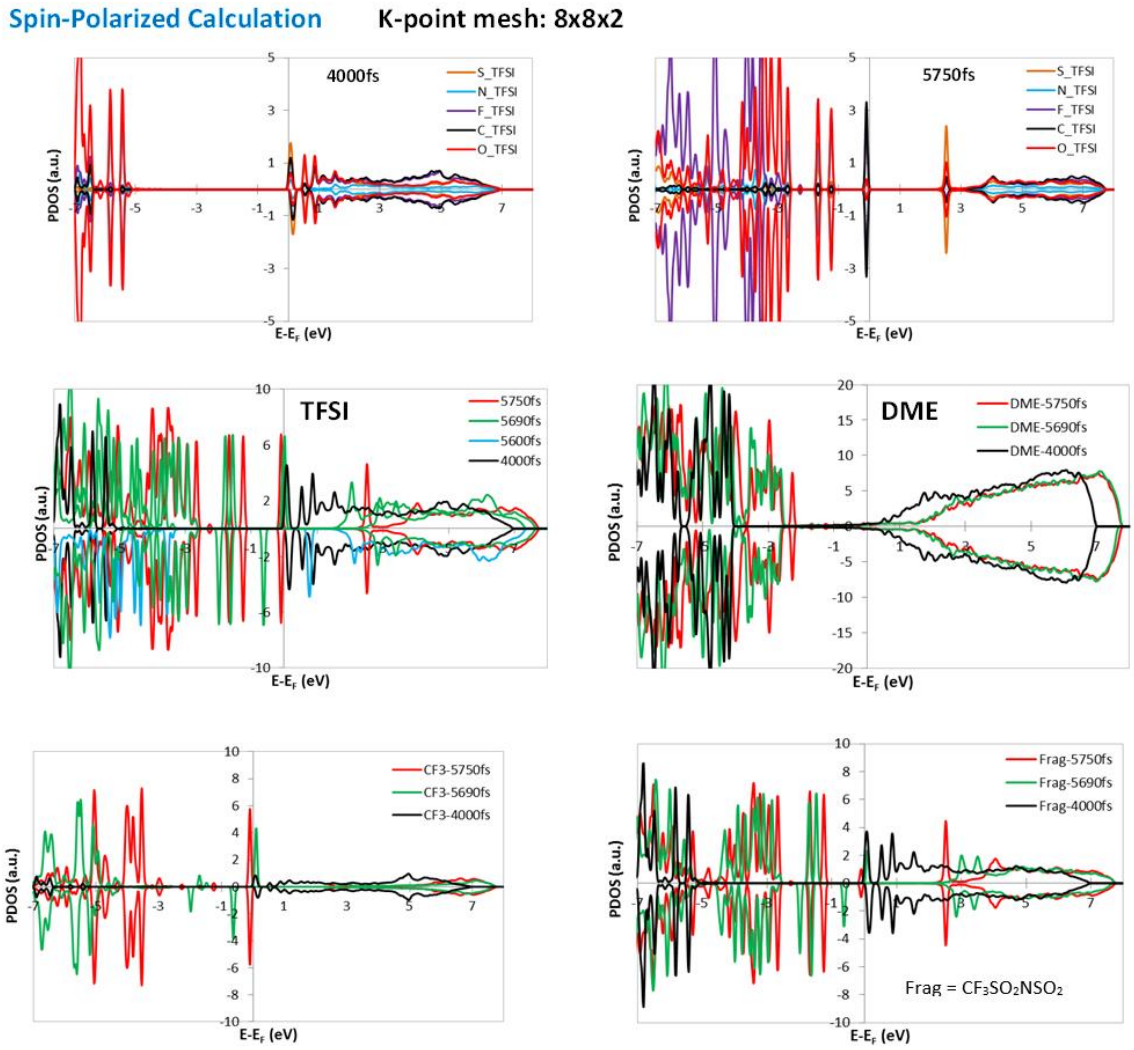

Figure A.8 Calculated density of states from snapshots of the reaction depicted in Figure 3.3 at different stages indicated by the times: 4000 fs (before the reaction started) and > 5600 fs during the reaction.

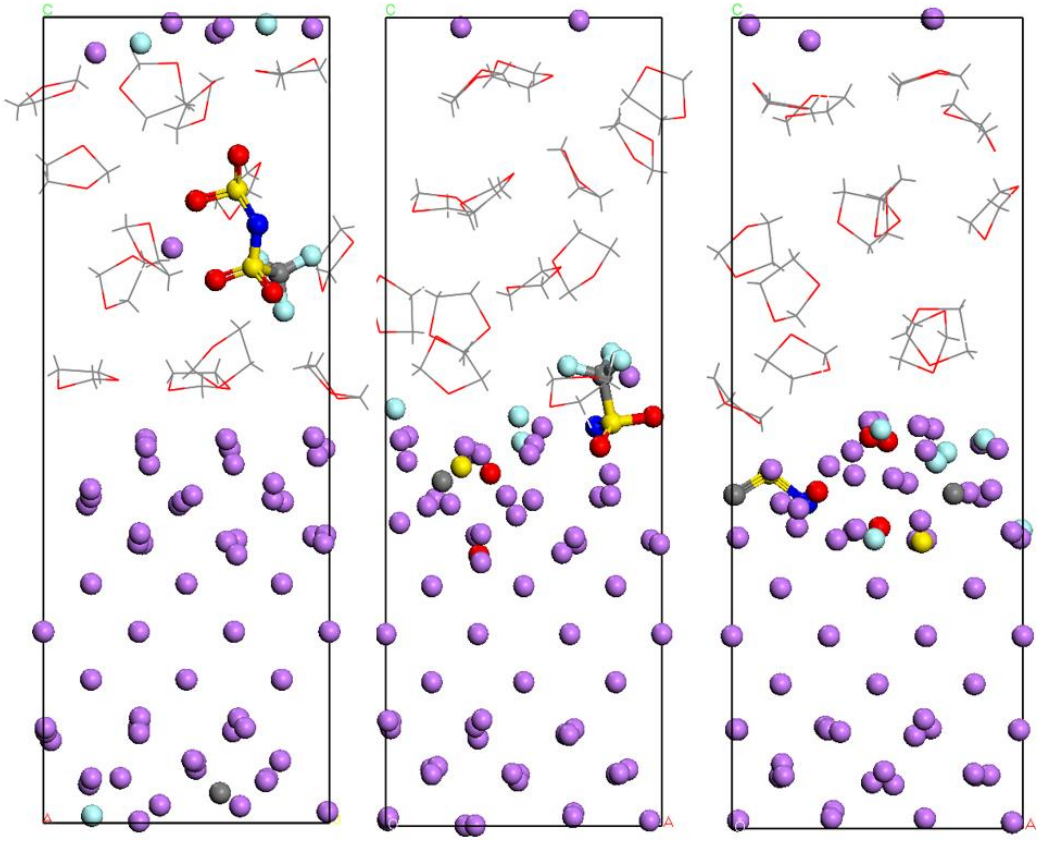

Figure A.9 Configuration of the system after 20ps of AIMD simulation of mixtures DOL/LiTFSI. Left: configuration 1; Middle: configuration 2; Right: configuration 3. Lines figures illustrate non-reduced molecules. Balls and sticks depict fragments of reduced LiTFSI.

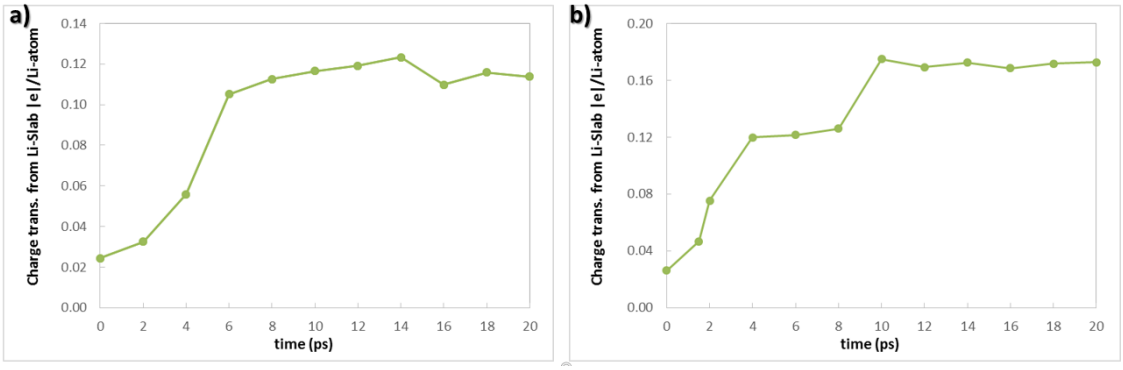

Figure A.10 Net charge evolution of the lithium-metal anode interacting with the DOL/LiTFSI electrolyte during 20 ps of simulation, in which the salt is (a) initially far from the surface and (b) close to it.

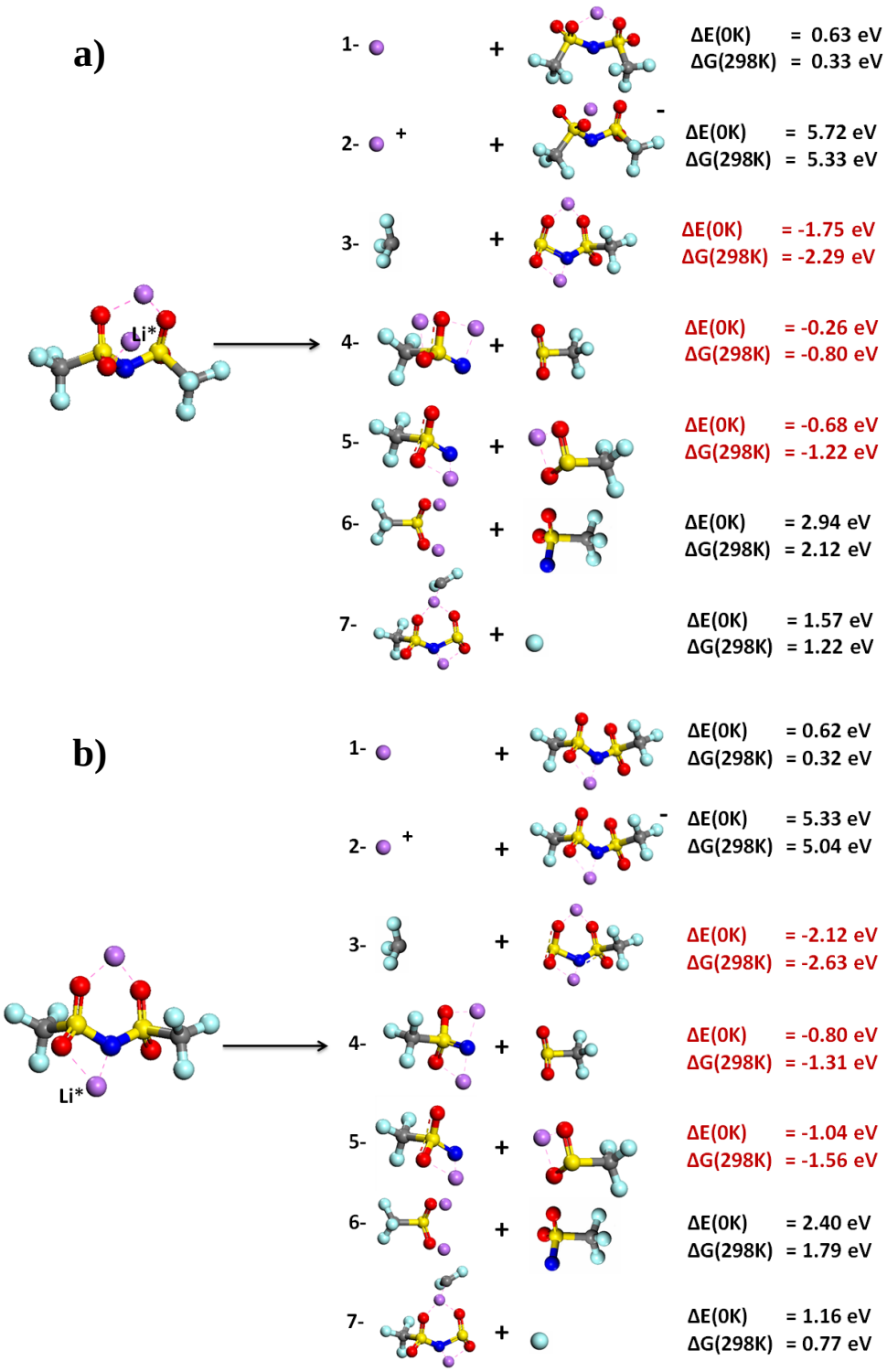

Figure A.11 Optimized geometries for reactions involving: a) Li-O and b) Li-N attack as reported in Table 3.2 (listed in order of appearance). Red font indicates a thermodynamically favorable reaction.

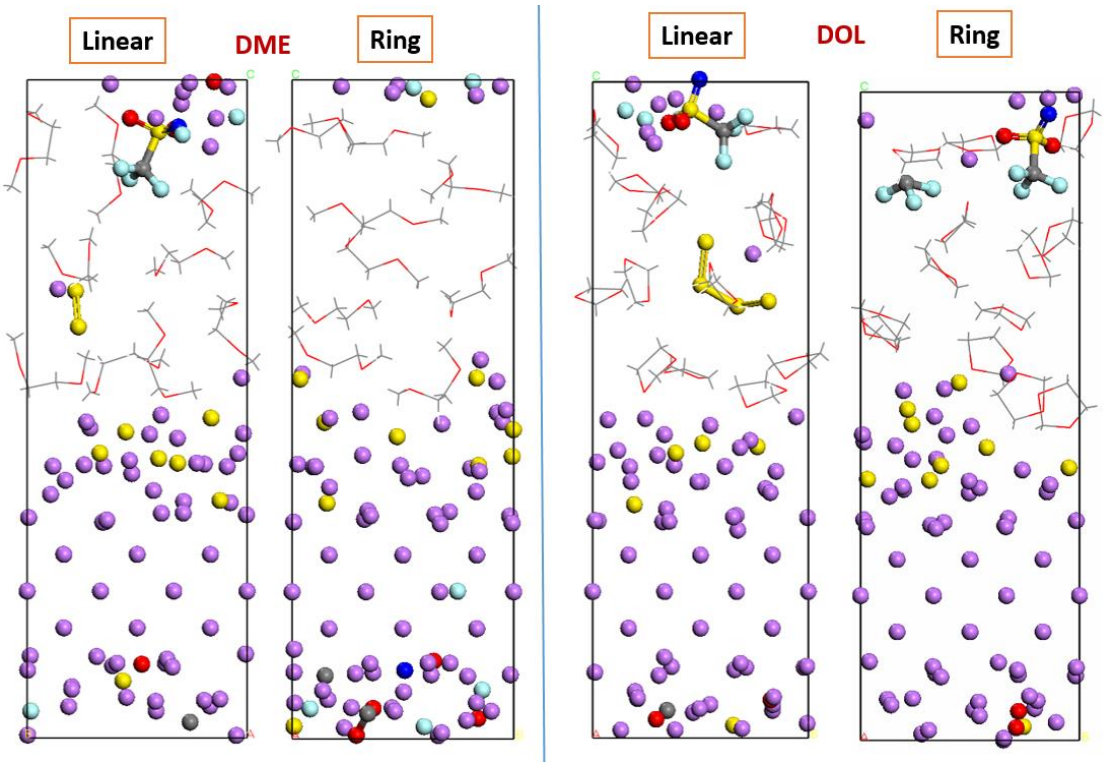

Figure A.12 Configuration of the system after 20ps of AIMD simulation of PS(right, linear)/Solvent(DME, DOL)/LiTFSI mixtures.

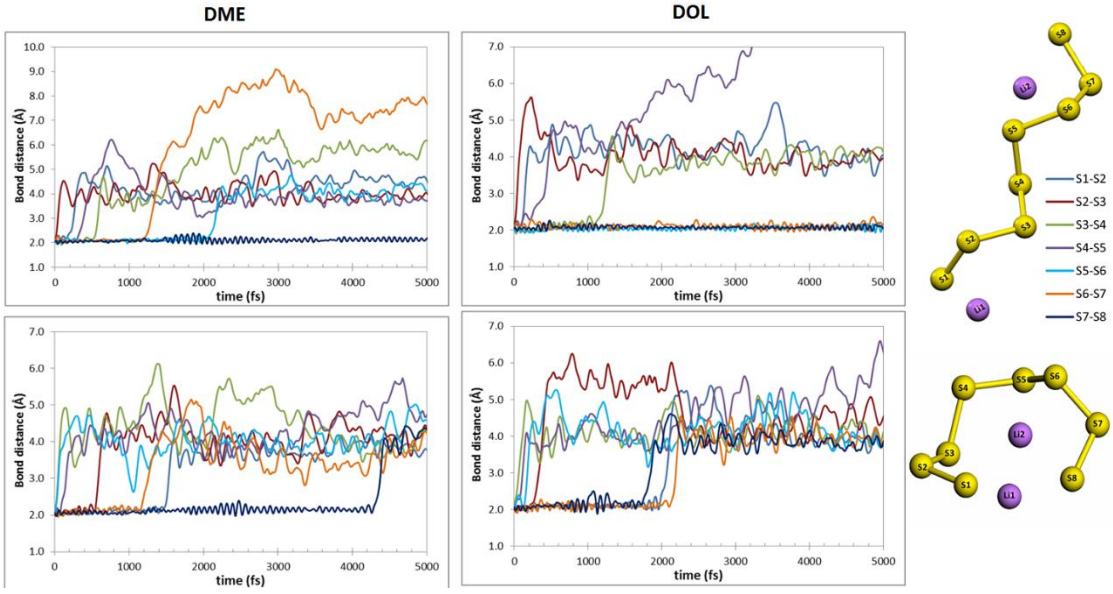

Figure A.13 S-S bond distance evolution in the PS for every case of study shown in Figure A.12.

A.2 Combining AIMD and *in situ* XPS techniques

In-situ XPS cell design and measurement

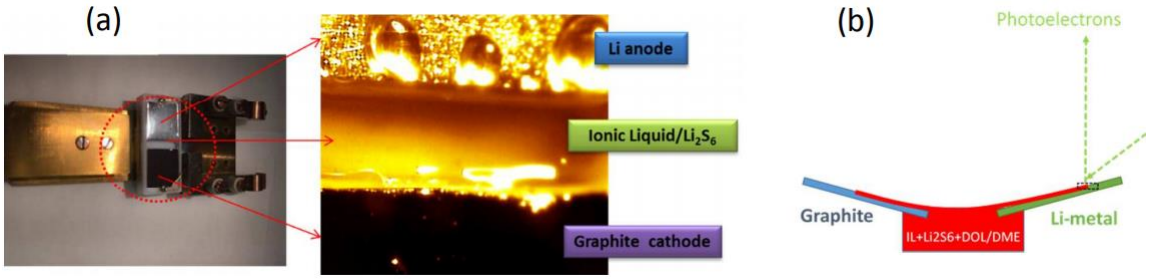

Figure A.14 The Li-S cell used for in-situ XPS characterization and the image of the anode, cathode, and electrolyte reservoir assembly and Schematic representation of XPS measurements on optimal Li-electrolyte interfacial regime.

The optimal electrode-electrolyte interfacial regime is chosen by placing the X-ray source on pure Li-metal and gradually moving towards the electrolyte until significant fluoride signal from TFSI anions is observed (see Figure A.14). The core-level XPS analyses were also carried out on graphite cathode-electrolyte interfaces. However, due to high wettability of the ionic liquid on graphite surfaces, the spectra are dominated by the ionic liquids as seen in Figure A.15.

S 2p core spectra analysis

Each species in S *2p* spectra is fitted as a doublet with binding energy separation of 1.16eV and peak intensity ratio of 0.511 to account for the spin-orbit components of $2p_{3/2}$ and $2p_{1/2}$. The S $2p_{3/2}$ of terminal sulfur (S_T^{1-}) and bridging sulfur (S_B^0) of lithium polysulfide (Li_2S_x with $x>1$) were observed at 161.6 and 163.3 eV. The S_B^0/S_T^{1-} represents the ratio of S $2p_{3/2}$ peak area and used as a qualitative indicator of polysulfide speciation.

All the peaks were fitted with Gauss-Lorentz fit and the peak area is used to calculate the atomic percentage of respective chemical species (see Table A.1 and Table A.2).

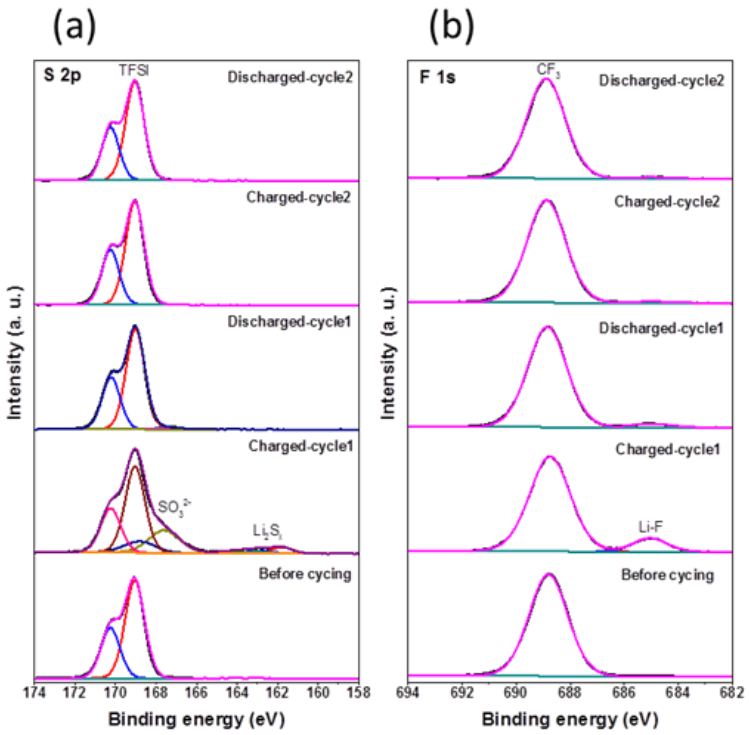

Figure A.15 The high-resolution XPS spectra of S 2p and F 1s at the graphite cathode before and after cycling.

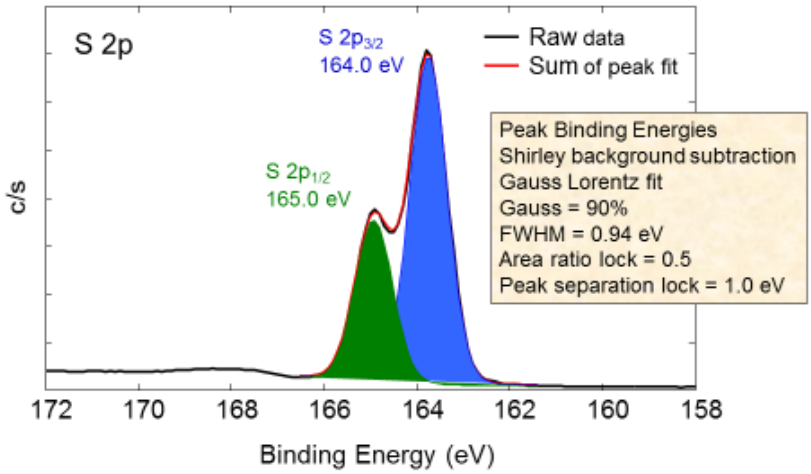

Figure A.16. The high-resolution XPS spectra of S 2p representing doublet arising from the spin-orbit components of $2p_{3/2}$ and $2p_{1/2}$. Also shown are the peak deconvolution constraints used in this study.

Table A.1. The atomic concentrations of sulfur species on the Li anode surface at each charged state.

Charged state	Concentration of S species (at.%)			
	TFSI	$SO_3^{2-}/S_2O_3^{2-}$	Li_2S_x (S_B^0 and S_T^{1-})	Li_2S (S^{2-})
before cycling	63	10	22	5
Charged-cycle1	53	12	30	5
Discharged-cycle1	27	14	49	10
Charged-cycle2	14	11	61	14
Discharged-cycle2	13	9	63	15

Table A.2. The atomic concentrations of fluorine species on the Li anode surface at each charged state.

Charged state	Concentration of F species (at.%)		
	CF_3	LiF	C-F
before cycling	89	11	0
Charged-cycle1	84	15	1
Discharged-cycle1	58	33	9
Charged-cycle2	46	44	10
Discharged-cycle2	42	47	11

Details about TFSI decomposition products and AIMD results

The following structures are extracted from the *ab initio* MD simulations of a 1M LiTFSI in DME or DOL electrolyte on a Li metal surface, see section 3.4.2. Li_2S_8 polysulfide species was included in some simulations (1M) to emulate the presence of PS at the anode side of the cell due to shuttle of long-chain of PS, see section 3.4.3. Several configurations and electrolyte components were studied. Our analysis is done on the basis of the products of electrolyte decomposition reactions near the metal surface, after 20ps of simulation. Fragments from the decomposition (anions or radical anions) are connected to Li ions and to other species (X) forming complexes of the type: X-Li-species-Li-X,

where the species can be atoms or fragments from the PS and salt decomposition: S, CO, NSO_2, F, C, O, N, CSO, and NS among others. Figures A.17-A.19 show the simulation cells after 20ps of AIMD simulations (left) and the extracted *X-Li-species-Li-X* configurations from the polysulfide and salt decomposition (side panels).

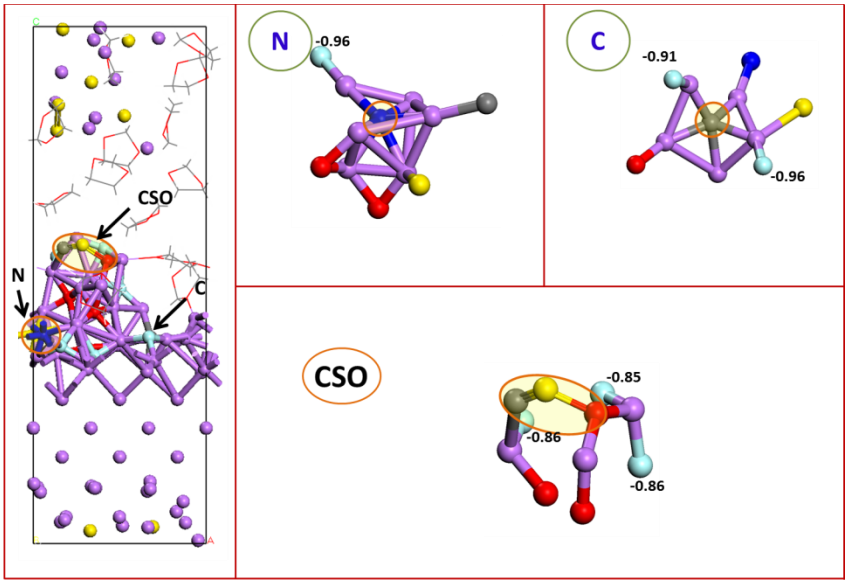

Figure A.17 Resulting structures from 20ps of AIMD simulations of 1M-LiTFSI in DOL (including 1M ring-Li_2S_8) electrolyte on a Li-anode. Electronic charges of F atoms are also given in extracted structures (panels on the right).

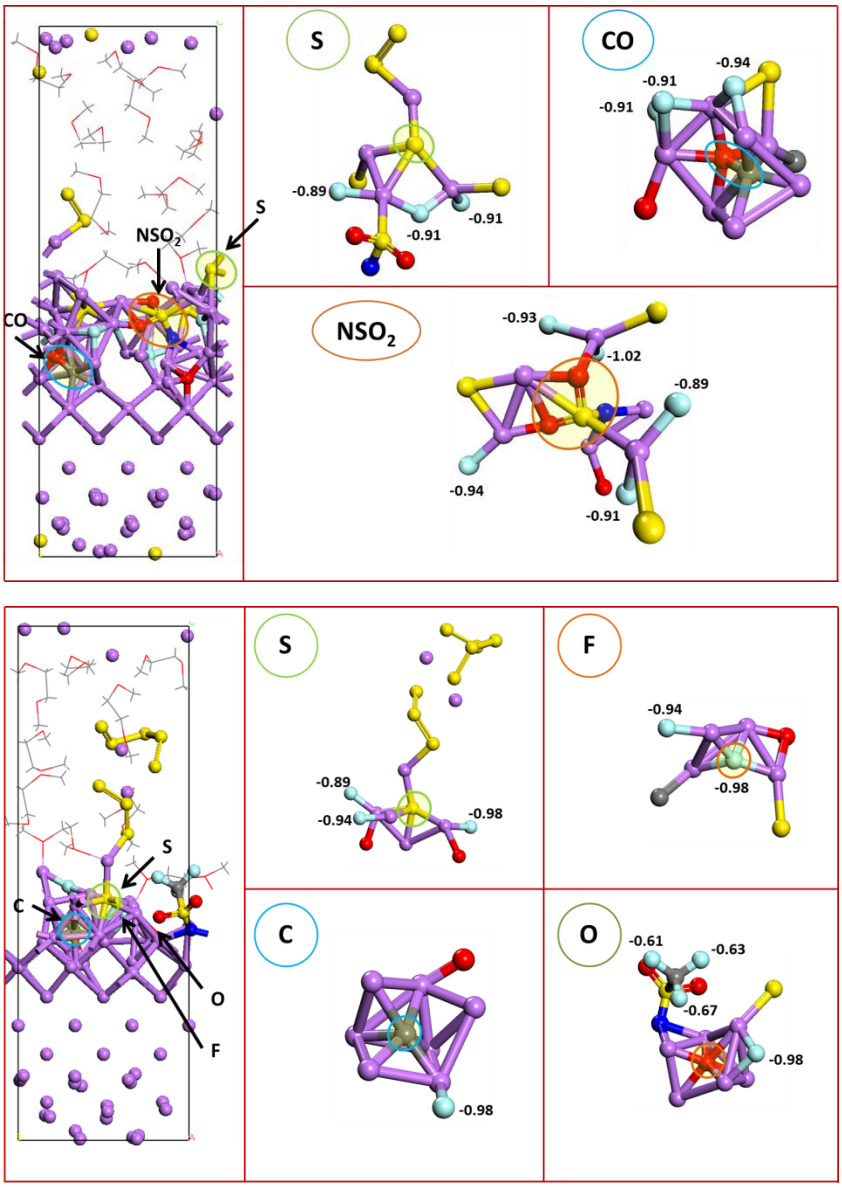

Figure A.18 Resulting structures from 20ps of AIMD simulations of 1M-LiTFSI in DME (including 1M Li_2S_8: linear (top) and ring (bottom)) electrolyte on a Li-metal surface. Electronic charges of F atoms are given in extracted structures (left panels).

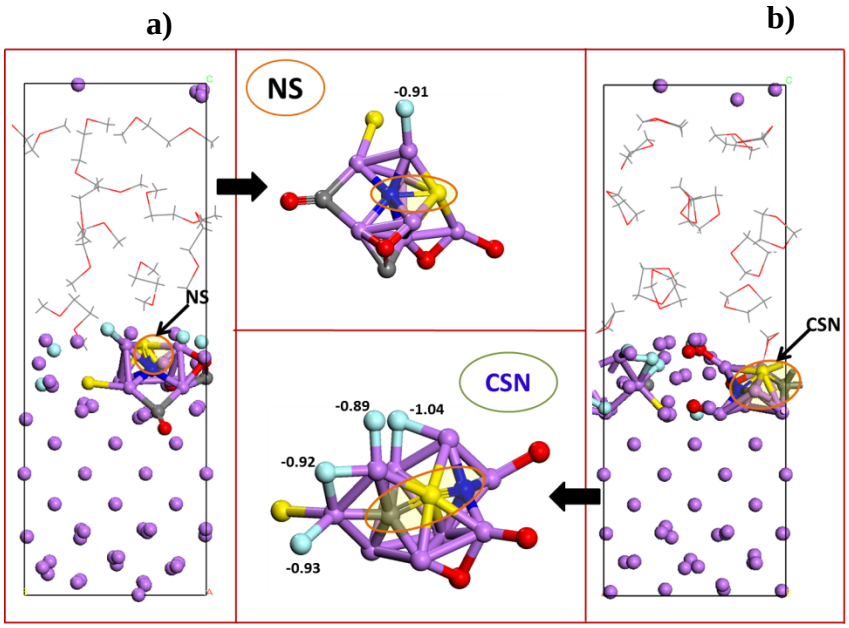

Figure A.19 Resulting structures from 20ps of AIMD simulations of 1M-LiTFSI in (a) DME (b) DOL. Electronic charges of F atoms are given in extracted structures (panels in the middle).

Imaging XPS analysis

The chemical imaging in larger window (800 X 800 μm) focused on IL droplet formed due to surface roughness of Li metal anode is used to visualize the TFSI anion decomposition process. The S 2p associated with sulfonyl groups and F 1s associated with CF_3 groups in pristine TFSI anion along with and F 1s associated with Li-F related species from decomposition reaction are monitored before and after first charging cycle (see Fig.S4). Following the 1st discharging cycle, the F 1s chemical state maps clearly show the decomposition of IL electrolyte with the decrease of intensity in CF_3 signal and replaced with Li-F related species intensity on the ionic liquid droplet. Interestingly S 2p map (Fig.S4) exhibits relatively less intensity drop after 1st discharging cycle indicating the sulfonyl groups tends to be more stable compared with the CF_3 groups of TFSI anion.

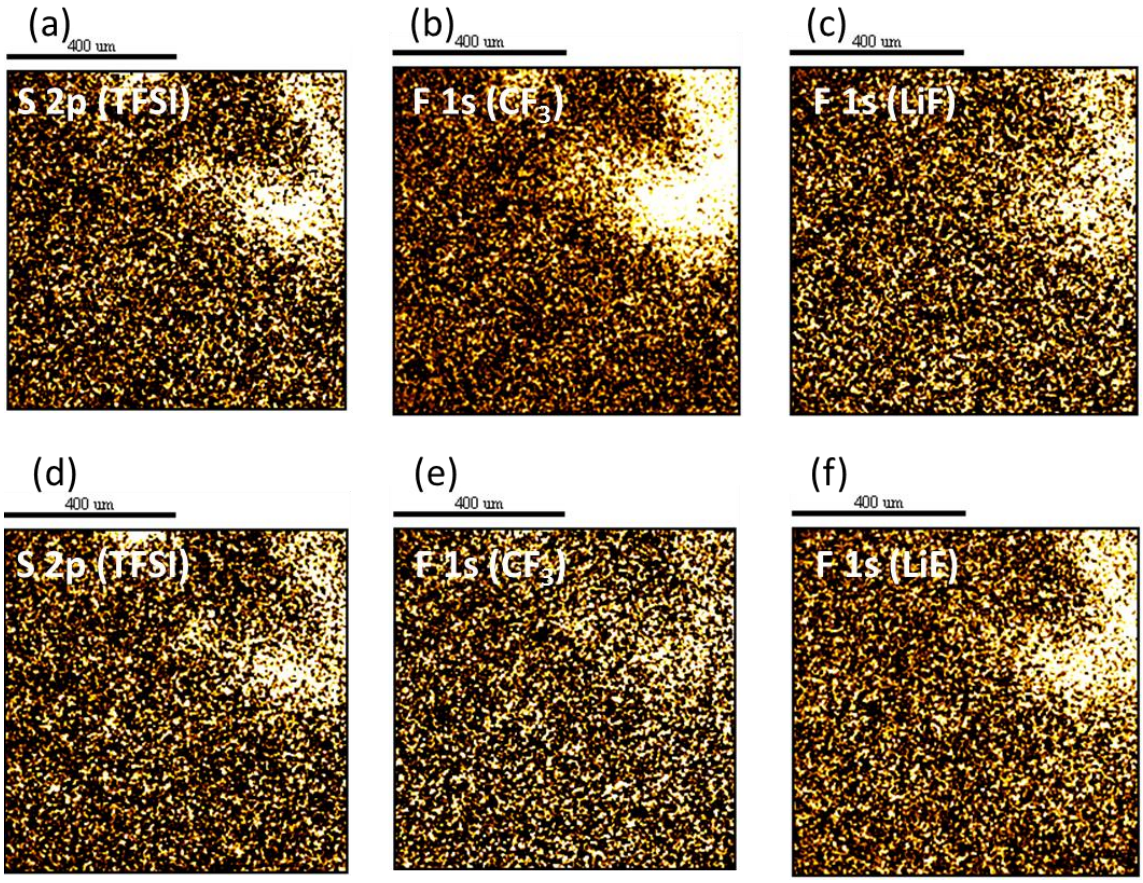

Figure A.20 The XPS chemical state maps of (a) S 2p (TFSI), (b) F 1s (CF3), and (c) F 1s (LiF) after 1st charging cycle and (d) S 2p (TFSI), (e) F 1s (CF3), and (f) F 1s (LiF) after 1st discharging cycle.

APPENDIX B

SUPPORTING INFORMATION FOR CHAPTER 4*

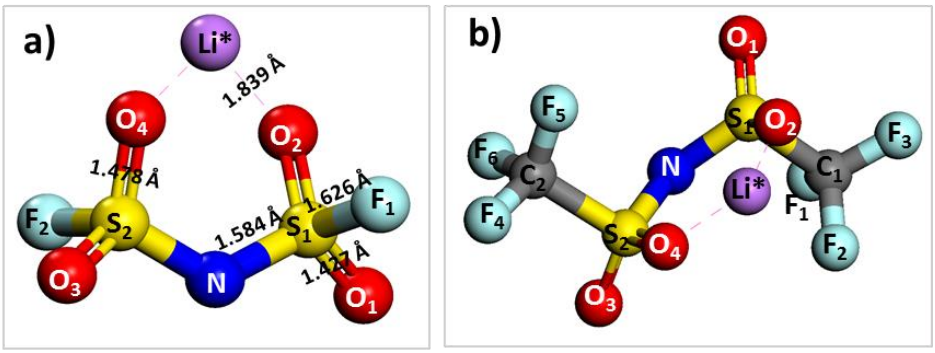

Figure B.1 Optimized structures of salt molecules: (a) LiFSI and (b) LiTFSI. Color code as in Figure 4.1.

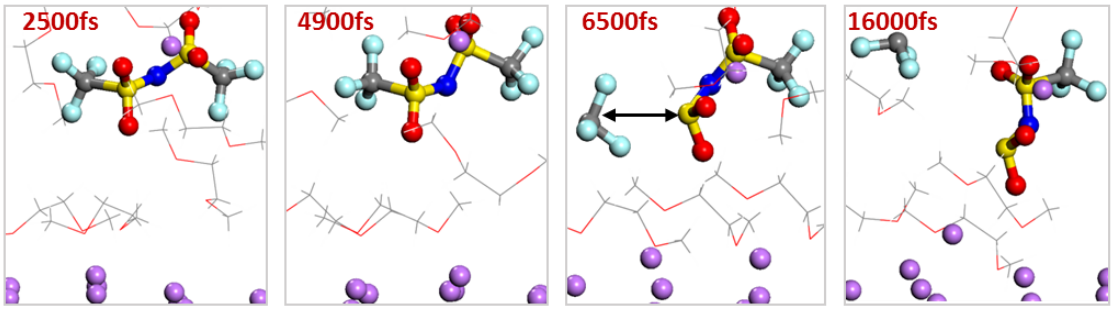

Figure B.2 1M-LiTFSI in DME reduction mechanism. Average charge of Li (from LiTFSI) is 0.88 (±0.01) |e| over the entire simulation time. Color code as in Figure 4.1.

* Supporting Information reprinted with permission from Luis E. Camacho-Forero, Taylor W. Smith, and Perla B. Balbuena. "Effects of High and Low Salt Concentration in Electrolytes at Lithium-Metal Anode Surfaces." *The Journal of Physical Chemistry C*, 2017, **121** (1), 182-194. Copyright © 2016 American Chemical Society.

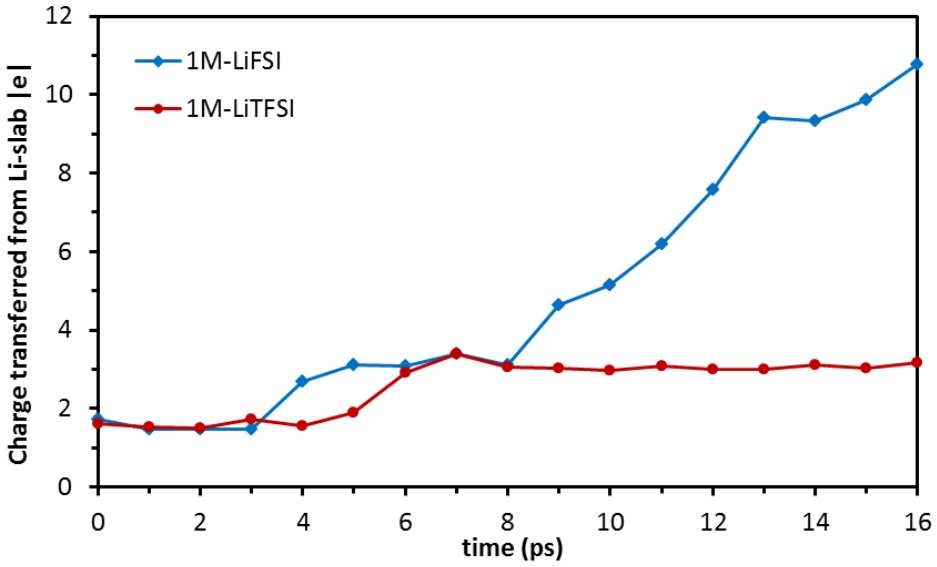

Figure B.3 Total **c**harge transfer from the Li anode to the electrolyte in 1M salt in DME. Non-zero initial charge (~2 |e|) is due to solvation/interaction of surface lithium atoms with the electrolyte from the initial model, see example in Figure B.10b.

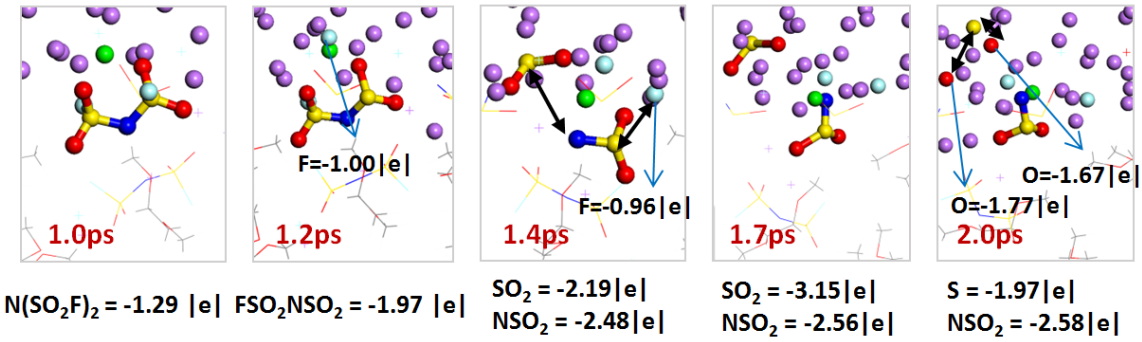

Figure B.4 2-LiFSI reduction mechanism in a 4M-LiFSI/DME solution. Average charge of Li (from LiFSI) 0.83 (±0.04) |e| over the entire simulation time. Color code as in Figure 4.1.

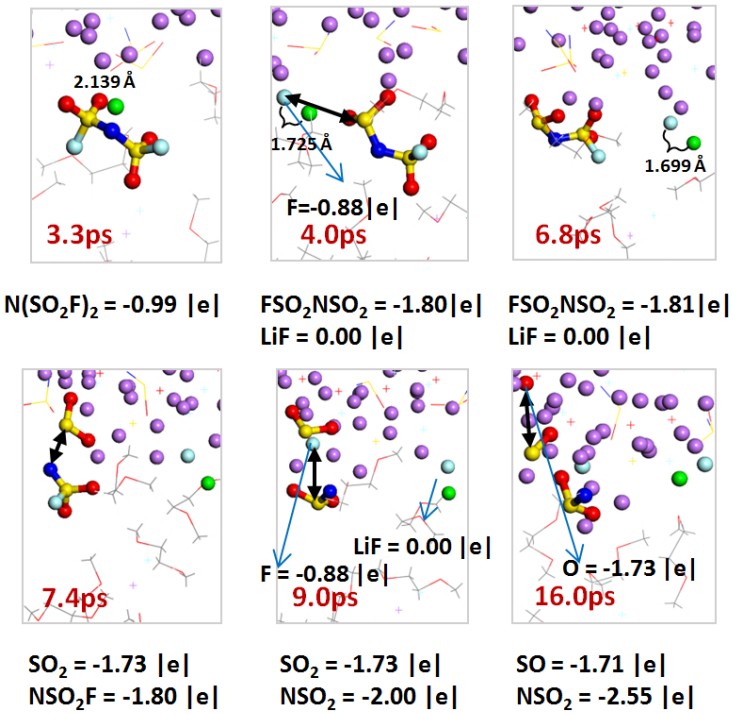

Figure B.5 3-LiFSI reduction mechanism in a 4M-LiFSI/DME solution. Average charge of Li (from LiFSI) 0.88 (±0.01) |e| over the entire simulation time. Color code as in Figure 4.1.

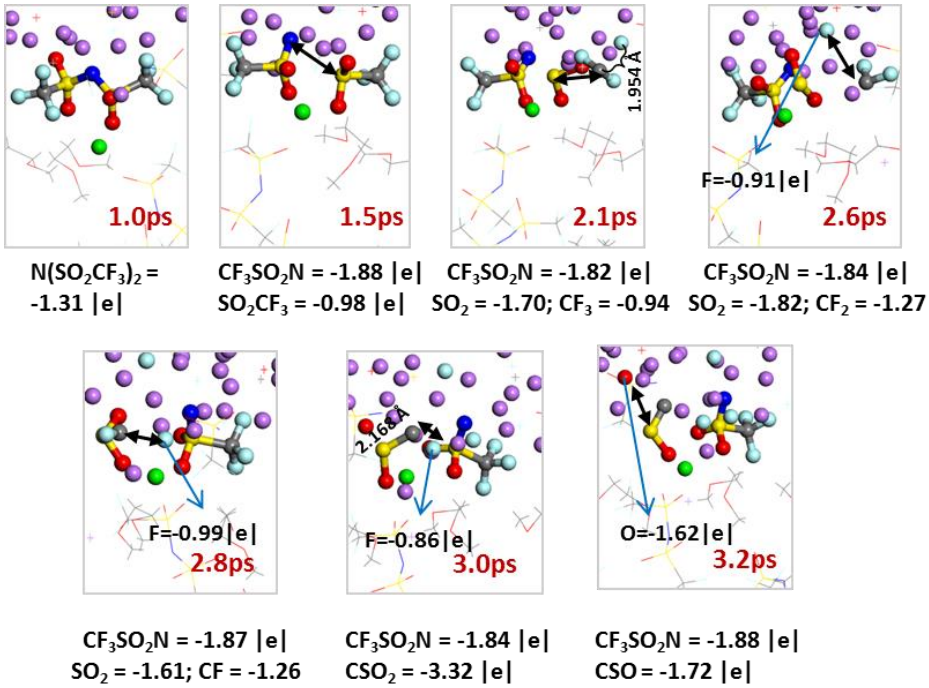

Figure B.6 1-LiTFSI reduction mechanism in a 4M-LiTFSI/DME solution. Average charge of Li (from LiTFSI) 0.88 (±0.01) |e| over the entire simulation time. Color code as in Figure 4.1.

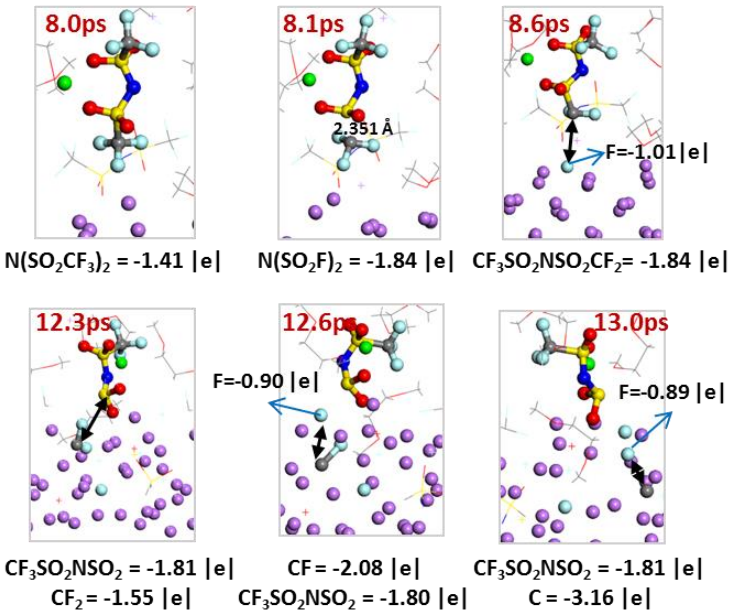

Figure B.7 2-LiTFSI reduction mechanism in a 4M-LiTFSI/DME solution. Average charge of Li (from LiTFSI) 0.88 (±0.01) |e| over the entire simulation time. Color code as in Figure 4.1.

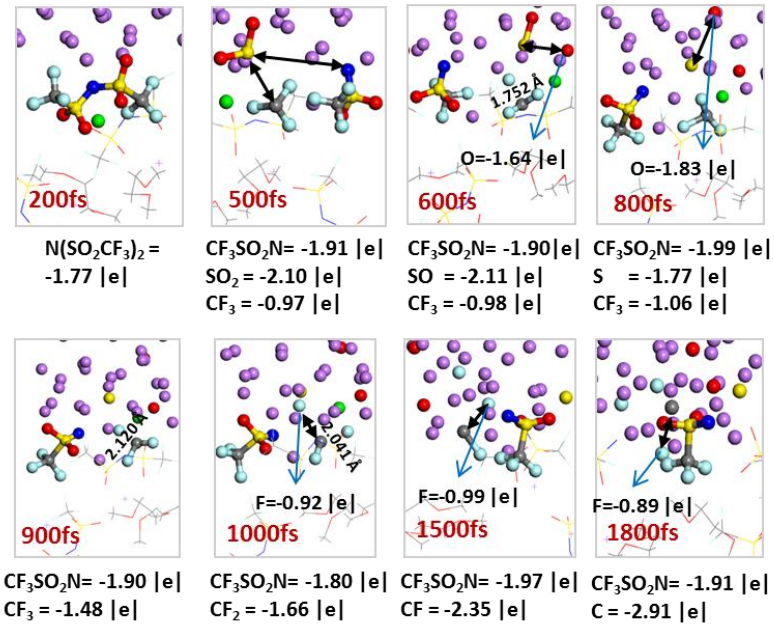

Figure B.8 3-LiTFSI reduction mechanism in a 4M-LiTFSI/DME solution. Average charge of Li (from LiTFSI) 0.85 (±0.01) |e| over the entire simulation time. Color code as in Figure 4.1.

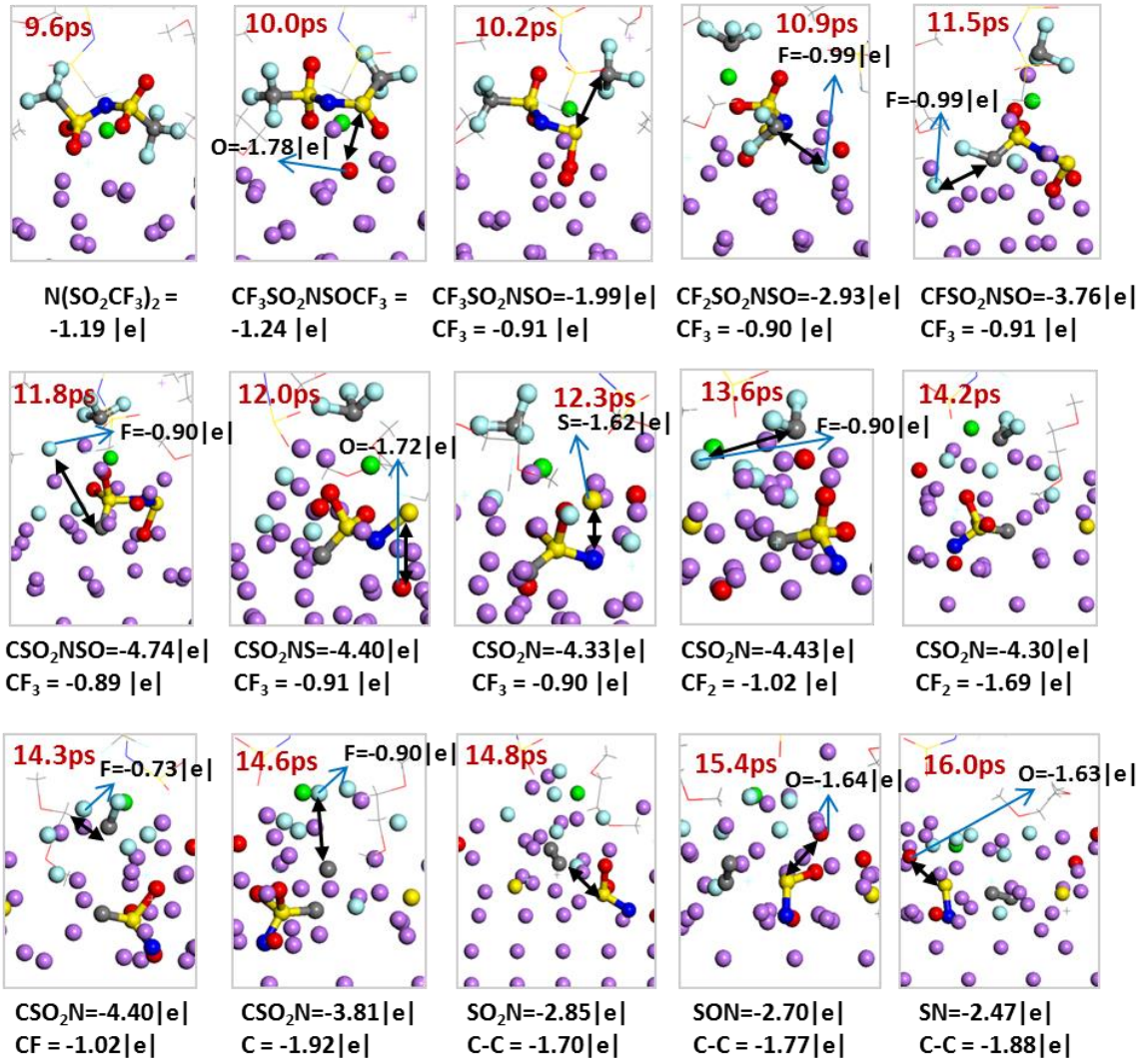

Figure B.9 4-LiTFSI reduction mechanism in a 4M-LiTFSI/DME solution. Average charge of Li (from LiTFSI) 0.87 (±0.03) |e| over the simulation entire time. Color code as in Figure 4.1.

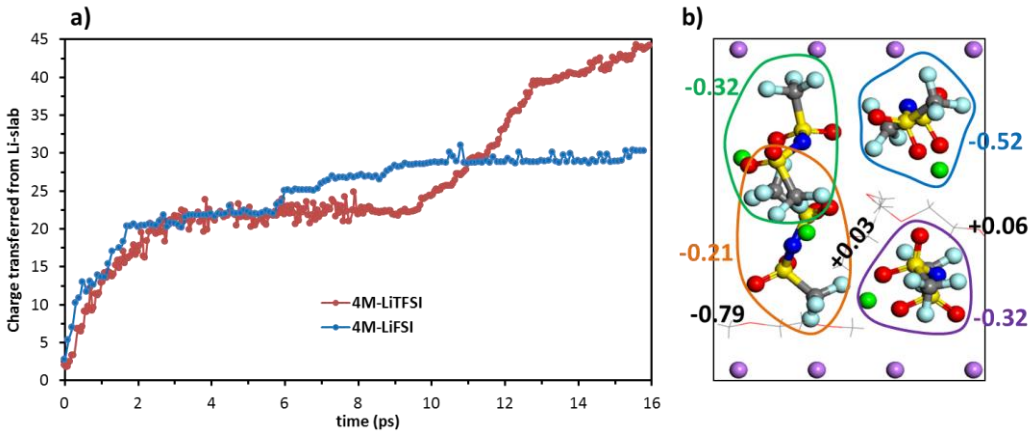

Figure B.10 a) Total charge transfer from the Li anode to the electrolyte in 4M salt in DME. Non-zero initial charge (~2 |e|) is due to solvation/interaction between surface lithium atoms with the electrolyte from the initial model. b) Charge distribution (in |e|) of the species forming the electrolyte mixture at time 0 ps. Here the 4M-LiTFSI solution was used as an example to illustrate the non-zero initial charge due to anode/electrolyte interactions for initial configurations as shown in Figure B.3 and Figure B.10a. Total electrolyte charge at 0 ps is -2.07 |e|. Color code as in Figure 4.1.

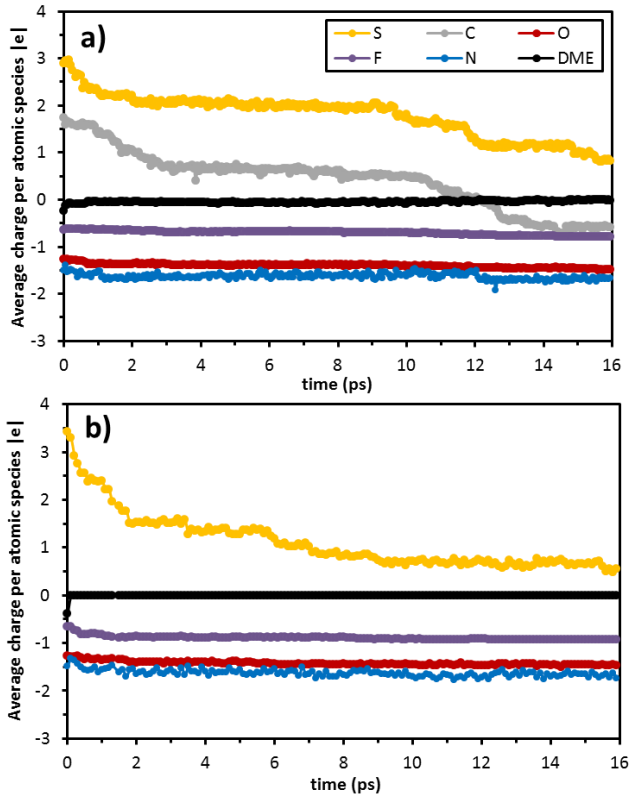

Figure B.11 Average charge per atomic species within salts and DME molecules. a) LiTFSI and b) LiFSI

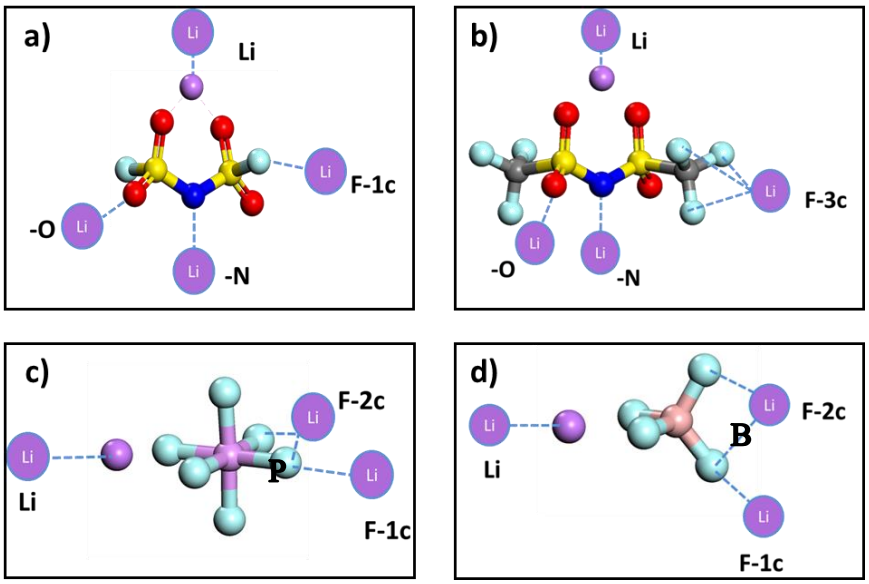

Figure B.12 Initial configurations used for study of Li^x (x=0, 1) attack to different salts: a) LiFSI, b) LiTFSI, c) $LiPF_6$, and d) $LiBF_4$. Color code as in Figure 4.1.

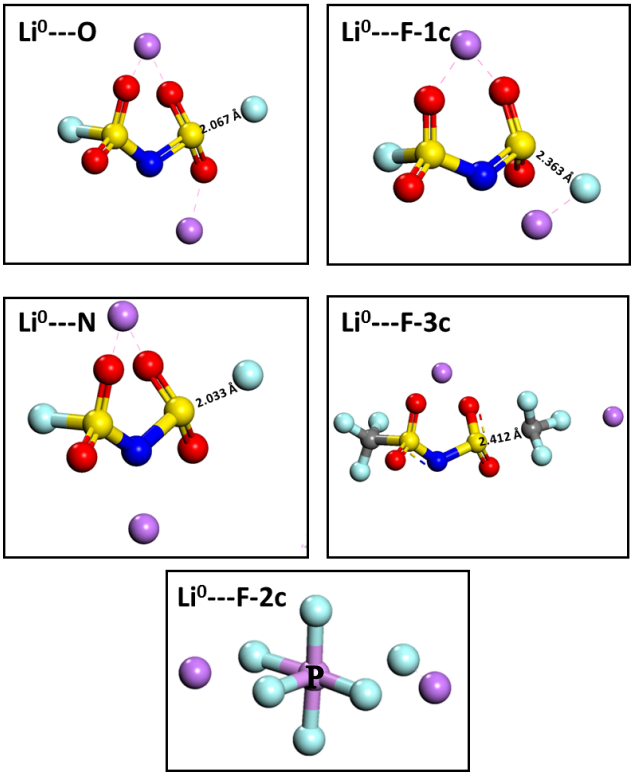

Figure B.13 Resulting optimized configurations formed from spontaneous reactions caused by Li^0 radical attack. Color code as in Figure 4.1.

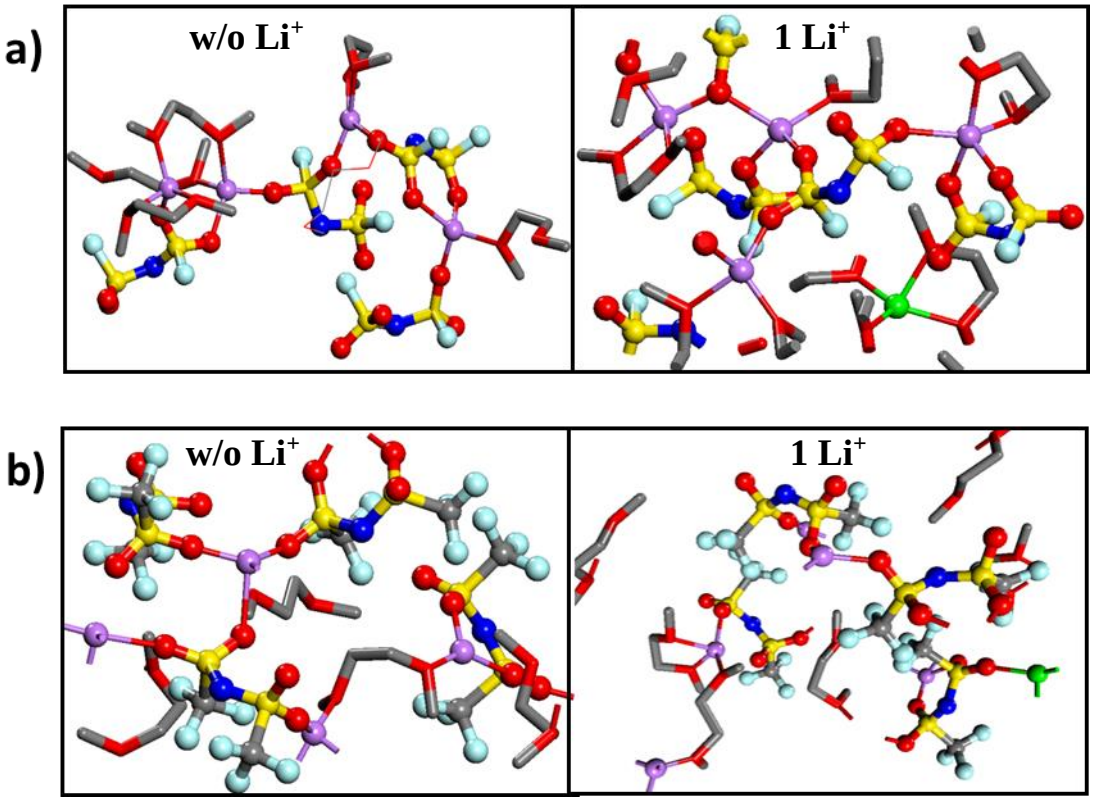

Figure B.14 4M-salt electrolyte solutions after 20ps of simulation time at 330K with different concentration of Li-ions. a) LiFSI and b) LiTFSI, respectively. Color code as in Figure 4.8. Hydrogen atoms are not shown for clarity.

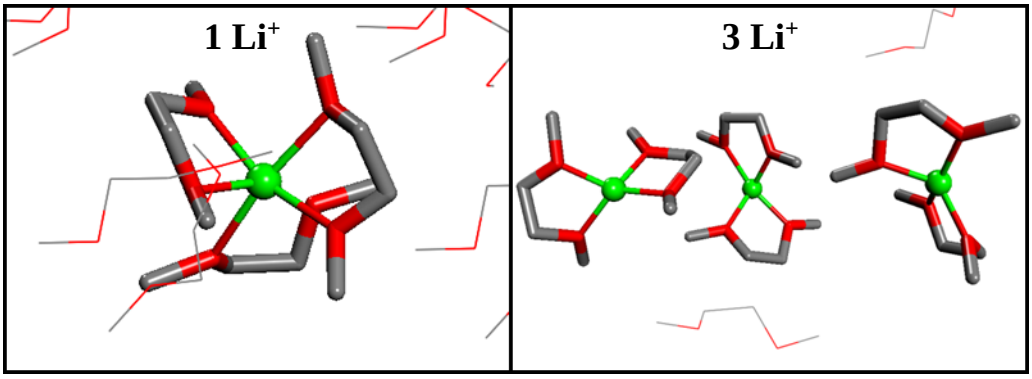

Figure B.15 Pure DME after 20ps of simulation time at 330K with different concentration of Li-ions. Color code as in Figure 4.8. Hydrogen atoms are not shown for clarity.

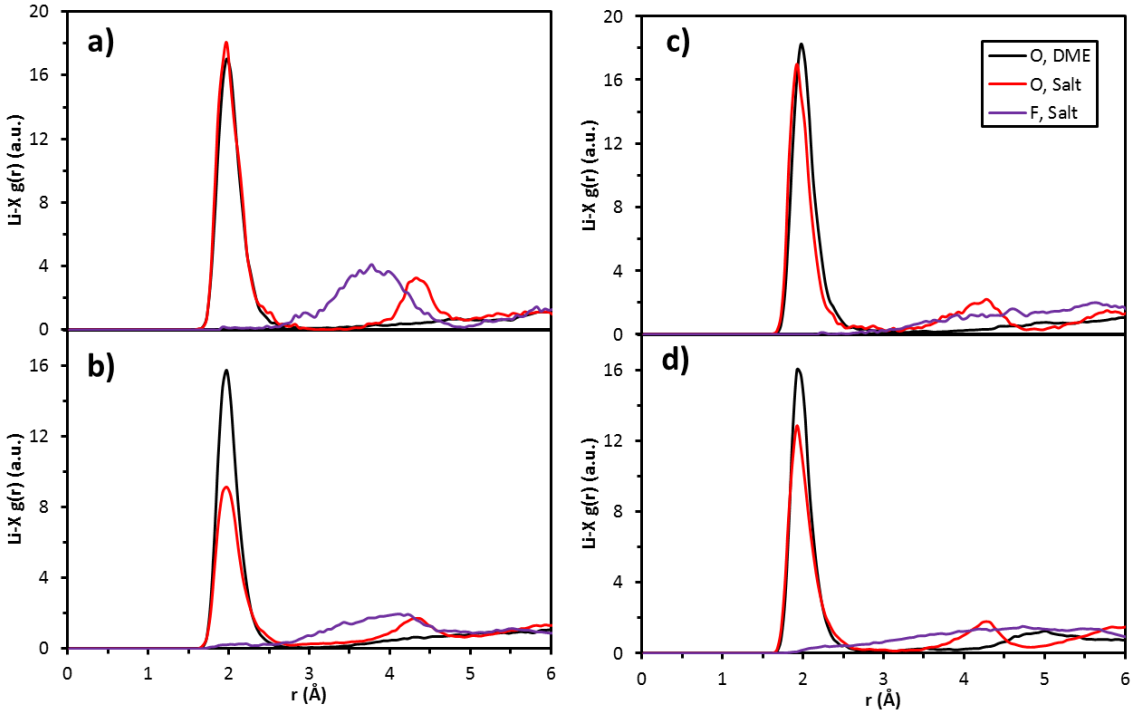

Figure B.16 Radial distribution function for Li^+--X (X=O and F atoms) pairs for solutions with one additional cation. a) 1M-LiFSI, b) 4M-LiFSI, c) 1M-LiTFSI, and d) 4M-LiTFSI.

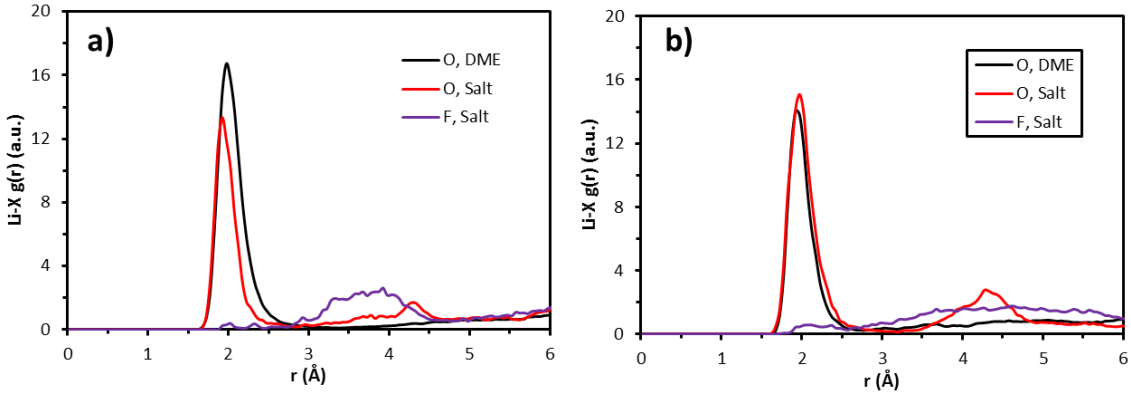

Figure B.17 Radial distribution function for Li^+--X (X=O and F atoms) pairs for solutions with three additional ions. a) 1M-LiFSI, and b) 1M-LiTFSI

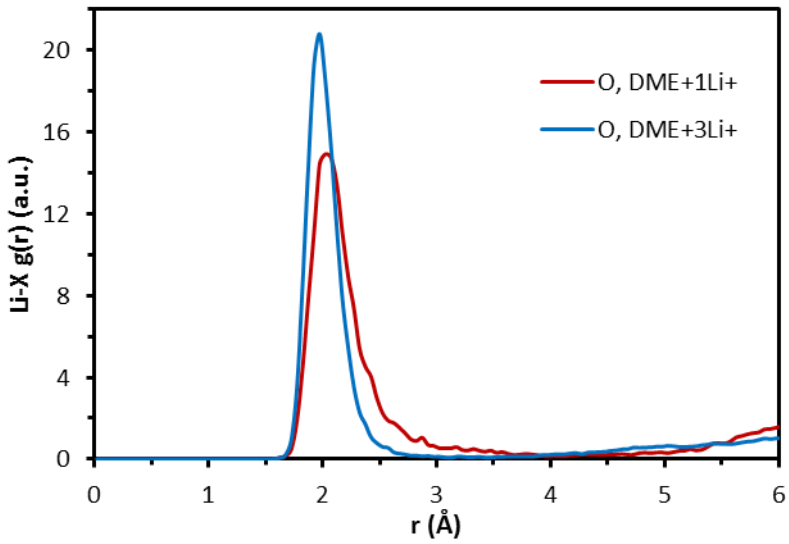

Figure B.18 Radial distribution function for Li^+--X (X=O and F atoms) pairs for pure DME with one and three additional ions.

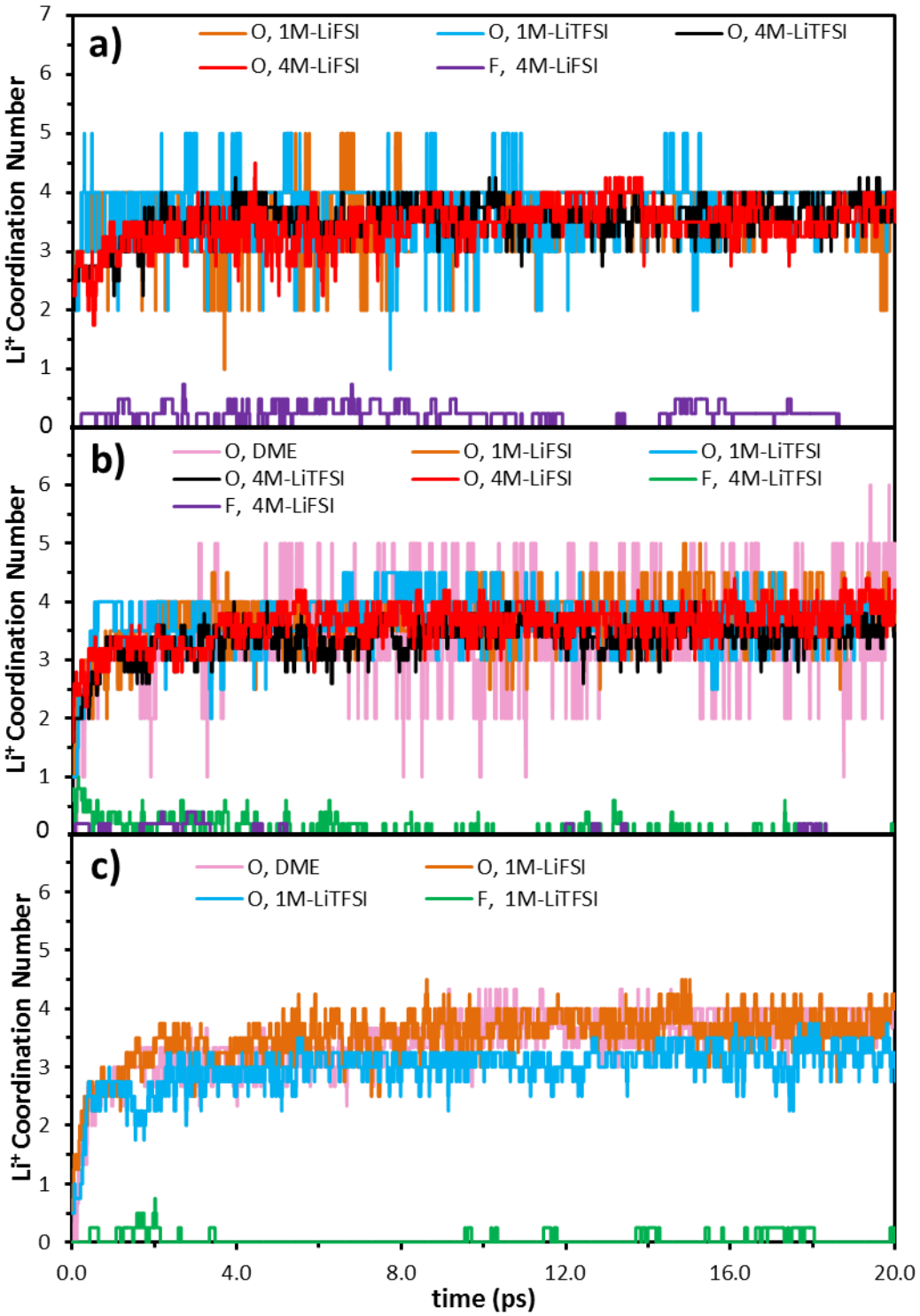

Figure B.19 Average coordination numbers calculated as a function of time under different concentrations of lithium ions: a) w/o Li, b) 1 Li^+, and c) 3 Li^+.

Table B.1 Calculated bond dissociation energies for LiFSI and LiTFSI from B3PW91/6-311++G(p,d).

Reactions	Dissociation Energies (eV)			
	Gas-phase		in DME	
	ΔE (0K)	ΔG (298K)	ΔE (0K)	ΔG (298K)
$LiFSI \rightarrow Li^+ + FSI^-$	5.77	5.44	0.62	0.31
$LiTFSI \rightarrow Li^+ + TFSI^-$ [ref. [129]]	5.96	5.64	0.75	0.43

Table B.2 Bond dissociation energies for the FSI- anion calculated from B3PW91/6-311++G(p,d).

Reactions	Bond Dissociation Energies (eV)	
	in DME	
	ΔE (0K)	ΔG (298K)
$FSI^- \rightarrow F + NS_2O_4F^-$	3.80	3.40
$FSI^- \rightarrow F^- + NS_2O_4F$	2.74	2.38
$FSI^- \rightarrow NSO_2F^- + SO_2F$	3.11	2.53
$FSI^- \rightarrow NSO_2F + SO_2F^-$	3.84	3.29

Table B.3 Average coordination numbers for the different solutions over 18 ps (2-20ps). Peak positions from RDF for O—Li and F—Li pairs.

System (in DME)	Average coordination number				RDF for X--Li^+			
	Total	O-- Li^+	F--Li^+	% from O	O_Salt (1st)--Li^+	O_Salt (2nd)--Li^+	O_DME--Li^+	F--Li^+
1M-LiFSI	3.77	3.74	0.00	99.2%	1.975	4.225	1.975	4.175
4M-LiFSI	3.79	3.51	0.21	92.8%	1.975	4.325	1.975	1.975 / 4.125
1M-LiTFSI	3.83	3.82	0.00	99.7%	1.975	4.125	1.975	-
4M-LiTFSI	3.70	3.61	0.00	97.6%	1.925	4.275	1.925	-
$1Li^+$	3.63	3.61	-	99.4%	-	-	2.025	-
1M-LiFSI+$1Li^+$	3.91	3.85	0.00	98.3%	1.975	4.325	1.975	3.775
4M-LiFSI+$1Li^+$	3.75	3.67	0.03	98.0%	1.975	4.325	1.975	4.125
1M-LiTFSI+$1Li^+$	3.81	3.75	0.00	98.5%	1.975	4.275	1.925	-
4M-LiTFSI+$1Li^+$	3.56	3.45	0.08	96.8%	1.925	4.275	1.925	-
$3Li^+$	3.62	3.58	-	98.9%	-	-	1.975	-
1M-LiFSI+$3Li^+$	3.69	3.62	0.00	98.0%	1.975	4.275	1.925	3.925
1M-LiTFSI+$3Li^+$	3.31	3.08	0.04	93.1%	1.925	4.275	1.975	-

APPENDIX C

SUPPORTING INFORMATION FOR CHAPTER 5*

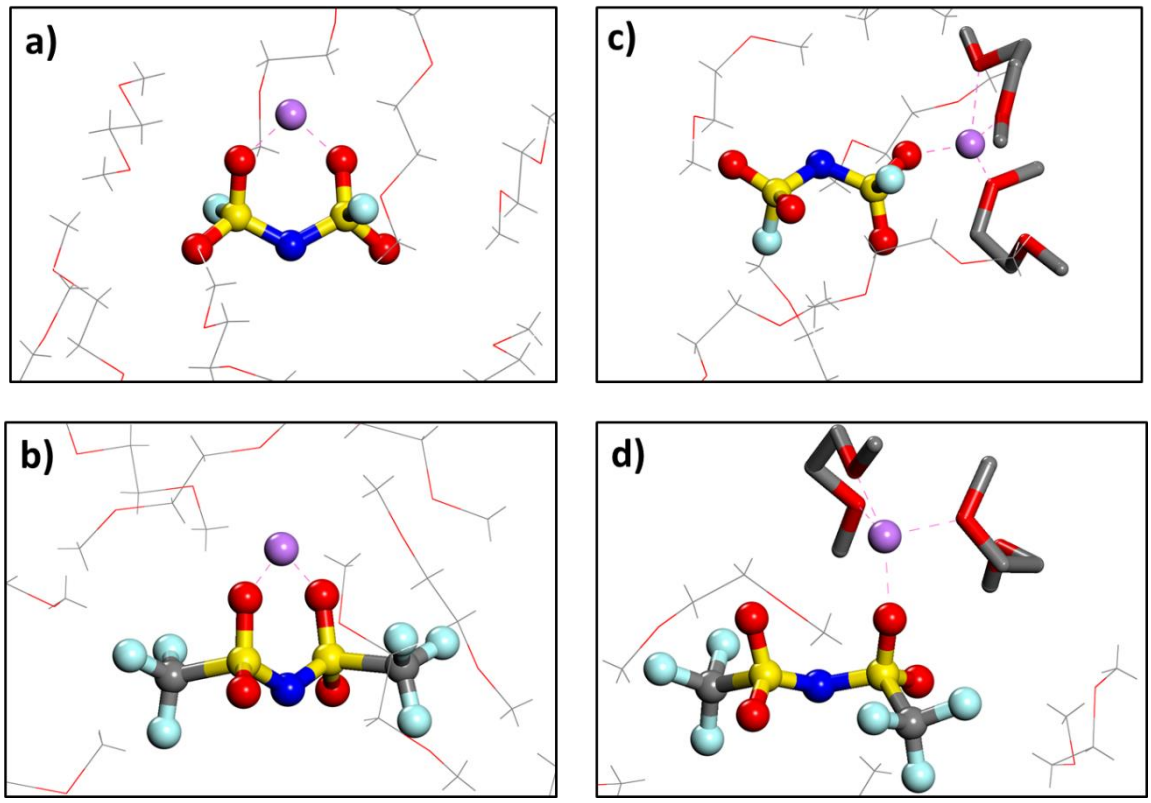

Figure C.1 Initial configurations of 1M solutions for AIMD simulations under electron-rich environments. (a-b) MM-relaxed and (c-d) AIMD-relaxed initial configurations. Color code as in Figure 5.1.

* Supporting Information reprinted with permission from Luis E. Camacho-Forero and Perla B. Balbuena. "Elucidating Electrolyte Decomposition under Electron-rich Environments at the Lithium-Metal Anode." *Physical Chemistry Chemical Physics*, 2017, **19**, 30861-30873. Reproduced by permission of the PCCP Owner Societies. Copyright © 2017 PCCP Owner Societies.

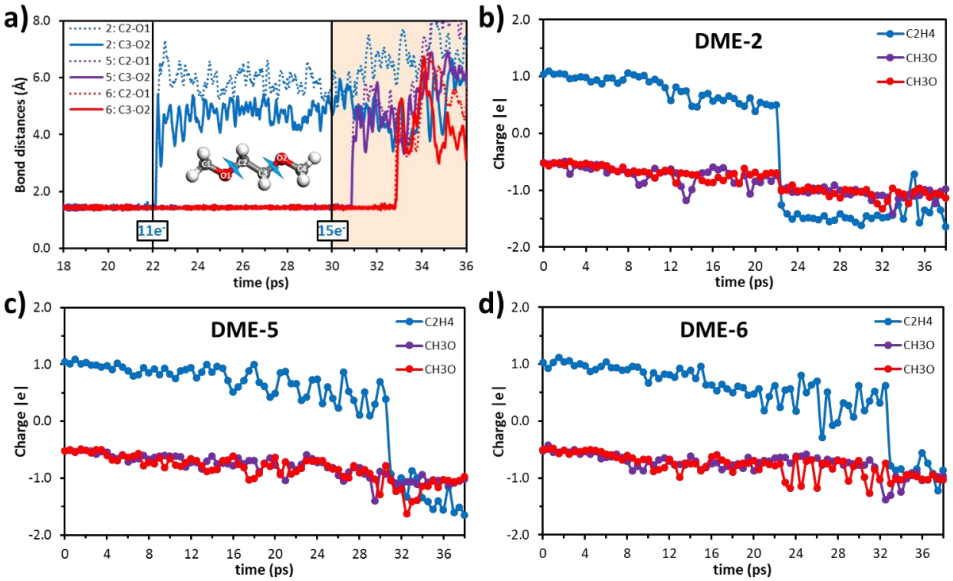

Figure C.2 DME reaction mechanism from AIMD simulations of pure DME with sequential addition of electrons. (a) C-O bond distances for reacting DME molecules. (b-d) Charges evolution of fragments from reacting DME molecules. Color code as in Figure 5.1.

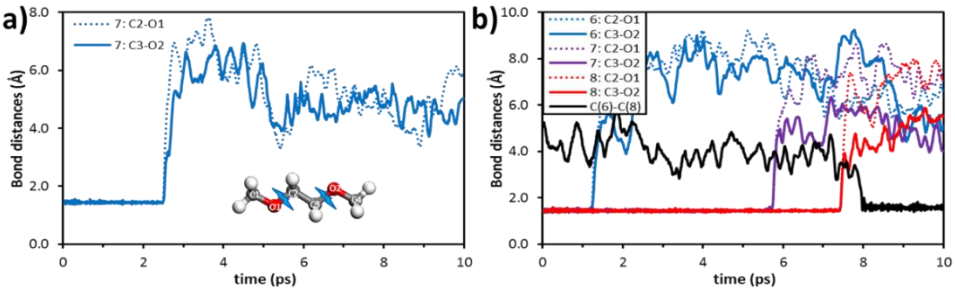

Figure C.3 Bond distance evolution for DME molecules from AIMD simulations of pure solvent with a constant number of excess electrons starting with the MM-relaxed initial configuration. (a) n_{eo}=11 and (b) n_{eo}=13 – also includes the C-C bond distance for the oligomer $(C_2H_4)_2^{2-}$.

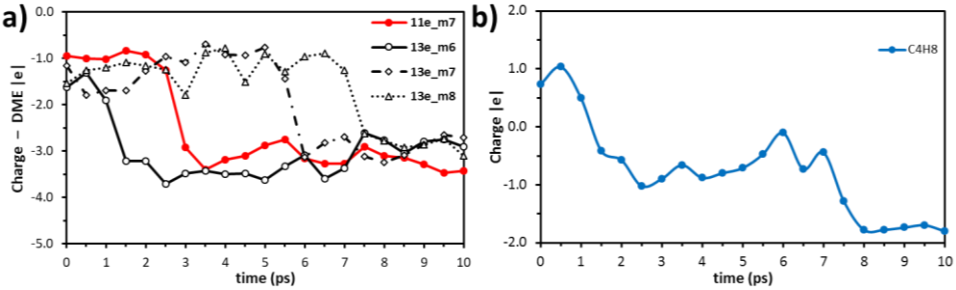

Figure C.4 Charge evolution of (a) reacting DME molecules and (b) $(C_2H_4)_2^{2-}$ from AIMD simulations of pure solvent with a constant number of excess electrons starting with the MM-relaxed initial configuration.

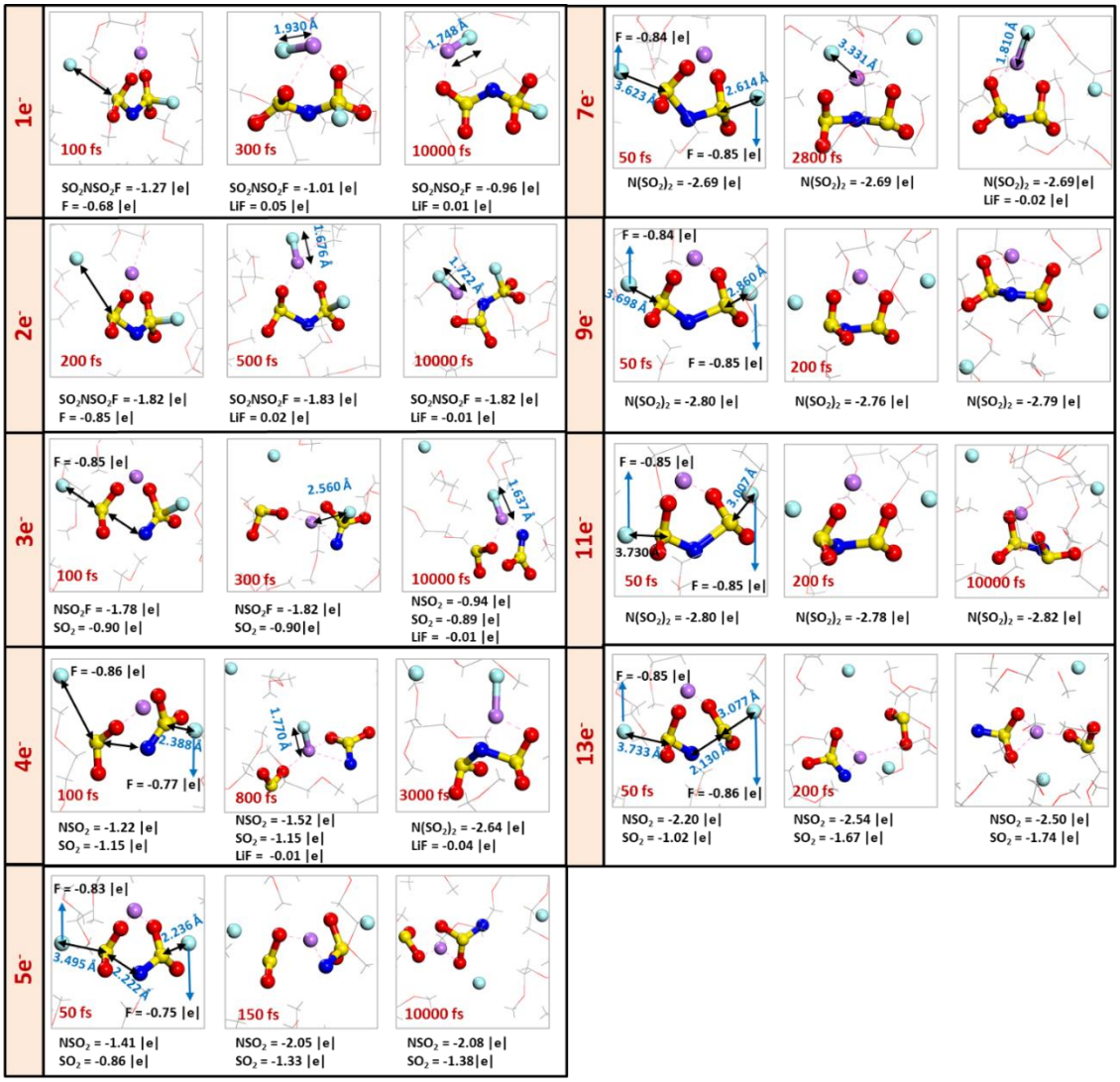

Figure C.5 LiFSI reduction mechanism from AIMD simulations of 1M LiFSI solutions with various number of excess electrons (n_{eo}) starting with the MM-relaxed initial configuration. Color code as in Figure 5.1.

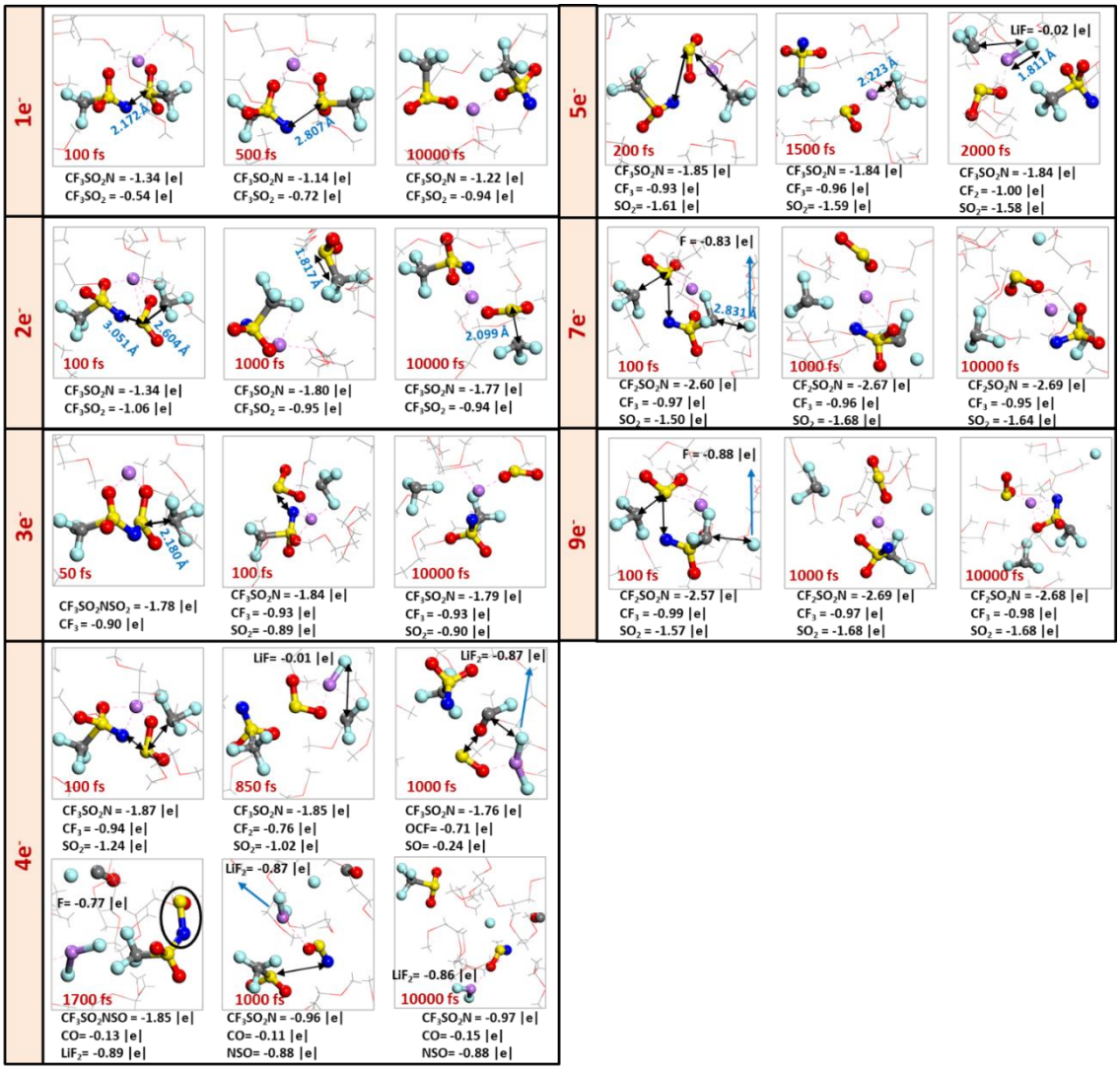

Figure C.6 LiTFSI reduction mechanism from AIMD simulations of 1M LiFSI solutions with various number of excess electrons (n_{eo}) starting with the MM-relaxed initial configuration. LiTFSI reduction involving DME redox reactions (n_{eo}= 11 and 13) are shown in Figure 5.7. Color code as in Figure 5.1.

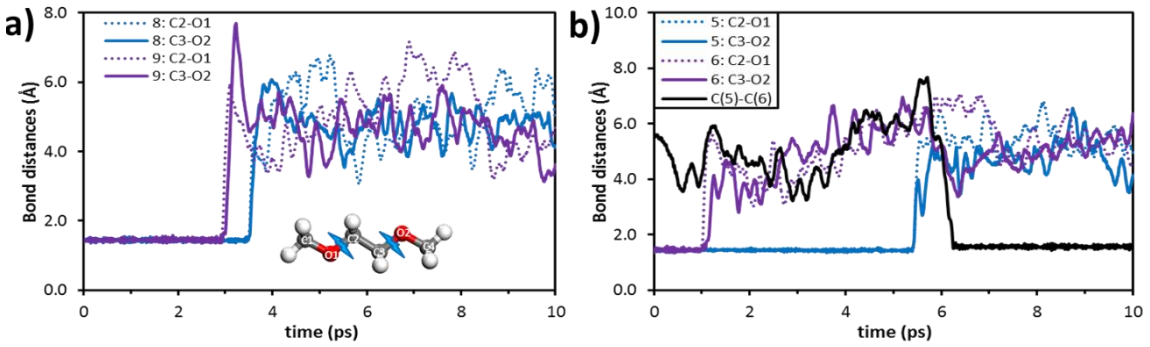

Figure C.7 Bond distance evolution for DME molecules from AIMD simulations of pure solvent with a constant number of excess electrons starting with the AIMD-relaxed initial configuration. (a) n_{eo}=11 and (b) n_{eo}=13 – also includes the C-C bond distance for the oligomer $(C_2H_4)_2^{2-}$.

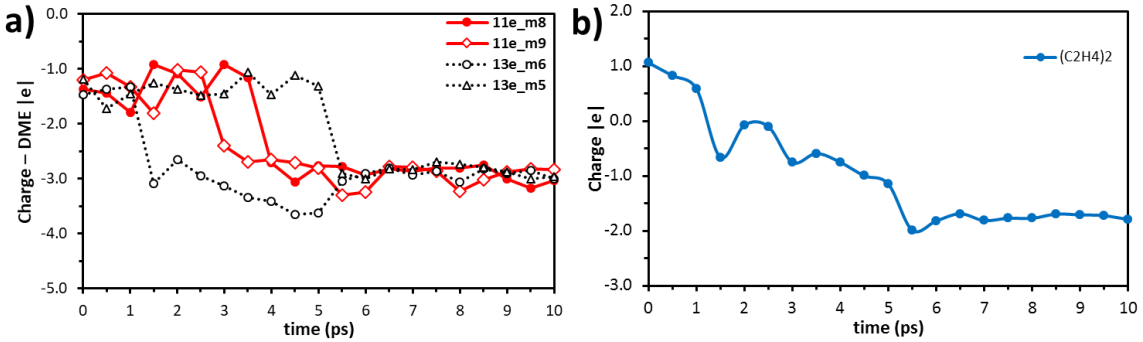

Figure C.8 Charge evolution of (a) reacting DME molecules and (b) $(C_2H_4)_2^{2-}$ from AIMD simulations of pure solvent with a constant number of excess electrons starting with the AIMD-relaxed initial configuration.

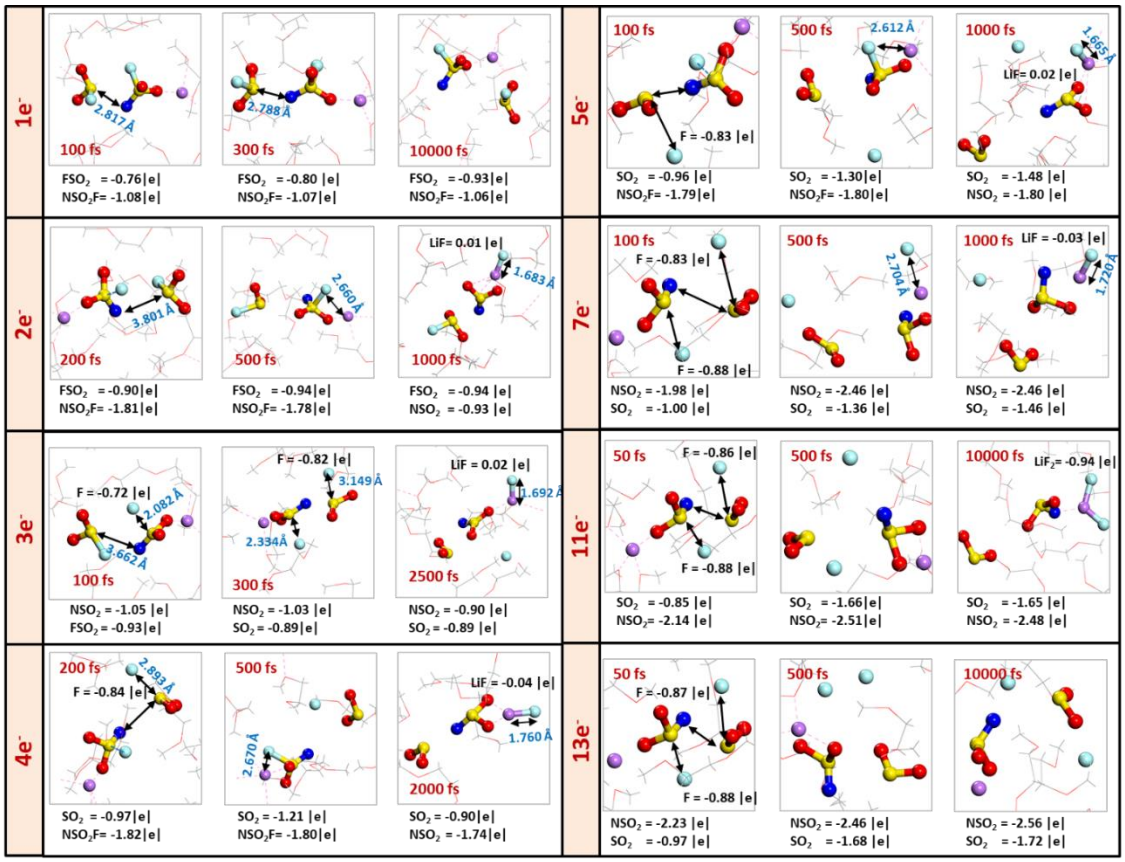

Figure C.9 LiFSI reduction mechanism from AIMD simulations of 1M LiFSI solutions with various number of excess electrons (n_{eo}) starting with the AIMD-relaxed initial configuration. LiFSI reduction involving DME redox reactions (n_{eo}= 9) are shown in Figure 5.9a. Color code as in Figure 5.1.

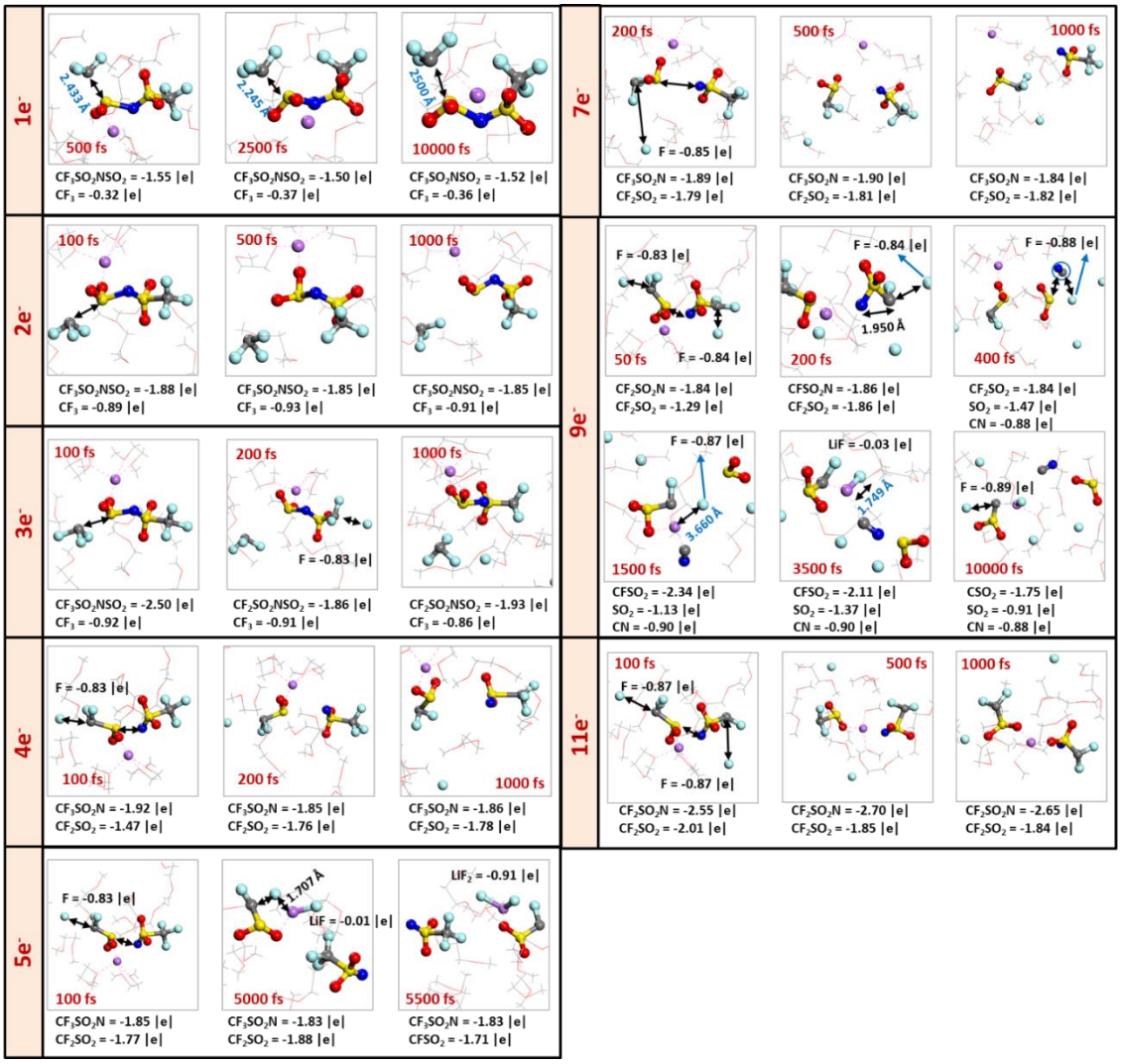

Figure C.10 LiTFSI reduction mechanism from AIMD simulations of 1M LiTFSI solutions with various number of excess electrons (n_{eo}) starting with the AIMD-relaxed initial configuration. LiTFSI reduction involving DME redox reactions (n_{eo}= 13) are shown in Figure 5.9b. Color code as in Figure 5.1.

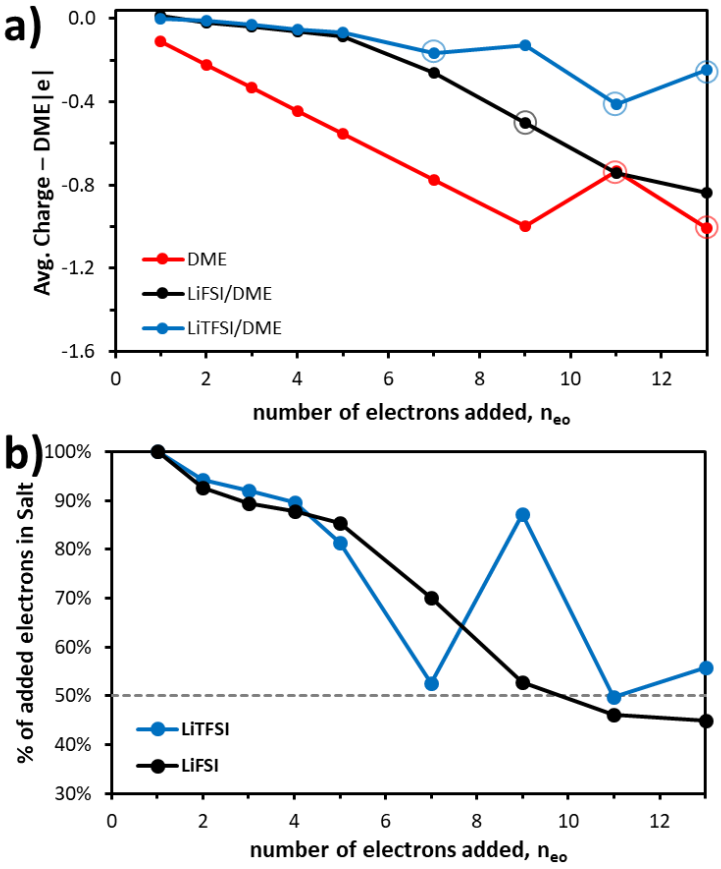

Figure C.11 Average Charges over 10 ps of AIMD in solutions starting with AIMD-relaxed configuration (sampled every 1 ps) as a function of the initial number of excess electrons. (a) Average charges of non-reacting DME. Circles indicate systems where reactions took place. (b) Percentage of added electrons accepted by the salts. The dotted line depicts the 1:1 electron distribution between salt and solvent.

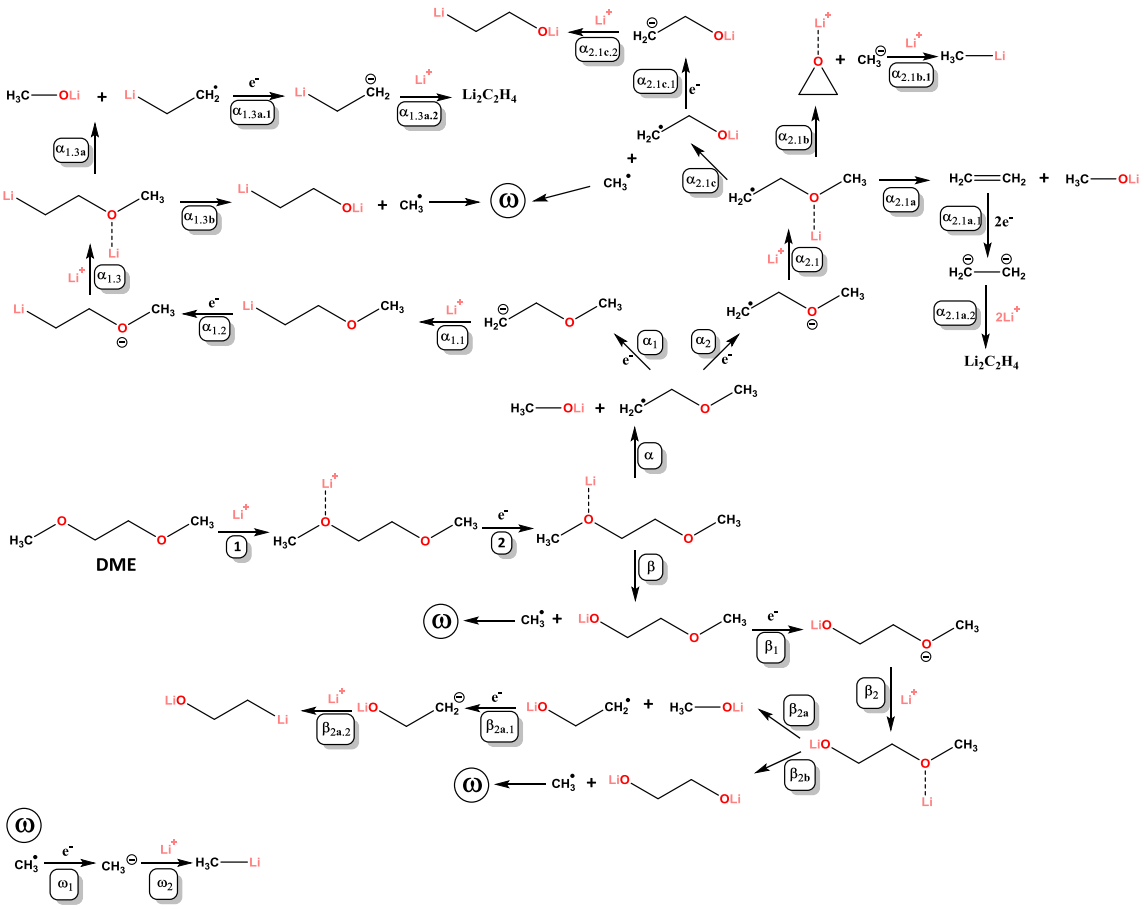

Figure C.12 All possible reaction pathways for DME decomposition under one Li-radical attack yielding C-O bond scission.

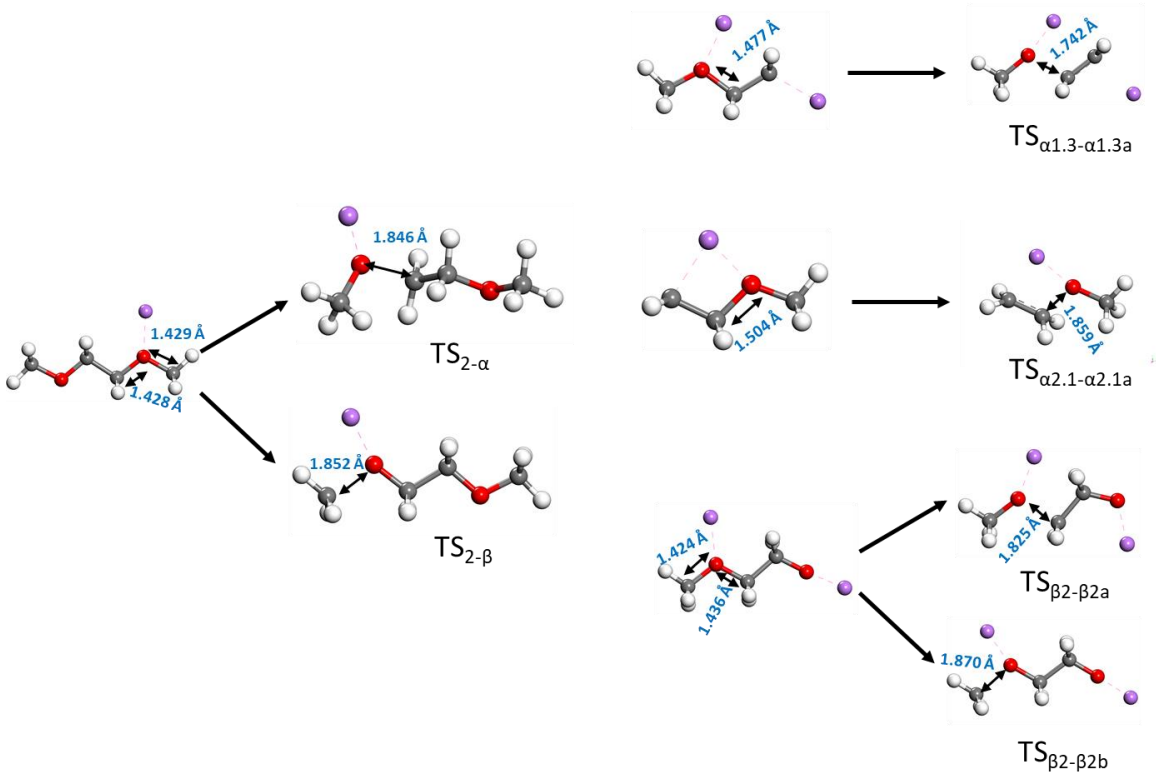

Figure C.13 Intermediates and transition states structures calculated from B3PW91/6-311++G(p,d). Color code as in Figure 5.1. Refer to Figure 5.10 for reactions numbering.

Table C.1 Calculated electron affinity (EA) for electrolyte components from B3PW91/6-311++G(p,d) in solvent (DME).

Molecule	E(0) (eV)	E(-1) (eV)	EA (eV)
DME (TTT)	-308.70	-308.71	-0.25
DME (TGT)	-308.70	-308.71	-0.27
LiFSI	-1359.08	-1359.13	-1.44
LiTFSI	-1834.59	-1834.64	-1.35

Table C.2 Summary of bond cleavage and fragments remaining after 10 ps of AIMD simulation in 1M solutions with AIMD-relaxed initial configurations. Structures in red are species neutrally charged. "Fragments w/ DME" makes allusion only to DME molecules decomposed due to a salt fragment.

number of electrons	LiFSI			LiTFSI		
	Initial Bond Cleavages	Salt fragments	fragments w/ DME	Initial Bond Cleavages	Salt fragments	fragments w/ DME
1	S-N	FSO_2, NSO_2F	-	C-S	CF_3--$SO_2NSO_2CF_3$	-
2	S-N, S-F	FSO_2, NSO_2, LiF	-	C-S	CF_3, $SO_2NSO_2CF_3$	-
3	S-N, S-F, S-F	SO_2, NSO_2, LiF, F^-	-	C-S, C-F	CF_3, $SO_2NSO_2CF_2$, F^-	-
4	S-N, S-F, S-F	SO_2, NSO_2, LiF, F^-	-	S-N, C-F	CF_2SO_2, NSO_2CF_3, F^-	-
5	S-N, S-F, S-F	SO_2, NSO_2, LiF, F^-	-	S-N, C-F, C-F	$CFSO_2$, NSO_2CF_3, LiF_2^-	-
7	S-N, S-F, S-F	SO_2, NSO_2, LiF, F^-	-	S-N, C-F	CF_2SO_2, NSO_2CF_3, F^-	-
9	S-N, S-F, S-F	SO_2, NSO_2, $2F^-$	$HNSO_2$, $CH_3O(CH_2)_2OCH_2^-$	S-N, C-F, C-F	SO_2, NC, CSO_2, LiF, $4F^-$	-
11	S-N, S-F, S-F	SO_2, NSO_2, LiF_2^-	-	S-N, C-F, C-F	CF_2SO_2, NSO_2CF_2, $2F^-$	-
13	S-N, S-F, S-F	SO_2, NSO_2, $2F^-$	-	S-N, C-F, C-F	CF_2SO_2, CSO_2N, $4F^-$	$HCSO_2N$, CH_3O^-, CH_3OCHCH_2

Table C.3 Calculated bond dissociation energies for DME from B3PW91/6-311++G(p,d) in solvent (DME).

Bond	ΔE_0 (eV)	ΔG_{298} (eV)
C_m-H_m	4.36	4.25
C_t-H_t	4.85	4.76
C_m-O	4.56	4.41
O-C_t	5.08	4.89

Table C.4 Calculated reaction energies and activation barriers for DME under one-lithium radical attack from B3PW91/6-311++G(p,d) in solvent (DME).

Reaction	Reaction Energy (eV)				
	ΔE	ΔE_{0K}	ΔE_{298K}	ΔH_{298K}	ΔG_{298K}
1	-0.70	-0.63	-0.63	-0.65	-0.36
2	-1.90	-1.92	-1.92	-1.92	-1.94
α	-0.12	-0.38	-0.33	-0.33	-0.56
α_1	-2.67	-2.69	-2.69	-2.69	-2.68
$\alpha_{1.1}$	-1.94	-1.87	-1.87	-1.89	-1.58
$\alpha_{1.2}$	-1.21	-1.23	-1.23	-1.23	-1.25
$\alpha_{1.3}$	-0.74	-0.68	-0.71	-0.71	-0.45
$\alpha_{1.3a}$	-0.63	-0.82	-0.78	-0.78	-0.98
$\alpha_{1.3a.1}$	-1.06	-1.12	-1.12	-1.12	-1.10
$\alpha_{1.3a.2}$	-2.35	-2.27	-2.28	-2.30	-1.96
$\alpha_{1.3b}$	0.57	**0.30**	0.36	0.36	**0.12**
α_2	-2.67	-2.69	-2.69	-2.69	-2.68
$\alpha_{2.1}$	-2.31	-2.22	-2.23	-2.25	-1.92
$\alpha_{2.1a}$	-0.52	-0.64	-0.62	-0.60	-1.09
$\alpha_{2.1a.1}$	-0.69	-0.85	-0.84	-0.84	-0.89
$\alpha_{2.1a.2}$	-5.41	-5.26	-5.28	-5.33	-4.68
$\alpha_{2.1b}$	2.68	**2.50**	2.53	2.55	**2.06**
$\alpha_{2.1c}$	4.25	**3.92**	3.89	3.89	**3.85**
$\alpha_{2.1c.1}$	-2.15	-2.16	-2.18	-2.18	-2.09
$\alpha_{2.1c.2}$	-2.11	-2.06	-2.05	-2.08	-1.81
β	-0.12	-0.40	-0.34	-0.34	-0.56
β_1	-1.24	-1.25	-1.25	-1.25	-1.28
β_2	-0.49	-0.44	-0.47	-0.47	-0.24
β_{2a}	0.03	-0.21	-0.13	-0.13	-0.53
$\beta_{2a.1}$	-2.15	-2.16	-2.18	-2.18	-2.09
$\beta_{2a.2}$	-2.11	-2.06	-2.05	-2.08	-1.81
β_{2b}	0.10	-0.16	-0.11	-0.11	-0.30
ω_1	-2.68	-2.69	-2.70	-2.70	-2.67
ω_2	-2.06	-1.97	-1.99	-2.01	-1.72
$TS_{2-\alpha}$	1.05	0.88	-	-	0.86
$TS_{\alpha1.3-\alpha1.3a}$	0.04	**-0.01**	-	-	**-0.02**
$TS_{\alpha2.1-\alpha2.1a}$	0.10	0.05	-	-	0.04
$TS_{2-\beta}$	0.97	0.80	-	-	0.75
$TS_{\beta2-\beta2a}$	1.04	0.90	-	-	0.92
$TS_{\beta2-\beta2b}$	1.09	0.94	-	-	0.94

Table C.5 Calculated reaction energies and activation barriers for DME decomposition via dehydrogenation due to anion attack from B3PW91/6-311++G(p,d) in solvent (DME).

Step	H_m+O--LiF		H_t+O--LiF	
	ΔE_{0K}	$\Delta G_{298.15K}$	ΔE_{0K}	$\Delta G_{298.15K}$
TS_1	-0.22	**0.24**	-0.13	**0.31**
1	-1.47	-1.48	-1.30	-1.31
TS_{1-2}	0.08	**0.08**		
2	-0.86	-1.34		
TS_{1-3}	0.19	**0.67**		
3	-1.50	-1.52		

APPENDIX D

SUPPORTING INFORMATION FOR CHAPTER 6*

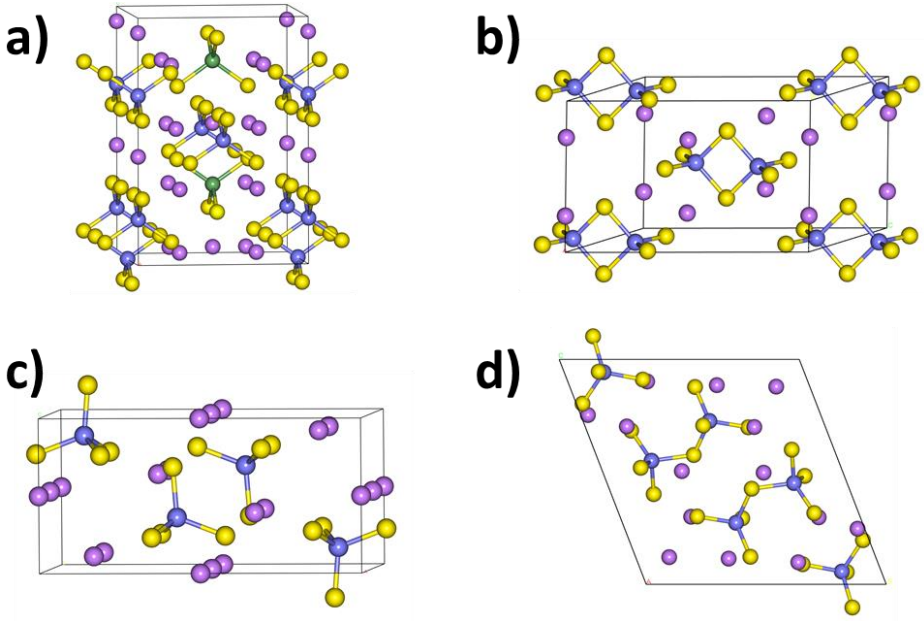

Figure D.1 Optimized crystalline structures for SSEs under investigation. (a) LGPS, (b) $Li_2P_2S_6$, (c) β-Li_3PS_4, and (d) $Li_7P_3S_{11}$.

Table D.1 Optimized crystallographic parameters, electronic band gap (E_g), simulation k-points, and ionic conductivities for the studied SSEs.

SSE	Crystallography								Eg (eV)		K-Points*	Conductivity (S cm^{-1})
	SG #	Space Group	a	b	c	α	β	γ	PBE	HSE06		
LGPS	105	P42MC	8.801	8.801	12.701	90	90	90	2.14	3.24	4x4x2	1.2×10^{-2} (ref.[195])
$Li_2P_2S_6$	12	C2/M	11.352	7.172	6.702	90	127	90	1.80	2.87	2x4x4	7.8×10^{-11} (ref.[193])
β-Li_3PS_4	62	PNMA	13.073	8.112	6.253	90	90	90	2.84	3.98	2x4x4	8.93×10^{-7} (ref.[194])**
$Li_7P_3S_{11}$	2	P-1	6.284	12.478	12.526	107	103	102	2.61	3.71	4x2x2	4.1×10^{-3} (ref.[196])

*Eg values were calculated using the double of k-points presented in this table. **nanoporous **β-Li_3PS_4**: 1.6×10^{-4} S cm^{-1} (ref.[194])

* Supporting Information reprinted with permission from Luis E. Camacho-Forero and Perla B. Balbuena. "Exploring Interfacial Stability of Solid-State Electrolytes at the Lithium-Metal Anode Surface." *Journal of Power Sources*, 2018, **396**, 782-790. Copyright © 2018 Elsevier B.V.

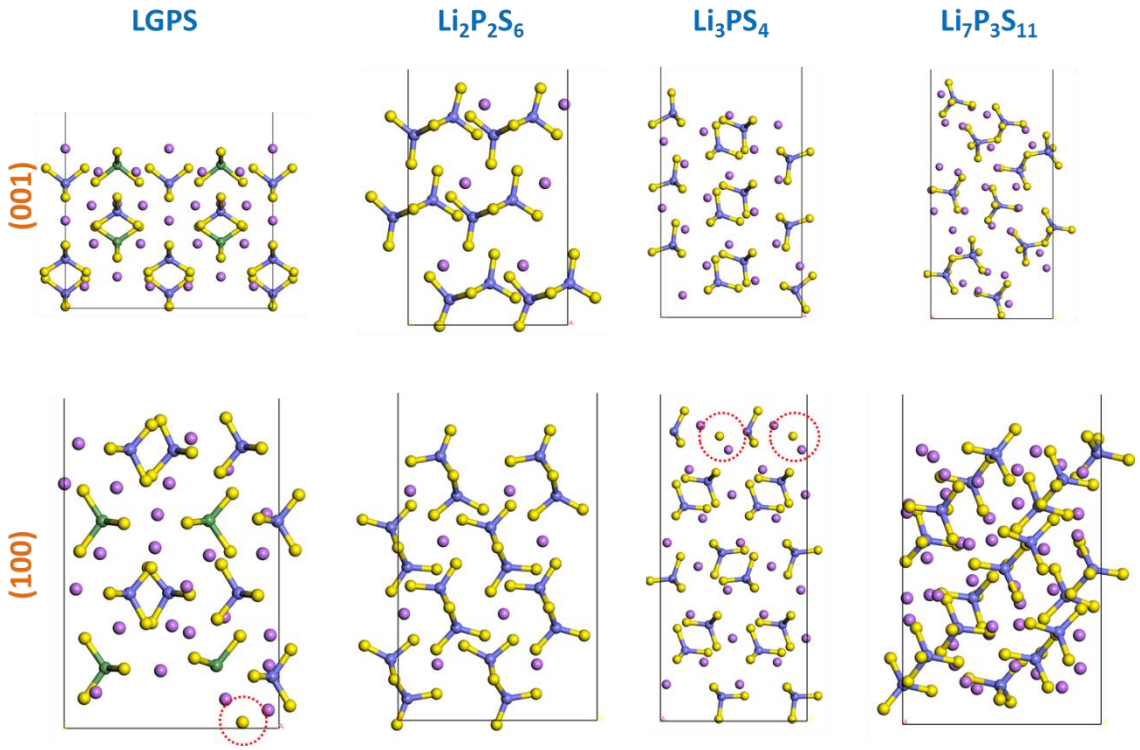

Figure D.2 Optimized cleaved (001) and (100) facets of LGPS, $Li_2P_2S_6$, Li_3PS_4, and $Li_7P_3S_{11}$ (from left to right).

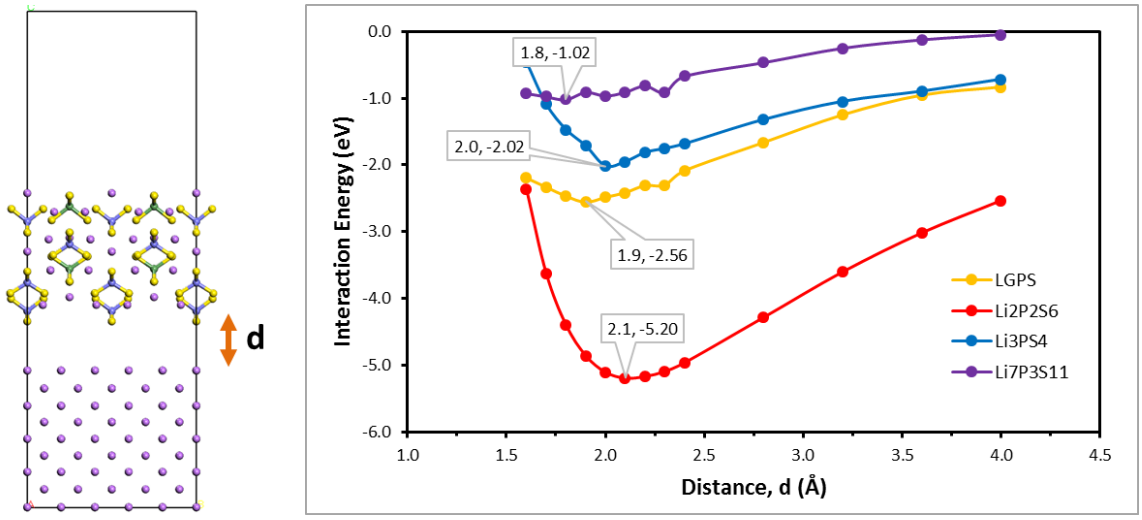

Figure D.3 (Left) illustration of the scanning scheme used to determine the equilibrium distance between the SSEs and Li-slab prior optimization. (Right) Interaction energy diagram as a function of separation distance (d).

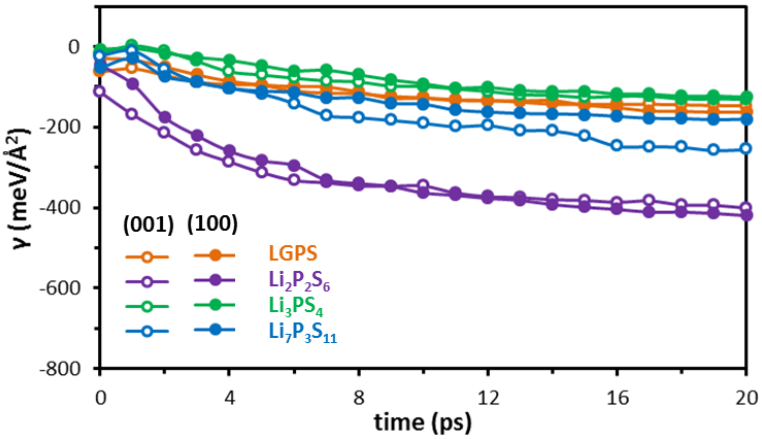

Figure D.4 Time evolution of Li/SSE interfacial energies (γ).

Table D.2 Lattice parameters and K-points used for SSE/Li-metal structure optimization and AIMD simulations.

SSE	(001)							(100)						
	a	b	c	α	β	γ	K-Points	a	b	c	α	β	γ	K-Points
LGPS	17.407	17.407	31.126	90	90	90	1x1x1	17.407	13.235	36.898	90	90	90	1x2x1
$Li_2P_2S_6$	10.839	14.057	33.774	90	90	90	2x2x1	14.057	13.586	38.161	90	90	90	2x2x1
Li_3PS_4	13.421	16.718	38.634	90	90	90	2x2x1	16.718	13.137	46.370	90	90	90	2x2x1
$Li_7P_3S_{11}$	13.169	13.124	44.740	90	90	102	2x2x1	13.124	13.148	39.840	90	90	107	2x2x1

Table D.3 Surface energy (σ) for the SSE facets and configurations shown in Figure D.2. The surface energy is calculated from the following equation[35]: $\boldsymbol{\sigma = (E_{SSE-slab} - n_{SSE-slab}E_{SSE-bulk})/2A}$. Where $E_{SSE\text{-}slab}$, $E_{SSE\text{-}bulk}$, $n_{SSE\text{-}slab}$, and A are the energy of surface, the energy of one unit of SSE in bulk, number of SSE units in the surface slab, and area, respectively.

SSE	σ (meV Å^{-2})	
	(001)	(100)
LGPS	17	42
$Li_2P_2S_6$	26	7
Li_3PS_4	28	50
$Li_7P_3S_{11}$	18	13

Table D.4 Change in free (void) volume for structures at the *initial* configuration (prior SSE/Li optimization) and after 20 ps of AIMD simulations.

SSE	Facet	Free Volume ($Å^3$)			%ΔV
		Initial	20 ps	ΔV	
LGPS	(001)	172	128	-44	-0.5%
	(100)	233	390	157	1.8%
$Li_2P_2S_6$	(001)	10	397	388	7.5%
	(100)	544	1094	550	7.6%
Li_3PS_4	(001)	283	425	143	1.6%
	(100)	441	701	260	2.6%
$Li_7P_3S_{11}$	(001)	453	865	412	5.5%
	(100)	162	698	536	8.2%

Table D.5 Radii cut-off for coordination numbers selected based on Radial Distribution Functions (RDF) and bond length from the bulk crystals (not shown).

Bond/Pair	d (Å)
Li-S	2.90
Li-Ge	2.95
Li-P	2.85
S-P	2.55
S-Ge	2.80

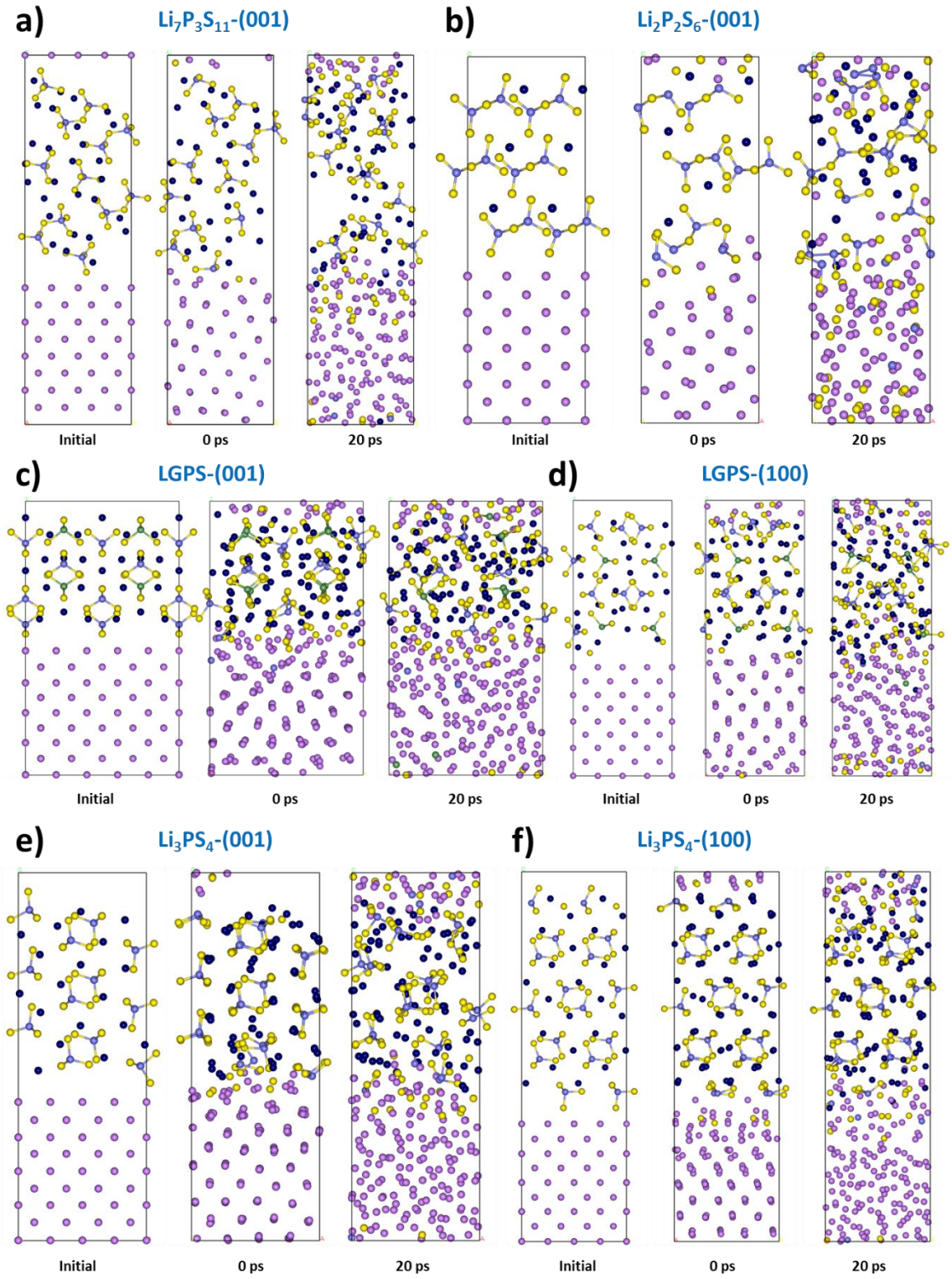

Figure D.5 Structural changes of SSE/Li model with optimization (0 ps) and AIMD simulations (20ps).

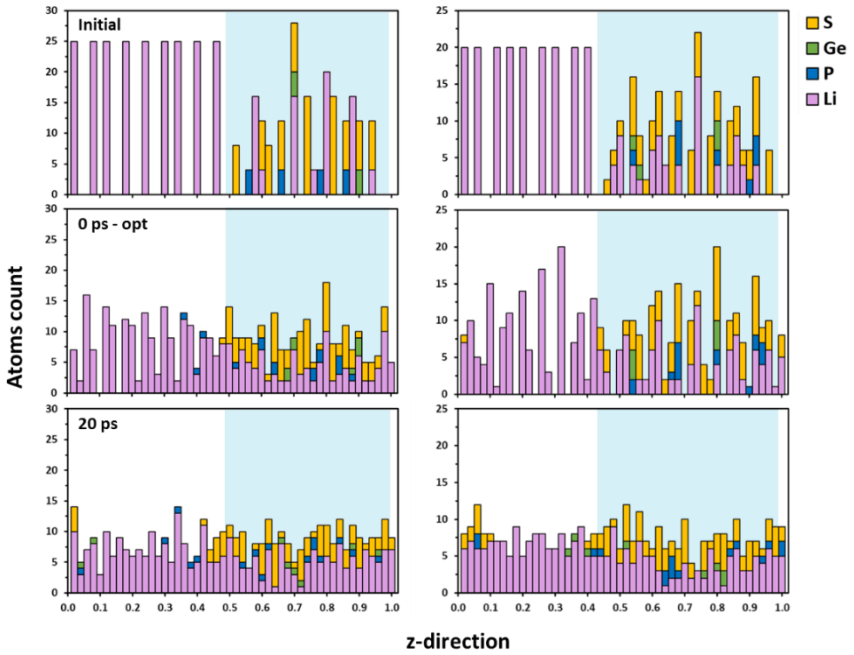

Figure D.6 Z-direction atom profile evolution of LGPS. (001) and (100) facets shown at the left and right, respectively.

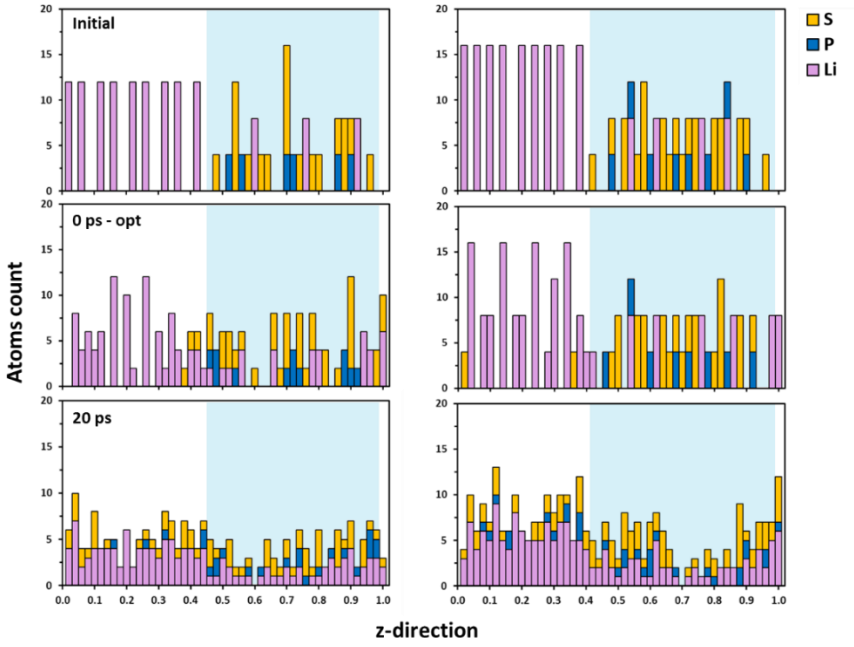

Figure D.7 Z-direction atom profile evolution of $Li_2P_2S_6$. (001) and (100) facets shown at the left and right, respectively.

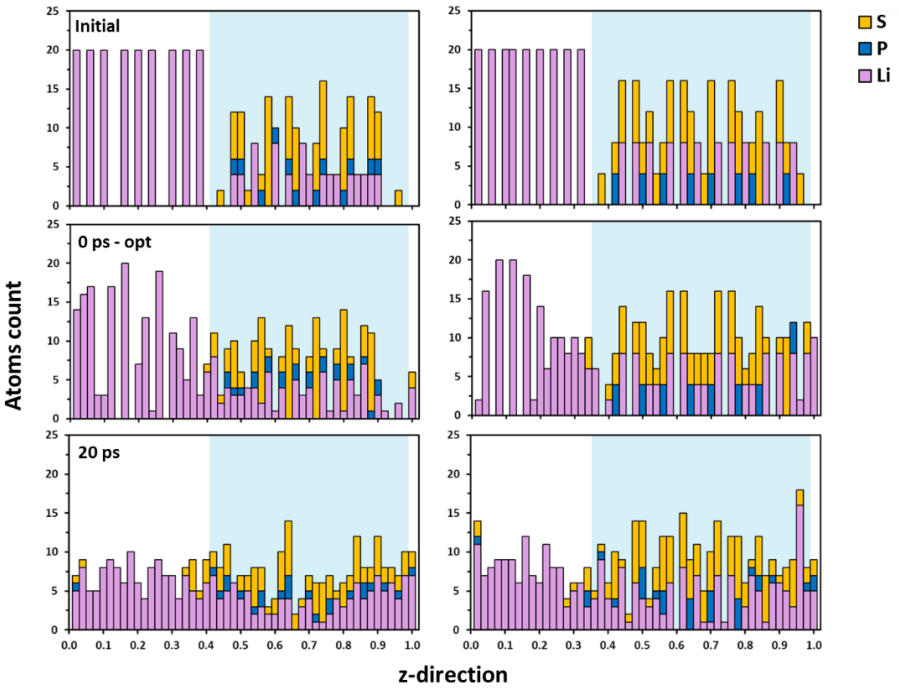

Figure D.8 Z-direction atom profile evolution of Li_3PS_4. (001) and (100) facets shown at the left and right, respectively.

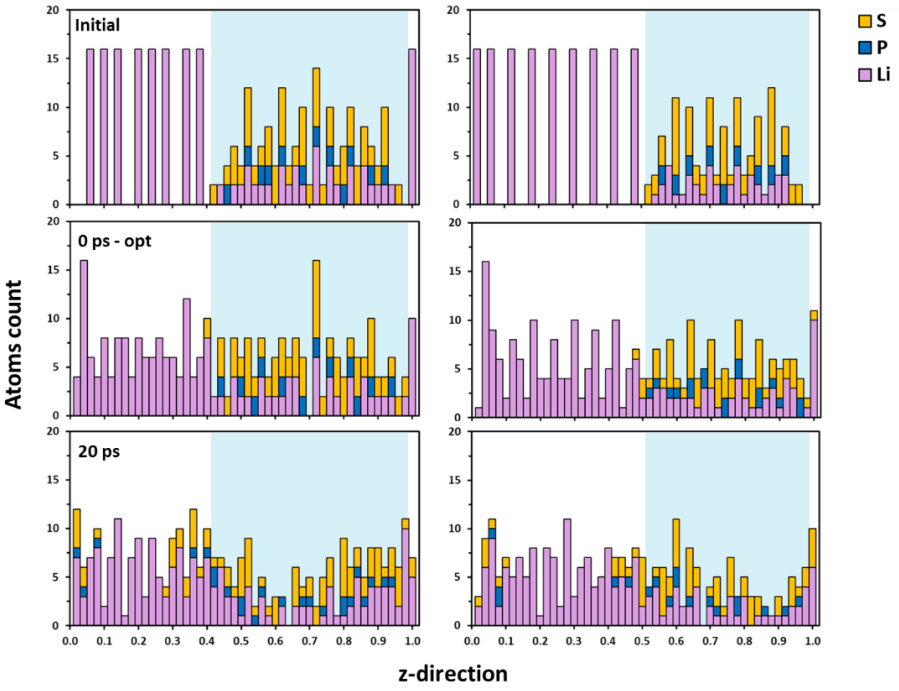

Figure D.9 Z-direction atom profile evolution of $Li_7P_3S_{11}$. (001) and (100) facets shown at the left and right, respectively.

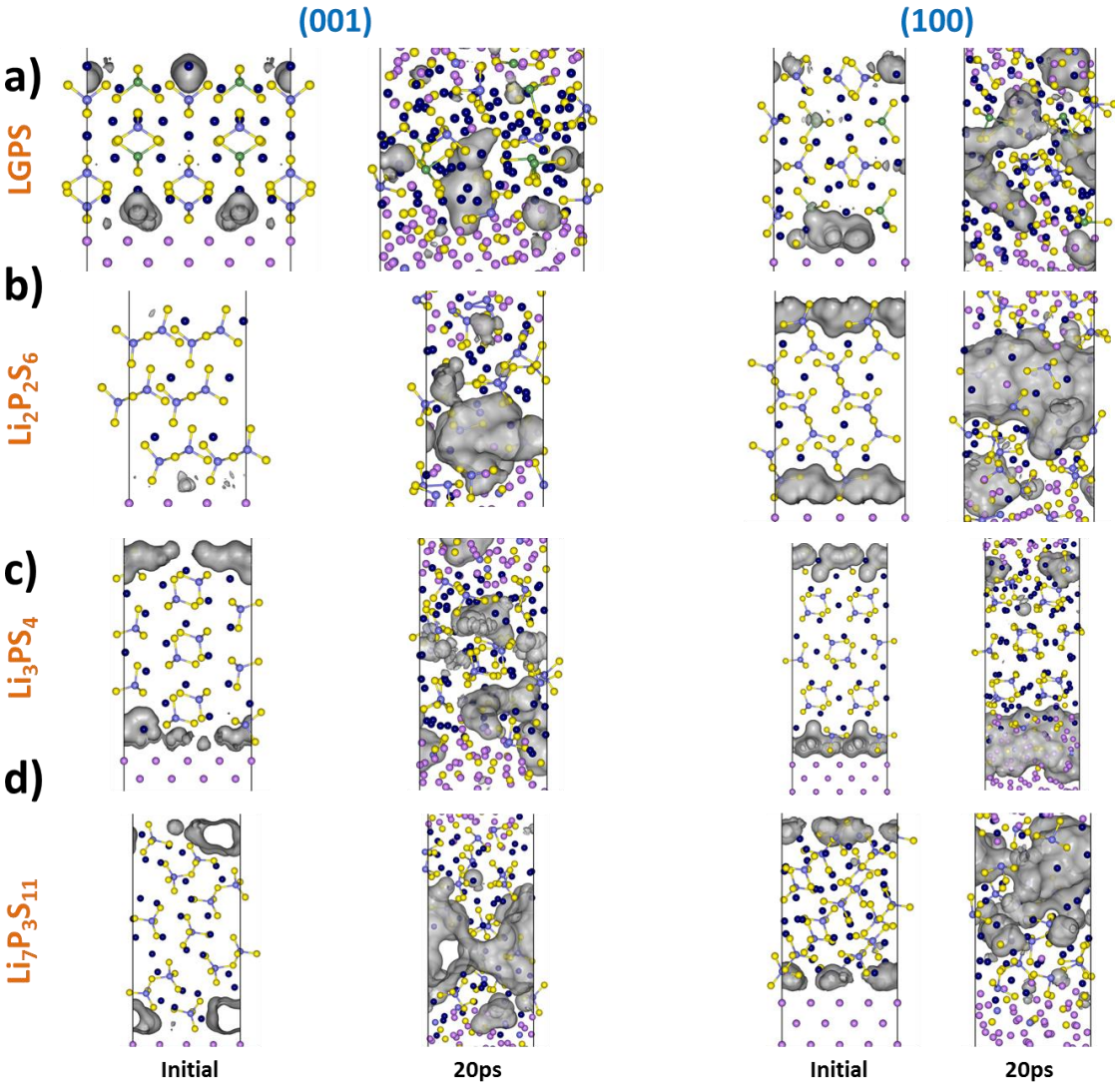

Figure D.10 void volume for SSE/Li models at the initial configuration (prior SSE/Li optimization) and after 20 ps of AIMD simulations.

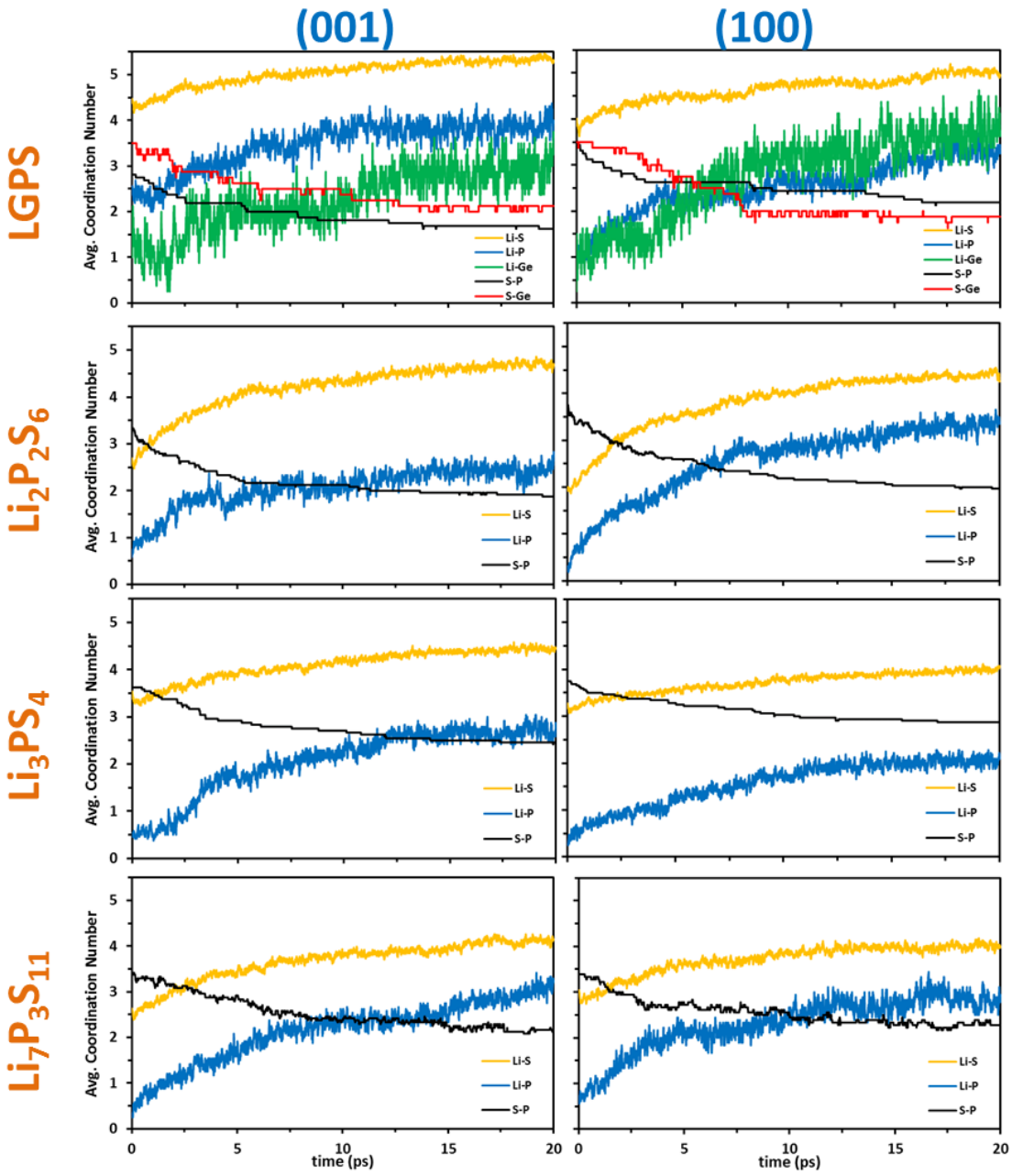

Figure D.11 Time-evolution of the average coordination number of Ge, P, and S surrounded by Li-species (Li-Ge, Li-P, and Li-S) and Ge and P surrounded by S-species (S-P and Ge-P).

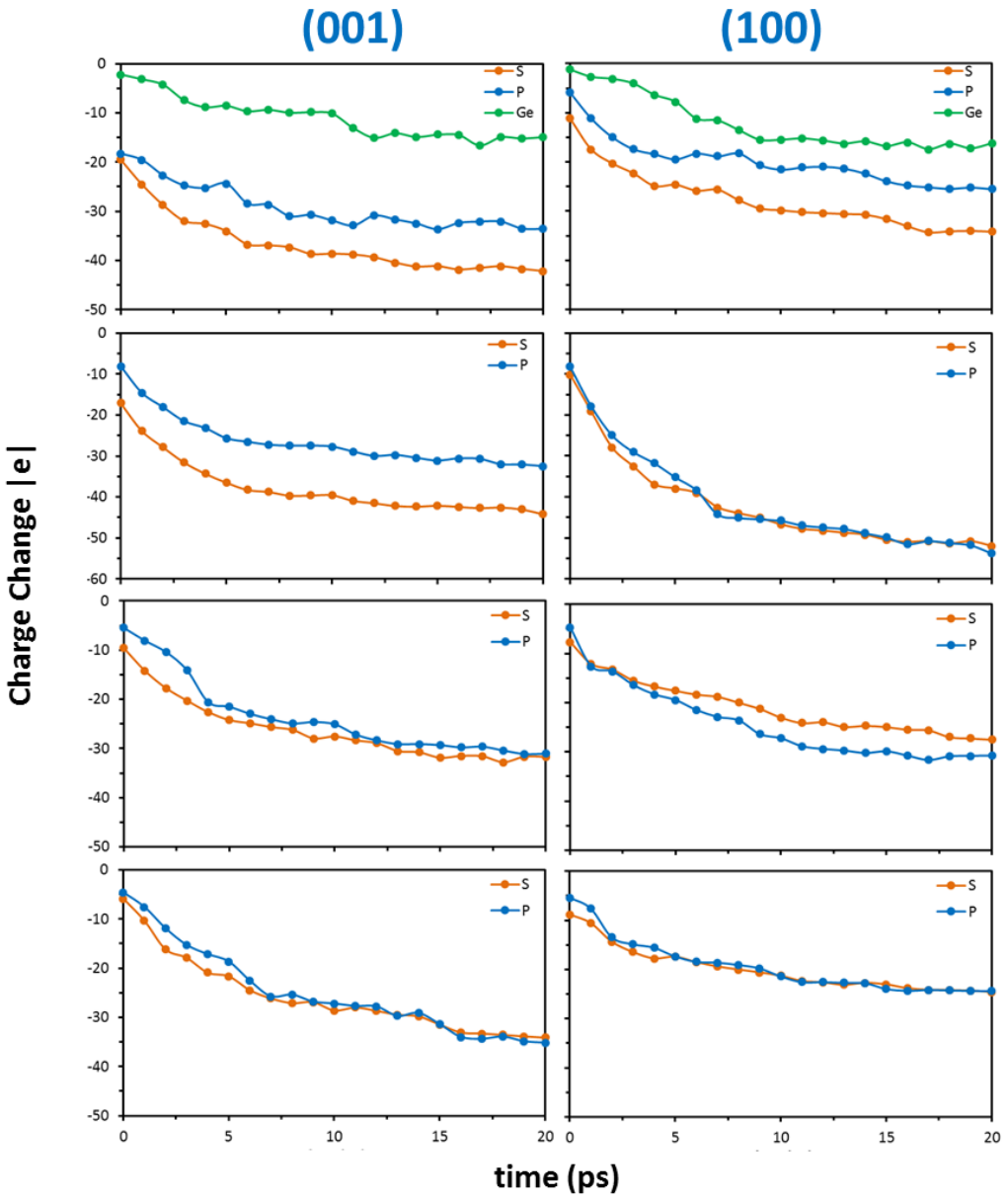

Figure D.12 Time-evolution of charge per species. Here, the charge change is calculated as a difference between the charges of the species at some point in the AIMD simulation minus the charge of each system before SSE/Li structural optimization.

The thresholds for charges were obtained using the following steps:

(i) Calculate the Bader charges of S, P, and Ge in all SSE materials under investigation.

(ii) Compute the average charge for every S, P, and Ge and multiply the result by 0.92 (to give 8% of fluctuations in the charge).

(iii) Use the values obtained in (ii) as the minimum charges for an atom to be considered non-reduced, i.e., as part of the pristine SSE.

(iv) Calculate the Bader charges of S, P, and Ge in Li_2S, Li_3P, and $Li_{15}Ge_4$, multiply the results by 0.92 (8% of fluctuations in the charge)

(v) Use the values obtained in (iv) as the maximum charges for an atom to be considered totally reduced, i.e., as if they were in Li_2S, Li_3P, and $Li_{15}Ge_4$ crystalline phases.

(vi) The atoms that fall in between the two limits are considered transient species or intermediates (partially reduced).

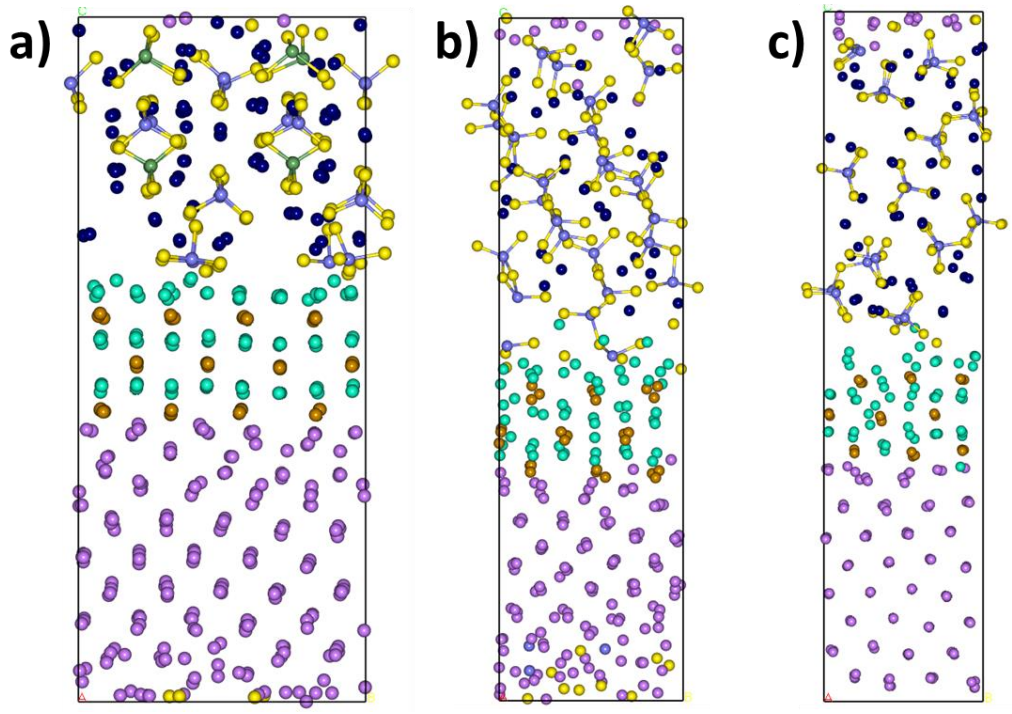

Figure D.13 Optimized SSE/Li_2S/Li configurations. (a) LGPS-(001), (b) $Li_2P_2S_6$-(100), and (c) $Li_7P_3S_{11}$-(001). Color code as described in Figure 6.8 in Chapter 6.

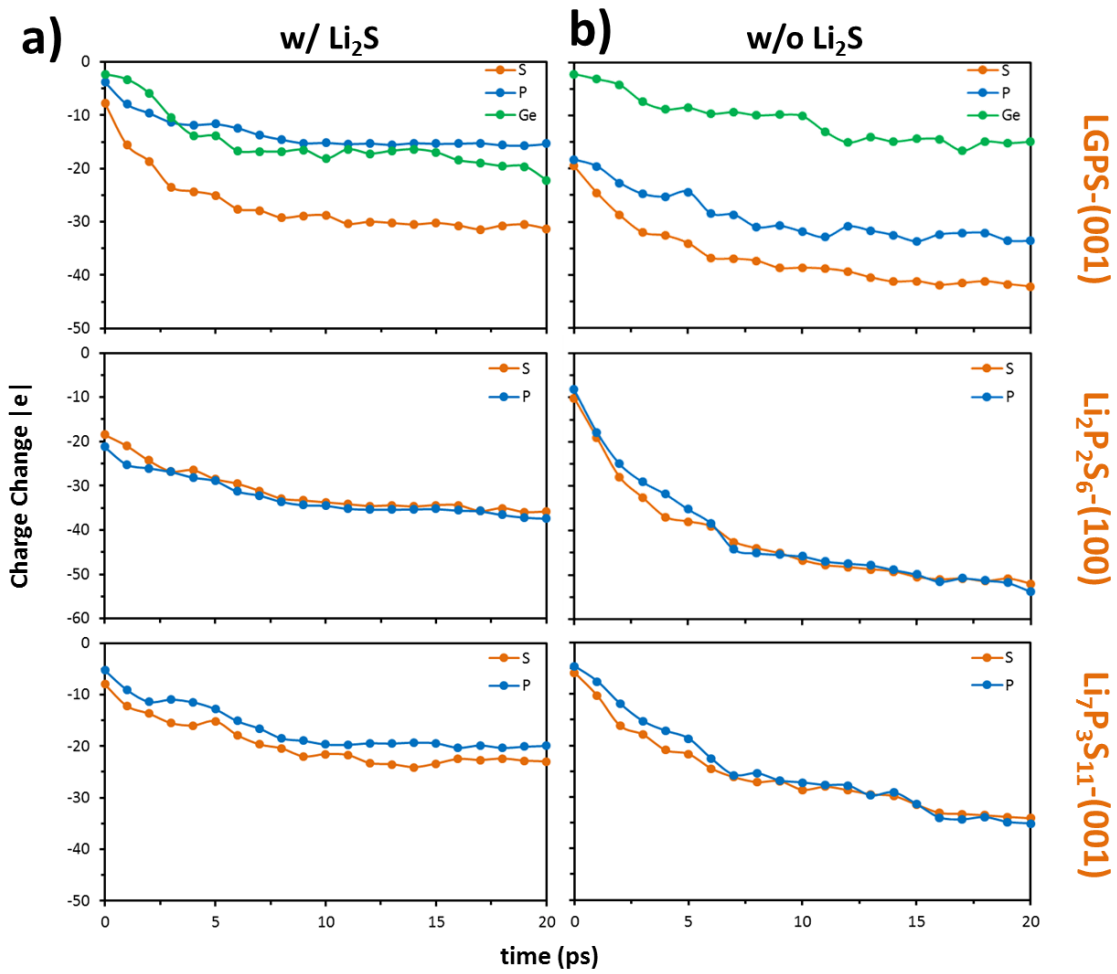

Figure D.14 Comparison of charge evolution per species for systems with and without Li_2S thin film. See caption Figure D.12 for details on how the charges change was calculated.

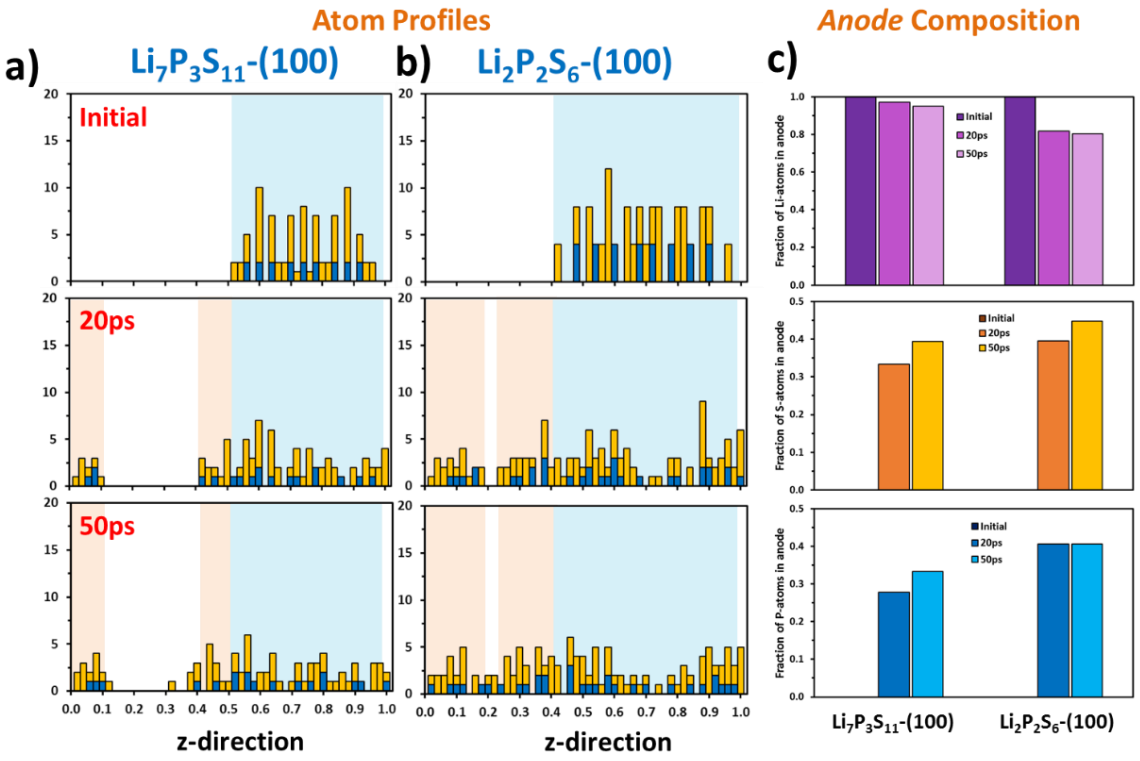

Figure D.15 Comparison of structural changes at 20 and 50 ps. Atomic profiles of (a) (100)-$Li_7P_3S_{11}$ and (b) (100)-$Li_2P_2S_6$. Light blue-shaded areas in (a) and (b) indicate the regions occupied by the SSE in the initial configuration. Light orange-shaded areas in (a) and (b) indicate the regions occupied by S or P species from the SSEs at 20 ps. (c) Comparison of anode atomic fractions at initial, 20 ps, and 50 ps of AIMD simulation.

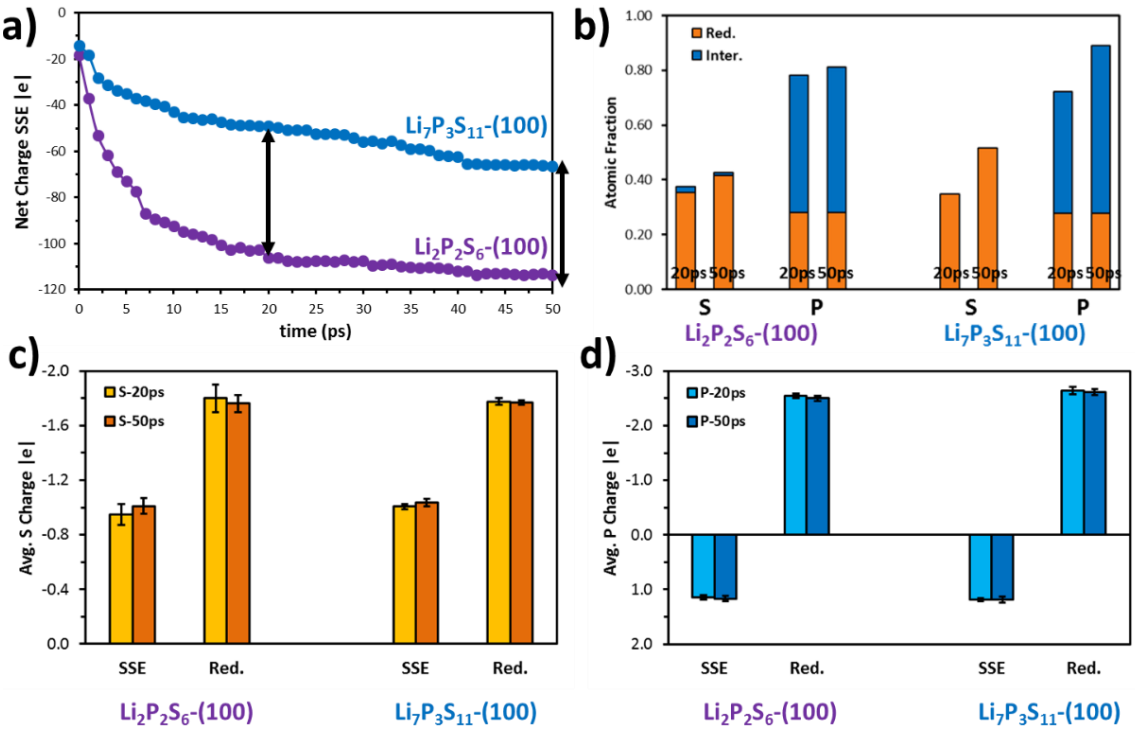

Figure D.16 Comparison of charge variations at 20 and 50 ps. (a) Net SSE charge evolution. (b) Partially (Inter.) and totally (Red.) reduced fractions per atomic species. (c) S and (d) P atomic average charges for all non-reduced (SSE) and totally reduced (Red.) atomic species along the 20 ps and 50 ps of AIMD simulations – sampled every picosecond.

Table D.6 Comparison of coordination number (CN) of atomic species (resulting from SSE's anions decomposition) at 20 and 50 ps.

SSE	CN atomic species ONLY			
	CN at 20 ps		CN at 50 ps	
	Li-S	Li-P	Li-S	Li-P
$Li_2P_2S_6$-(100)	6.1	7.3	6.3	7.1
$Li_7P_3S_{11}$-(100)	5.9	8.0	6.4	7.8

APPENDIX E

SUPPORTING INFORMATION FOR CHAPTER 7

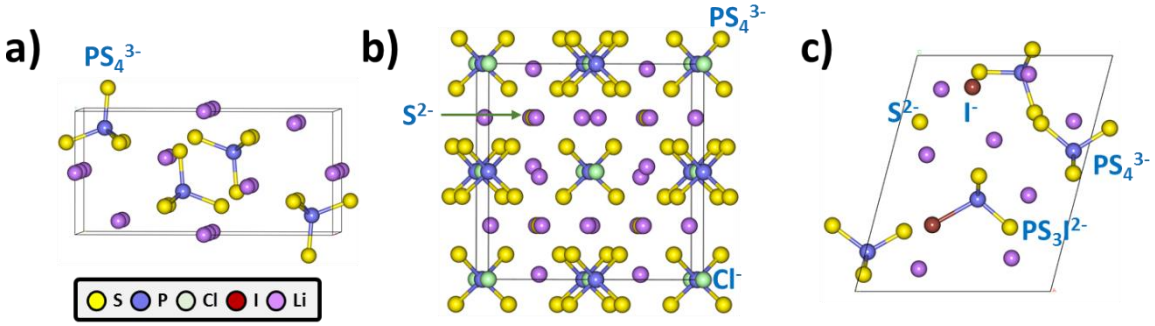

Figure E.1 Optimized crystalline structures for bulk SSEs under investigation: a) LPS; b) LPSCl; and c) LPSI.

Table E.1 Literature review of Li-ion diffusion properties in bulk LPS, LPSCl, and LPSI.

SSE	E_a (eV)	σ (mS cm^{-1})	D (cm^2 s^{-1}) x10^{-8}
LPS	0.36,[242] 0.32,[242] 0.41,[244] 0.19-0.65[264]	0.12,[242] 0.33,[242] 0.124,[244] 0.057,[244] 8.93x10^{-4},[194] 0.16,[194] 0.50,[247] 10[a 265]	1.4-7.2,[244] 0.52-1.8,[b 244] 3.8,[c 265] 1-10^2,[d 265] 1[e 265]
LPSCl	0.38,[243] 0.29,[266] 0.52,[239] 0.45,[237] 0.38, [245] 0.33[246, 267]	0.03,[243] 1.90,[243] 0.36,[266] 1.10,[239] 2.00,[239] 1.3x10^{-3},[f 245] 1.18,[267] 1.33,[246] 0.20[246]	7.70,[f 245] 92[g 267]
LPSI	0.27,[242] 0.30,[268] 0.20[221]	0.38,[242] 0.58,[268] 0.63,[222] 0.30[221]	-

*Theoretical calculations

**Different T (K): *a)* 450, *b)* 303, *c)* 373, *d)* 393, *e)* 383, *f)* 313, *g)* 345

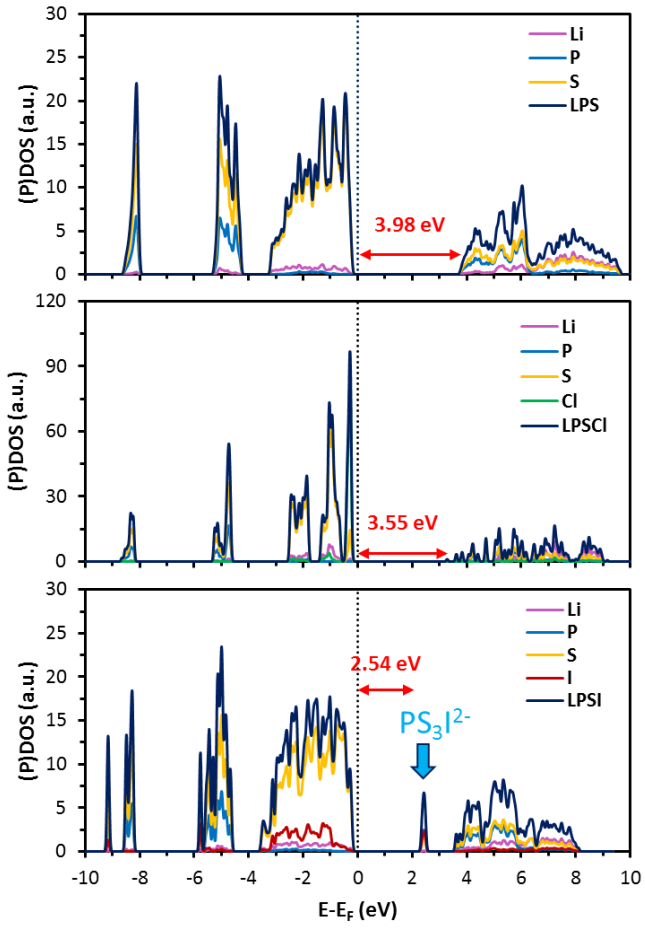

Figure E.2 Total and partial Density of States (DOS) of the three SSEs considered in this work: LPS (top), LPSCl (middle), and LPSI (bottom). DOS were calculated using the HSE06 hybrid functional.

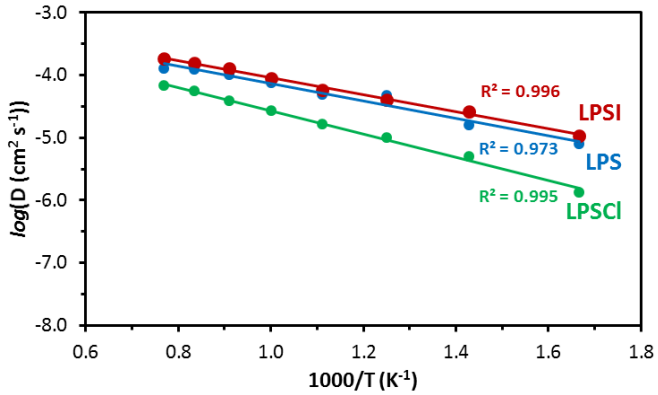

Figure E.3 Temperature dependence of the diffusion coefficient of Li-ion calculated from the MSD of AIMD trajectories over 100 ps. Coefficients of determination (R^2) are shown as a descriptor of the goodness of the fitting.

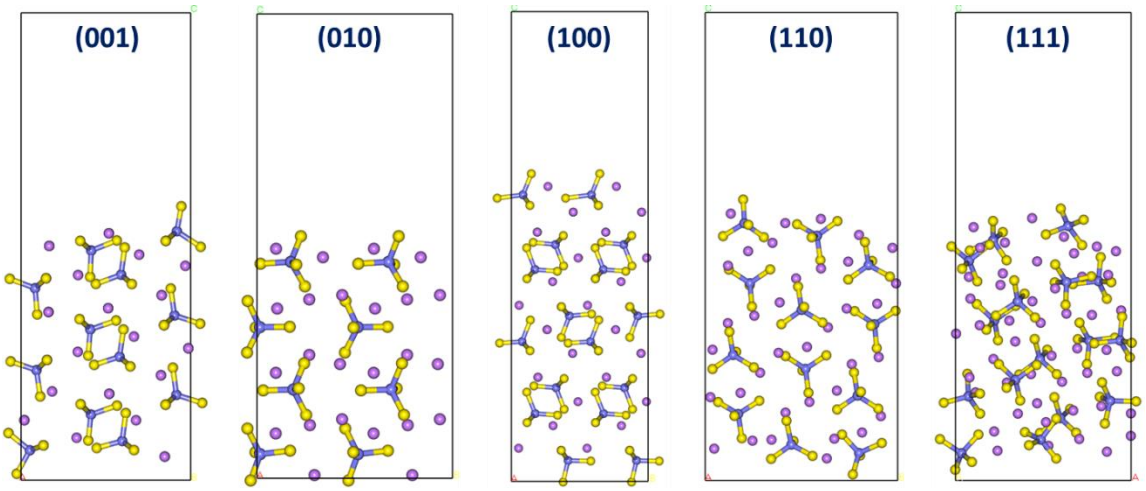

Figure E.4 Optimized cleaved facets of LPS. Color code as in Figure E.1.

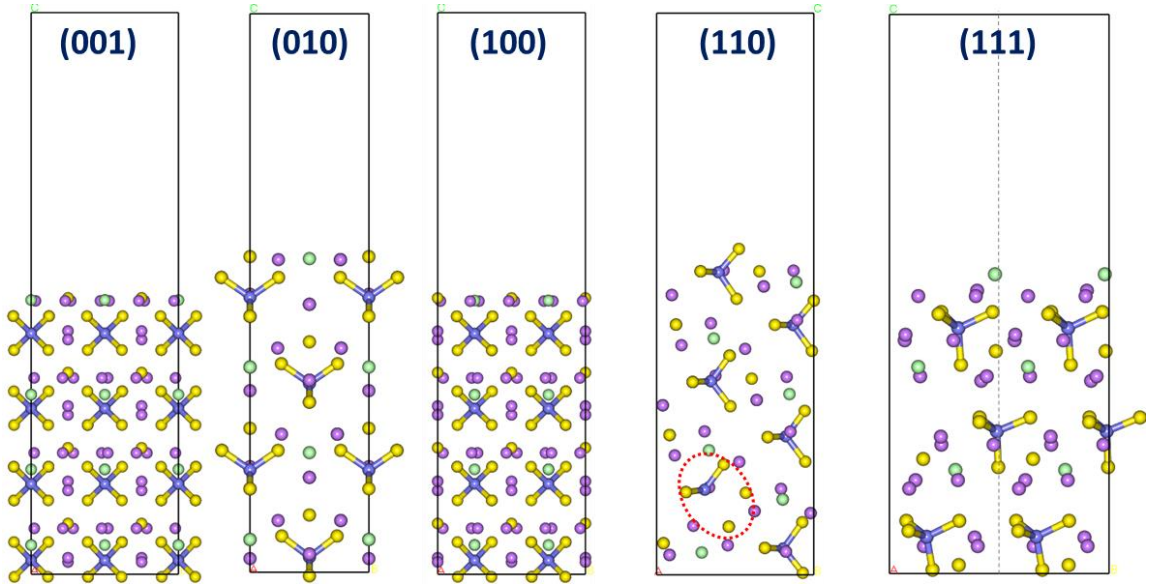

Figure E.5 Optimized cleaved facets of LPSCl. Color code as in Figure E.1.

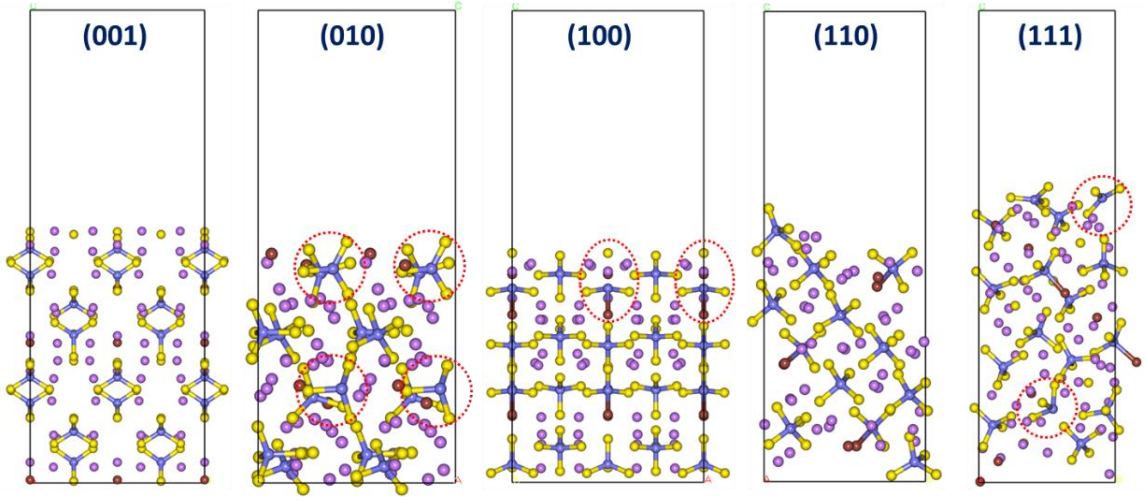

Figure E.6 Optimized cleaved facets of LPSI. Color code as in Figure E.1.

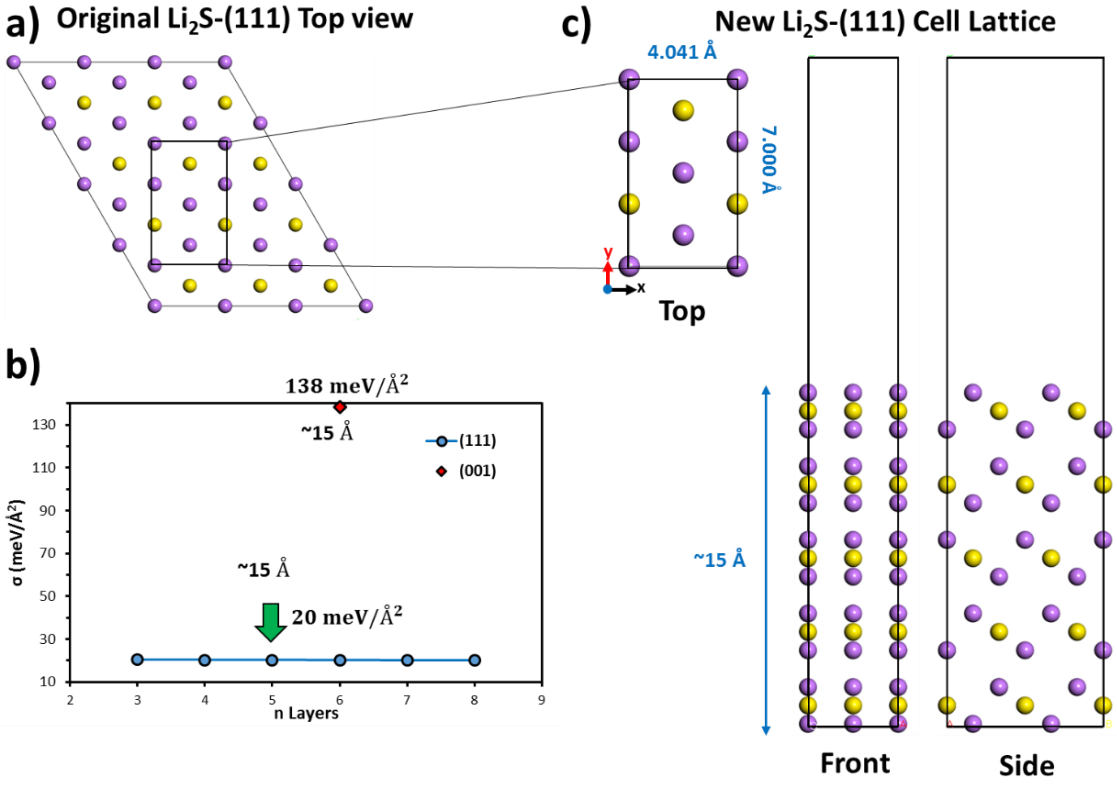

Figure E.7 Model of Li_2S cathode material. a) Top view of original hexagonal Li_2S (111) surface; b) surface energy for Li_2S (111) and (001); and c) New Li_2S (111) orthorhombic lattice surface. Same surface energy is obtained for the new system, therefore, equivalent surface. Color code as in Figure E.1.

Table E.2 Simulation k-points and optimized crystallographic parameters of bulk materials for the cathode model.

SSE	K-points	Crystallography						
		Space Group	**a (Å)**	**b (Å)**	**c (Å)**	**α**	**β**	**γ**
α-S_8	2x2x1	*Fddd*	10.254	12.610	24.366	90	90	90
Li_2S	4x4x4	*Fm-3m*	5.715	5.715	5.715	90	90	90

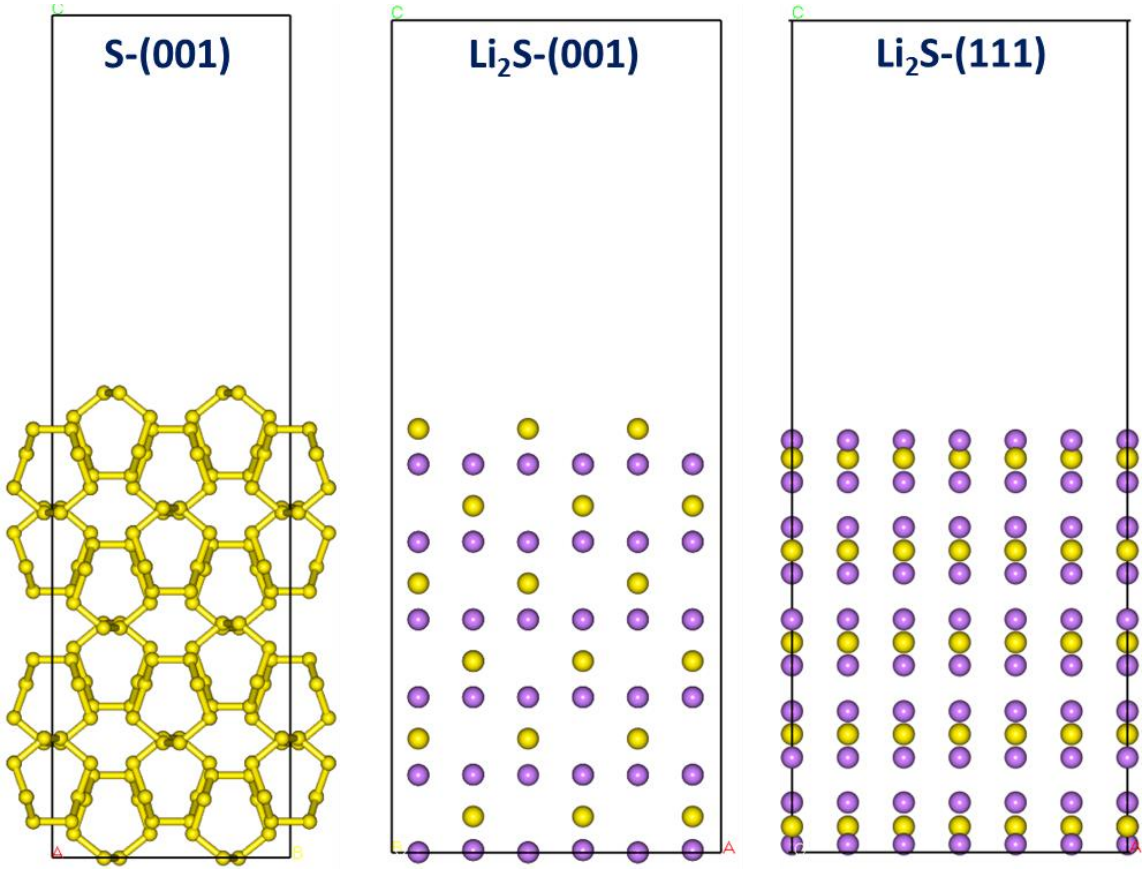

Figure E.8 Slab cathode models. Color code as in Figure E.1.

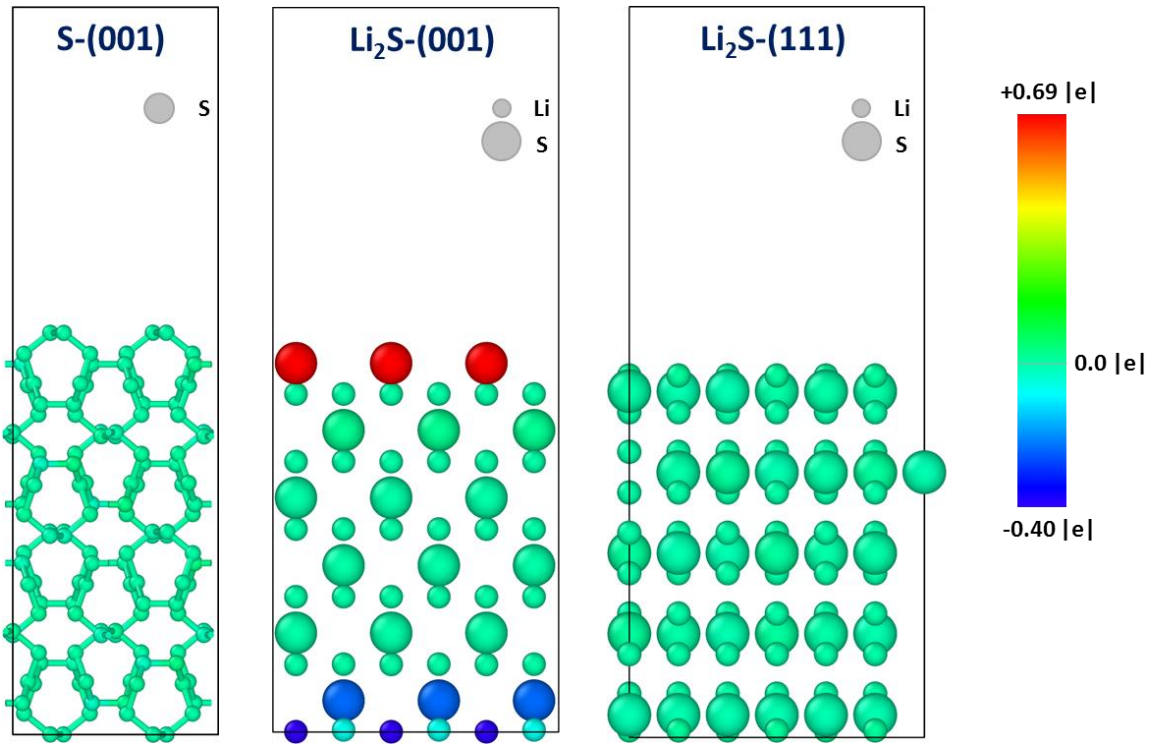

Figure E.9 Color-mapped structures with atomic Bader charge difference of the slab cathode models with respect to bulk charges, i.e., $\Delta CHG^{atom-i} = CHG^{atom-i}_{Slab} - CHG^{atom-i}_{bulk}$.

Table E.3 Summary and characteristics of SSE and cathode slab models investigated in this work. Supercell: MxN is the supercell size on the horizontal plane (*axb*) and *n*L stands for the number of stoichiometric layers along the *c*-axis. The thickness of the SSE-slab is h. The thickness of the cathode models is as described in section 7.3.4 of Chapter 7.

Electrolyte		**Cathode – MxN**			**SSE**	
SSE	**Facet**	**S-(001)**	**Li_2S-(001)**	**Li_2S(111)**	**MxN-(*n*L)**	**h (Å)**
LPS	(001)	1x1	3x2	3x1	1x1-(3L)	21
	(100)	1x1	3x2	3x1	1x2-(2L)	28
LPSCl	(001)	1x1	3x3	2x2	1x1-(2L)	19
LPSI	(001)	1x1	2x4	2x2	1x2-(2L)	22
	(100)	1x1	4x3	2x3	2x1-(2L)	19

Table E.4 Induced strain along *a* and *b* directions (on-plane) due to mismatch between the cathode slab model and the SSEs. Strains > 10% are shown in red.

Cathode	Electrolyte		Strain – Cathode (%)		Strain – SSE (%)	
	SSE	Facet	ε_a	ε_b	ε_a	ε_b
S-(001)	LPS	(001)	10.4	1.8	1.8	13.2
		(100)	10.4	0.4	13.2	0.4
	LPSCl	(001)	0.0	9.3	0.0	11.5
	LPSI	(001)	4.0	12.0	4.4	9.7
		(100)	7.3	12.0	9.7	6.4
Li2S-(001)	LPS	(001)	3.9	0.2	3.6	0.2
		(100)	1.6	0.2	0.2	1.5
	LPSCl	(001)	7.7	7.7	9.1	9.1
	LPSI	(001)	8.3	1.6	7.1	1.7
		(100)	1.6	1.6	1.7	1.6
Li2S-(111)	LPS	(001)	3.9	7.9	3.6	6.9
		(100)	1.6	7.9	6.9	1.5
	LPSCl	(001)	5.1	1.8	5.7	1.7
	LPSI	(001)	8.3	5.9	7.2	5.2
		(100)	5.9	1.6	5.2	1.6

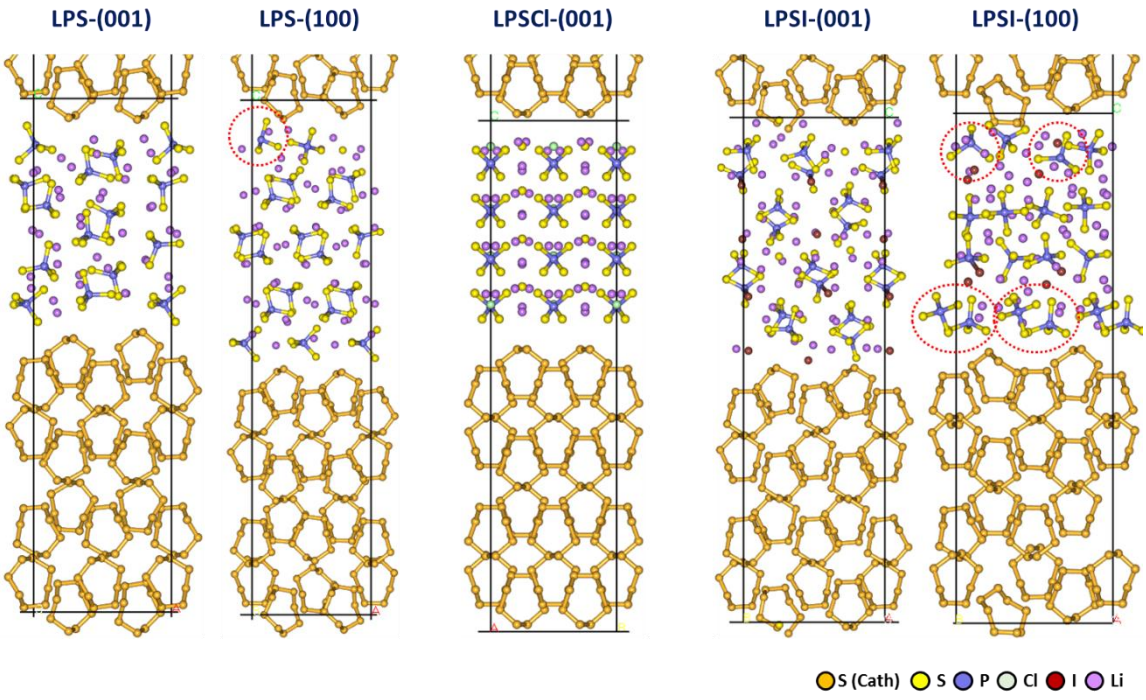

Figure E.10 Optimized S-(001)/SSE interfaces. Red dotted ovals indicate decomposition after structural optimization.

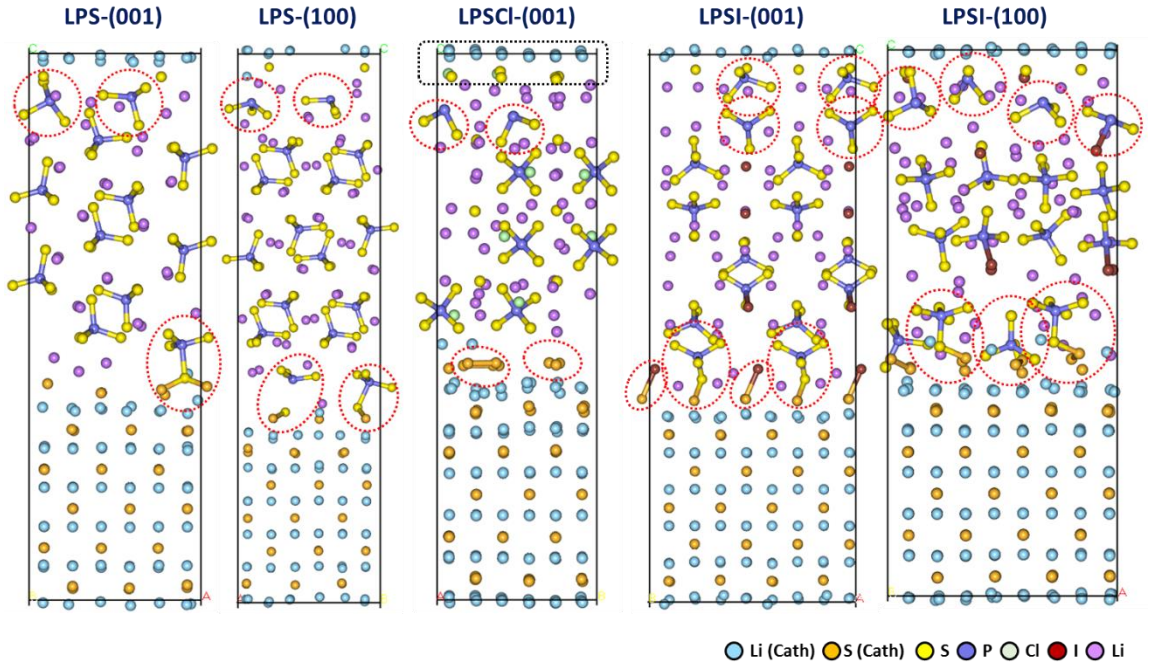

Figure E.11 Optimized Li_2S-(001)/SSE interfaces. Red dotted ovals indicate decomposition after structural optimization.

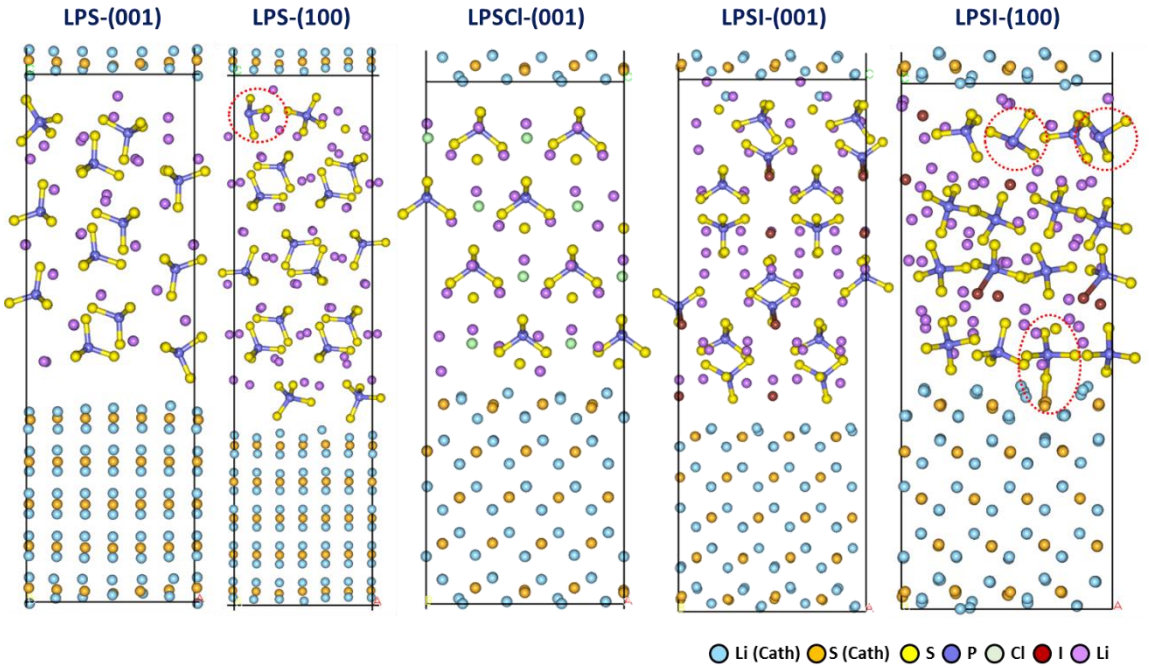

Figure E.12 Optimized Li_2S-(111)/SSE interfaces. Red dotted ovals indicate decomposition after structural optimization.

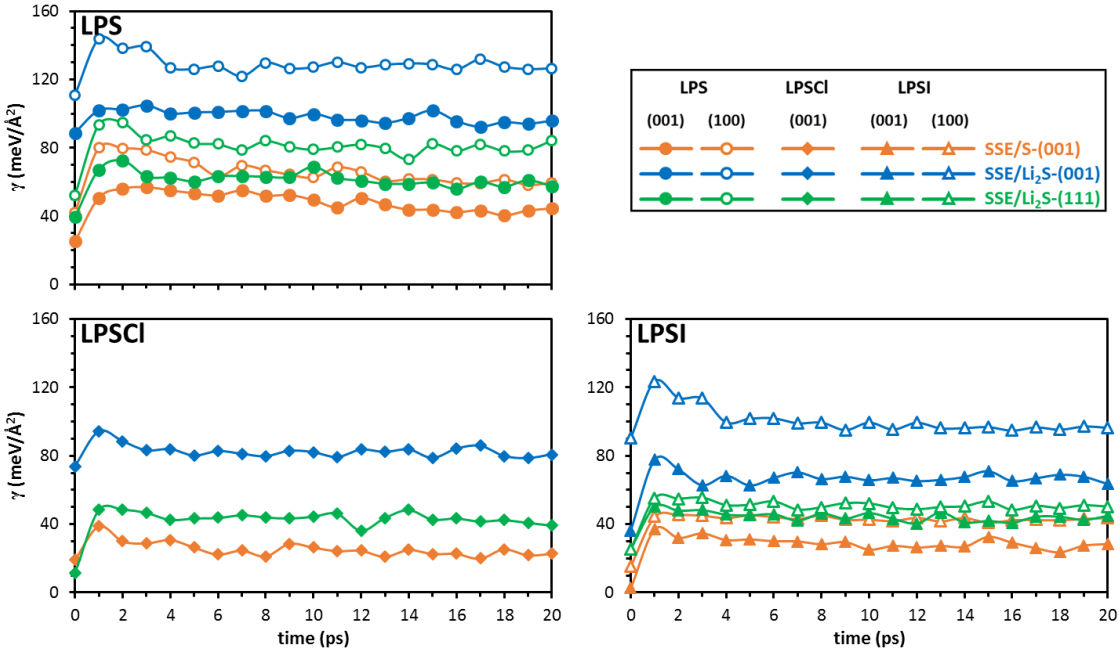

Figure E.13 Time evolution of S-cathode/SSE interfacial energies.

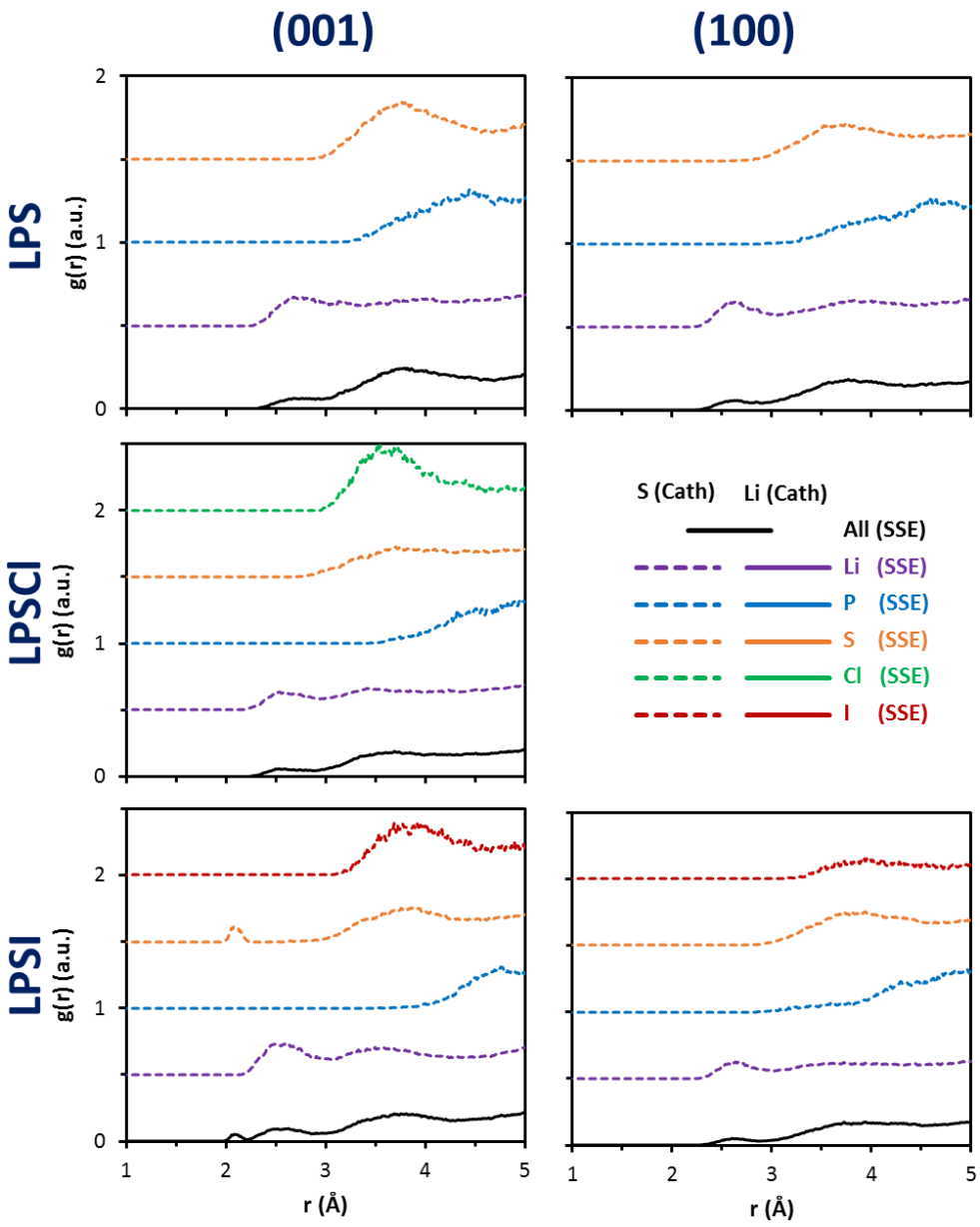

Figure E.14 Radial distribution functions g(r) between *i* (cathode: S, Li or all) – *j* (electrolyte: Li, S, P, I, Cl, or all) species for the S-(001)/SSE interfaces.

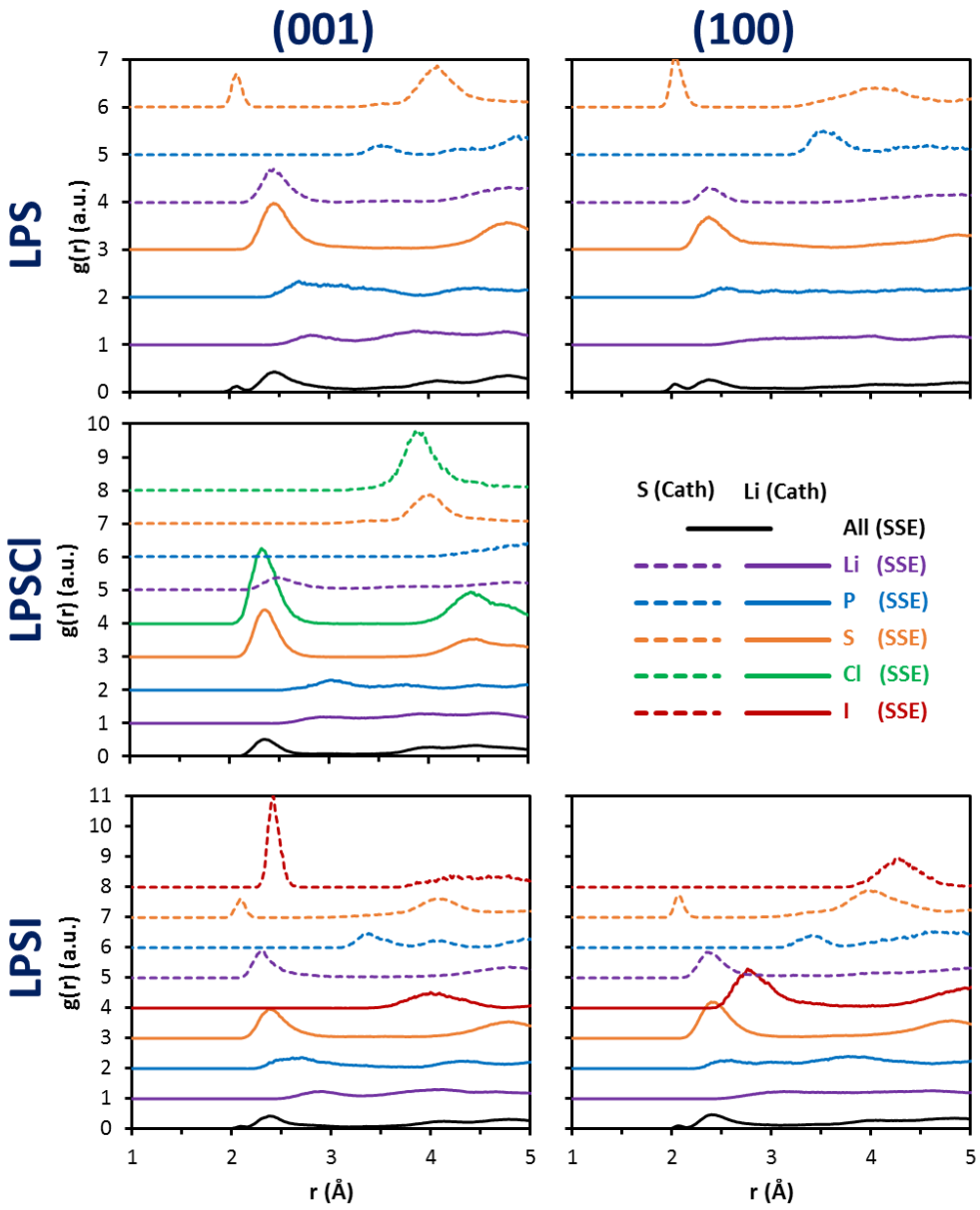

Figure E.15 Radial distribution functions g(r) between i (cathode: S, Li or all) – j (electrolyte: Li, S, P, I, Cl, or all) species for the Li_2S-(001)/SSE interfaces.

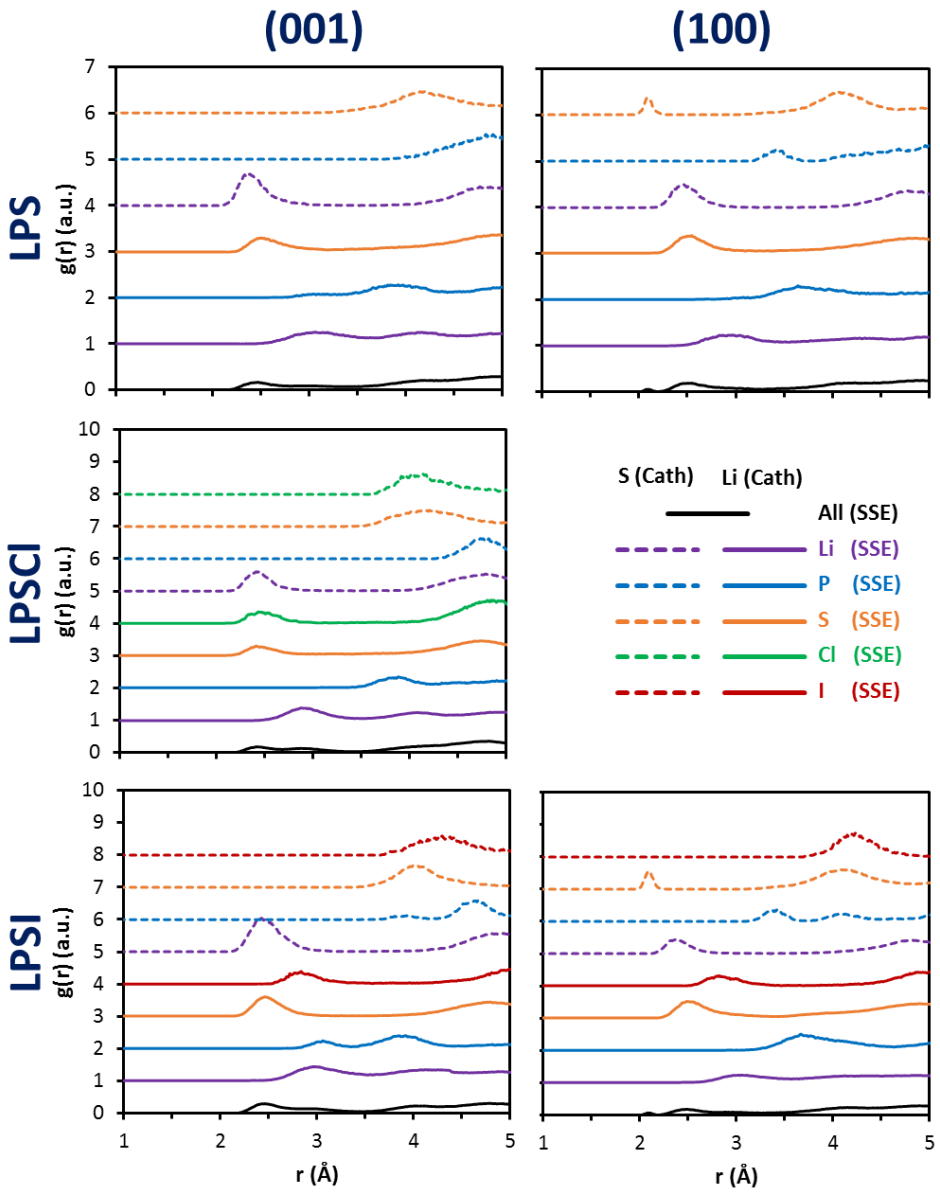

Figure E.16 Radial distribution functions g(r) between i (cathode: S, Li or all) – j (electrolyte: Li, S, P, I, Cl, or all) species for the Li_2S-(111)/SSE interfaces.

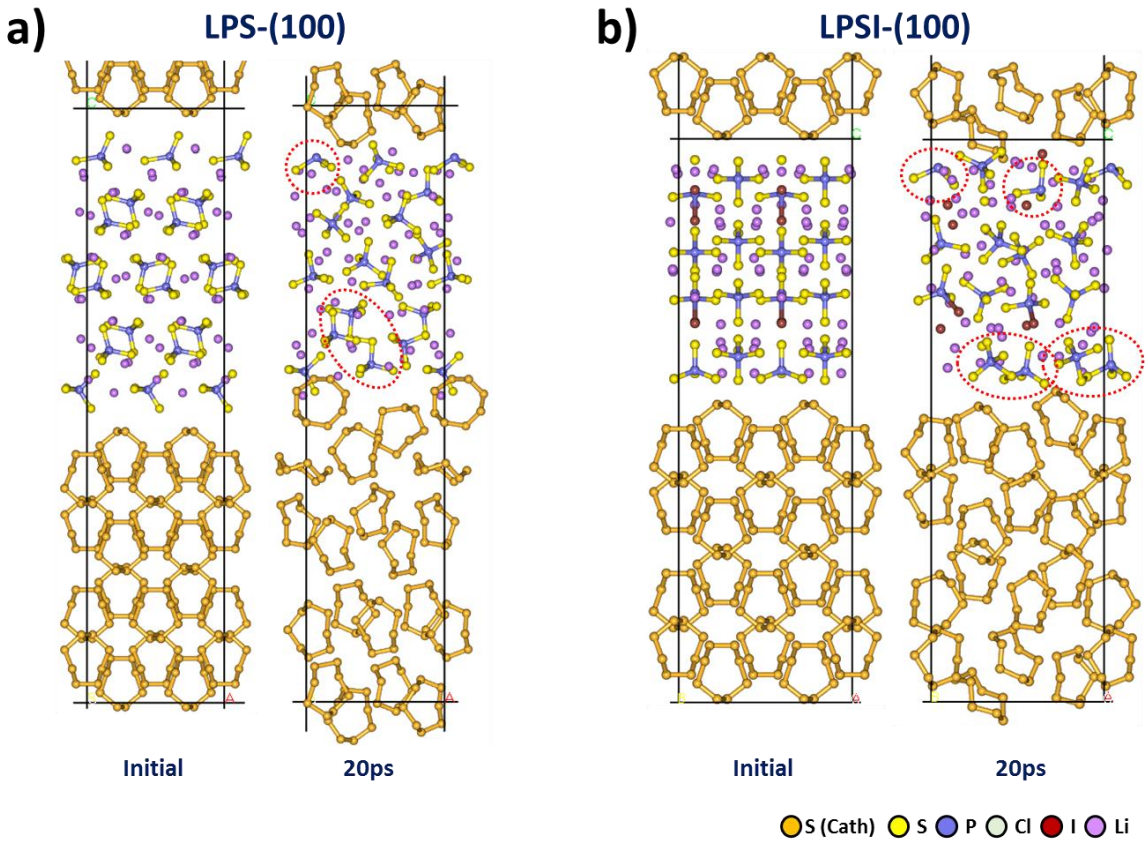

Figure E.17 Initial and final (after 20 ps of AIMD simulation) configurations of S-(001)/SSE models.

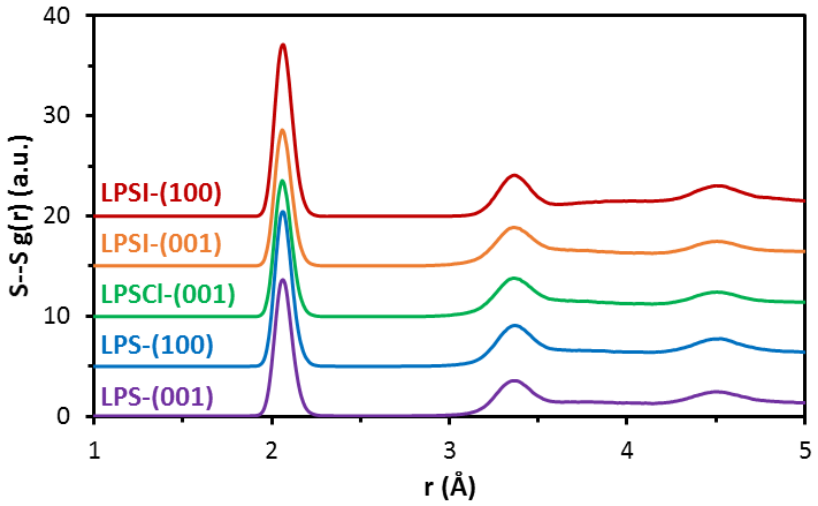

Figure E.18 Intramolecular S-S radial distribution functions g (r) of the S-(001) cathode model over 20 ps of AIMD simulation in contact with different solid electrolytes.

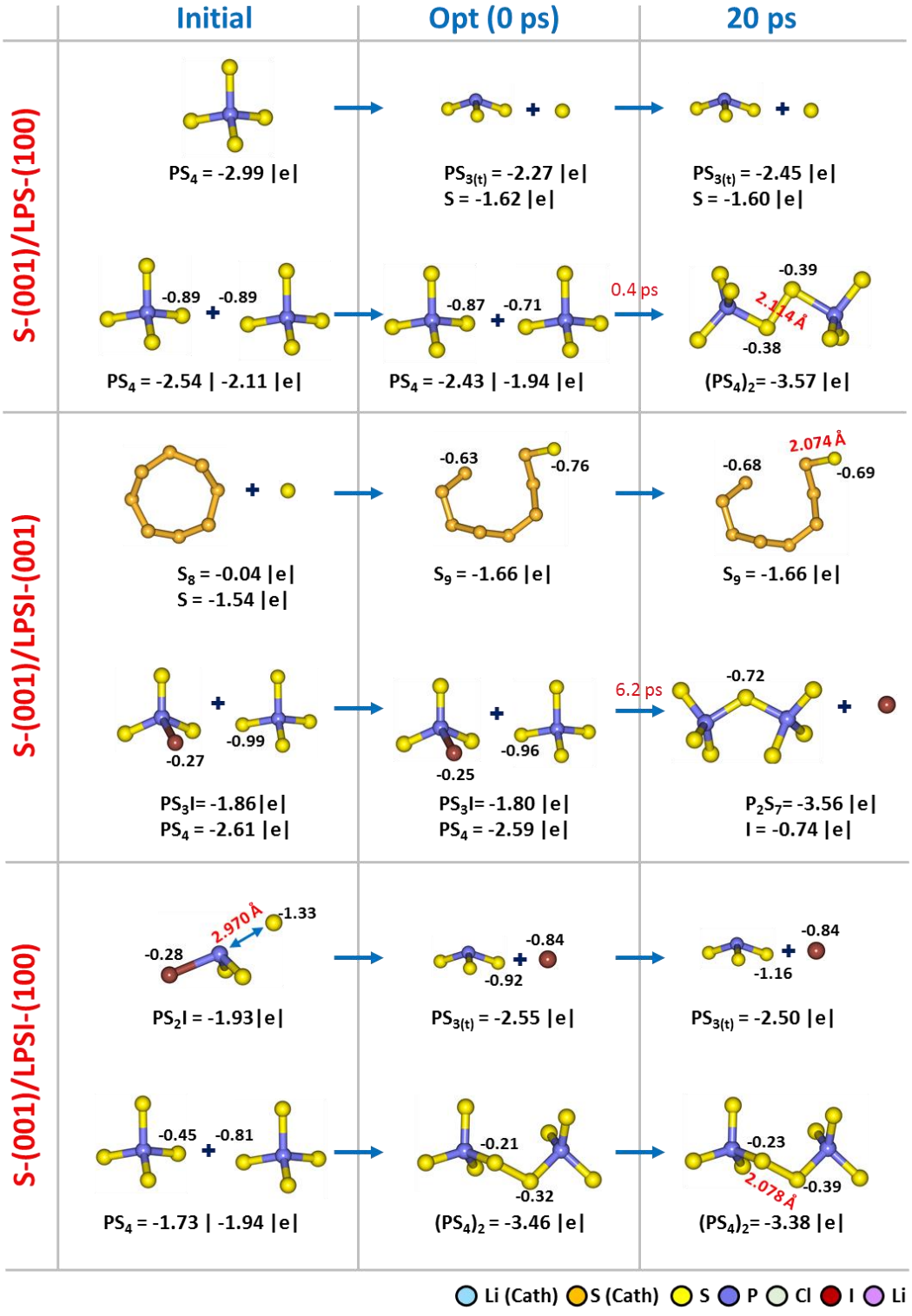

Figure E.19 Detailed reaction mechanisms (with net charges in |e|) for S-(001)/SSE interfaces.

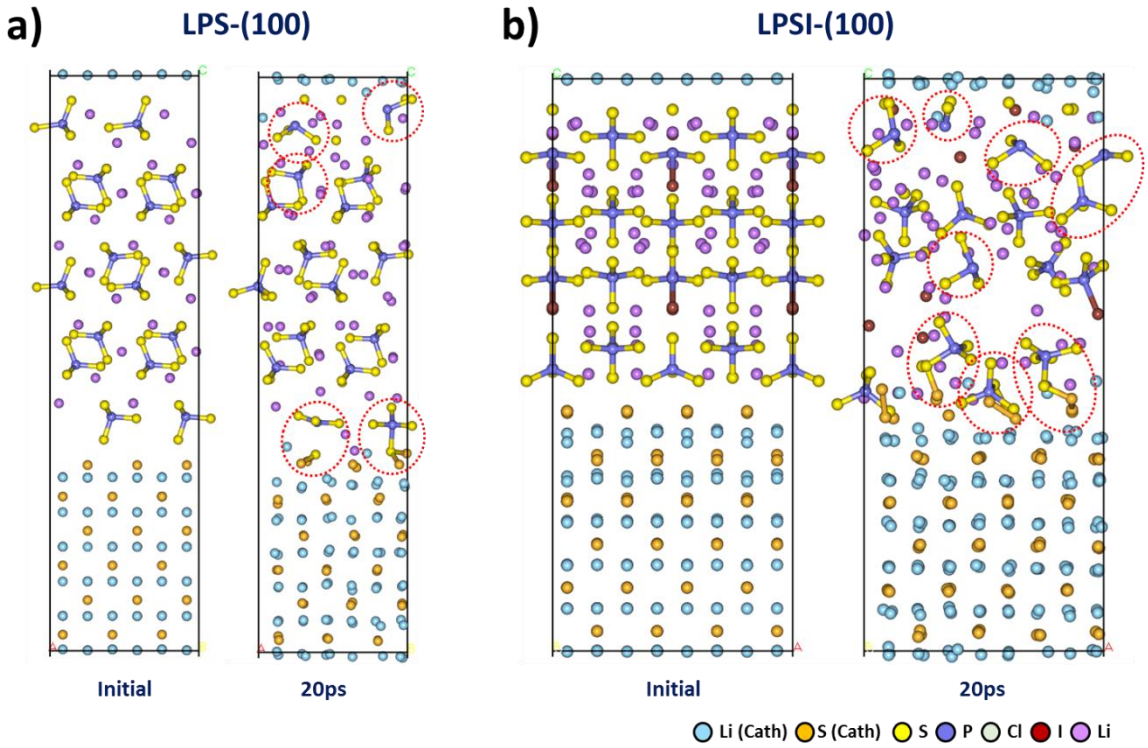

Figure E.20 Initial and final (after 20 ps of AIMD simulation) configurations of Li_2S-(001)/SSE interfaces.

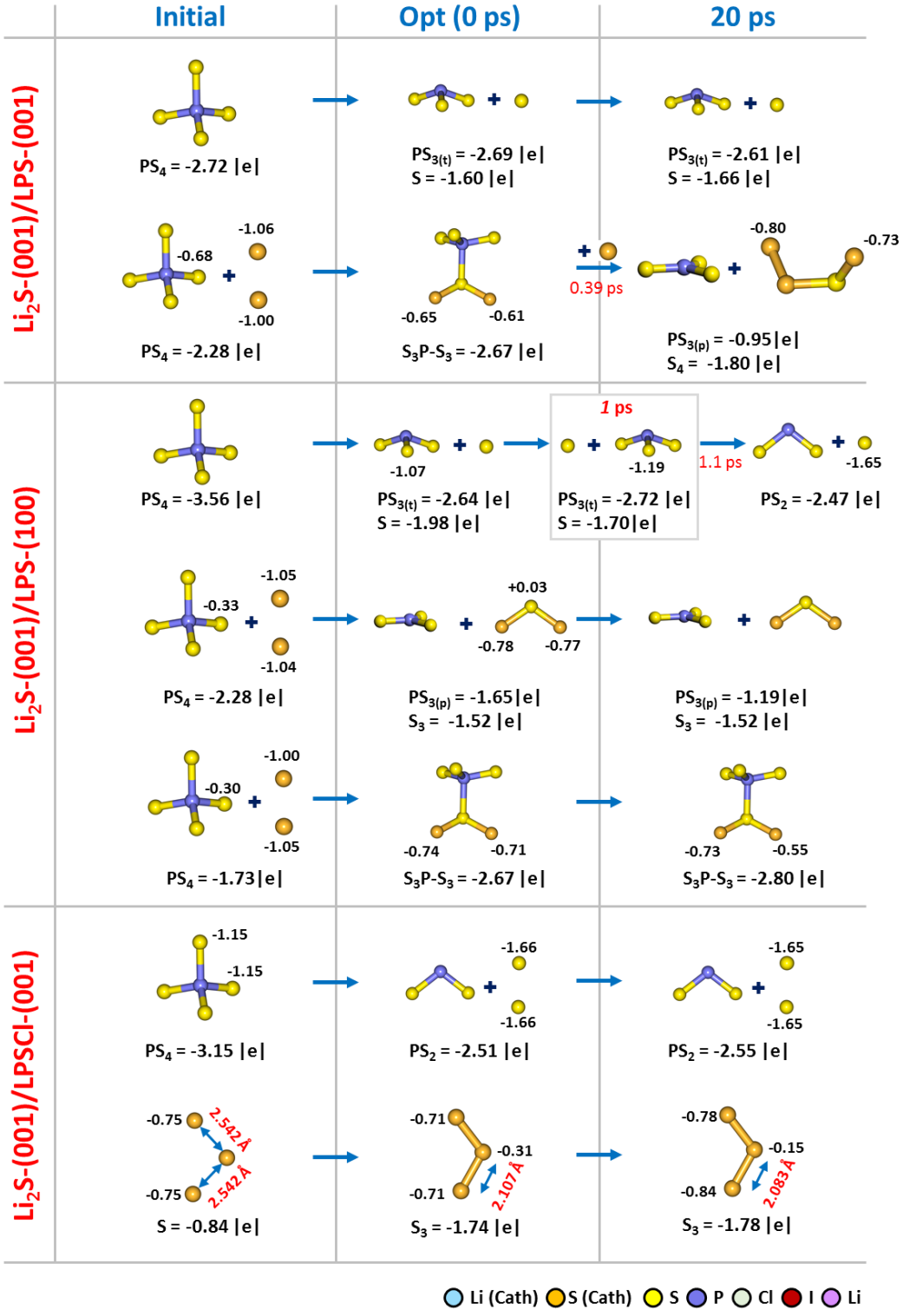

Figure E.21 Detailed reaction mechanisms (with net charges in |e|) for Li_2S-(001)/SSE interfaces.

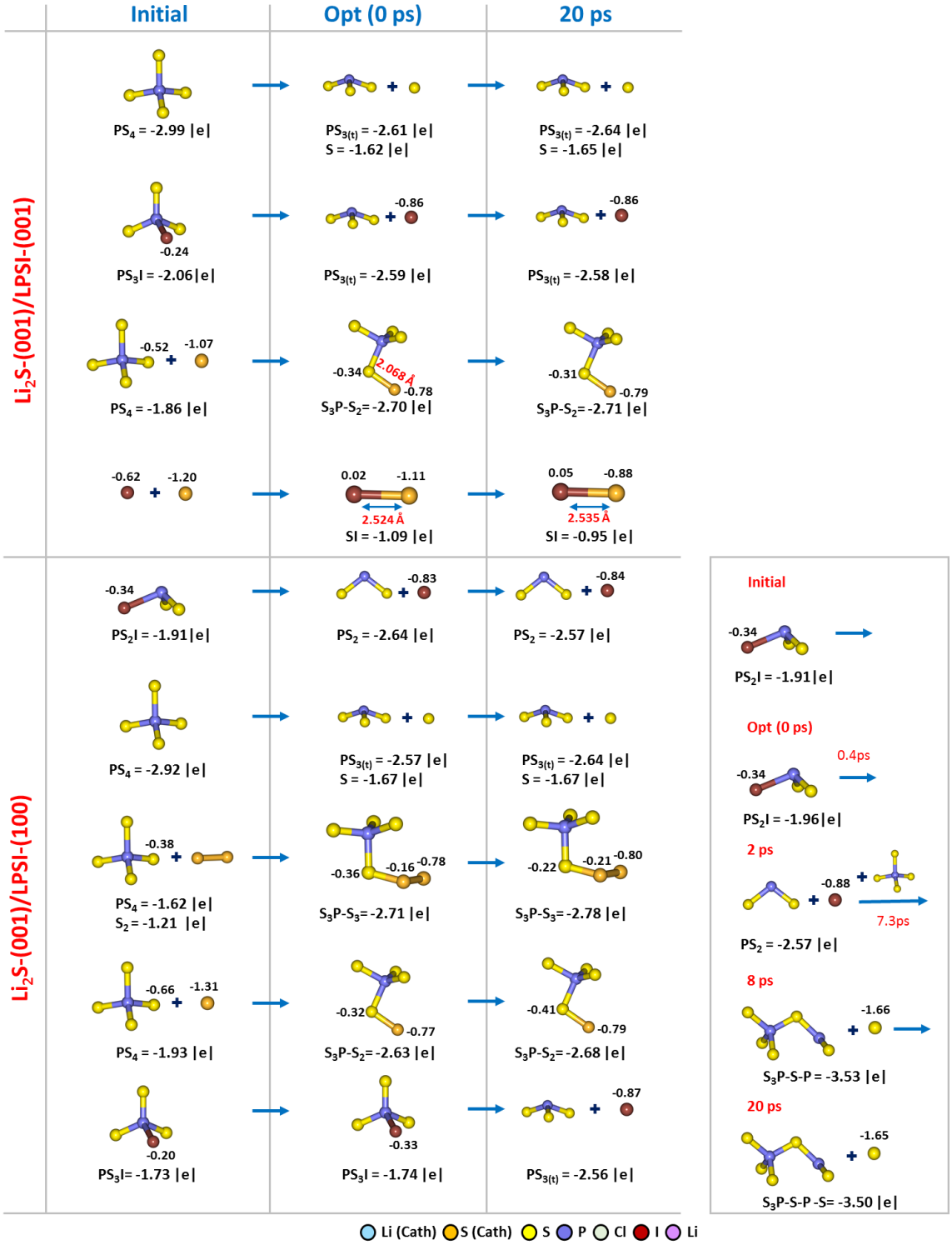

Figure E.21 Continued.

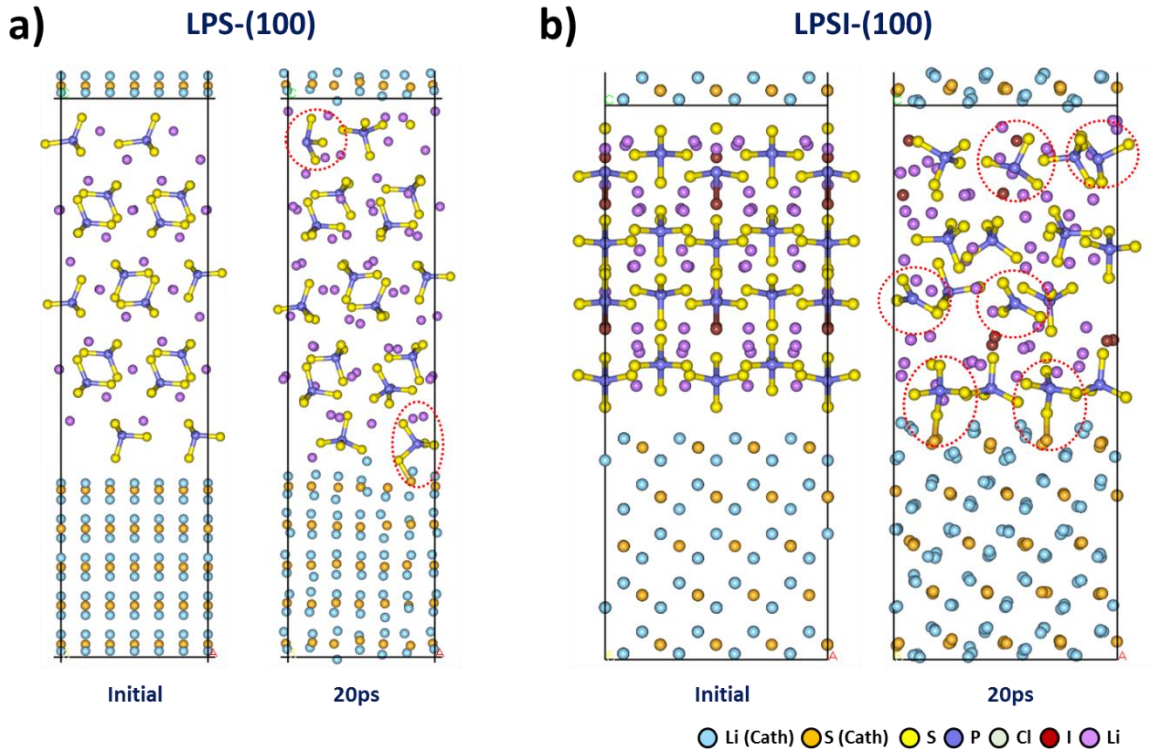

Figure E.22 Initial and final (after 20 ps of AIMD simulation) configurations of Li_2S-(111)/SSE models.

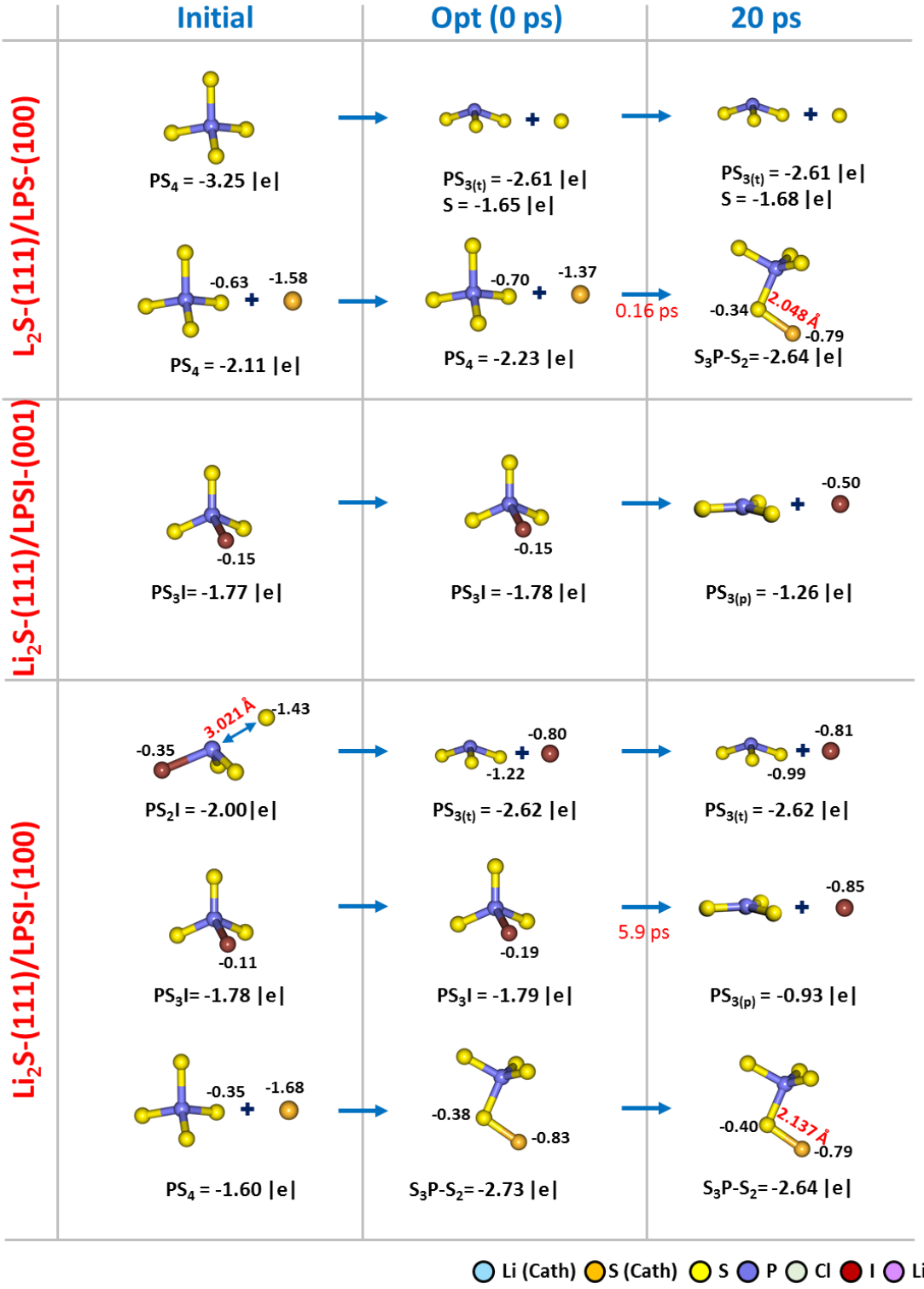

Figure E.23 Detailed reaction mechanisms (with net charges in |e|) for Li_2S-(111)/SSE interfaces.

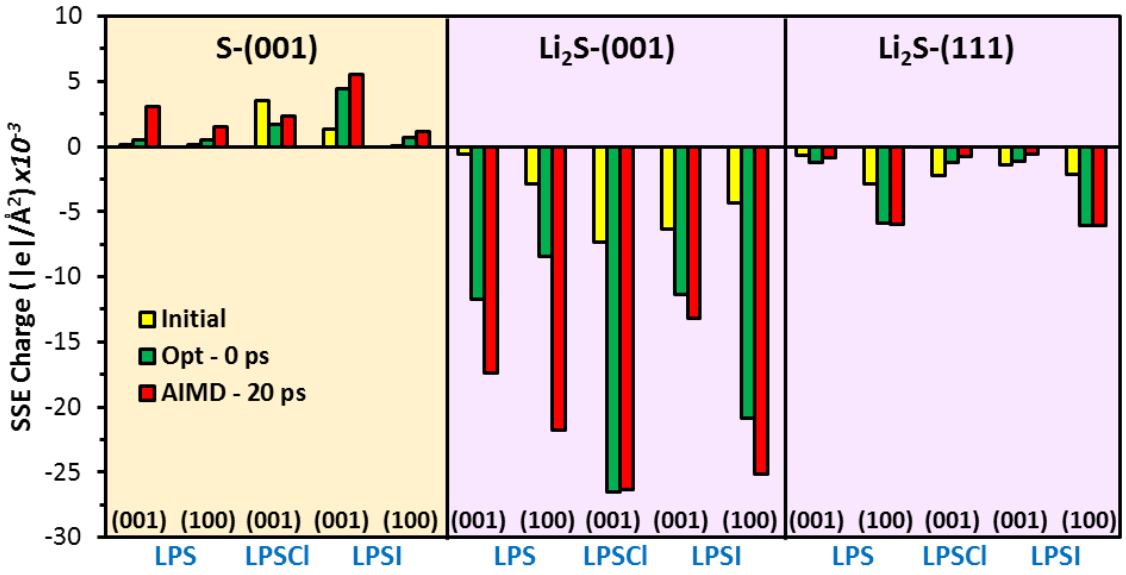

Figure E.24 Area-normalized net charge transfer from/to the SSE materials when in contact with the sulfur cathode model at the initial, optimized, and 20 ps configurations.

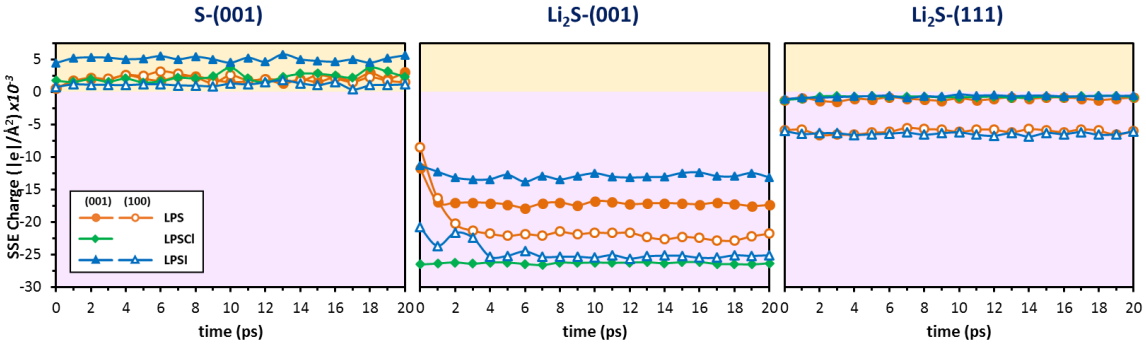

Figure E.25 Time evolution (over the 20 ps of AIMD simulations) of the net charge (per unit of area) of the SSEs due to the formation of the interface with the three S-cathode models.

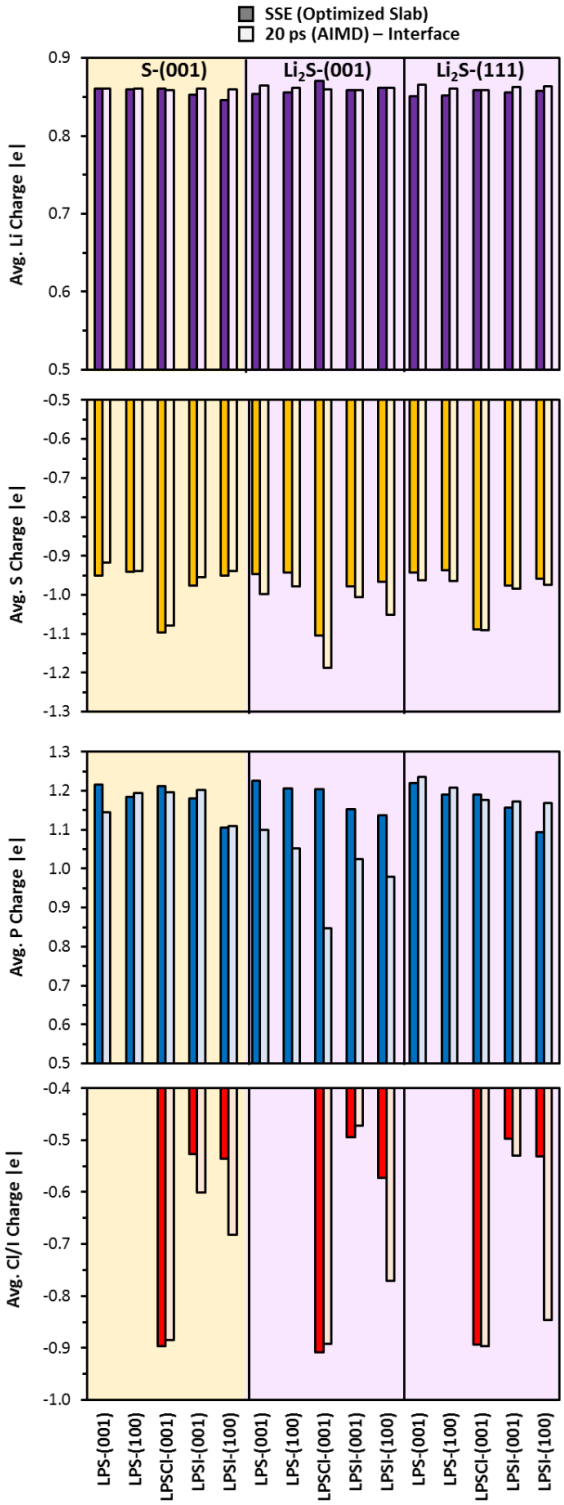

Figure E.26 Averaged atomic charge comparison of the SSEs atomic components at 20 ps of AIMD simulations and the DFT-optimized slab (no interface with cathode formed).

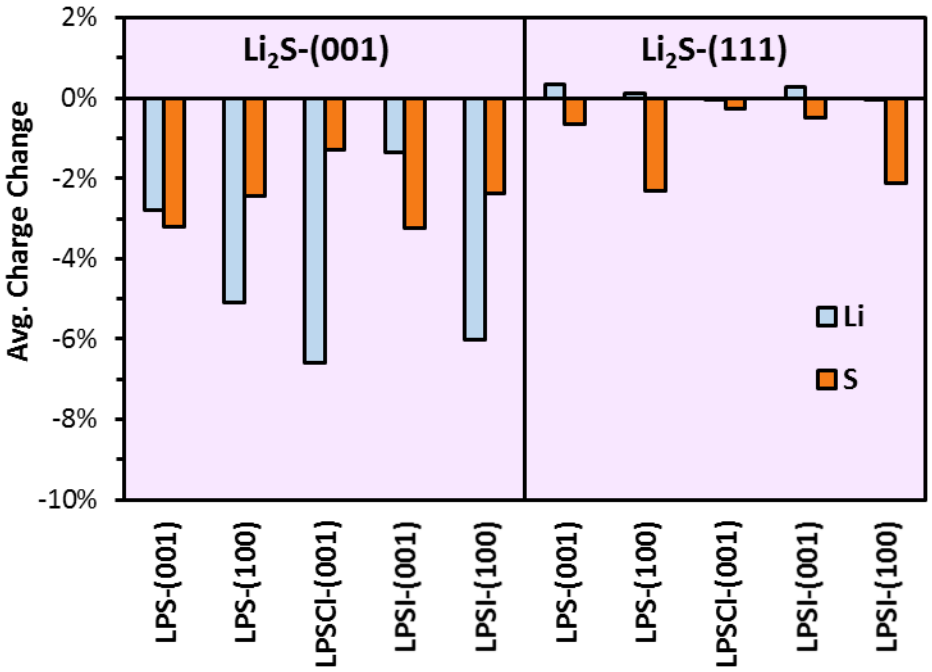

Figure E.27 Relative charge change of the Li_2S atomic components at 20 ps of AIMD simulations with respect to their charge in the (strained) DFT-optimized slab.

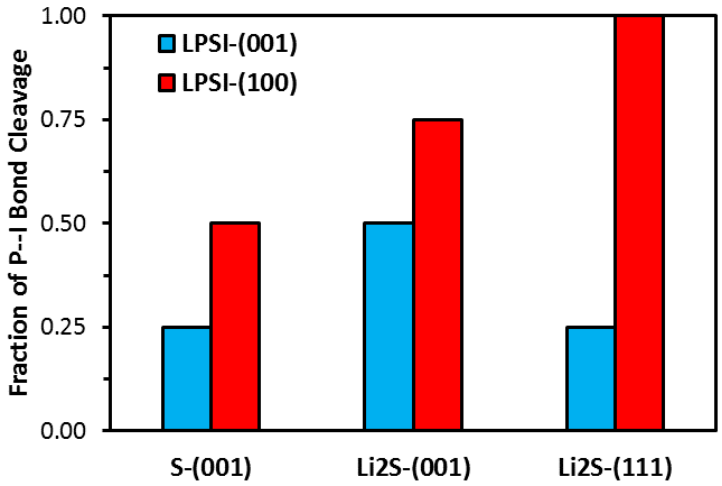

Figure E.28 Fraction of P-I bonds of the mixing anion (LPSI electrolyte) cleavage at the end of the 20 ps of AIMD simulations.

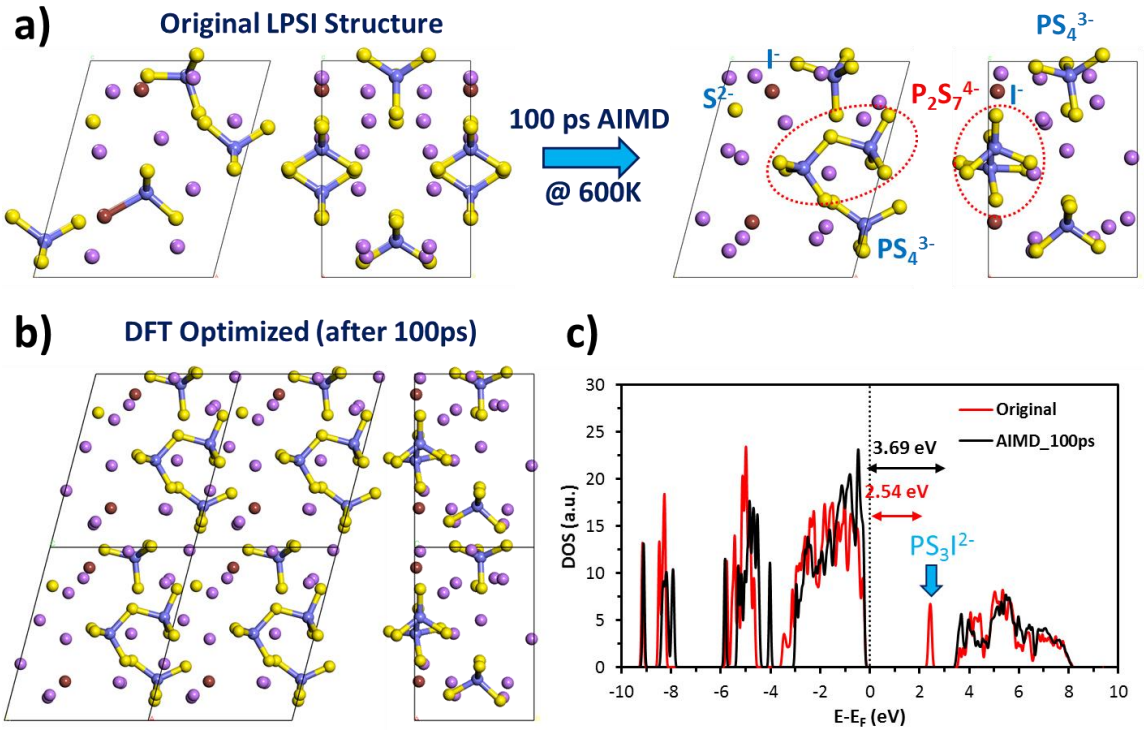

Figure E.29 Possible new structure of LPSI obtained from AIMD simulations. a) Chemical and structural changes of original reported LPSI structure after 100 ps of AIMD simulation at 600 K; b) DFT-optimized new structure (initial taken from 100 ps of AIMD); and c) comparison of the DOS for both original and new LPSI structures.

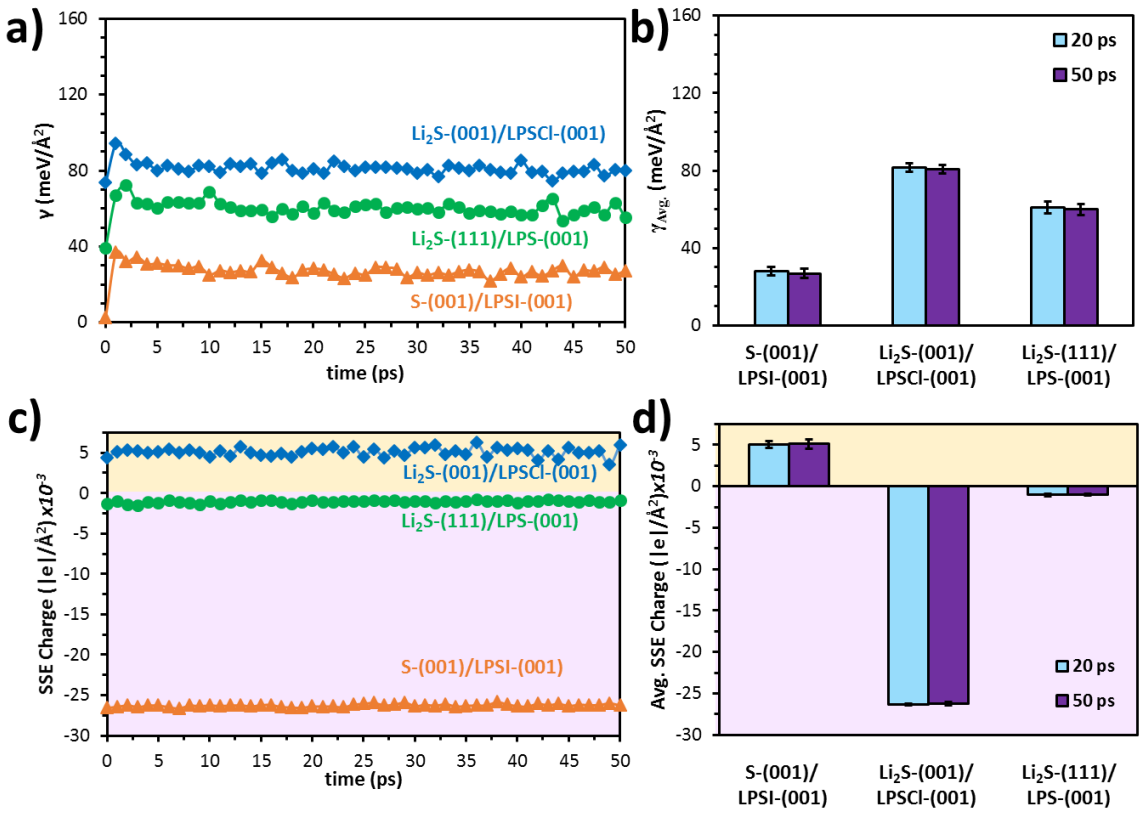

Figure E.30 Time evolution of (a) interfacial energy and (c) charge of the SSE for AIMD simulations up to 50 ps for three selected interfaces. Comparison of time-averaged b) interfacial energy and d) charge of SSE (per unit area) up to 20 and 50 ps. The averages of each property were obtained by sampling γ and the charge every picosecond from 5 ps to 20 or 50 ps (error bars show the standard deviation).